Elastic Actuator Line modelling for the Wake-induced Fatigue Analysis of Horizontal Wind Turbine

by

Hang Meng

A thesis
presented to the University of Waterloo
in fulfillment of the
thesis requirement for the degree of
Doctor of Philosophy
in
Mechanical and Mechatronics Engineering

Waterloo, Ontario, Canada, 2018

Examining Committee Membership

The following served on the Examining Committee for this thesis. The decision of the Examining Committee is by majority vote.

External Examiner: Dr. Jason Jonkman

Supervisor(s): Professor Fue-Sang lien

Internal Member: Professor Gregory Glinka

Internal Member: Professor Cecile Devaud

Internal-external Member: Professor Francis Poulin

Author's Declaration

I hereby declare that I am the sole author of this thesis. This is a true copy of the thesis, including any required final revisions, as accepted by my examiners. I understand that my thesis may be made electronically available to the public.

Abstract

The fatigue damage on wind turbine blades will threaten the safety and stability of the wind turbine and thus lower the efficiency and economy of the power generation system. The wake-induced fatigue plays an important role in this fatigue damage, which has not been deeply studied in the previous research of this domain. This is because the calculation of fatigue damage on a wind turbine blade under wake conditions will include the knowledge of wind turbine wake (fluid mechanics), composite structure modelling (solid structure modelling), aero-elastic modelling (coupling between fluid and structures), and fatigue analysis. Moreover, the anisotropic composite wind turbine blade, e.g. bendtwist coupling blade, will also bring challenges for the structural modelling. To propose a model to solve the above problems holistically is the motivation of the thesis. In this thesis, to construct the aero-elastic model under wake conditions for fatigue analysis, the elastic actuator line model is proposed and verified. To consider the anisotropic properties of composite wind turbine blade, e.g. bend-twist coupling wind turbine blade, the anisotropic wind turbine blade structure model is constructed. Based on the structure model and cross sectional analysis method (BECAS), the fatigue analysis methodology is proposed. Due to the similarity between the anisotropic wind turbine blade structure model and Maxwell's equation (electromagnetic equations), the FDTD method, which is a FDM based method and long been used in electromagnetic simulation, is applied to construct a novel anisotropic wind turbine blade structure model. Specifically, firstly, the actuator line model is validated in terms of thrust coefficient and flow field prediction. It is found that the nacelle effect has impact on the velocity profile around wake center region. And the proposed single-point nacelle model, single momentum source point smeared by Gaussian function, can be used to correct the prediction not only for RANS turbulence model but also for LES turbulence model. Secondly, Based on NREL SOWFA, the elastic actuator line model is constructed as an aero-elastic model for wake conditions to simulate the dynamic loading of wind turbine blade. The stochastic and deterministic wake-induced fatigue loading are reproduced by the proposed elastic actuator line model. Compared with the explicit elastic actuator line model, the implicit elastic actuator line can run with larger time step. However, the accuracy of implicit method will decrease. Thirdly, the performance of normal and bend-twist coupling wind turbine blade with anisotropic composite materials in wake conditions are studied by using the fatigue analysis methodology based on anisotropic structure model, cross sectinal analysis, and fatigue analysis method. Based on this fatigue analysis methodology, the fatigue life of NREL 5MW wind turbine blade is analysed. The predicted fatigue life (26.0187 years) of the main structure (spar caps) is very close to the design life (20 years). From the fatigue analysis for wind turbines in wake conditions, it is found that the wake-induced fatigue has a significant impact on the fatigue life of wind turbine blades (fatigue life drops from 26.0187 years to 1.7388 years under compact layout). And wind farm layout can affect the wake-induced fatigue damage (increase from 1.7388 years (compact

layout) to 6.9084 years (normal layout)). Furthermore, it is also found that the bend-twist coupling wind turbine blade can alleviate the fatigue load under wake condition. Lastly, the structure model based on FDTD method is constructed for anisotropic wind turbine blade and validated in terms of beams with deformation coupling, non-inertia coordinate system, and non-uniform sections (real wind turbine blade). The stability analysis for the proposed FDTD model is carried out, which shows that the root cause of the numerical instability for the proposed method is the highest-frequency mode in numerical model. Based on this analysis, the unconditionally stable explicit FDTD structure model is proposed and constructed, which strikes a balance between accuracy and efficiency. Compared with implicit method, the unconditionally stable explicit FDTD model overcomes its limitations on time step with little effect on its solution accuracy.

Acknowledgements

I would like to owe my first and deepest gratitude to Professor Fue-Sang Lien, my supervisor, for his constant and unconditional support and guidance. He taught me not only how to do research but also what the science and engineering are, which reshapes my academic and world view. It is a good memory of mine to work, study, and research with Professor Lien, which is also the treasure and a new chapter in my life. I am also deeply grateful to Professor Gregory Glinka, Professor Cecile Devaud, and Professor Francis Poulin. Their thoughtful suggestions help me improve the research work. I would also like to show my gratitudes to Dr. Jason Jonkman for his coming all the way from America. And I would like to thank my former supervisor in China, Yongqian Liu, who provides me with lots of knowledge and support. I am also grateful to my research group members, friends, visiting scholars in our lab, and teachers. They are beautiful notes which my life is composed of. Thank the NREL group for sharing the data and open-source code.

It is my pleasure to express my gratitude to my mother country, the People's Republic of China, and my parents, for the financial and spiritual support. Thanks also to my alma maters, the University of Waterloo and NCEPU.

This is the most wonderful journey that I have ever experienced. After finishing the thesis, I still realize there is plenty of research work to do in this domain. Knowledge has no limit. But I still wish my thesis could inspire some researchers or engineers in the way that I was inspired. Just as the Chinese modern philosopher Shi Hu said, "Maybe I am not the one who tastes the fruit of success in the end, but my every effort will never be wasted".

Table of Contents

List of Figures

List of Tables

Nomenclature

Characters

Symbol	Description	Unit
C_L or C_l	Lift coefficient	1
C_D or C_d	Drag coefficient	1
ρ	Density	kg/m^3
$\vec{f}_{2D}$	Aerodynamic force	N
c	Chord length	m
u_{rel}	Relative velocity magnitude	m/s
u_t	Tangential velocity	m/s
u_n	Normal velocity	m/s
α	Local angle of attack	$degree$
Ω	Rotational speed of rotor	rpm
Φ	Inflow angle	$degree$
β	Pitch angle	$degree$
a	Axial induction factor	1
a'	Tangential induction factor	1
ε	Gaussian radius	1
q	Displacement of beam element	m
EI	Stiffness of beam section	Nm^2
V	Velocity of beam element	m/s
M	Moment of beam section	Nm
N_c	Centrifugal force on the beam section	N
Δt	Time step	s

Abbreviations

Acronym	Description
CFD	Computational Fluid Dynamics
NREL	National Renewable Energy Laboratory
FAST	Fatigue, Aerodynamics, Structures, and Turbulence
SOWFA	Simulator fOr Wind Farm Applications
BECAS	BEam Cross section Analysis Software
CFL	Courant-Friedrichs-Lewy
BEM	Blade Element Mometum
BTC	Bend Twist Coupling

Chapter 1

Introduction

Wind power generation is a promising energy utilization way with a high level of commercial competence and less carbon emission. Today, there is 12239 MW wind power which has been installed in Canada. Among all the provinces, Ontario ranks the top one. For Ontario electrical grid, the wind power also accounts for more and more proportions (9% until now) on the whole power generation system. As a result, wind energy has a great impact on the daily life of the Ontario residents. However, plenty of technical problems arise for the wind energy utilization. Among them, wake effect is one of the most important issues.

For modern wind energy utilization, wind turbines are always clustered as a wind farm (e.g. the 132 MW wind farm in Ontario with 88 wind turbines), in which the wind turbines share the same management, maintenance, and electrical system. Unfortunately, the compact distance between wind turbines will make wake effect commonly exist in the current wind farms.

Due to the presence of rotating blades, the wake flow of upstream wind turbine is characterized by decreasing velocity and increasing turbulence intensity. As a result, the downstream wind turbine performance will be affected by the upstream wake. Generally speaking, wind turbine wakes can result in 10 %-20 % decline of whole power production and 5 %-15 % increase of fatigue load on the wind turbine rotor. Previous research and practice mainly concentrate on the wake effect of power loss. Since the study of wake-induced fatigue is an interdisciplinary research domain, including methods of wake modelling, aero-elastic modelling (including aerodynamics and structural modelling), fatigue analysis, few research papers were found in this domain compared with the research on the wake-induced power loss. However, the fatigue damage on the wind turbine blades will threaten the safety and stability of the wind turbine blade and thus lower the economy and efficiency of the power generation system. The fatigue issue is also a bottle-neck for the design of large wind turbine blade. As a result, how to simulate the dynamic loading under wake conditions and quantify the wake-induced fatigue damage accurately and efficiently is a problem. Moreover, the current fatigue mitigation method, such as bend-twist coupling

wind turbine blade, will also increase the difficulty of the first problem, which will also be seriously considered in this thesis. The motivations of the thesis will be comprehensively introduced in the following section.

1.1   Motivations

Wind turbine blades account for 13 % of the onshore wind turbine total cost according to the published data, which are obviously very important to the manufactures and operation companies. As a result, Fatigue damage analysis for wind turbine blade is significant for the design and maintenance of a wind turbine blade. However, the calculation of fatigue damage on a wind turbine blade will include the knowledge of wind turbine wake (fluid mechanics), anisotropic composite blade modelling (solid structure modelling), aero-elasticity (coupling between fluid and structures), and fatigue analysis. Furthermore, all of the mentioned models should be coupled together efficiently, because the fatigue analysis requires long simulation time (physical time). According to the research papers in this domain, there exist two difficulties in modelling the dynamic loading for the wake-induced fatigue.

On one hand, the design life of wind turbine blade is normally 20 years. During its life time, the wind turbine blade will suffer from the turbulence in the surrounding atmosphere and turbulent wind turbine wakes. Obviously, the simulation of this turbulent flow involves two scales of flow: atmospheric flow and wind turbine wake flow, which increases the computational cost for numerical models (e.g. CFD model for wind turbine wake). Moreover, the CFD model will also be coupled with the aero-elastic model to simulate the dynamic loading, which further raise the computational cost. In summary, the difficulty is the coupling between different scales of flows (atmospheric flow and wake flow) and the coupling between fluid models and aero-elastic models.

On the other hand, the wind turbine blade structure is complicated, because it is a twist composite structure with different airfoil shapes on different sections. Different sections of the airfoil, including the leading edge, trailing edge, and spar caps, consists of different composite material layers. For bend-twist coupling wind turbine blade, there exist orientation offset on the fibres of the composite, which makes the structure more anisotropic, i.e. bend and twist deformations are coupled together. The application of composite materials in wind turbine blade enhances the anisotropy of the structure, which will also bring challenges to the modelling of wind turbine blade structures. The conventional beam models are not accurate enough for the anisotropic beam modelling.

To propose a model to solve the above problems holistically is the motivation of the thesis. It should be mentioned here that the current research is inspired by the National Renewable Energy Laboratory 's work on coupling between SOWFA code (fluid mechanics

solver) and FAST 7.0 code (aero-elastic code). However, in the current research, instead of using modal approach in NREL FAST 7.0, a novel finite-difference-method based model is proposed to be the structure model, which is simple to be programmed and coupled with fluid mechanics solver. This FDM structure model is further improved and generalized by using FDTD method. Furthermore, the cross sectional analysis method (DTU BECAS) is employed to consider sectional stress (and strain) for different materials and the anisotropic properties of wind turbine blade. By using the proposed model, the wake-induced fatigue damage will also be studied, which will provide more understanding about the performance of normal and bend-twist coupling wind turbine blade under wake conditions.

1.2 Objectives and proposal

Based on the aforementioned two motivations, the two objectives of the thesis are as follows:

(1) To construct an aero-elastic model under wake conditions to simulate the dynamic loading on the wind turbine blade for fatigue analysis.

(2) To construct an advanced structure model, which considers the anisotropic properties of composite materials, for the above aero-elastic model.

The idea to solve the first problem is to use the actuator line, which is not only a wake model but also an aerodynamic model. If we can build a FDM based structure model which can be easily and efficiently coupled with actuator line model, then the aero-elastic model for wake conditions can be constructed. This is the first novelty of the thesis.

For the second problem, we further extend the proposed structure model to the anisotropic formulation by using the Newtonian method, in which we found that the derived equations are very similar to the Maxwell equations. As a result, a numerical method for Maxwell equations, namely FDTD method [4], is employed to solve the anisotropic structure equations. This method can strike a good balance between accuracy and efficiency. This is the second novelty of the thesis.

In this thesis, to finish these two objectives, a four-stage research is carried out, which are the four chapters in the thesis.

(1) During the stage one or Chapter 2, atmospheric and actuator line models based on NREL SOWFA code are introduced and validated in terms of flow field and thrust coefficient prediction. The individual wind turbine wake, multi-wake interactions, and wind turbine wakes in the wind farm are all studied. The comparison in terms of employing turbulence models is also carried out.

(2) In the stage two or Chapter 3, the elastic actuator line model is proposed and constructed, which is based on the two-way coupling approach combining the conventional actuator line and the proposed structure model. The proposed elastic actuator line model

is verified by comparing with NREL FAST 7.0. To enlarge the time step, an implicit formulation for elastic actuator line is also proposed and verified. By using the implicit elastic actuator line model, the characteristics of dynamic loading of wind turbine blade are studied.

(3) In the stage three or Chapter 4, the research focuses on the fatigue analysis methodology for the proposed elastic actuator line. The anisotropic beam model for composite wind turbine blade based on the FEM method is constructed and validated. To fill the gap between the dynamic loading from beam structure model and stress (and strain) time series for fatigue analysis, the cross sectional analysis method BECAS is employed. The fatigue analysis methodology is constructed. Based on this methodology, the performance of normal and bend-twist coupling wind turbines under wake conditions is studied.

(4) In the stage four or Chapter 5, the research focuses on improving the structural modelling for the proposed elastic actuator line. The anisotropic wind turbine blade structure model based on the FDTD method is proposed based on the formulation described in stage two. The structure model in this stage is the generalized formulation of the stage two model. The proposed FDTD model is further validated in this stage. In addition, the stability analysis for the proposed FDTD model is carried out to find out the root cause of numerical instability. Based on this analysis, the unconditionally stable FDTD structure model is proposed and verified, in which the time step can be enlarged without losing accuracy compared with implicit method. This approach strikes a balance between accuracy and efficiency.

In summary, for the first two stages, the elastic actuator line model is proposed, constructed, and verified. In the next two stages, the components in elastic actuator line model, including fatigue analysis and structure modelling, are refined and improved. The main body structure of the thesis is shown in Figure 1.1.
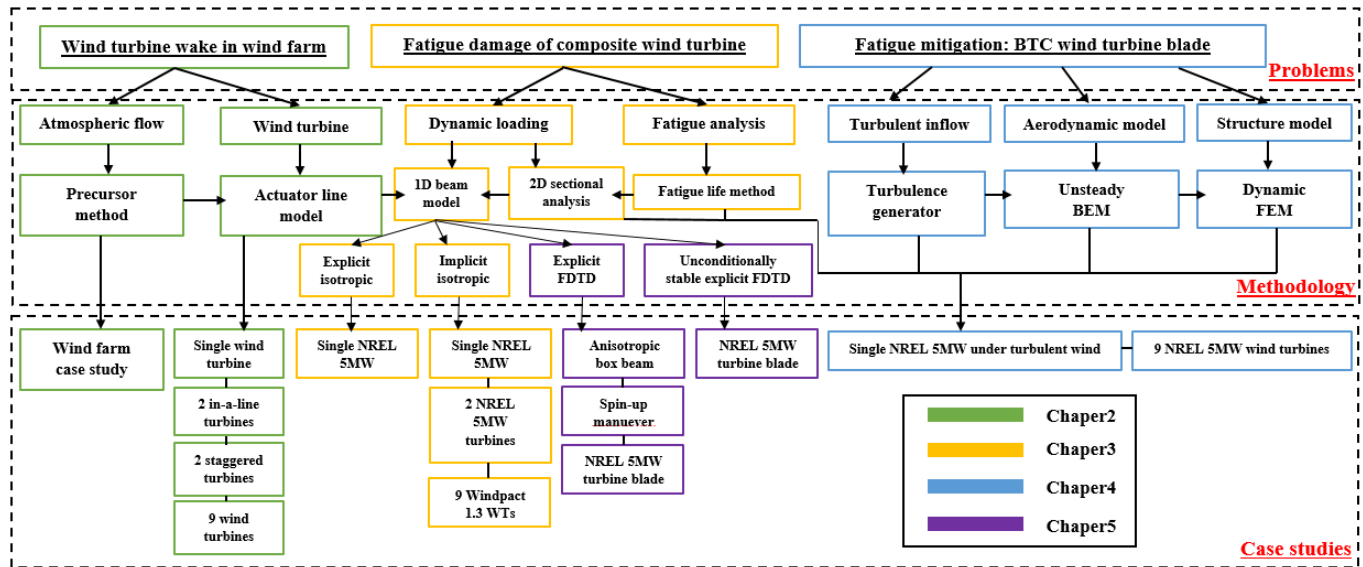
Figure 1.1 Thesis outline.

1.3 Literature review

In this section, the research papers related to the aforementioned topics are reviewed. Firstly, since wake modelling is the foundation of the elastic actuator line model in this thesis, the history and development of wake models are reviewed in Section 1.3.1. Secondly, the papers of observations about the wake-induced fatigue are introduced in Section 1.3.2 to back up our motivations in Section 1.1. Thirdly, the fatigue analysis method for wind turbine blade are reviewed in Section 1.3.3. The first three sections of literature review is related to the first objective in Section 1.2. The next two sections, including Section 1.3.4 and 1.3.5, are related to our second objective. In these two sections, the application of bend-twist coupling wind turbine blade and the anisotropic wind turbine blade models are also fully reviewed.

1.3.1 Wind turbine wake modelling

Wake models are the essential part for wake-induced fatigue analysis. The development of wind turbine wake models has mainly witnessed 3 stages.

The first stage is the semi-empirical modelling stage (1979-1988). In the beginning, Lissman proposed a model based on jet theory and empirical assumptions [5]. The Lissman model is feasible, but not practical. Then it was followed by Jensen wake model, which is based on the momentum integral equation [6]. Despite ideal assumptions are still required, this model has been proven to be efficient and effective by engineering practice and adopted by commercial software WindSim. Unlike Jensen model's uniform distribution assumption, Larsen presented an analytical model based on similarity solution theory [7].

Actually, Larsen model is more similar to the real wake flow in terms of velocity distribution, however, it often underestimated wake recovery which is caused by turbulence and restricts its application to the large wind farm. Unfortunately, this problem is common in the analytical wake models.

As a result, in the second stage (1991-1999), in order to consider the effect of turbulence, the Reynolds Average Navier-Stokes (RANS) method has occurred in this domain. Ainslie model is a two-Dimensional RANS model, which neglects radial and tangential velocities. Remarkably, a pre-calculated near wake velocity distribution is employed. Similarly, Taylor proposed a three-dimensional RANS model of one equation turbulence model, which accords with the observations in wind tunnel [8]. Then Crespo used a two-equation turbulence model based on the similar assumption of Taylor's, while discrepancy between its results and data from wind farm measurement was obvious [9]. All of models mentioned above are quasi-steady wake models in which near wake flows are pre-calculated. In addition, the turbulence intensity in wake flows is derived from the effective turbulence model so that dynamic wake flows in front of the downstream turbine is the superposition of steady and fluctuating wind [10]. Noticeably, in the first two stages, the ambient flows and each wake flow are simulated separately (except for the Crespo model). In addition, the average velocity field and turbulent velocity in wakes are simulated separately without concerning the atmospheric turbulence-turbine interaction (or turbine modelling). In fact, these models was firstly proposed to calculate the long-term power loss due to wind turbine wake in early years. The simplification is also due to the computational capability at that time. Although these models are rather efficient and still prevalent in the engineering practice until now, the lack of coupling between wake flows and ambient flow is still a limitation for unsteady modelling (like dynamic loading). Moreover, those in this and its previous stages are all conventional wind turbine wake models, which mainly concentrate on individual wake modelling.

As a result, in the next stage (2000-now), fully three-dimensional CFD wake models occur, which means that wake flows are simulated within the ambient flows in the wind farm, including all the turbines, terrain and atmospheric motion. These recent achievements are fully reviewed in Sanderse's paper in 2011 [11] and are briefly introduced in this section. The most striking characteristic of these recent works is the rotor modelling, which is in previous work too much simplified as a pre-calculated near wake velocity distributions. By employing the rotor modelling, complex phenomenon, e.g. tip vortex shedding (and root vortex) and dynamic loading, can be reproduced naturally. The first rotor model is proposed by Sorensen [12], which is the actuator disc model. For this model, the wind turbine rotor is represented as body force "disc", which is smoothed by applying a Gaussian function in the computational domain. Normal and heavy loading situations are successfully simulated in this case. It was followed by Leclerc's work [13] in 2004, in which the vortex ring is reproduced based on the actuator disc principle. This work is further tested by NREL wind

tunnel experiment [14]. As for the validation paper [15], actuator disc is proven to be an effective method to predict the far wakes in wind farm. However, the near wake vortex structure is different compared with full rotor computation (full-resolved blade, CFD), which will restrict its application on the dynamic loading simulation. Similar validations can also be found in the Mikkelsen's paper [16]. Although some limitations still exist (only valid for rotationally symmetric flow conditions), actuator disc is still commonly used not only in the unsteady simulation with LES [17], but also steady simulations due to its high efficiency. To better simulate the vortex structures and dynamic motions of blades in wakes, the actuator line model was proposed [18], in which blades are divided into numbers of elements . For each element, the body force is calculated from the tabulated airfoil data. This method is further studied and validated in Troldborg's paper in 2008 [19]. Research of LES simulation with actuator line can be found in Lu [20] and Conzemius's [21] paper. Next, the actuator surface occurs, in which the blades are represented as body force surfaces [22] [23]. However, finer grids are required for this method, which makes it too much time consuming for engineering practice. Despite these actuator models already give a rather trusty approximations for aerodynamic loading, the direct modelling of rotor is still worthwhile, in which the geometry of wind turbine is fully resolved. These direct modelling works [24][25][26][27]. Despite of its computational-consuming, it can still provide a more accurate, detailed and deep knowledge for the wind turbine wake aerodynamics compared with actuator models [28]. However its large computations and technical difficulties (e.g. meshing of the geometry) of direct modelling are still obstacles for its application on the wind farm simulation. In conclusion, considering accuracy and efficiency, actuator models are the most promising method to reproduce the unsteady wake flows in wind farm nowadays. Among them, actuator line models, which can be used to simulate complicated wake vortex structures and reproduce unsteady wake flows, will be employed in the thesis. However, most research until now on actuator line mainly concentrate on wake-induced effect of power loss and do not consider the elasticity of blades. Although wake flows can be reproduced by conventional methods, dynamic loading cannot be accurately predicted because of the absence of fluid-structure interaction simulation. Recently, research begin to concentrate on the coupling between CFD and structure models, which are, however, almost all one-way coupling methods [29][30], in which structural model does not have impact on the CFD model. Noticeably, NREL has made the first attempt on two-way coupling between LES model and its aero-elastic code [31]. More attempts and studies for its engineering application are still necessary on this realm. In order to fulfill our research objectives, knowledge of aero-elastic simulation of wind turbine is required. In the thesis, the elastic actuator line model is proposed and employed in Chapter 3, which is the two way coupling method between actuator line method and finite-difference-method based structure model. The foundation of elastic actuator line model will be studied in Chapter 2.

Except for the aforementioned models, there still exist three important wake models

in this domain, including vortex model [32], dynamic wake meandering (DWM) model [33], and effective turbulence method [34]. The vortex model, namely the lifting line or lifting surface model, is used for near wake computation and aerodynamic force prediction. This method is based on potential flow assumption (coupled with viscous boundary layer correction sometimes). The bound circulation of the wind turbine blade is first determined from the boundary condition (e.g. Kutta condition). The global flow field is determined by the induction law of Biot-Savart. The dynamic wake meandering model is proposed by Larsen in 2007. This model can capture the dynamic motion of the wind turbine wake, namely wake meandering, which is popular in the dynamic load simulation of wind turbine. The effective turbulence method is proposed by Frandsen, which is employed by GL guidlines for wind turbine certification. This model can be used to calculate the turbulence intensity distribution in the wake region.

1.3.2 Wake-induced fatigue

In the previous section, the wake modelling methods are introduced. In this section, the wake-induced fatigue will be reviewed to back up our motivations. In fact, numbers of previous experimental researches based on field observation support the significant wake-induced fatigue load on wind turbine blades. To begin with, the earliest observation about the wake effect on dynamic loading of wind turbine blades is Dahlberg's paper (1992), the loading data of four Danwin 23/180 kW turbines shows that the wind turbine wake caused a large increase of blade load variation [35]. Per Volund's paper in 1992 concluded two main effects of wakes on the dynamic load of wind turbine blades: Firstly the turbulence is higher in wake than that in the surroundings, which leads to the stochastic load fluctuations. Secondly the blade once per revolution enters and leaves the low speed area of the wake [36], which mainly accounts for the deterministic loading. Similar phenomena can also be found in the observation in the Vindeby off-shore wind farm (450 kW wind turbine) in Denmark [37]. Following research also observes large wake impact on the dynamic load exists not only on on-shore wind farms, but also on offshore ones [38]. In recent observations on the modern Mega-watt wind turbines in Yeong-heung Wind Farm (Korea) in 2014, large wake-induced fatigue was observed [39]. As known to all, the wind turbine is the biggest rotating machine[40], and the blade length is still getting larger. As a result, the fatigue of blades (especially wake-induced fatigue) should be seriously considered and studied. In this thesis, both stochastic and deterministic fatigue loading are studied, and the wake-induced fatigue damage is also researched based on the elastic actuator line model in Chapter 3 and FEM based aero-elastic code in Chapter 4. How to quantify the fatigue damage, or the fatigue analysis method, will be fully reviewed in the next section.

1.3.3   Fatigue analysis method of wind turbine blade

In the domain of fatigue analysis of a wind turbine blade, the moment-based methods are popular in the wind energy industry, because of the utilization of beam models and empirical load spectrum. It is convenient to provide root bending moments (highest bending moment along the blade) from beam models and empirical load spectrum rather than to provide the stress time series. As for the moment based method, the root bending moments, including flapwise and edgewise bending moments, is often used to calculate the Damage Equivalent Load (DEL) based on an M-N curve and the rainflow counting algorithm according to the reference number of load ranges [41–44]. Due to its simplicity and robustness, it is now also adopted in the recent research of bend twist coupling wind turbine blades [45]. However, the fatigue damage of different materials at a blade section cannot be calculated, which is also critical for bend-twist coupling turbine blade design. In order to show the fatigue life of different materials at different cross sections under different wake conditions, the stress-life method is used in this thesis.

In fact, a wind turbine blade is a kind of thin wall composite beam structure. For this kind of structure, there are mainly three methods for fatigue life prediction or fatigue damage analysis, including macroscopic models (fatigue life models or empirical models), phenomenological models (stiffness or strength degradation method), and progressive damage models. These three methods have been introduced comprehensively in the Anastasios' book[46]. The first category of fatigue life models is based on the S-N curves and Constant Life Diagrams (CLD). The fatigue damage is calculated by the empirical damage accumulation rules such as the Palmgren-Miner rule. The damage mechanism is not considered in this model. Contrary to the aforementioned empirical fatigue life models, the second category of models capture the physics of fatigue damage by introducing the fatigue metrics of residual strength or residual stiffness. The fatigue failure occurs when the certain limit of fatigue metric is reached. Despite the phenomenological models can capture the physical meaning of fatigue damage, it does not show better performance compared with the first category of empirical models in the case of variable amplitude loading which is presented in Nijssen's thesis [47]. In the author's view, this is because of the complicated mechanism involved in the fatigue damage of wind turbine blades. Therefore, further corrections and improvements are also required for the phenomenological models. The guidelines for safety factors of phenomenological models are also lacking. The main disadvantage of these two aforementioned methods is that they are limited to the uni-axial loading cases and do not take into account other stress components for fatigue life prediction, e.g. shear stress. But they are reasonable for slender beam structures, such as wind turbine blades, in which the normal stress in the beam axial direction is dominant. To deal with the complex loading patterns, the third category of models or progressive damage models are proposed based on principles of micro mechanics, in which one or more fatigue damage variables related

to the observable damage mechanisms are introduced to model the damage modes, such as transverse matrix cracks and de-laminations. Although this method is the most promising way to predict the fatigue life or the fatigue damage of composite structures, it is still computationally intensive for application. Few authors have applied this method in fatigue life prediction of wind turbine blades. As a result, the first category of fatigue life models, which is also suggested in the GL guidelines for wind turbine manufacturers, are adopted here to analyse the longevity and fatigue damage of different materials of wind turbine blades. The stress time series are reconstructed through the use of DTU BECAS based on the dynamic loading data from the aero-elastic model, e.g. elastic actuator line model.

1.3.4 Fatigue mitigation method for wind turbine blade: Bend-twist coupling wind turbine blade

In the previous section, the fatigue analysis methods are reviewed. In this section, an important fatigue mitigation method, namely bend-twist coupling wind turbine blade design, will be introduced. The bend-twist coupling (BTC) concept stems from aeronautical industry, and it has been successfully used in the design of F-86 Sabre and the Boeing B-47 Stratojet to mitigate the aerodynamic load (see the page 9 of [48]). For wind energy industry, nowadays, there are mainly two different kinds of BTC concepts: "twist-to-stall" and "twist-to-feather". As for the "twist-to-stall" turbine blade, the blade tends to operate in the stall region to reduce the load during instant wind speed increase. However, this BTC technique often makes the blade suffer from the flutter instability [49] and substantial fatigue damage. In fact, the "twist-to-stall" design is always adopted to capture more energy rather than to reduce the fatigue damage [50]. Instead of increasing the angle of attack to the stall region, the "twist-to-feather" blade is designed to decrease the angle of attack when the wind speed suddenly increases. Recent research concentrates on BTC with "twist-to-feather" because of its quick response to gusts and effective fatigue load mitigation effect [45]. The flutter instability and fatigue increase issue in "twist-to-stall" design are not obvious in BTC with "twist-to-feather" design. Nowadays, BTC design has been applied in large off-shore wind turbine blades (e.g. 5MW wind turbine blades). As a result, in this thesis, the "twist-to-feather" BTC blade will be studied and discussed.

In the area of "twist-to-feather" BTC blades, previous research mainly focused on the static analysis or the analysis of dynamic cyclic load [51, 52] of BTC blades based on 3D fully-blade-resolved FEM analysis to achieve higher coupling coefficient. However, for fatigue analysis, aero-elasticity of a wind turbine is also a dominant factor so that the governing equations of flow part and structural part should be coupled and solved together [53]. Due to its large computation cost, the 3D fully-blade-resolved method is less attractive to the researchers and engineers who study multiple wind turbines. Furthermore, the fatigue analysis of wind turbine blades requires large amount of loading time series, which further

increases the computational cost. Although there exist the spectrum method, in which the loading can be generated by using the empirical model, such as WISPERX spectrum [54], these methods are highly dependent on the structure of wind turbine blades and wind turbulence. With the change of structures of the blade and wind conditions (e.g. wake conditions), the nature of the spectrum will also change. As a result, an efficient aero-elastic model for BTC blades is required to generate loading time series. Models based on beam theory are popular in the aero-elastic models of wind turbine blades [53].

The idea of the beam theory is to split the 3D beam structure problem into a 2D cross-sectional analysis problem and a 1D beam modelling problem [55]. As for the 2D cross-sectional analysis problem, the previous models in the beam-theory domain always assume that the beam is made of homogeneous and isotropic materials. These models fail to simulate the anisotropic effects and warping effects caused by the composite materials (e.g. the bend-twist coupling induced by the fibre orientations). To overcome these problems, Giavotto et al. proposed a 2D FEM method to compute the generalized warping functions and cross-sectional properties for beam structures [56]. Based on this theory, the DTU BECAS was developed to analyse the cross-sectional properties of a wind turbine blade. For the 1D beam modelling, the anisotropic beam model on the basis of the aforementioned generalized 2D FEM cross-sectional analysis is also proposed by Kim et al [57]. In the present study, the DTU BECAS (generalized 2D cross-sectional analysis tool) and the anisotropic beam model will be used to generate the dynamic loading of wind turbine blades for fatigue analysis. The BTC effect will be discussed in the Chapter 4. This anisotropy has also been considered in NREL BeamDyn and DTU HAWC2.

1.3.5 Modelling of anisotropic composite wind turbine blade

The aforementioned bend-twist coupling wind turbine blade is anisotropic, which is challenging for structural modelling. The anisotropic beam modelling problem first occurred in the helicopter industry because of the application of composite materials in the helicopter rotor design to strengthen the blade and resist the fatigue damage [58]. The elastic coupling effects mentioned in the previous section (Section 1.3.4) make the displacement fields of the composite blade structure more complicated than the kinematic assumptions of ad hoc beam theories [59], such as Euler-Bernoulli beam theory [60]. In addition, in the classical beam theories or ad hoc beam theories, the structure is assumed to be made of materials with isotropic and homogeneous properties, which is not suitable for the anisotropic beam case. The progress of anisotropic beam modelling attributes to the work of Giavotto, Borri and Hodges [59]. Rather than constructing the consitutive relation between sectional forces and strain in an analytical way, e.g. ad hoc beam models, they build the generalized cross-sectional constitutive equations and three-dimensional warping functions by using linear finite element analysis, namely the linear cross-sectional analysis. In Hodges' book [58], it

is concluded that the three-dimensional anisotropic beam modelling problem can be split into the two-dimensional linear cross-sectional analysis and an one-dimensional nonlinear beam analysis.

Applying the cross-sectional constitutive law of two-dimensional cross-sectional analysis, Kim [61] studied the anisotropic beam model for wind turbine blades with finite element formulation. The nonlinear anisotropic beam model can capture the coupling effects and the inertia effects of the composite wind turbine blade [32]. It should be mentioned here that the beam model is more popular in the research and application than the fully blade resolved three-dimensional simulation in the domain of wind turbine blade structural modelling, because the beam model can be easily extended to the aero-elastic model by coupling it with the aerodynamic model. The aero-elasticity plays a pivotal role in the dynamics of wind turbine blade. By using the aero-elastic model, the dynamic response of wind turbine will be predicted, and the fatigue damage (or longevity) of the blade can be calculated, which is important to the economic evaluation, and the maintenance of the wind turbine.

According to the employed discretization methods, nowadays structral models of aeroelastic simulation for the wind turbine blade can be divided into three categories: beam models based on modal approach [62], multi-body dynamics (MBD) [63], and finite element method (FEM) [64] respectively. Among all these three methods, modal approach, to the author's best knowledge, is the most widely-used method. For example, famous commercial wind turbine aero-elastic softwares DTU FLEX5 [65] and NREL FAST [66] all employ modal approach as their discretization methods. Truncating the high frequency modes, the modal approach lowers the number of degrees of freedom (DOFs) of the structure, which highly boosts the efficiency of the simulation. Normally, the simulation of modal-approach based aero-elastic model is carried out with first three or four modes extracted from finite element model [67]. However, the first three or four modes do not include the torsional modes that are important for the anisotropic wind turbine blade. For the MBD model, the structure is discretized into several bodies that are connected with each other by different joints. DTU HAWC1 employs MBD as its discretization method. It should be mentioned here that the aforementioned anisotropic beam model that is proposed by Kim[61] for HAWC2 is based on the FEM formulation, which will also be employed in Chapter 4.

In the thesis, a novel anisotropic beam model based on finite-difference time-domain (FDTD) method [68] is proposed for the anisotropic wind turbine blade. There are two important features for this model. Firstly, instead of using aforementioned modal approach, MDB method, and FEM, the FDTD method is utilized to discretize the governing equations, which is a finite difference method. In fact, FDTD method is one of the most popular technique to solve electromagnetic problem (or Maxwell's equations), which was first proposed by K. Yee in the 1970s[69]. With its decades' development, the FDTD method is proven to be an effective method to simulate the non-linear dynamic Maxwell's equations

with a wide range of frequencies. Due to its finite-difference nature, the formulation of the numerical model is simpler and intuitive than the MDB or FEM. By using the leapfrog scheme in time, the equations are solved element by element alternately and explicitly, which avoids solving the system simultaneously (e.g. global matrix in FEM) and improves the efficiency of the simulation. For the Maxwell's equations, it is obvious that there exist two sets of equations in terms of electric field and magnetic field respectively, in which the FDTD can be applied directly. For the structural model of wind turbine blade case, normally speaking, we only have one set of equations in terms of displacements. In the author's views, this is the main reason why there is no previous research that applies FDTD method to structural modelling of wind turbine blade. In this research, to make the structural models adapt to the FDTD method, the aforementioned one set of equations in terms of displacement are manipulated into two sets of equations in terms of velocity (and angular velocity) of beam elements and sectional moment (and force) as dependent variables. This is the second important feature of the proposed model. Noticeably, the two sets of dependent variables are coincidently what are required for the aero-elastic model. Specifically, the velocities (and angular velocities) of beam elements are used for the coupling between the aerodynamic model and structural model. This idea of modelling was proposed in Chapter 3, and it will be generalized in Chapter 5. The sectional moments (and forces) are used in the fatigue damage calculation. Obviously, the aforementioned two features provide the proposed model with advantages over the previous method of structural modelling of wind turbine blade.

1.3.6   Chapter summary

In this chapter, the problem, objectives, motivations, and the previous research work are all comprehensively introduced to support the motivation and novelty of the present research work. From the literature review, firstly, the wake-induced fatigue is very significant in nowadays onshore and offshore wind farms. However, secondly, the current wake models are mostly for the study of wake-induced power loss, in which the structural deformation is not considered. Moreover, thirdly, the fatigue mitigation method, e.g. bend-twist coupling wind turbine blade, provide the modelling of wind turbine blade with lots of challenges. As a result, its meaningful to deal with the modelling of aforementioned problems, which will be illustrated in the following chapters.

Chapter 2

Actuator line model

2.1 Principle of actuator line model

The reason why conventional fully-blade-resolved CFD simulation is computationally expensive for wind turbine case is that the blade geometry should be resolved, which increases the number of cells and limits the time step because of the Courant–Friedrichs–Lewy(CFL) condition. Instead of resolving the blade geometry, in actuator line model, the blade effect is simplified by applying rotating body forces in the structured background mesh, which also actuates the flow field as the real wind turbine blades. The body forces can be calculated in the Blade-Element-Momentum (BEM) manner, in which the forces are predicted according to the 2D aerodynamics of the airfoil, namely velocity triangle as the following Figure 2.1. Specifically, the lift and drag coefficients and forces are determined by the local velocites through 2D tabulated data (C_L and C_D curves) for each blade element. The equation for the body force per unit length (or aerodynamic force) are shown in the Equation (2.1).

$$\vec{f}_{2D} = \frac{1}{2}\rho u_{rel}^2 c(C_L(\alpha)\vec{e}_L + C_D(\alpha)\vec{e}_D) \tag{2.1}$$

Where ρ is the air density, and c is the chord length of the airfoil. C_L and C_D are life and drag coefficients respectively, which are functions of local angle of attack (α) and Reynolds number (Re). $\vec{e}_L$ and $\vec{e}_D$ are unit vectors of lift and drag forces. u_{rel} is the relative velocity magnitude, which is calculated by Equation (2.2).

$$u_{rel} = \sqrt{(u_t)^2 + (u_n)^2} = \sqrt{[\Omega r(1 + a')]^2 + [u_\infty(1 - a)]^2} \tag{2.2}$$

Based on Equation (2.3), the local angle of attack α can be calculated according to the local velocities, including u_t and u_n (tangential and normal velocities), which are shown in Figure 2.1.

$$\alpha = \Psi - \beta = \arctan(\frac{u_n}{u_t}) - \beta \tag{2.3}$$

In Equation 2.3, Ψ and β are inflow angle and pitch angle respectively. Equation (2.3) is very similar to calculation of angle of attack in BEM method. However, from Equation (2.2), the most obvious difference between BEM model and actuator line model in terms of aerodynamic force prediction can be illustrated, which is the calculation of axial and tangential induction factors, namely a and a' in Equation (2.2). These two factors quantify the induced velocity from the vortex system around the rotating wind turbine blades, including bounding vortex, tip vortex, and root vortex. When the thrust coefficient C_T is higher than 0.5 (or axial induction factor is above 0.4), the near wake region of wind turbine becomes turbulent, which breaks the laminar flow assumptions of BEM. To remedy this problem, the empirical corrections, such as Glauert correction, should be employed. For actuator line model, the applied body forces will produce vorticity by which the vortex system around wind turbine can be generated without laminar flow assumption. The induction factors a and a' are contained the local velocities. Specifically, the aforementioned body forces $\vec{f}$ occurs in the Navier-Stokes equations as the momentum source.
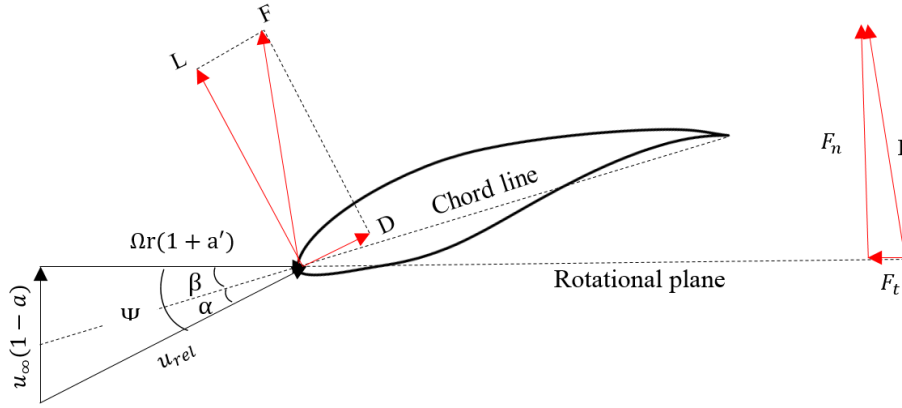
Figure 2.1 Velocity triangle for the airfoil in the local inertia coordinate system.

$$\rho\frac{\partial u_i}{\partial t} + \rho u_j \frac{\partial u_i}{\partial x_j} = -\frac{\partial p}{\partial x_j} + \mu\frac{\partial^2 u_i}{\partial x_j \partial x_j} + f_i, \quad \frac{\partial u_i}{\partial x_i} = 0 \tag{2.4}$$

In Equation (2.4), the body force components f_i are not directly equal to the components of local aerodynamic force $\vec{f}_{2D}$. To avoid singularity caused by the applied forces, Gaussian function (or kernel function) is employed to smear the forces $\vec{f}_{2D}$ in the flow field. The formula to calculate the effect $\vec{f}_\varepsilon$ of local aerodynamic forces $\vec{f}_{2D}$ located at $\vec{x}$ to the grid point whose cell center is located at $\vec{c}_a$ is shown in Equation (2.5).

$$\vec{f_\varepsilon} = f_{2D} \otimes \eta_\varepsilon, \quad \eta_\varepsilon = \frac{1}{\varepsilon^2 \pi^{\frac{3}{2}}} e^{-\left(\frac{|\vec{x}-\vec{c}_a|}{\varepsilon}\right)^2} \tag{2.5}$$

In this equation, ε is the parameter to control the concentration and radius of the Gaussian function. $\otimes$ represents the convolution operator, which is illustrated in Equation (2.6). The body force $\vec{f}$ for each grid point is the summation of the effects of all the actuator points (or kernels), see Equation (2.6) and Figure 2.2.

$$\vec{f}(\vec{x}) = \sum_{i=1}^{B} \int_0^R \vec{f}_{2D}(\vec{c}_a(r)) \eta_\varepsilon(|\vec{x} - \vec{c}_a(r)|) dr \tag{2.6}$$

In this Equation, B is the number of the blades, and R is the rotor radius. r is the span-wise distance. The actuator points are distributed along r direction, and dr is the length of actuator line element.
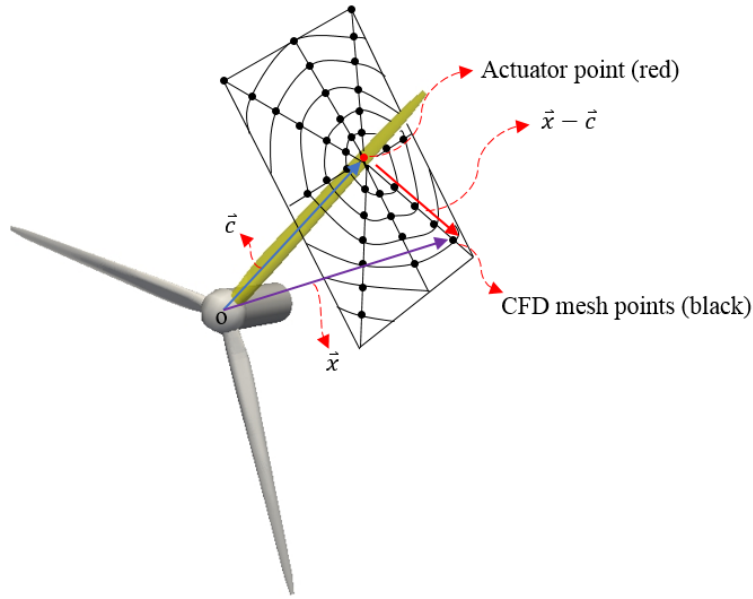
Figure 2.2 Sketch of actuator line model.

From the previous statement, it can be found that actuator line model has two important functions. On one hand, the actuator line model is an efficient rotor model to perturb the flow field and generate the wind turbine wake flow, which is also a feasible way to connect the macro scale simulation (atmospheric simulation) and micro scale simulation (wind turbine wake). On the other hand, the actuator line model is also an aerodynamic model with less assumptions compared with widely-used BEM model. In the following sections, these two aspects will be validated by using wind tunnel experiment data.

2.1.1 Turbulence models for wind turbine wake

The vortex system around the wind turbine blades will break down at the end of near wake region because of turbulence effect. In the far wake region, the ambient flow turbulence (atmospheric turbulence) will help the wake velocity recover. As a result, the turbulence model is necessary for the wind turbine wake simulation. There are two types of models that are widely used in this domain: Reynolds-averaged Navier-Stokes method (or RANS model) and large eddy simulation technique (LES). Generally speaking, the RANS model is enough for the prediction of wind turbine wake velocity profile in wind tunnel experiment, which has been proven by several validation cases. It indicates that the wake flow itself is rather "isotropic". In the author's opinion, there are two reasons why LES attracts attentions of researchers recently. Firstly, the atmospheric flow (near wall flow) in wind farm is naturally anisotropic. The second reason is that a wide range of perturbations of velocity can be simulated by LES which is essential to the dynamic loading and fatigue damage of wind turbine. In the following part, two typical models : standard $k - \epsilon$ two-equation model and LES model with Smagorinsky and one-equation SGS models will be introduced in sequence.

When the Reynolds number keeps on increasing, the solution of Navier-Stokes equations becomes chaotic. It is hard to capture the small scale eddies (e.g. Kolmogorov scale eddy) in high Reynolds number flow by using the current numerical methods because of the high computational cost and the restriction of grid number. However, the coarse grid will remove the small eddies, which dissipate the kinetic energy of large eddies in high Reynolds number flow. To solve this problem, in RANS method, the velocity (and other flow variables) are decomposed into time averaged component $\overline{u}$ and fluctuating component u', namely Reynolds decomposition. Instead of solving the original equations, the equations of averaged component $\overline{u}$ are solved, which is more "smooth" and less chaotic. The effect of the removed small eddies is modelled by several added equations. The Reynolds averaged incompressible Navier-Stokes equations of motion in conservation form are as follows:

$$\rho \frac{\partial \overline{u}_i}{\partial t} + \frac{\partial}{\partial x_j}(\rho \overline{u}_i \overline{u}_j + \rho \overline{u'_i u'_j}) = -\frac{\partial P}{\partial x_i} + \frac{\partial (2\mu S_{ij})}{\partial x_j} + f_i, \quad \frac{\partial \overline{u}_i}{\partial x_i} = 0 \qquad (2.7)$$

In Equation (2.7), S_{ij} is the strain-rate tensor:

$$S_{ij} = \frac{1}{2}\left(\frac{\partial \overline{u}_i}{\partial x_j} + \frac{\partial \overline{u}_j}{\partial x_i}\right) \qquad (2.8)$$

In Equation (2.7), the negative of term $\rho \overline{u'_i u'_j}$ is called Reynold stress tensor:

$$\tau_{ij} = -\rho \overline{u'_i u'_j} \qquad (2.9)$$

In the $k - \epsilon$ model, the turbulence kinetic energy k equation and dissipation rate equation ϵ equation, are used to model the Reynold stress tensor τ_{ij} based on the Boussinesq assumption, which is given in the following equation:

$$\tau_{ij} = 2\mu_T S_{ij} - \frac{2}{3}\rho k \delta_{ij} \tag{2.10}$$

where μ_T is the eddy viscosity, which is a function of k and ϵ:

$$\mu_T = \rho C_\mu \frac{k^2}{\epsilon} \tag{2.11}$$

The equation of turbulence kinetic energy is:

$$\rho \frac{\partial k}{\partial t} + \rho \bar{u}_j \frac{\partial k}{\partial x_j} = \tau_{ij} \frac{\partial \bar{u}_i}{\partial x_j} - \rho\epsilon + \frac{\partial}{\partial x_j}[(\mu + \frac{\mu_T}{\sigma_k})\frac{\partial k}{\partial x_j}] \tag{2.12}$$

The equation of dissipation rate is:

$$\rho \frac{\partial \epsilon}{\partial t} + \rho \bar{u}_j \frac{\partial \epsilon}{\partial x_j} = C_{\epsilon 1}\frac{\epsilon}{k}\tau_{ij}\frac{\partial \bar{u}_i}{\partial x_j} - C_{\epsilon 2}\rho\frac{\epsilon^2}{k} + \frac{\partial}{\partial x_j}[(\mu + \frac{\mu_T}{\sigma_\epsilon})\frac{\partial \epsilon}{\partial x_j}] \tag{2.13}$$

The above equations (2.12) and (2.13) compose the famous $k - \epsilon$ two equation model. The values of closure coefficients in the above two equations are:

$$C_{\epsilon 1} = 1.44 \quad C_{\epsilon 2} = 1.92 \quad C_\mu = 0.09 \quad \sigma_k = 1.0 \quad \sigma_\epsilon = 1.3 \tag{2.14}$$

From Equation (2.10), it can be seen that the turbulence viscosity is isotropic due to the properties of the fluctuating components. In RANS method, the fluctuating components represent the very small eddies, which dissipates the kinetic energy and obviously isotropic. To overcome this limitation, the LES method occurs, which was firstly proposed to simulate the atmospheric flow. Contrary to the Reynolds decomposition in RANS model, the velocity (and other variables) is decomposed into two parts: resolved proportion $\tilde{u}$ and sub-grid-scale proportion u'. The decomposition is realized by using explicit or implicit LES filter. Among these two parts, the resolved proportion represents the resolved large eddies, which could be anisotropic. The Navier-Stokes equations and continuity equation for the resolved proportion (or filtered equations) are as Equation (2.15).

$$\frac{\partial \tilde{u}_i}{\partial t} + \frac{\partial}{\partial x_j}(\widetilde{u_i u_j}) = -\frac{1}{\rho}\frac{\partial \tilde{p}}{\partial x_i} + 2\nu\frac{\partial \tilde{S}_{ij}}{\partial x_j} - \frac{\partial \tau_{ij}^r}{\partial x_j}, \quad \frac{\partial \tilde{u}_i}{\partial x_i} \tag{2.15}$$

S_{ij} is the strain rate tensor which has been defined in Equation (2.8). τ_{ij}^r is the residual stress tensor, which represents the interactions between resolved and unresolved proportions. Different sub-grid scale models (SGS) are proposed to model the residual stress tensor τ_{ij}^r.

Two SGS models will be introduced, including Smagorinsky model and one-equation eddy-viscosity model.

The Smagorinsky SGS model is firstly proposed in 1963 [70]. In this model, it is assumed that the residual stress tensor complies with the follow Equation (2.16).

$$\tau_{ij}^{r} = \frac{2}{3} k_{sgs} \delta_{ij} - 2\nu_{sgs} \tilde{D}_{ij}^{dev} \tag{2.16}$$

In Equation (2.16), ν_{sgs} is the sub-grid scale eddy viscosity. $\tilde{D}_{ij}$ is the resolved scale strain rate tensor, which is defined by the Equation (2.17). $\tilde{D}_{ij}^{dev}$ is the deviatoric tensor of $\tilde{D}_{ij}$. k_{sgs} is the sub-grid scale kinetic energy.

$$\tilde{D}_{ij} = \frac{1}{2}\left(\frac{\partial \tilde{u}_i}{\partial x_j} + \frac{\partial \tilde{u}_j}{\partial x_i}\right) \tag{2.17}$$

In Smagorinsky SGS model, k_{sgs} and ν_{sgs} are calculated by Equations (2.18) and (2.19).

$$k_{sgs} = \frac{C_k \Delta^2 \sqrt{2\tilde{D} : \tilde{D}}}{C_\varepsilon} \tag{2.18}$$

$$\nu_{sgs} = (C_s \Delta)^2 \sqrt{2\tilde{D} : \tilde{D}} \tag{2.19}$$

Where : is the double inner product. In Equations (2.18) and (2.19), C_k and C_ε are two constants whose typical values are 0.094 and 1.048 respectively. Δ is the sub-grid length scale. C_s can be calculated by Equation (2.20).

$$C_s^2 = C_k \sqrt{\frac{C_k}{C_\varepsilon}} \tag{2.20}$$

To overcome the deficiency of Smagorinsky SGS model in high Reynolds number flows, the one-equation eddy-viscosity SGS model was proposed [71]. Equation (2.16) is also employed in this SGS model. The ν_{sgs} is defined in Equation

$$\nu_{sgs} = C_k \sqrt{k_{sgs}} \Delta \tag{2.21}$$

And the transport equation of k_{sgs} is shown in the Equation (2.22).

$$\frac{\partial \rho k_{sgs}}{\partial t} + \frac{\partial \rho \tilde{u}_j k_{sgs}}{\partial x_j} - \frac{\partial}{\partial x_j}[\rho(\nu + \nu_{sgs})\frac{k_{sgs}}{\partial x_j}] = -\rho \tau_{ij} : \tilde{D}_{ij} - C_\varepsilon \frac{\rho k_{sgs}^{\frac{3}{2}}}{\Delta} \tag{2.22}$$

The first term at the right hand side is the production term, which can be calculated by Equation (2.23).

$$-\rho\tau_{ij} : \tilde{D}_{ij} = [-\frac{2}{3}\rho k_{sgs}\delta_{ij}+2\rho\nu_{sgs}\tilde{D}_{ij}^{dev}] : \tilde{D}_{ij} = -\frac{2}{3}\rho k_{sgs}\frac{\partial \tilde{u}_k}{\partial x_k}+\rho\nu_{sgs}\frac{\partial \tilde{u}_i}{\partial x_j}(2\tilde{D}_{ij}-\frac{1}{3}tr(2\tilde{D}_{ij})\delta_{ij})$$
(2.23)

In this thesis, the Smagorinsky SGS model will be used in wind tunnel case with low Reynolds numbers. The one-equation eddy-viscosity SGS model is employed in the wind farm simulation case with high Reynolds numbers. The turbulence models in this thesis are shown in Figure 2.3.
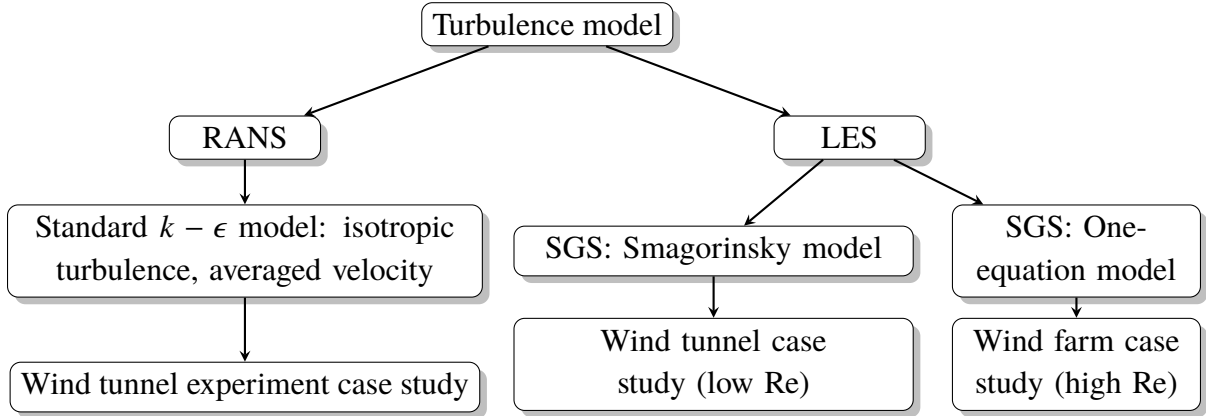
Figure 2.3 Turbulence models for actuator line.

2.1.2 Parameters

There are mainly four undetermined parameters in the actuator line model: actuator width Δ_b, cell size of background mesh Δ_{grid}, Gaussian radius ε, and time step Δt. Based on the experience of previous researchers [72], there are some guidelines for these four parameters. The first parameter should be determined is the Δ_b, which represents the spacing of actuator line. It is suggested that there should be 30 to 60 actuator points along the blade (normally 40). Δ_b can be determined by the number of actuator points and the blade radius. Δ_{grid} is suggested to be slightly larger than Δ_b ($\Delta_{grid} \geq \Delta_b$). The projection radius or Gaussian radius ε is important to the predicted aerodynamic force, which is suggested to be equal to $2\Delta_{grid}$. Although there are some research on the optimization of ε in which the distribution of ε is non-uniform [73], the uniform ε is still used in this thesis because of its simplicity. The parameter Δt is firstly restricted by the CFL number, which should be less than 1. Another requirement for the Δt is that the actuator line should not pass one single cell within one time step. Or the maximum time step is Δ_{grid} divided by ΩR, where Ω and R are rotational speed and tip radius respectively. The latter requirement is more restrictive, which often makes the CFL number less than 0.2. The flowchart of parameters determination is

shown in Figure 2.4. It should be mentioned here that the guidelines of parameters are for the LES based actuator line model, which will also be applied in the simulations with RANS turbulence model.
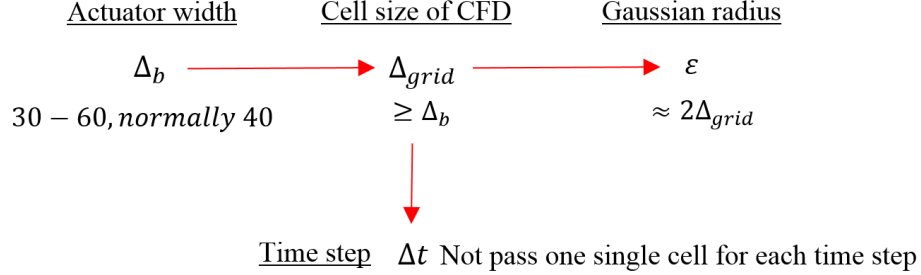
Figure 2.4 Determination of parameters.

2.1.3 Pressure-Implicit with Splitting-Operators (PISO) algorithm

PISO is an Navier-Stokes equation unsteady solver for Equation (2.7). Similar to the Semi-Implicit Method for Pressure-Linked Equations (SIMPLE) algorithm, the equation for pressure is derived in PISO by combining the momentum equation and mass conservation equation, because there is no explicit equation for pressure. The numerical form of Equation (2.7) is as follows:

$$\frac{\rho}{\Delta t}(u_i^{n+1} - u_i^n) = H(u_i^{n+1}) - \nabla_i p_i^{n+1} + S_i \tag{2.24}$$

In Equation (2.24), H is the finite-volume operator, and S_i is the source term. The derived Poisson equation (by taking divergence on both side of Equation (2.24) to eliminate u_i^{n+1}) for pressure is:

$$\nabla_i^2 p_i^{n+1} = \nabla_i H(u_i^{n+1}) + \nabla_i S_i + \frac{\rho}{\Delta t} \nabla_i u_i^n \tag{2.25}$$

To further decouple the pressure from the momentum equations, the solution process is split into several steps (splitting operator), normally including one predictor step and two corrector steps. Specifically the velocity field is firstly predicted by using the pressure value of the last time step:

$$Au^* + H'u^* = \frac{\rho}{\Delta t}u_i^n - \nabla_i p_i^n + S_i \tag{2.26}$$

A and H' are diagonal matrix and off-diagonal matrix of the finite-volume operator of u_i^*, which is the predicted velocity. The pressure field can be corrected by the following Poisson equation:

$$\nabla_i^2(A^{-1}p^*) = \nabla_i[A^{-1}(\frac{\rho}{\Delta t}u_i^n - H'u^*) + A^{-1}\nabla_i S_i] \tag{2.27}$$

Then the velocity field can be corrected in the first corrector:

$$u^{**} = A^{-1}(\frac{\rho}{\Delta t}u_i^n - H'u^*) - A^{-1}\nabla_i p_i^* + A^{-1}S_i \tag{2.28}$$

which is followed by the correction of pressure:

$$\nabla_i^2(A^{-1}p^{**}) = \nabla_i[A^{-1}(\frac{\rho}{\Delta t}u_i^n - H'u^{**}) + A^{-1}\nabla_i S_i] \tag{2.29}$$

The second corrector is very similar to the first corrector:

$$u^{***} = A^{-1}(\frac{\rho}{\Delta t}u_i^n - H'u^{**}) - A^{-1}\nabla_i p_i^{**} + A^{-1}S_i \tag{2.30}$$

The calculated pressure p^{**} and u^{***} have at least second order time accuracy. Since actuator line model is an unsteady model, the PISO solver in OpenFOAM is employed to solve the Navier-Stokes equations. In this thesis, the combination of actuator line model and PISO solver is a two-way coupling. Specifically, the actuator line model samples the local velocity in the flow field before the predictor step to calculate the body forces. In the first predictor step, the calculated body forces are smeared in the flow field as source term S_i in Equation (2.26) by using Gaussian function. The flowchart of actuator line model is shown in the Figure 2.5. It should be mentioned here that the coupling between actuator line model and PISO solver is weak coupling. In the following sections, several validation cases are carried out to validate the actuator line model in terms of aerodynamic force and wake velocity profile predictions. The unsteady airfoil aerodynamics is not considered in the simulation cases of conventional actuator line model.
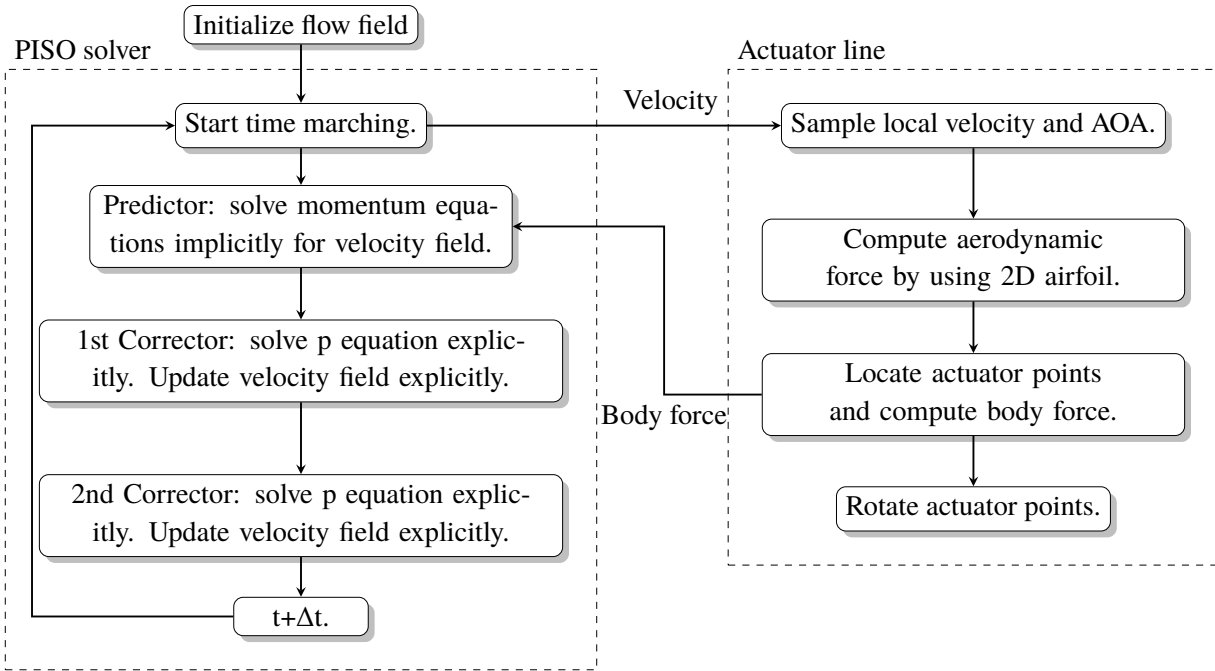
Figure 2.5 Flowchart of the actuator line model based on PISO solver.

2.2 Validation case study: Krogstad wind tunnel experiment I

2.2.1 Test case description

The advantage of actuator line model is that it can generate turbulent wake flow and simulate the dynamic aerodynamic loading at the same time in an efficient and feasible way. In this section, the Krogstad wind tunnel experiment will be used to validate the actuator line model in terms of wake flow prediction and dynamic load calculation. This Krogstad experiment is a series of "blind tests" for the wind turbine wake models, which is carried out at the Norwegian University of Science and Technology (NTNU) on October, 2011 [74]. As for the wind tunnel test section, the width and height are 3m and 2m respectively. Its length is almost 12 m long. The reference wind speed ranges from 7 to 15 m/s. The turbulence intensity of the wind tunnel is 0.3%.

Figure 2.6 S826 airfoil shape.
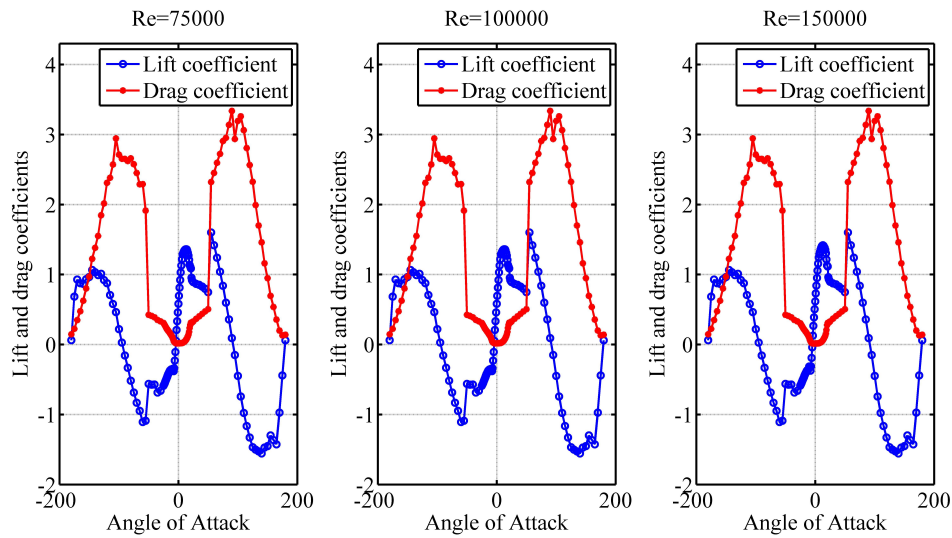
Figure 2.7 The lift and drag coefficients of S826 airfoil for different Reynold numbers.

For experiment I, only one single three-bladed turbine is used for the test. The diameter of the rotor is 0.894m, and the hub height is 0.817m. The same airfoil is used all along the span, which is NREL S826 airfoil. The shape of the airfoil is shown in Figure 2.6. The lift and drag coefficients for S826 (Re=75000 to 150000) are also presented in Figure 2.7. The blade is made of aluminum and very stiff under the loading of the designed blade, which means that no obvious elastic deformation during the test. The tested wind turbine is illustrated in Figure 2.8 (a). The chord and twist distributions of the blade are shown in the Figure 2.8 (b). The data of lift and drag coefficients is from the computational results of Xfoil, in which the 3D rotational augment (stall delay) is not considered.

(a) Krogstad wind turbine [74].
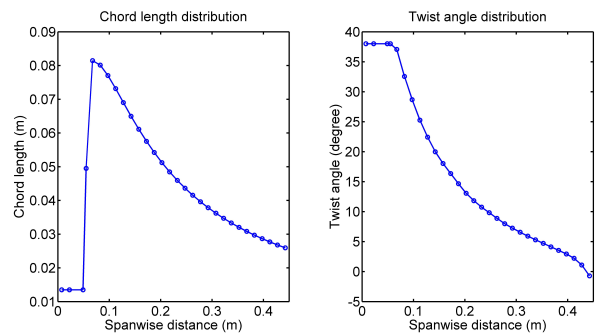
(b) Chord and twist distribution.

Figure 2.8 Wind turbine and its structural properties for the Krogstad wind tunnel test.

For the numerical model, the cell size of the background mesh (wind tunnel) is 0.15 m. Three-level mesh refinement is applied to the background mesh to refine the rotating and wake region of actuator line. The finest mesh size is 0.018 m, which is slightly higher than

the actuator width (0.011 m) according to the aforementioned empirical rule. The Gaussian radius ε of actuator line model is 0.036. The total number of cells is 3.74 million, which can be seen in Figure 2.9. The surrounding walls of wind tunnel are modelled as non-slip boundary conditions. The turbulent kinetic energy k_b at the inlet boundary (Dirichlet boundary condition) can be calculated according to the turbulence intensity (I_{inlet}) at the inlet by using Equation (2.31).

$$k_b = \frac{3}{2}(U_{ref}I_{inlet})^2 \tag{2.31}$$
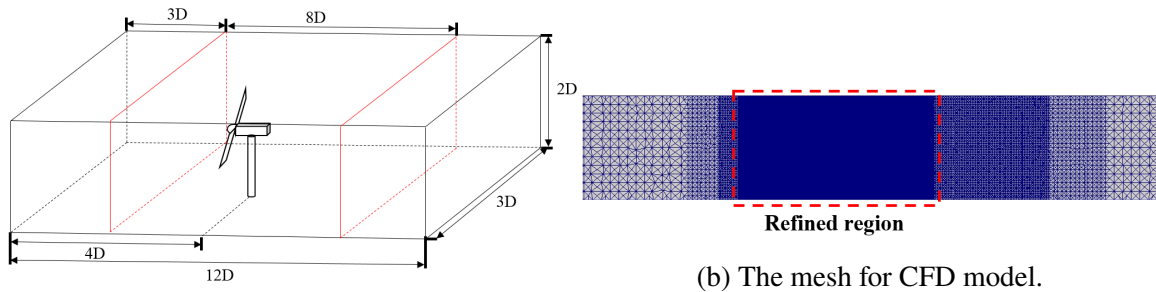
(a) The sketch of mesh for Krogstad wind tunnel test.

(b) The mesh for CFD model.

Figure 2.9 Mesh of Krogstad wind tunnel test.

As for the boundary conditions, the incoming free-stream turbulence intensity I_{inlet} is 0.23 % (for the empty wind tunnel), and reference wind speed U_{ref} is 10 m/s. The turbulent kinetic energy k_b at the boundary is calculated to be 0.0008 m^2/s^2 according to Equation (2.31). According to the paper of the wind tunnel test, the turbulence intensity dropped from 0.23% at the inlet position to 0.22% at the 3D downstream position. Based on this fact, the boundary condition for turbulent dissipation rate ϵ_b can be calculated by the following equation:

$$\epsilon_b \approx \frac{\Delta k U_{ref}}{L_d} \tag{2.32}$$

In Equation (2.32), Δk is the variation of turbulent kinetic energy along the distance, and L_d is the distance for the variation. The calculated turbulent dissipation rate ϵ_b is 0.000252 m^2/s^3. The outlet boundary conditions for turbulent kinetic energy and dissipation rate are all Neumann boundary conditions (zero gradient). The time step is 0.0005 s, which is constant during the simulation. After 10 s (physical time) simulation, the simulated wind turbine wake is fully developed in the wind tunnel, which is illustrated in Figure 2.10. From Figure 2.10, it can be seen that the wake region slightly expands behind the rotor. This is because of the recovery of pressure in near wake region. The pressure experiences a sharp decrease on the rotor section. As a result, the wake will expand to absorb more

momentum for the pressure recovery. This result can also be achieved by Betz theory (based on Bernoulli equation potential flow), which means that the near wake region conforms to the potential flow theory. The pressure will fully recover to the inflow condition at around 1D downstream of the rotor, which is at the end of near wake region in this case. Beyond the near wake region, turbulence will play an important rule on the development of wake flow. The wake region does not further expand significantly downstream because of the low turbulence intensity of ambient flow (0.23%).
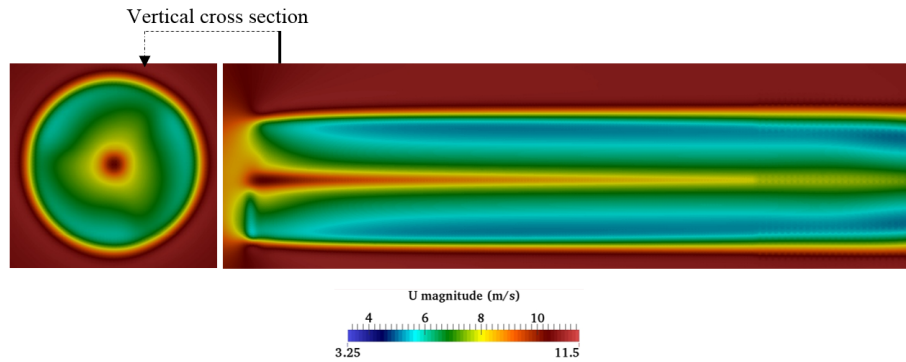
Figure 2.10 The velocity magnitude contour of the single wind turbine.

In addition, the wake vortex structure can be seen in the Figure 2.11. The helical vortex structure is not obvious because of the high rotational speed of wind turbine (1281.8 r/min). At that time, the performance parameters of wind turbine, including power output, thrust force, and tangential force, become stable though this is an unsteady simulation. Then the values of variables related to the aerodynamic force and wake profile will be sampled and compared with the measured data in the wind tunnel quantitatively.
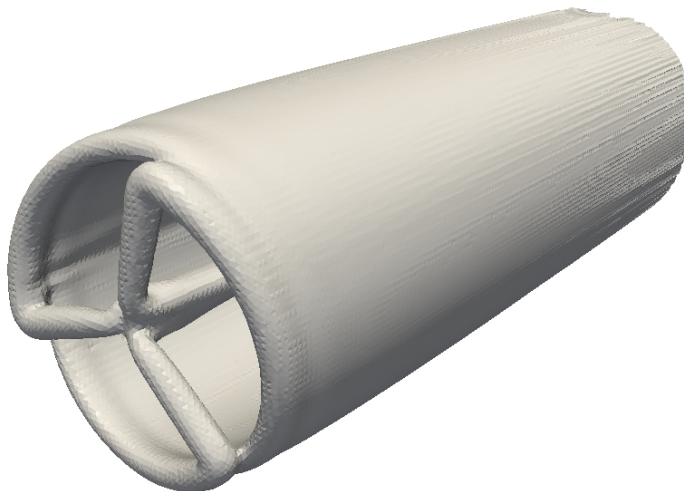
Figure 2.11 The vortex structure of wind turbine wake.

Firstly, the predicted thrust coefficients C_t under different tip speed ratios λ will be compared with the measured data. λ can be calculated by using Equation (2.33).

$$\lambda = \frac{\Omega R}{U_\infty} \tag{2.33}$$

U_∞ is the inflow wind velocity. The formula of C_t is shown in the following equation:

$$C_t = \frac{T}{\frac{1}{2}\rho A U_\infty^2} = \frac{T}{\frac{1}{2}\rho \pi R^2 U_\infty^2} \tag{2.34}$$

A in the above Equation (2.34) is the swept area of wind turbine rotor. The C_t quantifies how much momentum in the inflow is transformed into the thrust force of the rotor, which is also an important component of aerodynamic force. It should be mentioned here that the original Blade Element Momentum (BEM) method is only suitable for lightly-loaded turbine whose C_t is lower so that its wake shape is perfect helix. To correct the prediction of BEM in high C_t case, empirical corrections, e.g. Glauert correction, are required. The actuator line model can predict the aerodynamic force without this lightly-loaded assumption and empirical corrections, because its wake is simulated by CFD. The comparison between the predicted thrust coefficients by actuator line model and the measured data is shown in Figure 2.12. In Figure 2.12, each point indicates a experimental or simulation (fixed inlet wind speed, variable rotational speed for different λs) case. Generally speaking, the prediction of actuator line has a good agreement with the test data. The actuator line slightly underestimates the thrust force at $\lambda = 2$ because this wind turbine operates in the deep stall region when $\lambda \leq 3$. In the deep stall region, the flow field is highly unsteady, and the real lift and drag coefficients may slightly deviate from the tabulated data. Since thrust force is an important component of aerodynamic force as mentioned before, the actuator line model is preliminarily validated to be a good aerodynamic model.

In addition, as mentioned before, actuator line model can also reproduce the wind turbine wake flow, including near wake and far wake flows. In Krogstad experiment I, the horizontal velocity profile (longitudinal velocity) at the hub height will be sampled in two sections: 1D and 3D downstream, which represent near wake and far wake respectively. The sketch for the test sections is shown in Figure 2.13. The inlet velocity is 10 m/s, and the tip speed ratio (λ) of the operating wind turbine is 6 (or rotational speed is 1281.8 r/min), which is the optimum operating condition for the test wind turbine. The turbulence intensity of the incoming free-stream is 0.23 %. The normalized wake velocity deficit ($1 - \frac{U_{wake}}{U_{ref}}$) is used to depict the velocity profile in the wake region. Obviously, when the deficit is higher, the velocity is lower.

The comparison between the predicted wake profile (actuator line) and measured data is shown in Figure 2.14.
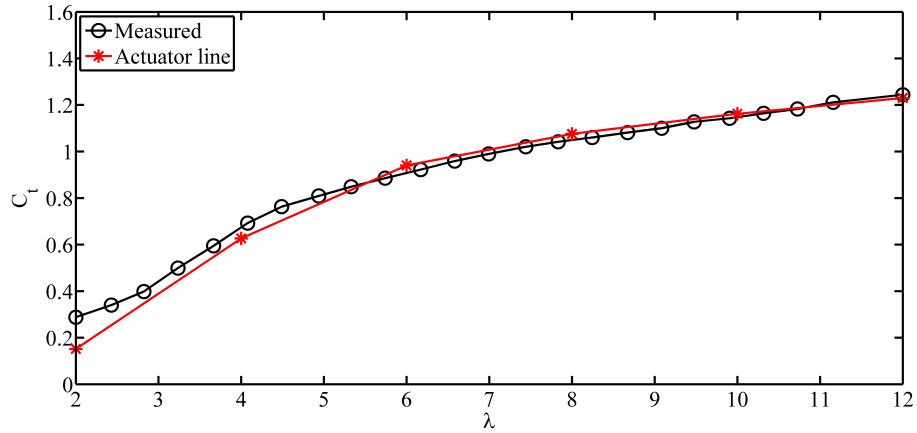
Figure 2.12 Comparison between the predicted thrust coefficients of actuator line and measured data.
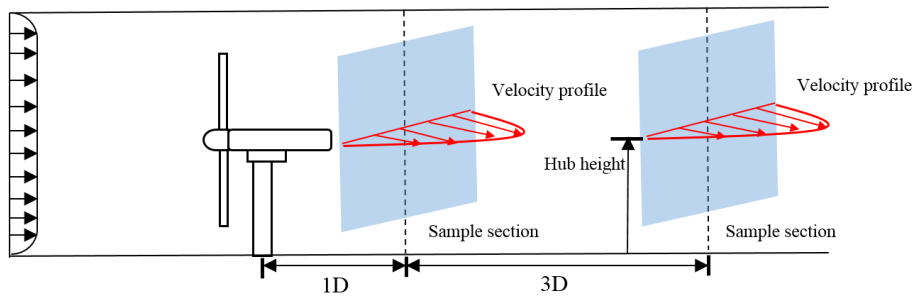
Figure 2.13 The sketch of velocity-profile test section for single wind turbine (D is the diameter of the rotor).

In Figure 2.14, it can be found that the actuator line model performs very well in the shear region (between outer flow and wake). However, in the region of wake center, the actuator line model significantly underestimates the time-averaged velocity deficit (or overestimates the velocity magnitude), not only for 1D but also 3D. This phenomenon can be also found in the Krogstad paper, in which the measured data is compared with the prediction of actuator line model (Sorensen & Mikkelsen) [74]. Krogstad comments this discrepancy that "it predicts virtually no velocity reduction behind the nacelle". In the author's view, this is caused by the absence of the nacelle in the conventional actuator line model, in which only blades effects are modelled. On one hand, in the paper of Krogstad blind test, the model with resolved nacelle (fully geometry resolved) shows good agreement with the measured data around the wake center. On the other hand, in reality, the nacelle will indeed cause momentum loss of the flow. In the next section, the nacelle will be modelled in the framework of actuator line.
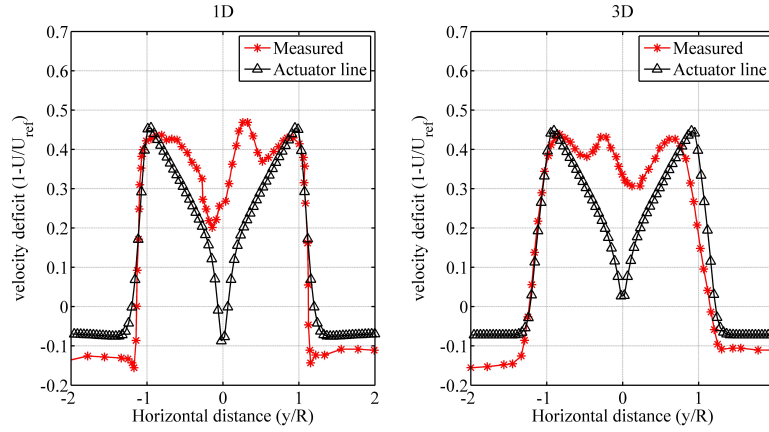
Figure 2.14 The comparison between predicted velocity profile (actuator line model) and measured data in single wind turbine case.

2.2.2 Actuator line model with nacelle model

In this section, a simple nacelle model is proposed to simulate the nacelle effect. In order to maintain the advantages of actuator line model, the nacelle is modelled as a point source of body force, which is smeared in the flow field according to the following equation:

$$\vec{f}(\vec{x}) = \vec{f}_{nacelle} \frac{1}{\varepsilon^2 \pi^{\frac{3}{2}}} e^{-\left(\frac{|\vec{x}-\vec{x_0}|}{\varepsilon}\right)^2} \tag{2.35}$$

In Equation (2.35), $\vec{f}_{nacelle}$ is the strength of the point source, which is also the magnitude of the aerodynamic force on the nacelle. ε is the smeared radius. x_0 is the center of the nacelle. To calculate the $\vec{f}_{nacelle}$, it is assumed that the discrepancy around the wake

center region is caused by the nacelle. Therefore the rate of momentum loss is equal to the magnitude of aerodynamic force on the nacelle, which can be calculated by using the following equation:

$$f_{nacelle,x} = \pi R_{dis}^2 (U_{a,x}^2 - U_{m,x}^2) \tag{2.36}$$

In Equation (2.36), $f_{nacelle,x}$ is the longitudinal component of the momentum loss. The other components of momentum loss are neglected, because the momentum loss mainly occurs along the longitudinal direction (inflow direction). R_{dis} is the radius of the region of the aforementioned discrepancy (the control volume is apparently a cylinder, in this case R_{dis} is the hub radius). $U_{a,x}$ and $U_{m,x}$ are the average values of aforementioned predicted and measured velocities. After several trials, $\varepsilon = 0.2$ is determined to be the optimum Gaussian radius, which balances the accuracy and numerical stability. The results are shown in Figure 2.15. The blue curve does not look symmetric, because, in the author's view, is that the cells in the support domain of nacelle model is not symmetrically distributed in the simulation case.
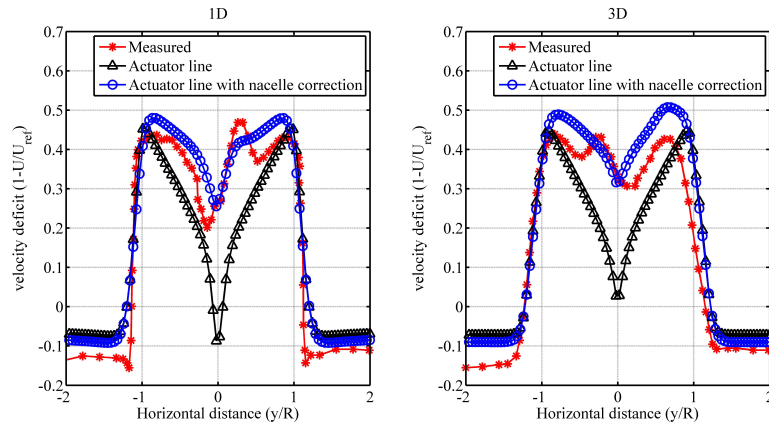
Figure 2.15 The comparison between predicted velocity profile (actuator line model with and without nacelle model) and measured data in single wind turbine case.

In Figure 2.15, the predicted values of actuator line with nacelle correction has a very good agreement with the measured data in both near wake region (1D) and initial far wake region (3D). Mainly two conclusions can be drawn in this validation case. Firstly, the nacelle model or nacelle correction is necessary for actuator line model, especially for the simulation of wind tunnel experiment case (or small wind turbines), in which the nacelle is relatively large. Secondly, the nacelle effect can be modelled by a point source of body force, which is smeared in the flow field by Gaussian function.

Two interesting phenomena can be observed in Figure 2.15. Firstly, the wake of nacelle becomes stronger from 1D to 3D (the wake deficit is increasing). In the author's view,

this is because of the momentum diffusion between the wakes of rotor and nacelle, which is enhanced by the high turbulence intensity in wake region. Secondly, the wake deficit around rotor tip recovers very slowly, because the turbulence intensity of ambient flow is much lower. These two phenomena can be not only found in the experiment data but also reproduced by the actuator line model, which indicates that the turbulence intensity of ambient flow plays important role in the development of wake.

The validation case in this section is about the single wind turbine wake. In the next section, the wake interaction cases, including tandem and staggered wind turbines, are used to validate the capability of actuator line model in predicting wake profiles when the wakes interact with each other.

2.3 Validation case studies: Krogstad wind tunnel experiment II and III

2.3.1 Experiment II: tandem wind turbines

The case of tandem wind turbines or two in-a-line wind turbines has been commonly used in the research of wind turbine wake, because this is the worst case scenario of wake effect. For single wind turbine wake, it is still possible to derive the analytical solution for wake profile. As for the tandem wind turbines, the wake of downstream wind turbine immerses in and interacts with the upstream wake, which makes it difficult to predict the wake profile of downstream turbine in the analytical way, which assumes the ambient flow to be uniform flow and linear wake superposition. According to the previous research, the analytical wake model will have negative wake deficit in some cases if linear superposition method is employed, which is obviously unreasonable. This is also the reason why numerical model (or CFD model) attracts attention recently. In Krogstad wind tunnel experiment II, the tandem-wind-turbine case is carried out, which is shown in Figure 2.16 and Figure 2.17.

The tip speed ratios of the upstream and downstream turbines are 6 and 4 respectively, which means that the rotational speeds of the upstream and downstream turbines are 1281.8 r/min and 854.53 r/min under 10 m/s inflow wind speed . The downstream turbine operates under this condition to achieve the optimum local tip speed ratio, because the flow velocity drops nearly $\frac{1}{3}$ in front of the downstream turbine compared with the ambient flow. The velocity magnitude contour is shown in Figure 2.18. From this figure, it can be seen that the wind turbine wakes are fully developed. The downstream turbine is fully immersed in the upstream turbine wake, which is non-uniform. The vortex structure of two wind turbine wakes are shown in Figure 2.19.

The horizontal velocity (longitudinal) profiles are measured at 1D and 2.5D sections behind the downstream wind turbine at the hub height. The results of actuator line model

Figure 2.16 The tandem-wind-turbine experiment [1].
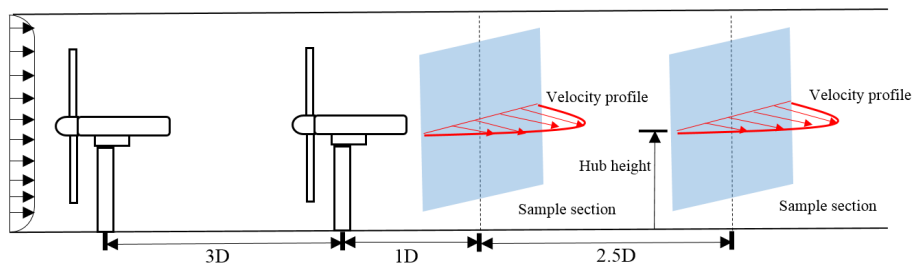
Figure 2.17 The sketch of velocity-profile test section for tandem wind turbines (D is the diameter of the rotor).
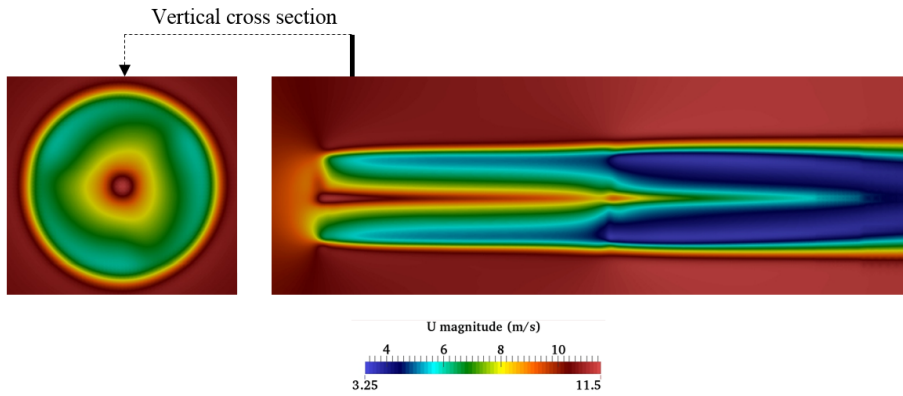
Figure 2.18 The velocity magnitude contour for the tandem wind turbines.

(a) Lateral view.

(b) Front view.

Figure 2.19 The vortex structure of tandem wind turbines.

are compared with the measured data in Figure 2.20. Although this is the wake profile of downstream wind turbine, the same issue in experiment I can also be found in this comparison, which is that the velocity deficit behind the nacelle is underestimated. The previous issue can also be addressed by the nacelle model in last section. The comparison between the actuator line model and measured data is shown in the Figure 2.21.
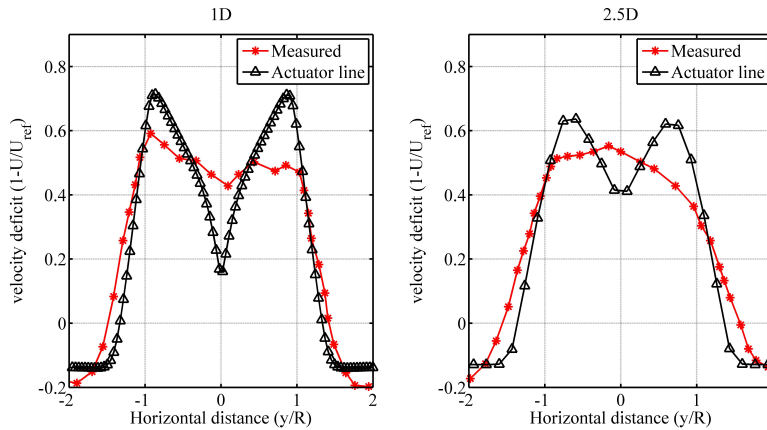
Figure 2.20 The velocity profile at 1D and 2.5D sections for tandem wind turbines (behind downstream wind turbine).

From Figure 2.21, it can be seen that the discrepancy around the nacelle region is reduced by the nacelle model. But there still exists slight discrepancy around the rotor tip region. In the author's opinion, the reason for this discrepancy are two fold. On one hand, the uniform distribution of Gaussian radius is not the optimum one for actuator line, which will influence the effect of actuator line model. The force distribution of upstream wind turbine in this case is shown in Figure 2.22. In some recent research papers of the actuator line parameters, it is also found that the non-uniform distribution can achieve higher accuracy. On the other hand, the discrepancies of upstream and downstream wind turbine wake will

34
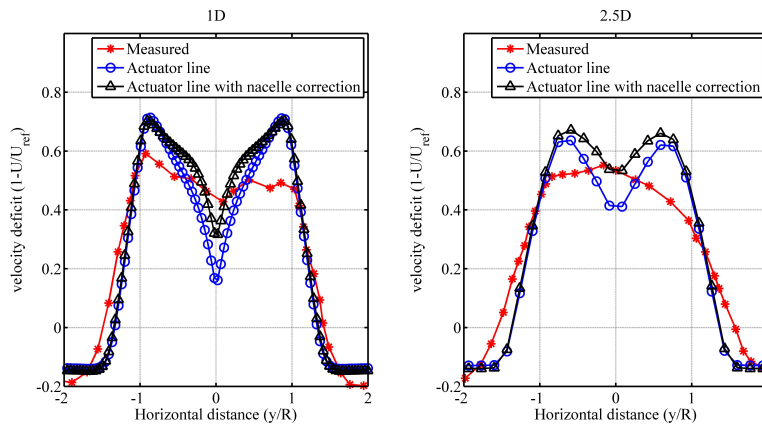
Figure 2.21 The velocity profile at 1D and 2.5D sections for tandem wind turbines (with and without nacelle model).

be superimposed in this region, which further enlarges the discrepancy.

From both experimental data and simulation results, it can be seen that the wake of downstream turbine recover faster than that of upstream wind turbine when we compare Figure 2.21 with Figure 2.15. As mentioned in the last section, this issue is caused by the high turbulence intensity of upstream wind turbine wake, which is obviously the ambient flow for the downstream wind turbine wake.
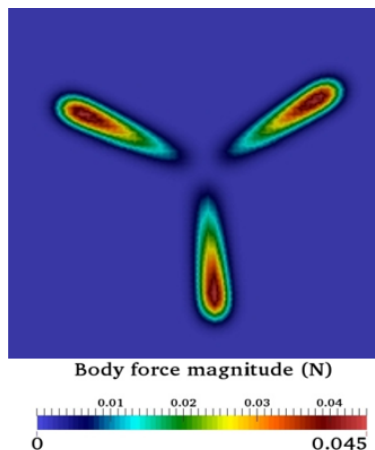
Figure 2.22 The force distribution of upstream wind turbine for tandem wind turbines.

2.3.2   Experiment III: staggered wind turbines

The experiment III is about two staggered wind turbines. In the wind farm, the wind turbines are staggered to mitigate the wake effect from upstream wind turbine. The wakes of upstream and downstream wind turbines will interact with each other. In Krogstad wind

tunnel experiment III, two turbines with the same rotor and hub height are used, which is shown in Figure 2.23. The distance between the two turbines is 3D, and the horizontal offset distance to the center line of wind tunnel is 0.2 m. The wind speed profiles are measured at the 1D and 3D behind the second wind turbine at the hub height (0.8 m), which is illustrated in Figure 2.24. The tip-speed-ratios of upstream and downstream wind turbines are 6 and 4.75 respectively, which means that the rotational speeds of two wind turbines are 1281.8 and 1014.8 r/min.

Figure 2.23 The two staggered wind turbines in Krogstad wind tunnel experiment [2].
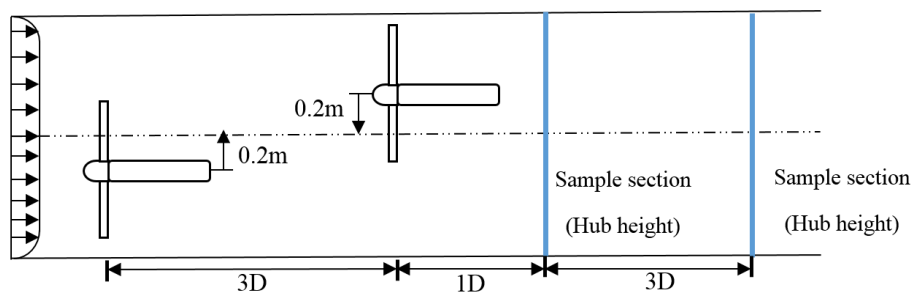
Figure 2.24 The sketch of staggered wind turbines (D is diameter of rotor)

The velocity magnitude contour of staggered wind turbines is shown in Figure 2.25. Since there exist an horizontal offset between the center-lines of the two staggered wind

turbine rotor, the flow field is highly asymmetric compared with the previous tandem-wind-turbine case.
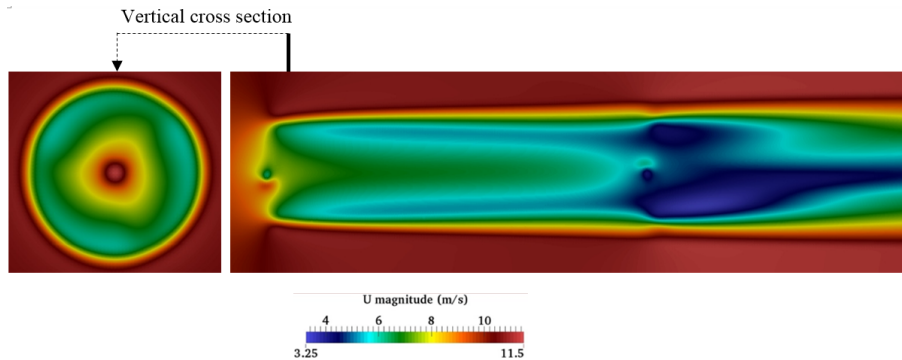
Figure 2.25 The velocity magnitude contour for the staggered wind turbines.

The calculated wind turbine wake profiles are compared with the measured data in Figure 2.26. The wake profiles of actuator line model have a good agreement with the measurements. It should be mentioned that there is no nacelle model in this case, but the results do not show underestimation of wake deficit as previous cases. It can be concluded that the effect of nacelle is weakened by the wind turbine rotor because of the staggered layout. This phenomenon can also be observed in Krogstad's paper [2].
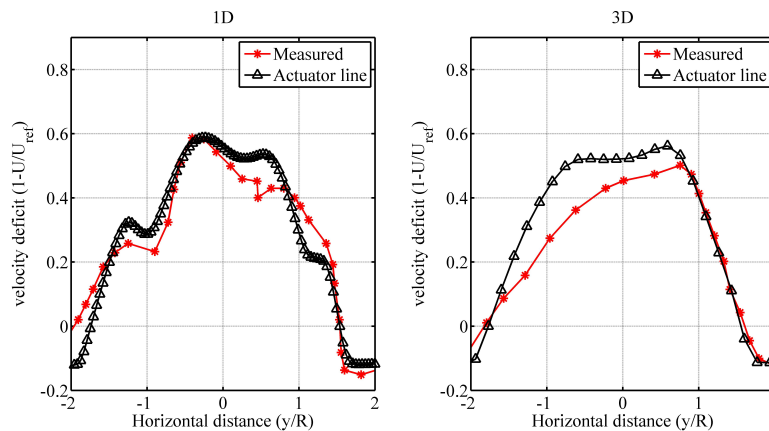
Figure 2.26 The velocity profile at 1D and 3D sections for staggered wind turbines (without nacelle model).

2.4   Comparison between LES and RANS

In the previous sections, the RANS turbulence model (standard $k - \epsilon$ model) is employed. In this section, the LES turbulence model with Smagorinsky SGS model is employed in

37

this section to simulate the wake flow for single Krogstad wind turbine case, which will be compared with the results of RANS model. The mesh in the previous sections are also used in the current simulation case, and the nacelle model in the previous sections is also implemented. The parameters, including the actuator width (0.011 m), Gaussian radius (0.036), and time step (0.0005 s), are all the same as that of case with RANS model. After simulation of 15 s (physical time), the flow field becomes fully turbulent, which can be seen from Figure 2.27.
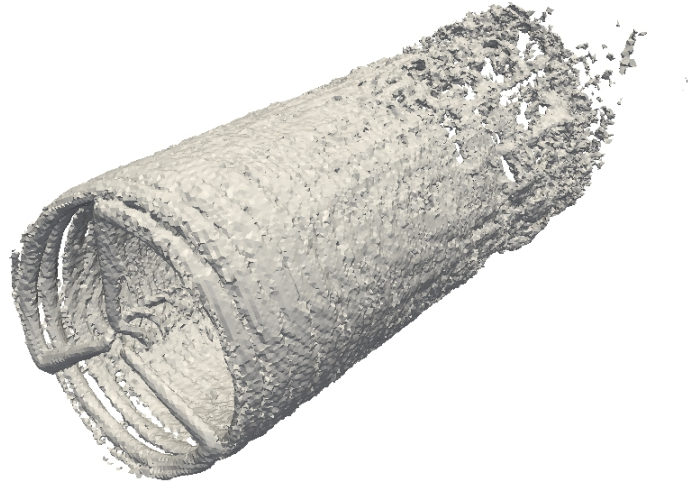
Figure 2.27 Vortex structure of the single Krogstad wind turbine (LES model).

By comparing with the vortex structure of LES model (Figure 2.27) and RANS model (Figure 2.11), it can be found that the vortex structure breaks down at around 3D behind wind turbine for the case of LES, which is not observed in the case of RANS model. This can also be observed in Figure 2.28, in which near and far wake regions are very clear. As a result, the LES model can capture more information of the wake flow.
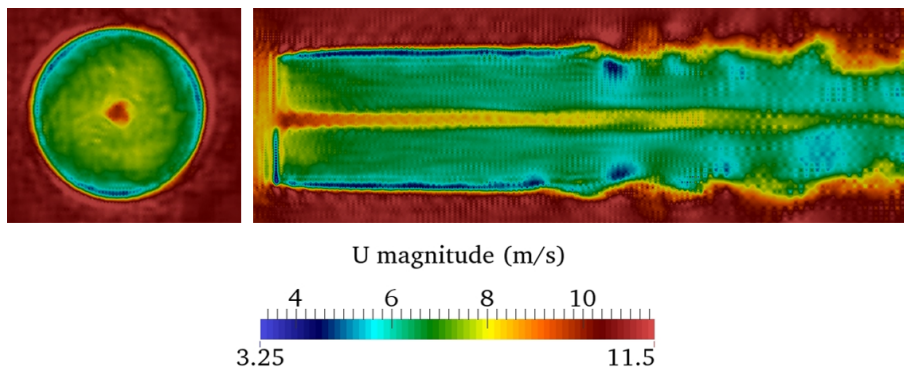
Figure 2.28 The velocity magnitude contour for the staggered wind turbines using LES model.

The velocity profiles (horizontal line) sampled behind the wind turbine (1D and 3D) of

RANS model and LES model are compared in Figure 2.29. Firstly, it can be seen that the prediction of LES model matches well with the measured data, which is better than that of RANS model in the single wind turbine case. Secondly, the proposed nacelle model also works well for the actuator line with LES model. Thirdly, there is a obvious overshoot in the prediction of LES model, which is caused by the overprediction of aerodynamic force in the blade tip region that is mentioned in the previous section. As a result, the LES model is more sensitive to the body force of actuator line.
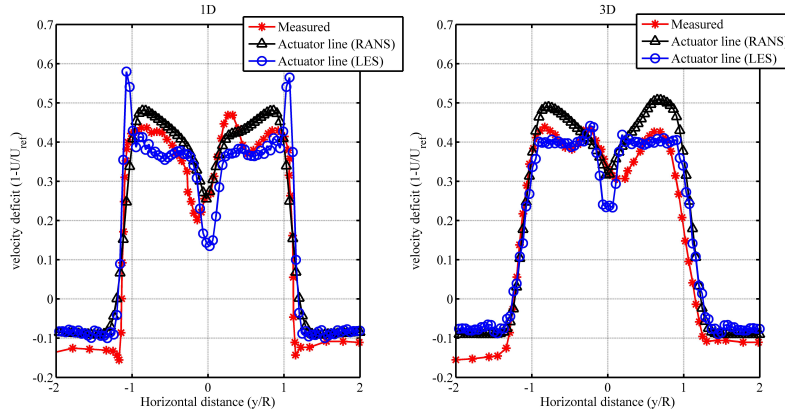
Figure 2.29 The sketch of staggered wind turbines with nacelle model (D is diameter of rotor)

2.5 Comparison between actuator line model and fully-blade-resolved method

In the previous sections, the validation cases for actuator line model, namely the comparisons between the measured data and prediction results of actuator line model, are carried out to validate the actuator line model, from which the accuracy of actuator line model is illustrated. In this section, the comparison between actuator line model and fully-blade-resolved method is carried out to illustrate the efficiency of the actuator line model.

The NREL 5MW wind turbine blade is selected to be the research subject in this section. The NREL 5MW baseline wind turbine is an offshore wind turbine and designed by NREL, which is shown in Figure 2.30. It is a three-bladed upwind horizontal wind turbine. Its rated power is 5MW. The diameter of its rotor is 126 m with 90 m hub height. The cut-in, rated, and cut-out wind speeds are 3 m/s, 11.4 m/s, and 25 m/s respectively. The rated rotational speed is 12.1 rpm. The geometry of NREL 5MW wind turbine blade is presented in Figure 2.30. The airfoil distribution and the lift coefficients are shown in Figure 2.31 and 2.32.

In this case, the inlet velocity is 10 m/s, and the rotational speed is 9.55 rpm. The meshes for actuator line model and fully-blade-resolved method are shown in Figure 2.34
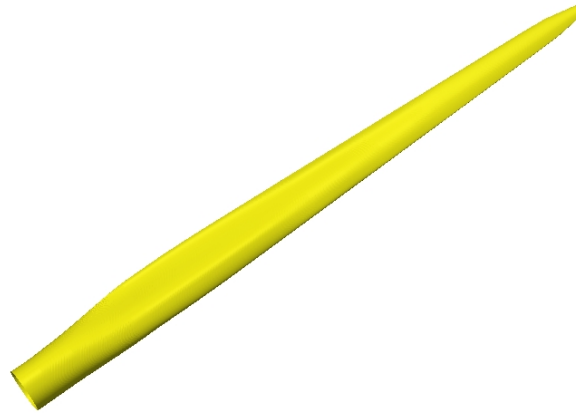
Figure 2.30 NREL 5MW wind turbine blade geometry.

| 1 | ---------- | DU40 | 2 | ---------- | DU35 | 3 | ---------- | DU30 |
| 4 | ---------- | DU25 | 5 | ---------- | DU40 | 6 | ---------- | NACA64 |
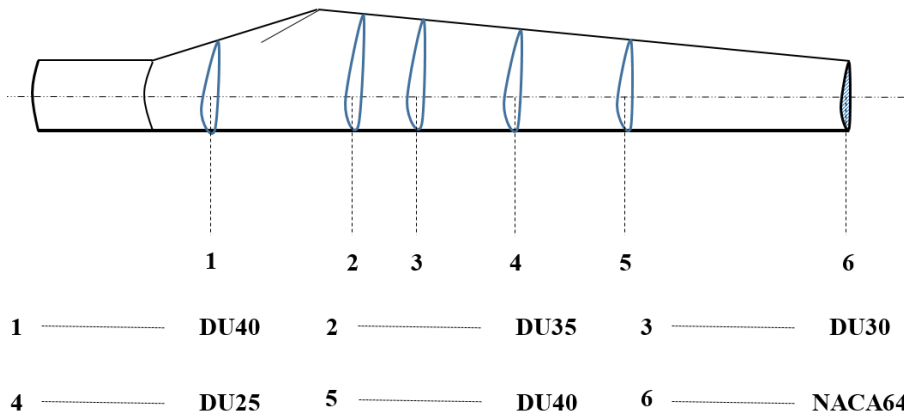
Figure 2.31 NREL 5MW wind turbine blade.
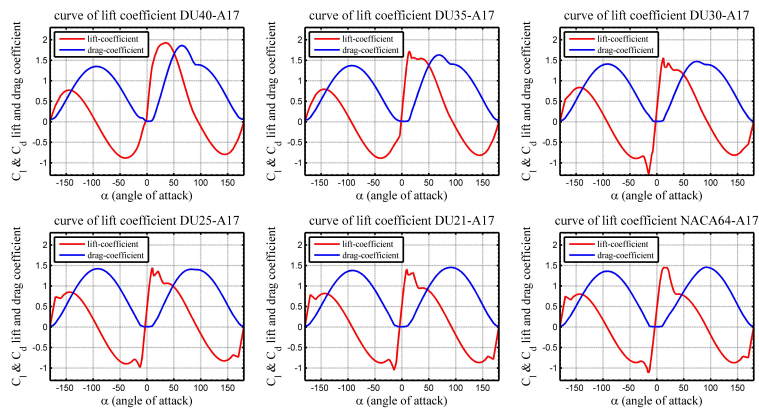
Figure 2.32 Lift and drag coefficients for the airfoils of NREL 5MW wind turbine blade.
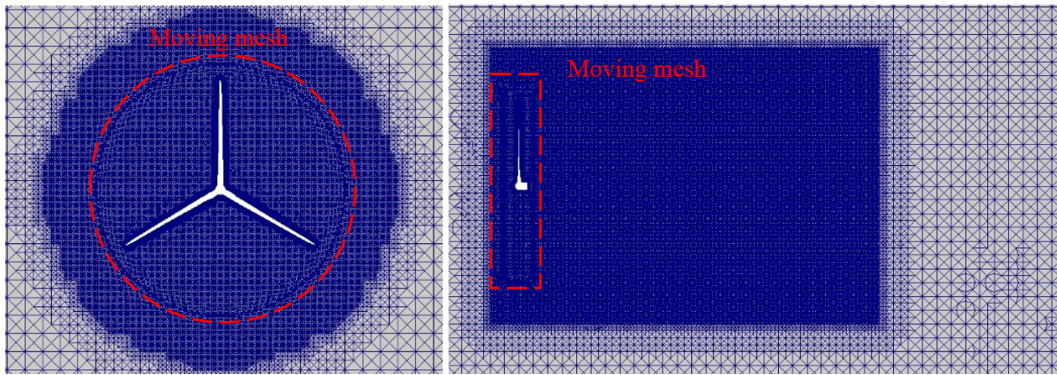
Figure 2.33 Mesh for the fully-blade-resolved simulation.

and 2.33 respectively. For the fully-blade-resolved method, dynamic mesh in OpenFOAM is employed to simulate the rotating wind turbine blades. Specifically, the mesh of fully-blade-resolved method is split into two regions, including the rotating region (see Figure 2.33, red box) and stationary region. The rotating region rotates with the rotational speed of rotor, namely 9.55 rpm. The arbitrary mesh interface (AMI) method in OpenFOAM is employed to build the coupling between rotating and stationary regions. Standard $k - \epsilon$ model is employed as the turbulence model.
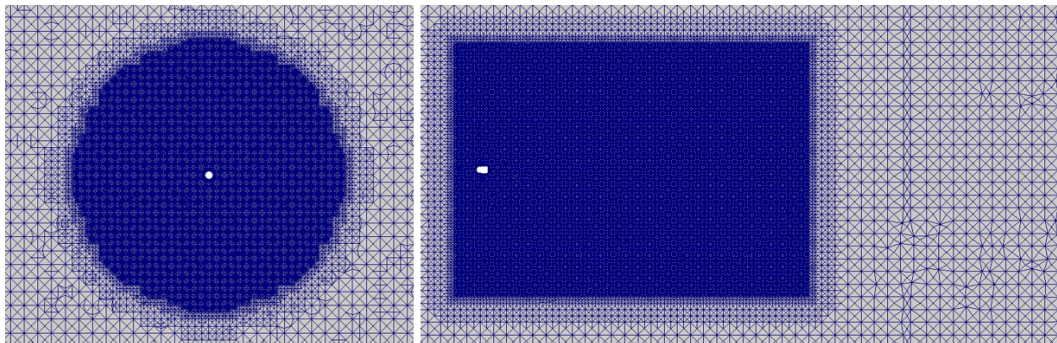
Figure 2.34 Mesh for the actuator line simulation.

From the figures of results (see Figure 2.35 and 2.36), it can be found that the simulated vortex structures and flow fields (velocity magnitude) are very similar for the two methods. compared with 2.7 million cells for actuator line model, 4.6 millions cells is used in fully-blade-resolved case to resolve the geometry of the blade ($y^+ \approx 100$). Moreover, the time step for fully-blade-resolved method is $1 \times 10^{-5} s$ according to the CFL condition, while the time step of actuator line model is $5 \times 10^{-3} s$, because the mesh size of actuator line model is larger than that of fully-blade-resolved method. In this simulation case, it can be seen that the actuator line model is an effective simulation model for wind turbine wake, which strikes good balance between accuracy and efficiency. It should be mentioned here that there is no quantitative comparison between the blade-resolved method and actuator line model. Here
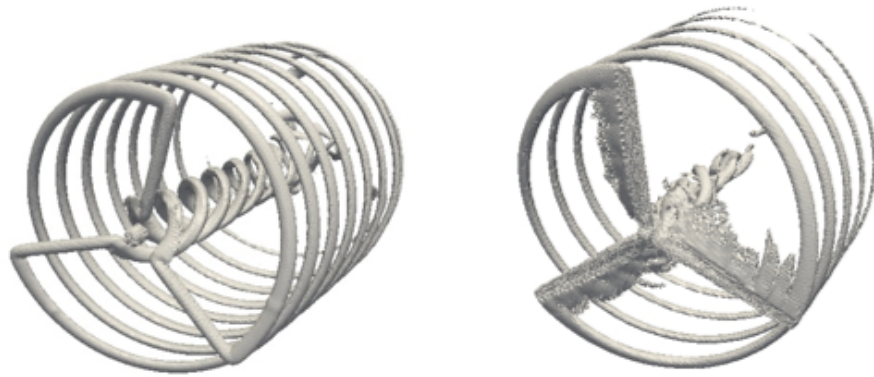
Figure 2.35 Vortex structures of actuator line model and fully-blade-resolved method.

the mesh sizes for the blade-resolved method and actuator line model are determined by the typical methods. The mesh size for the blade-resolved method is determined by the yplus (40-200). The mesh size for the actuator line model is determined by the suggested method in Section 2.1.2.
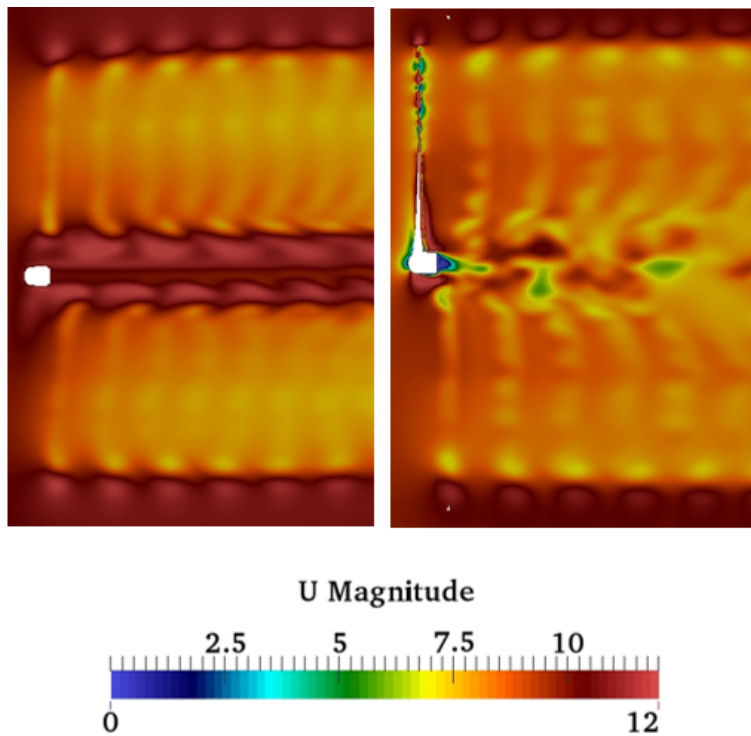
Figure 2.36 The comparison between the calculated flow field of actuator line model and fully-blade-resolved method (m/s).

2.6 Atmospheric simulation: precursor method

2.6.1 Principle of precursor method

Obviously, the initial and boundary conditions are very important for the CFD simulation. It is relatively easy to determine these conditions for wind tunnel case with uniform and low turbulence intensity inflow conditions. However, for the turbulent atmospheric flow with log-law profile in the wind farm, they are difficult to determine. In fact, the atmospheric flow is mainly driven by the pressure gradient force and dragged by the frictional force on the surface of the ground. As a result, instead of prescribing the velocity profiles, the idea of precursor method is to generate the initial and boundary conditions in a "physical way". Specifically, the constant pressure gradient force is applied in the flow field as body forces to drive the flow, and the frictional forces are applied on the surface as shear forces to drag the flow. The sketch of the precursor method is shown in Figure 2.37.

The pressure gradient can be calculated according to the longitudinal wind velocity at the specific height (e.g. hub height). The upper boundary is bounded by the "capping inversion" (or reversed temperature profile), which is similar to the real atmosphere. This "capping inversion" is generated by introducing potential temperature transport equation (see Equation (2.37), $\bar{\theta}$ represents the potential temperature, and q_j represents the heat flux). The boundary conditions of the surrounding walls are all cyclic boundary conditions to make the flow circulate in the computational domain. After several iterations, the "atmospheric flow" becomes fully turbulent.

$$\frac{\partial \bar{\theta}}{\partial t} + \frac{\partial}{\partial x_j}(u_j \bar{\theta}) = -\frac{\partial}{\partial x_j}(q_j) \tag{2.37}$$

For the neutral atmosphere case with 3 km × 3 km × 1 km (mesh size 20 m, time step 0.5 s), the flow becomes fully turbulent after 20000 s (physical time), which is presented in Figure 2.37 (a). The longitudinal velocity at 90 m height (hub height) is 8 m/s. Figure 2.37 (b) shows the instantaneous velocity field, in which the velocity gradient (vertical) can be seen. Another important issue for the precursor method is the shear force on the surface, which can be calculated by the Schumann wall stress model, which will be introduced in the following subsection.

2.6.2 Schumann wall shear stress model

Since atmospheric turbulence is anisotropic, LES model is very suitable for atmospheric flow simulation. However, it is very computationally expensive to resolve the near wall region, because the scale of the turbulence becomes extremely small in this region. Actually the wind turbine operates in the "log-law" region of atmosphere. The near wall effects can

(a) The sketch of precursor method

(b) The velocity field simulated by precursor method (m/s)
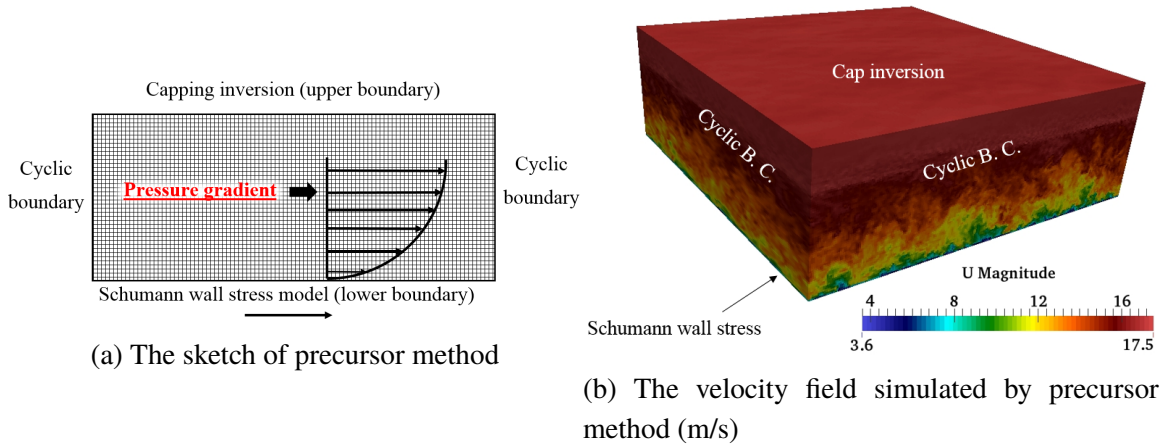
Figure 2.37 Illustration and simulation result of precursor method

be simplified by using wall shear stress model. Instead of resolving the near wall region, the Schumann wall stress [75] are added on the wall surface to reproduce the "log-law" boundary layer flow. The Schumann wall shear stress is introduced in this section. The shear stress is related to the friction velocity u^*, which can be calculated by the velocity and height of the first cell center (subscript $\frac{1}{2}$) and the log law. In Equation (2.38), the brackets represent the horizontal average.

$$u_* = \frac{\kappa \langle \tilde{u}_{\frac{1}{2}} \rangle}{\ln(\frac{z}{z_0} + f(L))} \tag{2.38}$$

In this equation, L is the Obukhov length which represents the buoyancy effect on turbulent flows. In neutral atmosphere, $f(L)$ is zero. The sketch of Schumann wall stress model is as follows:
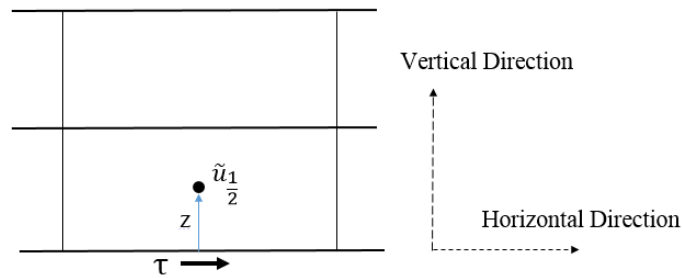
Figure 2.38 The sketch of Schumann wall stress model

The next important question is how to calculate the wall stress τ of each grid. Schumann assumed that the wall stress τ is proportional to the local velocity of the first grid, which is shown in the equation below:

44

$$\tau = -u_*^2 \frac{\tilde{u}_{1/2}}{\langle \tilde{u}_{1/2} \rangle} \tag{2.39}$$

The calculated wall shear force τ will be applied in the flow field to simulate the wall effect of the ground. It should be mentioned here that the precursor method does not guarantee the log law profile. As a result, the precursor method can be validated by comparing with log law profile. For the case in the previous subsection, the calculated mean velocity profile matches well with the log-law profile, which can be seen in Figure 2.39. It can be seen that precursor method has a very good agreement with the log law in the region where wind turbines operate (0 - 200 m).
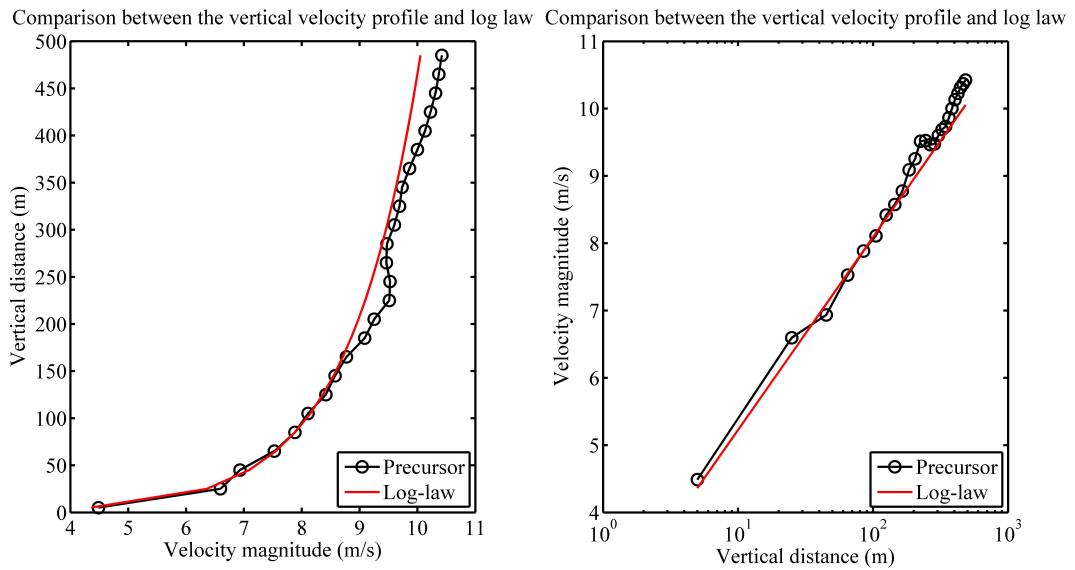
Figure 2.39 Comparison between the predicted vertical velocity profile and the log-law profile.

2.7   Case study: wind farm with 9 wind turbines

In the previous sections, the wind turbine wake and atmospheric flow are all studied and simulated by using actuator line model and precursor method respectively. In this section, the aforementioned two method will be coupled together to simulate the wake flow in atmospheric flow of a wind farm. A wind-turbine cluster with nine WindPACT wind turbines is studied. This wind farm will also be used in the following chapters to study the dynamic loading on the wind turbine blade.

2.7.1 Case description

The WindPACT wind turbine model in this case is a 1.5 MW wind turbine, which is a typical scale wind turbine in application. The blade of WindPACT wind turbine is a 33 m length blade. S818, S825, and S826 are used in different sections of the blade, which is shown in Figure 2.40. The lift and drag coefficients for actuator line models are shown in Figure 2.41. The twist and chord distributions are illustrated in the Figure 2.42. The parameters for the WindPACT wind turbine are given in Table 2.2.
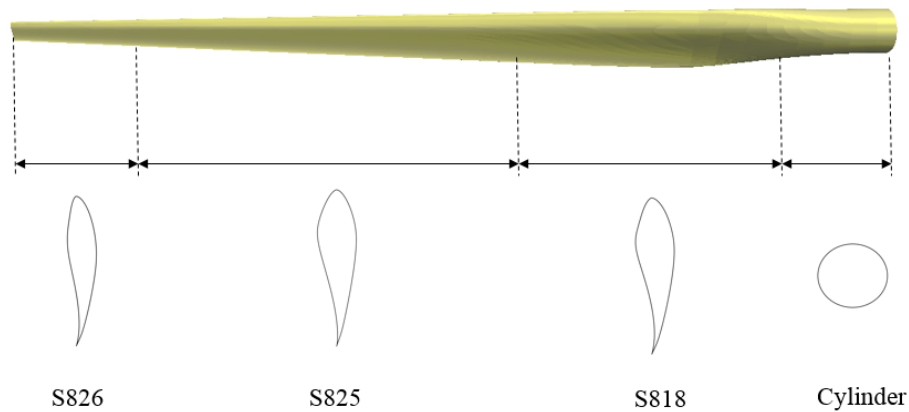
Figure 2.40 WindPACT wind turbine and the airfoil distribution.

Table 2.1 Parameters of WindPACT wind turbine.

Distance from root (m)	Airfoil	Chord (m)	Twist (^{o})
0	Cylinder	1.89	10.5
0.7	Cylinder	1.89	10.5
7	S818	2.8	10.5
15.75	S825	2.16	2.5
24.5	S825	1.52	0
33.25	S826	0.875	-0.6

The mesh in Section 2.6 will be used in this case as the background mesh. The background mesh is refined around the wind farm region. The refined region is highlighted with red, which is shown in Figure 2.43. The layout of the wind turbines is also shown in Figure 2.43. The longitudinal distance between wind turbines is 5D, and the lateral distance between wind turbines is 3D. In this case, the mesh size is refined to be 1.25 m, and the refined mesh is illustrated in Figure 2.43. In the previous section, the flow field in the wind farm becomes fully turbulent after 20000 s. The boundary values (from 20000 - 20400 s) of the atmospheric simulation with background mesh are stored and mapped to the inlet

boundary conditions of the refined mesh case, in which the outlet boundary is zero gradient boundary condition for velocity. The body forces of pressure gradient are also stored in the background mesh case and applied in the refined mesh case. This methodology is included in the SOWFA code and presented in Figure 2.44.
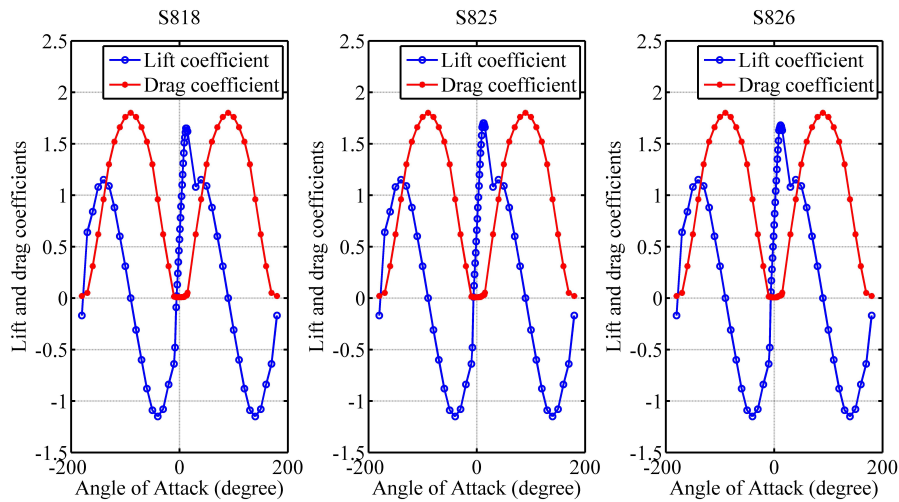
Figure 2.41 The lift and drag coefficients for the airfoils of WindPACT wind turbine.
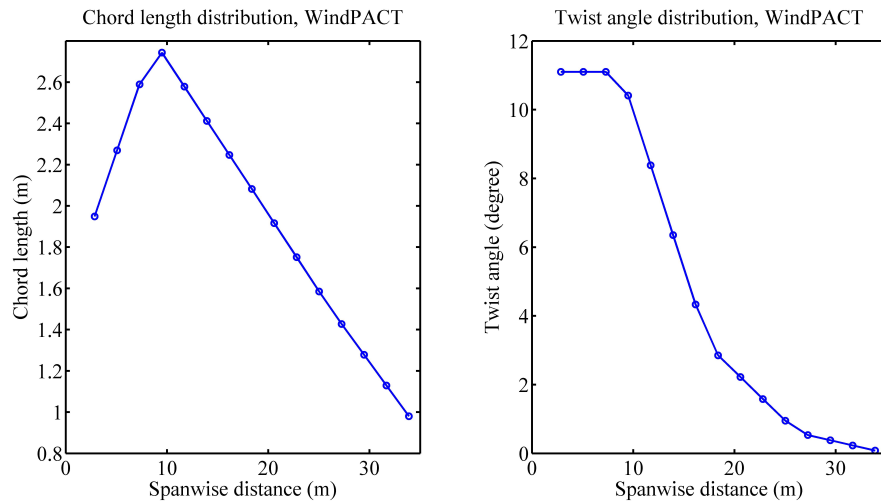
Figure 2.42 Geometric properties of WindPACT wind turbine.

2.7.2 Results and discussion

The simulated velocity field is shown in Figure 2.45, in which the fully turbulent flow can be found. It can be also seen that the wake flow of the nine wind turbines is meandering.
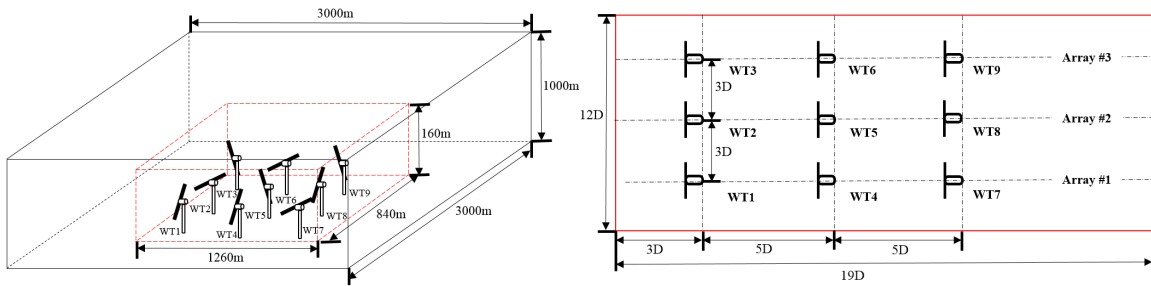
(a) The sketch of nine WindPACT wind turbines. (b) The layout of the nine-wind-turbine wind farm.
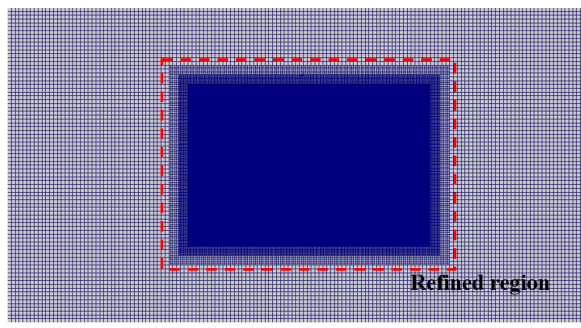
(c) Mesh for the simulation case.

Figure 2.43 Illustration of layout and mesh of the wind farm case.
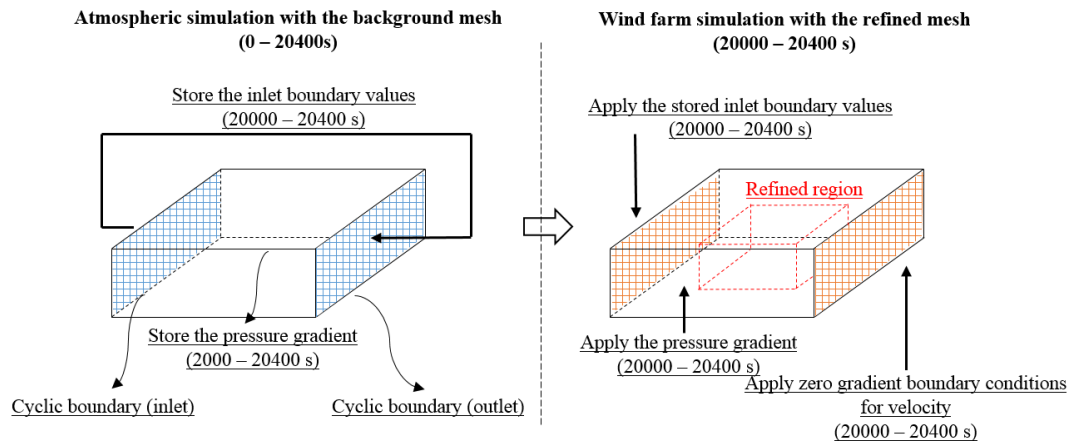
Figure 2.44 Simulation methodology of wind farm case.

Table 2.2 Parameters of WindPACT wind turbine.

Parameters	Value
Hub height	84 m
Rotor diameter	70 m
Cut-in speed	3 m/s
Rated speed	11.5 m/s
Cut-out speed	27.6 m/s
Rated power	1.5 MW
Rotational speed	20.5 rpm

Obviously, the wake flow is asymmetric in the wind farm. The downstream wind turbines are all fully immersed in the upstream wind turbine wakes (blue region). It should also seen in Figure 2.45 that the wakes of nine wind turbines interact with each other, and the wind farm wake also occurs behind the wind-turbine cluster. The power outputs and their average values of the nine wind turbines are shown in Figures 2.46 and 2.47 respectively. In Figure 2.46, the power outputs of downstream wind turbines (WT 4, 5, 6, colored with red and green) are obviously lower than that of the upstream wind turbine (WT 1, 2, 3, colored with red). Similar to the observations in the real wind farm, a huge power output decrease can be found in the comparison between the first upstream wind turbine and the second wind turbine. No clear power decrease is observed in the comparison between the second turbine and the third one. This phenomenon can be seen in all three arrays of wind turbine as evident in Figure 2.46. The simulation period in this case is 400 seconds due to the high computation cost. In the following research the simulation period is increased to 600 seconds. In the future, the author would further improve the simulation period to achieve better statistical convergence.
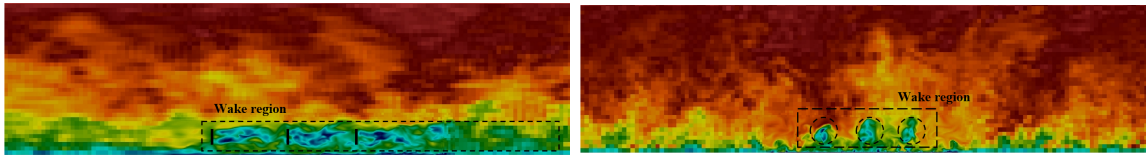
(a) The cutting plane of velocity magnitude along the streamwise direction.

(b) The cutting plane of velocity magnitude along the spanwise direction.
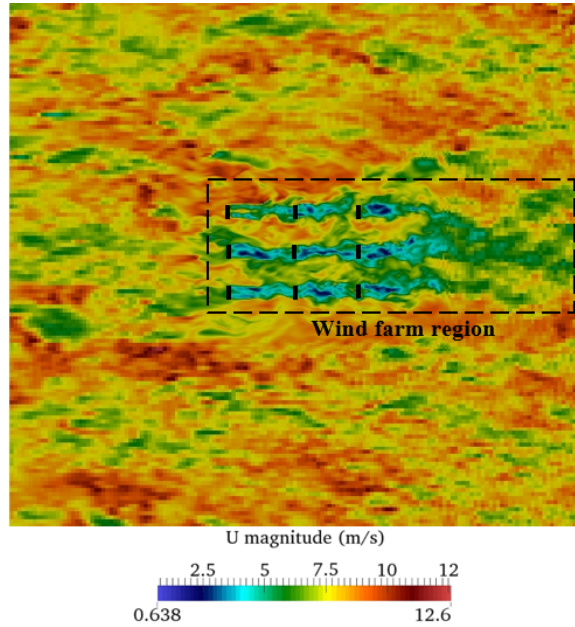
(c) The horizontal cutting plane at the hub height.

Figure 2.45 Simulation result of wind farm with nine WindPACT wind turbines.
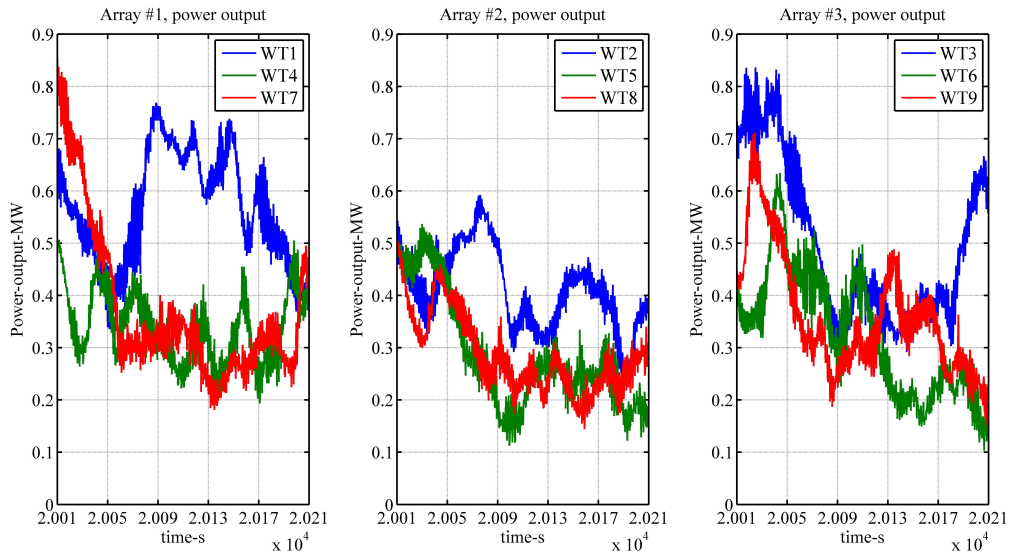
Figure 2.46 Comparison between the fluctuating power output of wind turbines.
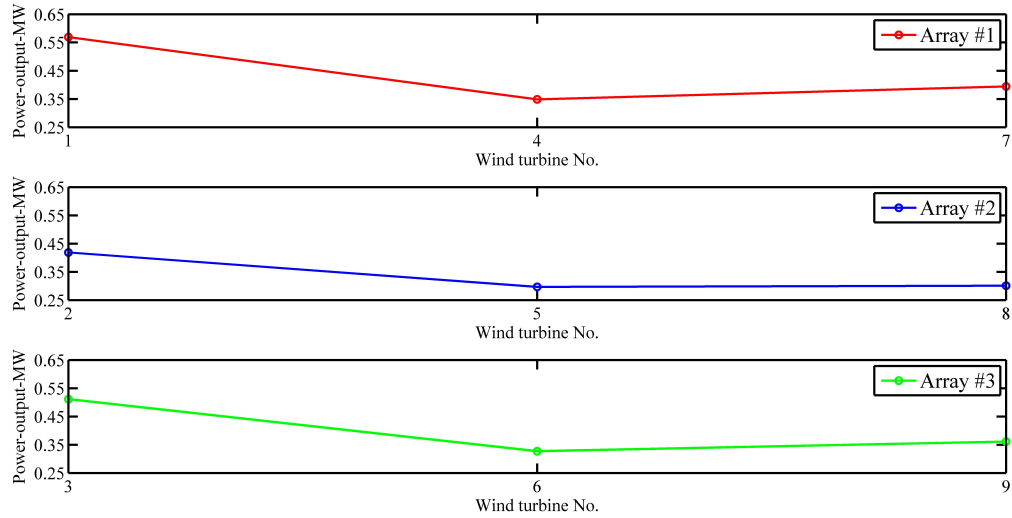
Figure 2.47 Comparison between the average power output of wind turbines.

2.8 Chapter summary

In this chapter, actuator line model is fully introduced and validated by using wind tunnel experiment data in terms of aerodynamic force and wake flow predictions, which are important to the dynamic loading of wind turbine blade. In addition, the precursor method in SOWFA (simulator for wind farm application) code [76] is also introduced for atmospheric flow simulation, which is preliminarily verified by log-law profile. The results in terms of wake loss of the coupled model of actuator line and precursor method are also reasonable. From the simulations above, firstly, it is found that the nacelle effect is not considered in the conventional actuator line model, which may affect the velocity profile around the wake center. The nacelle model is proposed to model the nacelle effect effectively, which is validated in this chapter. Secondly, it can be found that the structural deformation is not considered in the conventional actuator line model, which is significant to the fatigue damage of wind turbine blade. To solve this problem, the elastic actuator line model will be proposed in the next chapter.

Chapter 3

Elastic actuator line model

In the previous chapter, the actuator line model has been introduced and validated in terms of flow field and aerodynamic force prediction. From the previous study, it is found that the actuator line model can predict the wake flow and aerodynamic loading accurately. From the wind farm case, it is found that the actuator line model can predict wake induced power loss, which is very similar to the observations. However, from the structure side, there are still several important factors, including gravitational force, inertia force, and elastic force, which are neglected in actuator line model. They are neglected because they have less effect on the power output of wind turbines. But these factors play important roles in the dynamic loading of wind turbine blade, which is the foundation of wake induced fatigue analysis of wind turbine blade.
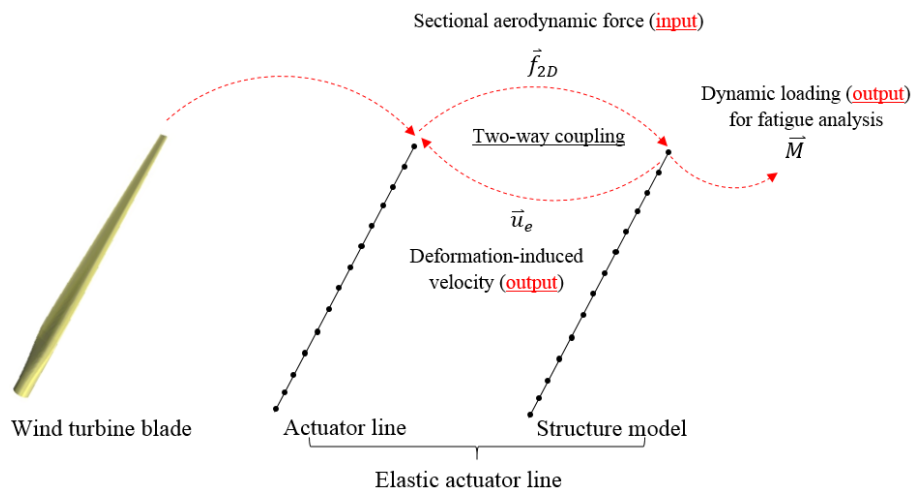
Figure 3.1 Principle of elastic actuator line model.

To consider these factors, the structural model for wind turbine blade is built and coupled with actuator line model in this thesis. The coupled model is called "elastic actuator line

53

model". It should be mentioned here that the coupling between actuator line model and the structural model is a two-way coupling, which is presented in Figure 3.1 and Figure 3.2. Obviously, the actuator line model provides the structural model with aerodynamic force. The aerodynamic force of actuator line model is also influenced by the structural model, because the local angle of attack will change due to the elastic deformation of wind turbine blade. Equation (2.3) in actuator line model turns into Equation (3.1) in elastic actuator line model. $u_{e,n}$ and $u_{e,t}$ are two velocity components for actuator line element or blade element, which are induced by the elastic deformation. The position of the nodes are passed from the structural model to the aerodynamic model (in addition to the velocities) in the current model. The orientation change has not been considered in the current model.

If the structure model is a black box (red box in Figure 3.2), its input is the aerodynamic force from actuator line model, and the outputs of the black box are the velocity of blade element under the rotating coordinate system and the dynamic loading (see Figure 3.1). In the following sections, the structure model for elastic actuator line will be constructed, and the proposed elastic actuator line model will also be verified.

$$\alpha = \Psi - \beta = \arctan(\frac{u_n + u_{e,n}}{u_t + u_{e,t}}) - \beta \tag{3.1}$$
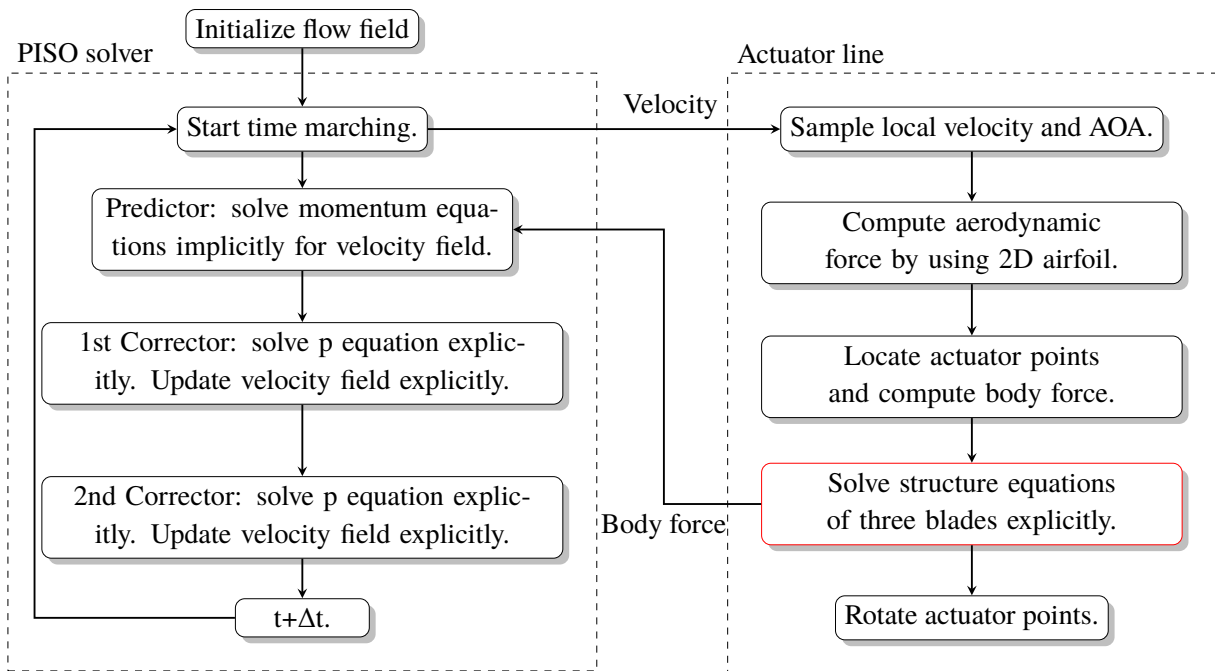
Figure 3.2 Flowchart of the elastic actuator line model based on PISO solver.

3.1 Explicit elastic actuator line

3.1.1 Theoretical equations

Since wind turbine blade is a slender structure whose one dimension is much larger than the other two (see Figure 3.1), it can be simplified as a cantilever beam. Due to its large aspect ratio, its beam equations can be further reduced by applying the Euler-Bernoulli assumptions [60]. The simplified beam equations are called "Euler-Bernoulli beam", which will be the structure model for elastic actuator line in this section. The derivations based on kinematics analysis and equilibrium equations of beam section are shown in the Appendix A. The local coordinate system of the beam equations is shown in Figure 3.3. From Figure 3.3, it can be seen that the local coordinate system is attached on the rotating blade, which is non-inertia coordinate system so that the inertia forces should be introduced. In the local coordinate system, there exist three dimensions, including direction 0 (out-of-plane), direction 1 (in-plane), and direction 2 (span-wise). Direction 0 is along the principle axis of the main shaft. Direction 2 is defined to be along the span-wise direction. Direction 1 is perpendicular to both direction 2 and direction 0 following the right-hand rule. Each rotating blade will has one local coordinate system. The subscript of variables indicates which direction it follows. The partial differential equations of wind turbine blade structure is presented in Equations (3.2) - (3.4). It should be mentioned here that only deflections along direction 0 and 1 are considered in this chapter. In the next two chapters, the other 4 degrees of freedom (another deflection and 3 torsions) will be considered. The current model also neglects the geometric nonlinearity, change in the centrifugal forces associated with the transverse deflections, Coriolis forces (nonlinear), blade coning and pitching, and blade coning and pitching. In the next stage research, the author would further improve these models in terms of these factors.

$$\rho_s(r)\frac{\partial^2 q_0}{\partial t^2} + \frac{\partial^2}{\partial r^2}(EI_{00}(r)\frac{\partial^2 q_0}{\partial r^2} + EI_{01}(r)\frac{\partial^2 q_1}{\partial r^2}) - \frac{\partial}{\partial r}(N_c(r)\frac{\partial q_0}{\partial r}) - f_{2D,0} - f_{g,0} = 0 \quad (3.2)$$

$$\rho_s(r)\frac{\partial^2 q_1}{\partial t^2} + \frac{\partial^2}{\partial r^2}(EI_{11}(r)\frac{\partial^2 q_1}{\partial r^2} + EI_{10}(r)\frac{\partial^2 q_0}{\partial r^2}) - \frac{\partial}{\partial r}(N_c(r)\frac{\partial q_1}{\partial r}) - f_{2D,1} - f_{g,1} = 0 \quad (3.3)$$

$$N(r) = \int_r^R \rho_s(r)\Omega^2 r dr \quad (3.4)$$

In Equations (3.2) - (3.4), q indicates the displacement of each section, which is the dependent variable in the above equations. r and t represent span-wise direction (direction 2) and time, which are independent variables in the above equations. ρ_s is the mass per unit
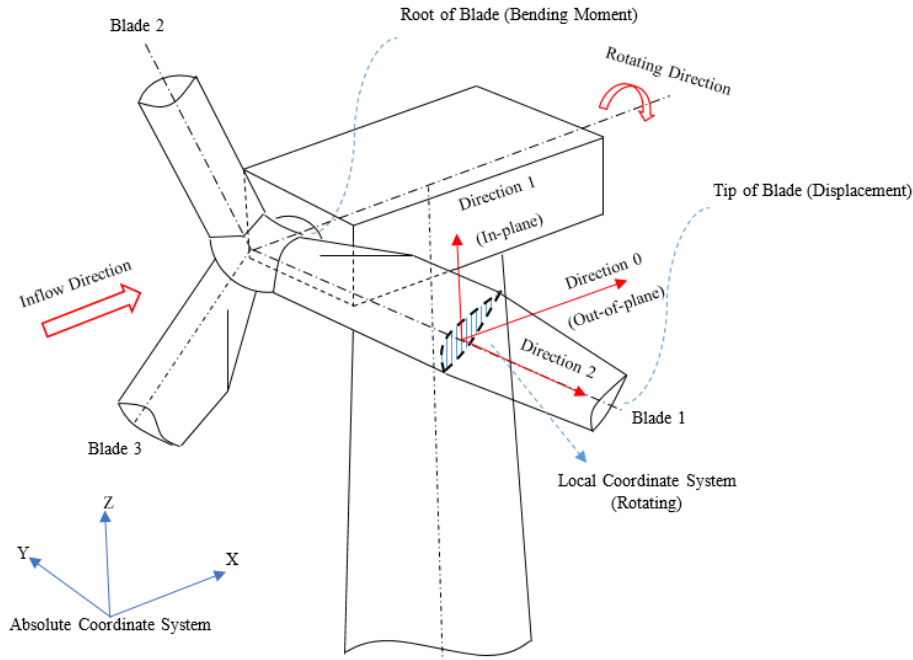
Figure 3.3 The coordinate system of structure model.

length for each beam section. EI represents the stiffness of the cross section. N_c and f_g are the centrifugal force and gravitational force on each cross section. The root of the beam is clamped, and the tip is assumed to be free end.

There are two obvious difficulties in solving these equations numerically. Firstly, the presence of the high order terms (second order in time and fourth order in space) will complicate the numerical discretization and the implementation of boundary conditions. In addition, high order schemes often cause instability. For example, the central difference schemes with fourth or higher order are unstable when the high-order boundary schemes are implemented. Secondly, the two governing equations are coupled together, which can be seen from the second term in Equations (3.2) - (3.3). The coupling effect is caused by the structural twist of the wind turbine blade. Contrary to the conventional beam structure, wind turbine blade sections are non-uniform and twisted (twist angle is also non-uniform from 0° to 10°), which is shown in Figure 3.4. The stiffness in Equation (3.2) - (3.3) can be derived according to the edgewise (EI_e) and flapwise (EI_f) stiffness, which is shown in Equation (3.5) - (3.7). This coupled equations require to be solved simultaneously, which is computationally expensive. In addition, the derivative of EI should be dealt with in the simulation. The equations are solved alternatively because the simultaneous equation has high order time and spatial derivatives, which makes the numerical model very unstable. Lowering the order of derivatives and solving alternatively is an effective method to solve this problem for FDM model.

56

$$EI_{00} = EI_e - (EI_e - EI_f)\cos^2\theta \tag{3.5}$$

$$EI_{11} = EI_f + (EI_e - EI_f)\cos^2\theta \tag{3.6}$$

$$EI_{01} = EI_{10} = \sin 2\theta\left(\frac{EI_e - EI_f}{2}\right) \tag{3.7}$$
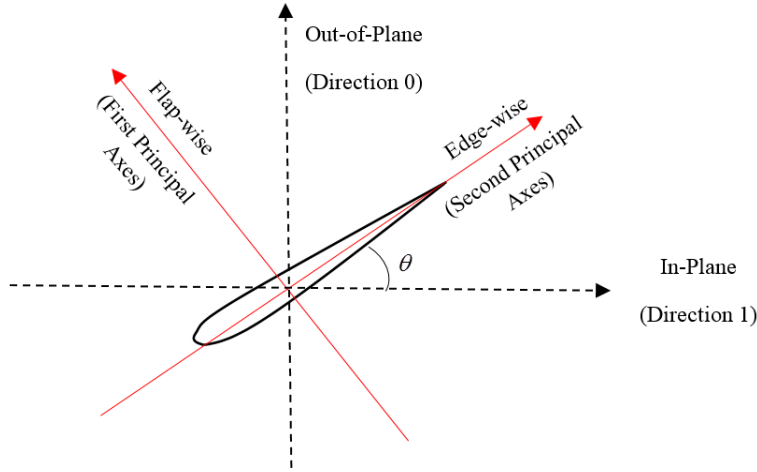
Figure 3.4 Illustration of structural twist of wind turbine blade.

In this thesis, to overcome the aforementioned two difficulties, two sets of variables are introduced, including deformation-induced velocity V and M (and S). They are defined by the following Equations (3.8) - (3.10).

$$V_0 = \frac{\partial q_0}{\partial t}, \quad V_1 = \frac{\partial q_1}{\partial t} \tag{3.8}$$

$$M_0 = EI_{00}(r)\frac{\partial^2 q_0}{\partial r^2} + EI_{01}(r)\frac{\partial^2 q_1}{\partial r^2}, \quad M_1 = EI_{11}(r)\frac{\partial^2 q_1}{\partial r^2} + EI_{10}(r)\frac{\partial^2 q_0}{\partial r^2} \tag{3.9}$$

$$S_0 = N_c(r)\frac{\partial q_0}{\partial r}, \quad S_1 = N_c(r)\frac{\partial q_1}{\partial r} \tag{3.10}$$

After substituting Equations (3.8) - (3.10) into Equations (3.2) - (3.4), the original governing equations are transformed to a new formulation (Equations (3.11) - (3.16)):

$$\rho_s(r)\frac{\partial V_0}{\partial t} + \frac{\partial^2 M_0}{\partial r^2} - \frac{\partial S_0}{\partial r} - f_{2D,0} - f_{g,0} = 0 \tag{3.11}$$

$$\rho_s(r)\frac{\partial V_1}{\partial t} + \frac{\partial^2 M_1}{\partial r^2} - \frac{\partial S_1}{\partial r} - f_{2D,1} - f_{g,1} = 0 \tag{3.12}$$

$$\frac{\partial M_0}{\partial t} = EI_{00}(r)\frac{\partial^2 V_0}{\partial r^2} + EI_{01}(r)\frac{\partial^2 V_1}{\partial r^2} \tag{3.13}$$

$$\frac{\partial M_1}{\partial t} = EI_{11}(r)\frac{\partial^2 V_1}{\partial r^2} + EI_{10}(r)\frac{\partial^2 V_0}{\partial r^2} \tag{3.14}$$

$$\frac{\partial S_0}{\partial t} = N_c(r)\frac{\partial V_0}{\partial r} \tag{3.15}$$

$$\frac{\partial S_1}{\partial t} = N_c(r)\frac{\partial V_1}{\partial r} \tag{3.16}$$

Although the number of governing equations increases from two to six by applying this substitution and transformation method, it brings three advantages. Firstly, the orders of derivatives are reduced, which can be seen from Equations (3.11) - (3.16) that the highest orders of derivatives for time and space are first order and second order respectively. This avoids the aforementioned difficulty of high order scheme for the time and spatial derivatives. Secondly, the above equations can be solved alternatively rather than simultaneously. Specifically, the variable V is solved first based on M and S of previous time step. Then the M and S will be updated by using the new V. Lastly, the variables V and M represents the deformation induced velocity and bending moments, which are the required output for elastic actuator line model (see Figure 3.1). For example, V_0 and V_1 are related to $u_{e,t}$ and $u_{e,n}$ in Equation (3.1), which is one "bridge" between actuator line model and structure model (see Figure 3.1). The relation between them is shown in Equation (3.17).

$$u_{e,t} = -V_1, \quad u_{e,n} = -V_0 \tag{3.17}$$

The root of the blade is clamped, which is the boundary condition (mixed boundary condition) for V. V and its first order spatial derivative are zero. This boundary condition is shown in Equation (3.18).

$$\frac{\partial V_0}{\partial r} = 0, \quad V_0 = 0, \quad \frac{\partial V_1}{\partial r} = 0, \quad V_1 = 0 \tag{3.18}$$

The tip of the blade is free end, which is the boundary condition (mixed boundary condition) for M. M and its first order spatial derivative (shear force) are zero. This boundary condition is shown in Equation (3.19).

$$\frac{\partial M_0}{\partial r} = 0, \quad M_0 = 0, \quad \frac{\partial M_1}{\partial r} = 0, \quad M_1 = 0 \tag{3.19}$$

In summary, our problem is to solve the Equations (3.11) - (3.16) under the boundary conditions of Equations (3.18) - (3.19), which is an initial and boundary value problem. In the next subsection, the numerical equations will be presented to solve the proposed governing equations.

3.1.2 Numerical model

Forward Euler method is used to discretize the time derivative, which means that the numerical model is explicit. The numerical discretization of the structural model (Equations (3.11) - (3.16)) is shown in Equations (3.20) - (3.26). The time accuracy is further increased to 2nd order in Chapter 5 by employing leapfrog scheme.

$$\frac{V_{0,i}^{n+1} - V_{0,i}^{n}}{\Delta t} = -\frac{1}{\rho_{s,i}}\frac{(\delta^2 M_0)_i^n}{\Delta r^2} + \frac{1}{\rho_{s,i}}\frac{(\delta S_0)_i^n}{\Delta r} + \frac{f_{2D,0,i}^n + f_{g,0,i}^n}{\rho_{s,i}} \tag{3.20}$$

$$\frac{V_{1,i}^{n+1} - V_{1,i}^{n}}{\Delta t} = -\frac{1}{\rho_{s,i}}\frac{(\delta^2 M_1)_i^n}{\Delta r^2} + \frac{1}{\rho_{s,i}}\frac{(\delta S_1)_i^n}{\Delta r} + \frac{f_{2D,1,i}^n + f_{g,1,i}^n}{\rho_{s,i}} \tag{3.21}$$

$$\frac{M_{0,i}^{n+1} - M_{0,i}^{n}}{\Delta t} = (EI_{00})_i\frac{(\delta^2 V_0)_i^{n+1}}{\Delta r} + (EI_{01})_i\frac{(\delta^2 V_1)_i^{n+1}}{\Delta r^2} \tag{3.22}$$

$$\frac{M_{1,i}^{n+1} - M_{1,i}^{n}}{\Delta t} = (EI_{11})_i\frac{(\delta^2 V_1)_i^{n+1}}{\Delta r} + (EI_{10})_i\frac{(\delta^2 V_0)_i^{n+1}}{\Delta r^2} \tag{3.23}$$

$$\frac{S_{0,i}^{n+1} - S_{0,i}^{n}}{\Delta t} = N_{c,i}\frac{(\delta V_0)_i^{n+1}}{\Delta r} \tag{3.24}$$

$$\frac{S_{1,i}^{n+1} - S_{1,i}^{n}}{\Delta t} = N_{c,i}\frac{(\delta V_1)_i^{n+1}}{\Delta r} \tag{3.25}$$

$$N_{c,i} = \sum_{j=i}^{N_s} \rho_{s,j}\Omega^2 r_j \Delta r \tag{3.26}$$

The finite difference operators in Equations (3.20) - (3.26) are shown in Equations (3.27) - (3.28).

$$\delta^2 M_i = M_{i-1} - 2M_i + M_{i+1} \quad \delta^2 V_i = V_{i-1} - 2V_i + V_{i+1} \tag{3.27}$$

$$\delta S_i = S_i - S_{i-1}, \quad \delta V_i = V_{i+1} - V_i \tag{3.28}$$

As mentioned in the previous subsection, the numerical model will be solved alternatively and explicitly. Firstly, V will be solved based on the M, S, and $\vec{f}_{2D}$ in previous time step according to Equations (3.20) - (3.21). Secondly, M and S in the next time step will be solved based on the updated V according to Equations (3.22) - (3.26). The flowchart of the solution procedure is shown in Figure 3.5. This procedure will be repeated in the solution procedure.

The physical meaning for the Equations (3.20) - (3.21) is the Newton's second law or equilibrium equations, which means that the external loading drives the blade element to deform or the dynamics of the beam. Equations (3.22) - (3.26) indicate the Hooke's law or relation between deformation curvatures and elastic forces or the kinematics of the beam. In the author's opinion, these equations can be solved alternatively, because each set of equations represents a single physical process.
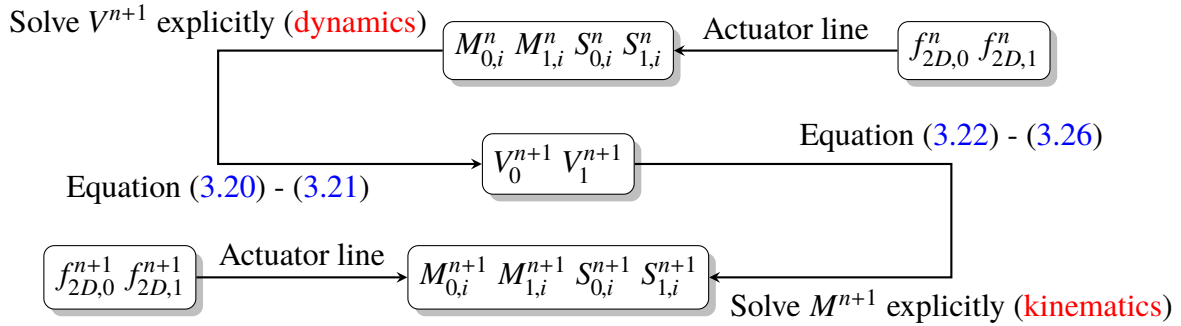
Figure 3.5 Flowchart of the numerical structure model.

For the numerical partial differential equations in explicit formulation, it is necessary to derive the largest time step (or CFL number). To derive the necessary condition of the time step for the proposed numerical model, the stability analysis is carried out, which is shown in Appendix B. To simplify the stability analysis, the coupled terms and centrifugal terms are dropped. The above Equations (3.20) - (3.25) turn into simplified formulation of Equations (3.29) - (3.32).

$$\frac{V_{0,i}^{n+1} - V_{0,i}^{n}}{\Delta t} = -\frac{1}{\rho_{s,i}} \frac{(\delta^2 M_0)_i^n}{\Delta r^2} + \frac{f_{2D,0,i}^n + f_{g,0,i}^n}{\rho_{s,i}} \tag{3.29}$$

$$\frac{V_{1,i}^{n+1} - V_{1,i}^{n}}{\Delta t} = -\frac{1}{\rho_{s,i}} \frac{(\delta^2 M_1)_i^n}{\Delta r^2} + \frac{f_{2D,1,i}^n + f_{g,1,i}^n}{\rho_{s,i}} \tag{3.30}$$

$$\frac{M_{0,i}^{n+1} - M_{0,i}^{n}}{\Delta t} = (EI_{00})_i \frac{(\delta^2 V_0)_i^{n+1}}{\Delta r} \tag{3.31}$$

$$\frac{M_{1,i}^{n+1} - M_{1,i}^{n}}{\Delta t} = (EI_{11})_i \frac{(\delta^2 V_1)_i^{n+1}}{\Delta r} \tag{3.32}$$

The stability condition for the time step is shown in equation below.

$$\Delta t \leq \sqrt{\frac{\rho_s}{EI}} \frac{\Delta r^2}{2} \tag{3.33}$$

In this equation, $\frac{\rho_s}{EI}$ is the minimum value of $\frac{\rho_{s,i}}{EI_i}$ of all the sections. This condition will be used in the case study to select the appropriate time step for the simulation. The boundary conditions for V, M, and S are shown in Figure 3.6.
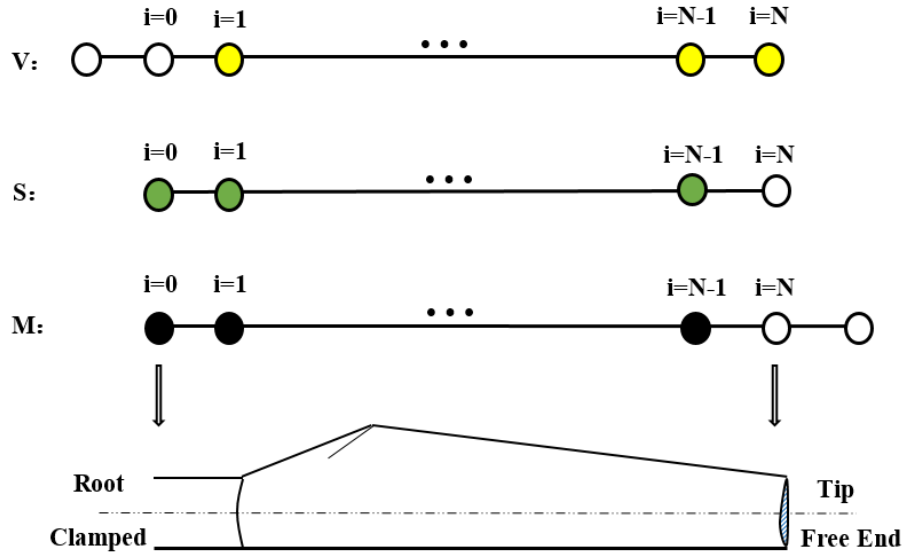
Figure 3.6 The boundary condition for the numerical structure model. (The hollow circle indicates the value is 0.)

The programming code is illustrated in Appendix G.1.

3.2 Verification and case study

3.2.1 Verification case 1

A comparison between the results of the proposed elastic actuator line model and the NREL FAST 7.0 on the dynamic loading of single NREL 5MW wind turbine is carried out. NREL FAST 7.0 has long been used for aero-elastic simulation of single wind turbine in wind energy industry. As a result, the comparison is an efficient and effective method to verify

the newly proposed elastic actuator line model in the previous section. The NREL 5MW is used to be the research object of comparison.

As mentioned in the previous section, the rotor diameter and the hub height of NREL 5MW wind turbine are 126 m and 90 m respectively. The rated rotational speed is set to be 12.1 rpm, and the cut-in, rated, and cut-out wind speed are 3 m/s, 11.4 m/s, and 25 m/s respectively. In verification case 1, the inlet wind condition is set to be the steady wind of 5 m/s. The rotational speed is set to be 9.16 rpm. The tip speed ratio (TSR) for the 5 m/s wind velocity is around 12 (high TSR value). The TSR is well above the operational TSR of wind turbine. This is a numerical verification for the proposed model. The structural properties of NREL 5MW wind turbine blade are shown in Figure 3.7.

For the turbulence model, the standard $k - \epsilon$ turbulence model is employed. The PISO solver is used to couple velocity and pressure fields. The inlet boundary condition is uniform inflow boundary condition (Dirichlet boundary condition). The outlet boundary condition is zero gradient boundary condition (Neumann boundary condition). The boundary conditions of surrounding walls are non-slip boundary conditions (Dirichlet boundary condition). The proposed elastic actuator line model will be employed as the aeroelastic model, in which the actuator line model is coupled with the simplified beam model (3.29) - (3.32) through aerodynamic force ($\vec{f}_{2D}$) and deformation induced velocity ($\vec{u}_e$), which is shown in Figure 3.1. The data of tip displacements and root moments is recorded from 0 s (no deformation) to 6 s. The mesh of CFD model in this case is shown in Figure 3.8. There are 40 nodes for each blade (which is similar to the node number of actuator line model). The aerodynamic forces are all from the actuator line model in this case. The lack of the statistical convergence also play a role in my view because the simulation period is only 30s.
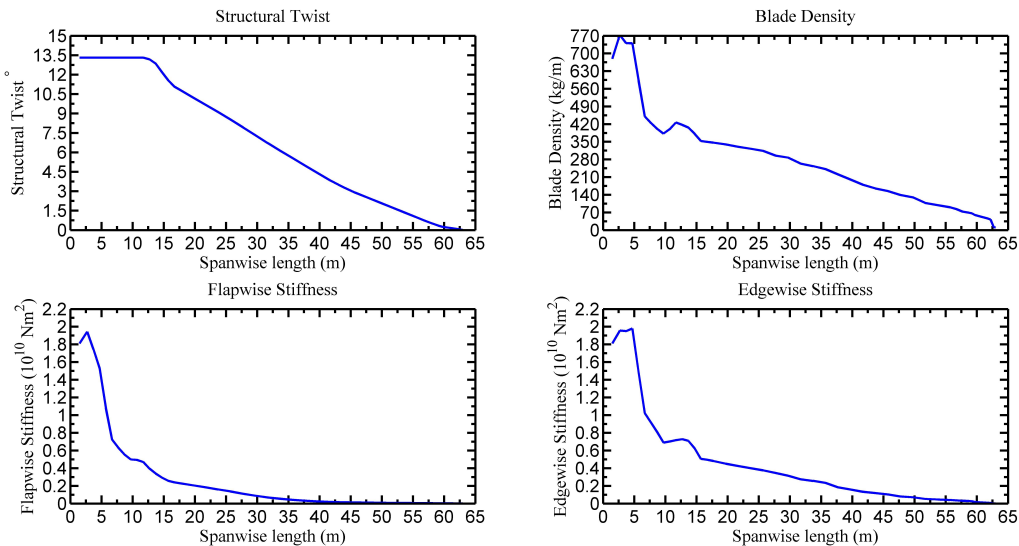
Figure 3.7 The structural properties of NREL 5MW wind turbine blade.
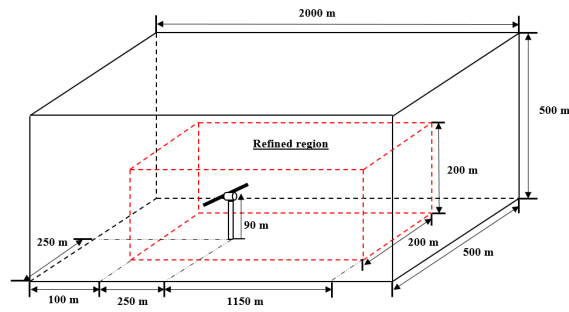
(a) The sketch of single NREL 5MW wind
turbine (refined region is colored by red).
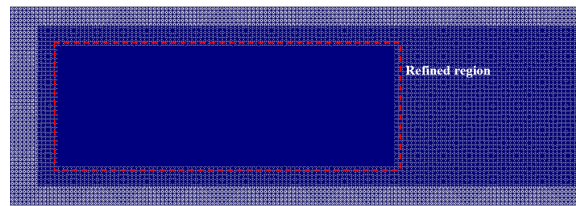
(b) Mesh of single NREL 5MW wind turbine case.

Figure 3.8 Illustration of mesh for single NREL 5MW wind turbine case.

3.2.2 Results and discussion

The calculated root bending moments and tip displacements of three blades (in the directions of out-of-plane and in-plane, see Figure 3.3) are compared with the results of NREL FAST, which are shown in Figures 3.10 and 3.11. Equation (3.33) is used to derived the time step.

It can be seen from these results that the bending moments and displacements are of the same order of magnitude as the results of NREL FAST, which are what we expected. This basically verifies the derived time step, because there is no numerical divergence during simulation. However, the fluctuation patterns of moment and tip displacement of the elastic actuator line are still different from the result of the NREL FAST. The difference is very obvious in the out-of-plane direction (or 0 direction) defined in Figure 3.1 and 3.9. Moreover, the fluctuation of moment and tip displacement from elastic actuator line are more smooth. Noticeably, these fluctuations will have impact on the fatigue damage of the wind turbine blade. The oscillation in moments time series, in my view, is because of the existence of the high-frequency modes in the structure model (explicit model).

To further quantify the errors of this simplified model, two indices are employed. Specifically, the fluctuation of root bending moment in the direction 0 is lower than that of the direction 1, while the mean value of root bending moment in the direction 0 is larger (viz., the mean value of bending moment in direction 1 is nearly 0 Nm). As a result, we use normalized Root-Mean-Square-Error (RMSE) to quantify the solution accuracy in the
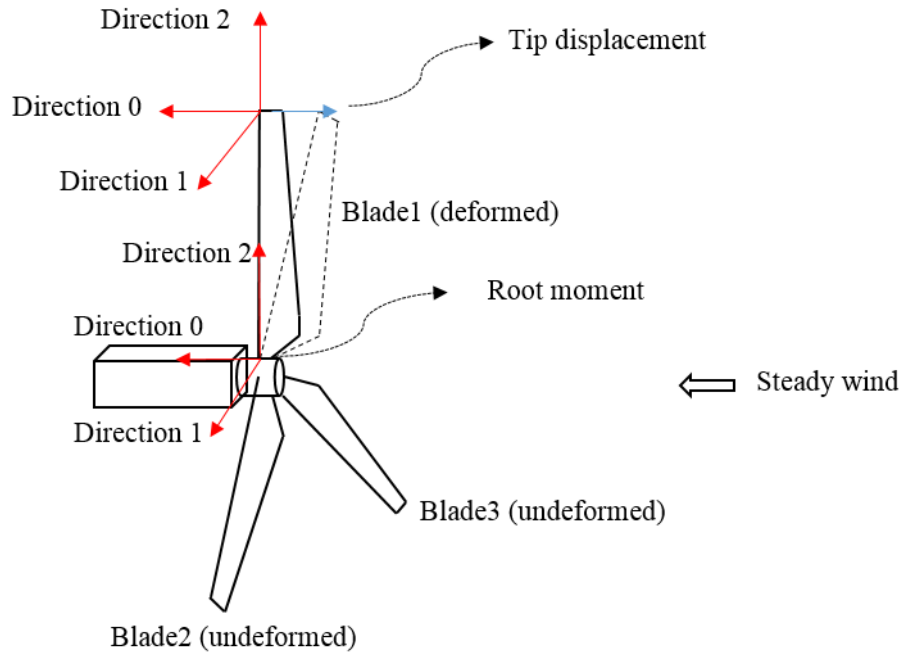
Figure 3.9 Sketch of coordinate system of the blade in the case study.
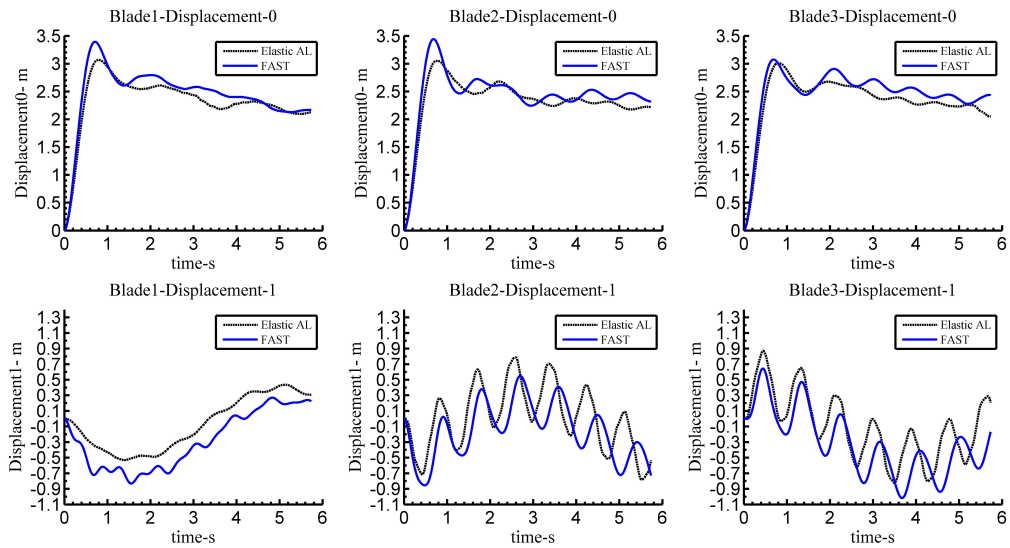
Figure 3.10 Out-of-plane (up) and in-plane (down) blade tip displacements obtained with the simplified equations (3 Blades) at tip speed ratio (TSR) = 12
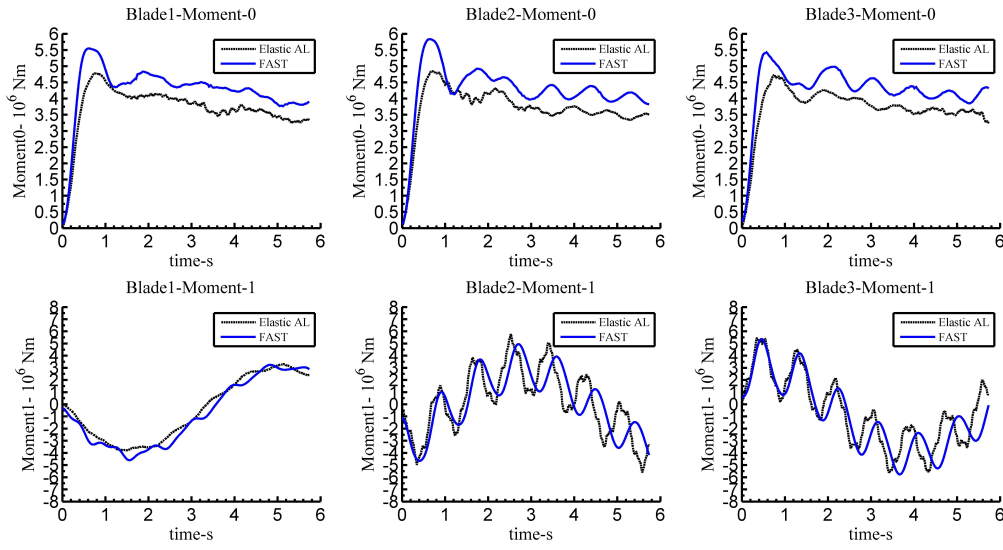
Figure 3.11 Out-of-plane (up) and in-plane (down) blade root bending moments obtained with the simplified equations (3 Blades) at tip speed ratio (TSR) = 12

direction 0 and Pearson correlation coefficient R_{cor} to quantify the solution accuracy in the direction 1. The RMSE and R_{cor} are shown in Equations (3.34) - (3.35).

$$RMSE = \frac{\sqrt{\frac{1}{n} \sum_{i=1}^{n} (y_i - \hat{y}_i)}}{Mean(\hat{y}_i)} \tag{3.34}$$

$$R_{cor} = \frac{n \sum_{i=1}^{n} \hat{y}_i y_i - \sum_{i=1}^{n} \hat{y}_i \sum_{i=1}^{n} y_i}{\sqrt{n \sum_{i=1}^{n} \hat{y}_i^2 - (\sum_{i=1}^{n} \hat{y}_i)^2} \sqrt{n \sum_{i=1}^{n} y_i^2 - (\sum_{i=1}^{n} y_i)^2}} \tag{3.35}$$

The y_i represents the predicted data from the elastic actuator line model, and $\hat{y}_i$ is the predicted data from NREL FAST. The "n" represents the number of data. The results of prediction accuracy are illustrated in Table 3.1 - 3.2.

Table 3.1 Accuracy of the elastic actuator line model in comparison with FAST in terms of root bending moments obtained with simplified equations (TSR = 12).

Root moment	Blade1	Blade2	Blade3
RMSE (0 direction)	14.35 %	15.03 %	14.80 %
R_{cor} (1 direction)	99.10 %	77.73 %	86.33 %

From Table 3.1 - 3.2, more information of simplified model is found. Although this simplified model can provide reasonable results (the order of magnitude), we can still see at least two problems in the current simplified mode:

Table 3.2 Accuracy of the elastic actuator line model in comparison with FAST in terms of tip displacement obtained with simplified equations (TSR = 12).

Tip displacement	Blade1	Blade2	Blade3
RMSE (0 direction)	7.02 %	7.60 %	7.31 %
R_{cor} (1 direction)	97.90 %	66.12 %	79.04 %

1. The normalized RMSE of root bending moment in the direction 0 is erroneous (around 15 %).

2. Although RMSE of tip displacement in the direction 0 is less than 10 %, the correlation coefficients (R_{cor}) of tip displacement in the direction 1 for blade 2 are lower than 70 % (the coordinate system is defined in Figures 3.3 and 3.9.

The problems are most likely due to the absence of the structural twist term and the centrifugal term.

3.2.3 Verification case 2

To prove our speculation in the discussion of verification case 1, the neglected terms (coupled terms and centrifugal terms) are considered according to Equations (3.11) - (3.16). The time step is determined according to Equation (3.33). It is expected that the complete equations (Equations (3.11) - (3.16)) can achieve higher accuracy compared with the simplified equations (Equations (3.29) - (3.32)). Since the time step is derived based on the simplified equations, this also verifications of its effectiveness on the complete equations. To comprehensively verify the proposed model, the case with low tip speed ratio (TSR = 6) is also carried out.

3.2.4 Results and discussion

The results of the complete equations are shown in Figures 3.12 (tip displacement) and 3.13 (root moment). From these two figures, the simulation with complete equations captures the fluctuations of the tip displacements and root moments very well. The accuracy of the complete model is shown in Tables 3.3 - 3.4. Compared with the results of the simplified model, the accuracy of the complete model is obviously increasing (Compare the Tables (3.1) - (3.2) with Tables (3.3) - (3.4). Specifically, all RMSEs are less than 10 % and correlation coefficients R_{cor} are more than 90 %. This indicates that the absence of structural twist term and centrifugal term will cause at least 5 % error increase of root moment RMSE in the direction 0 (see Figure 3.3).

The accuracy of results for a lower tip speed ratio (TSR = 6) are shown in Figures 3.14 - 3.15 and Tables 3.5 - 3.6.
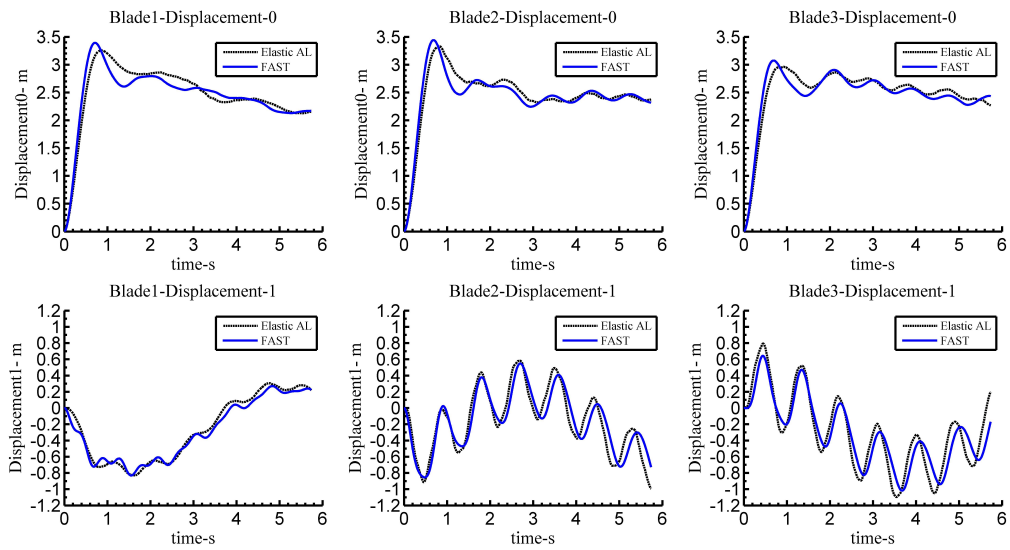
Figure 3.12 Out-of-plane (up) and in-plane (down) blade tip displacements obtained with the complete equations (3 Blades) at tip speed ratio (TSR) = 12
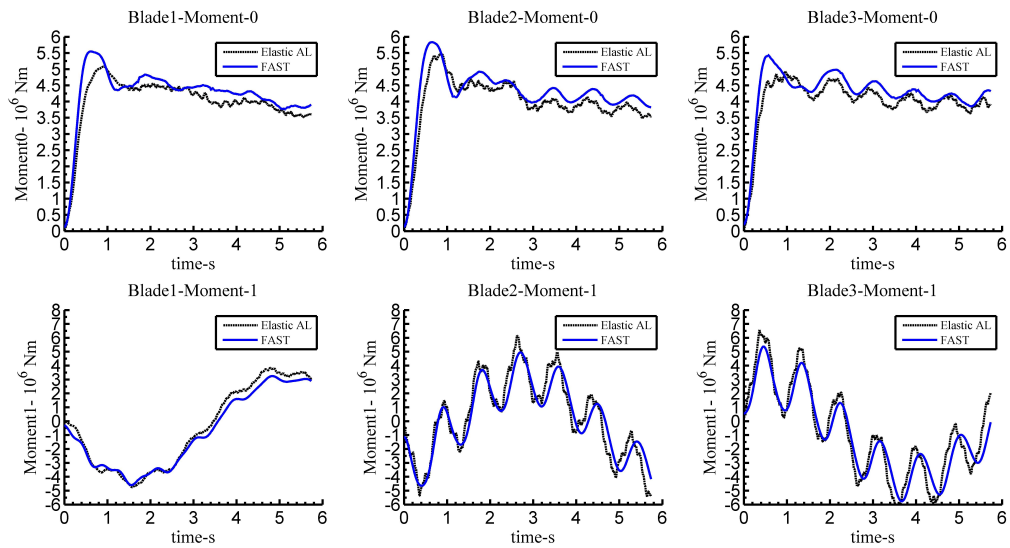
Figure 3.13 Out-of-plane (up) and in-plane (down) blade root bending moments obtained with the complete equations (3 Blades) at tip speed ratio (TSR) = 12
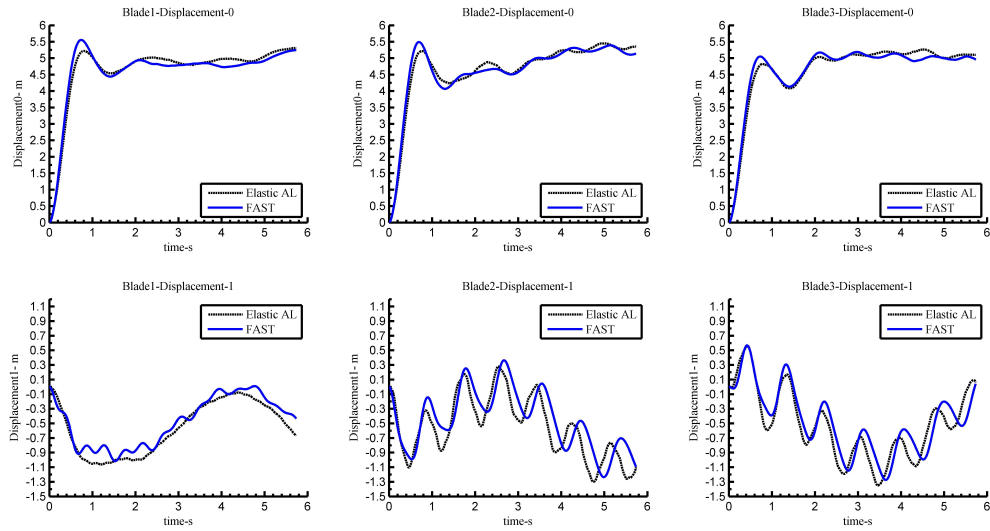
Figure 3.14 Out-of-plane (up) and in-plane (down) blade tip displacements obtained with the complete equations (3 Blades) at tip speed ratio (TSR) = 6
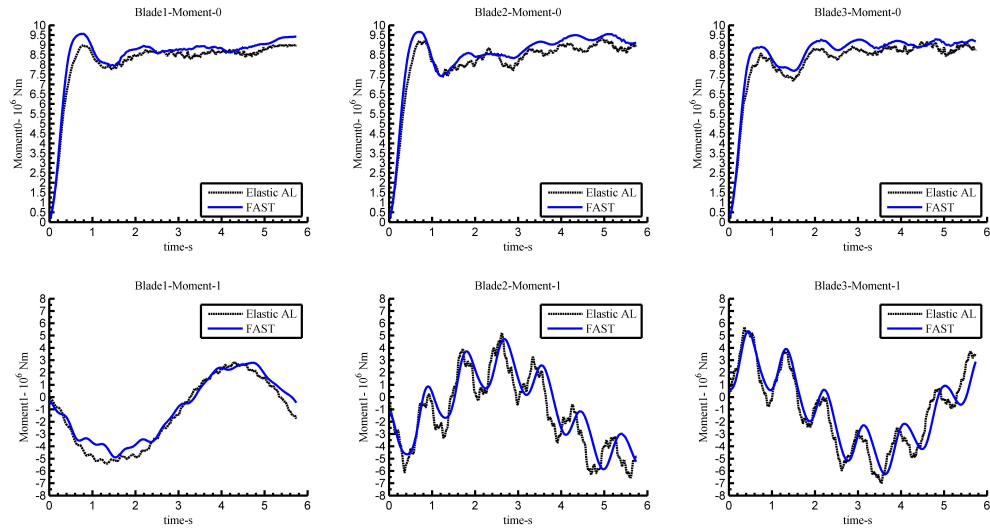
Figure 3.15 Out-of-plane (up) and in-plane (down) blade root bending moments obtained with the complete equations (3 Blades) at tip speed ratio (TSR) = 6

Table 3.3 Accuracy of the elastic actuator line model in comparison with FAST in terms of root bending moments obtained with complete equations (TSR = 12).

Root moment	Blade1	Blade2	Blade3
RMSE (0 direction)	8.86 %	9.20 %	8.37 %
R_{cor} (1 direction)	99.78 %	95.09 %	95.40 %

Table 3.4 Accuracy of the elastic actuator line model in comparison with FAST in terms of tip displacement obtained with complete equations (TSR = 12).

Tip displacement	Blade1	Blade2	Blade3
RMSE (0 direction)	6.64 %	6.03 %	5.45 %
R_{cor} (1 direction)	99.39 %	92.74 %	93.01 %

Table 3.5 Accuracy of the elastic actuator line model in comparison with FAST in terms of root bending moments obtained with complete equations (TSR = 6).

Root moment	Blade1	Blade2	Blade3
RMSE (0 direction)	4.89 %	5.52%	4.98 %
R_{cor} (1 direction)	98.57 %	89.99 %	93.49 %

Table 3.6 Accuracy of the elastic actuator line model in comparison with FAST in terms of tip displacement obtained with complete equations (TSR = 6).

Tip displacement	Blade1	Blade2	Blade3
RMSE (0 direction)	3.69 %	3.41 %	3.15 %
R_{cor} (1 direction)	99.10 %	84.80 %	91.91 %

The results of elastic actuator line still match well with those of NREL FAST 7.0. The accuracy is very similar to that for higher tip speed ratio. From these comparisons, the proposed elastic actuator line model is preliminarily verified.

3.2.5   Case study: two staggered NREL 5MW wind turbines

In the previous subsections, the theoretical and numerical formulations of the proposed elastic actuator line model are established. The preliminary verification of the proposed model is performed. For this subsection, the present elastic actuator line model will be employed to analyse the loading of two staggered NREL 5MW wind turbines.

In this case, the neutral atmosphere boundary conditions, which are shown in Equation (3.36) - (3.38), is used at inlet. The wind speed at hub height (90 m) is set to be 10 m/s. The rotational speed of the rotor is assumed to be fixed, which is a limitation of the simulation
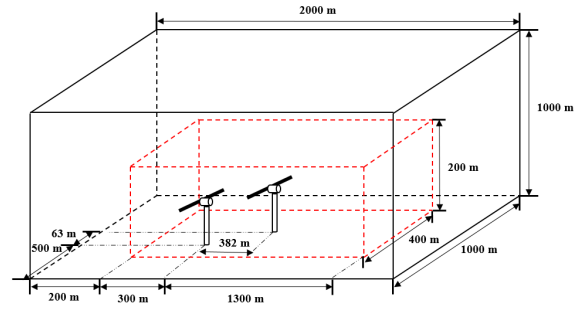
(a) The layout of staggered wind turbines.
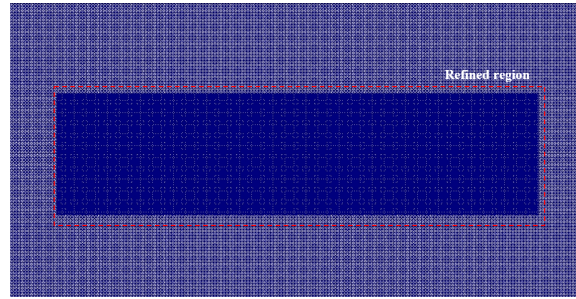
(b) The mesh for the CFD model.

Figure 3.16 Illustration of layout and mesh of simulation case.

case. Roughness length z_0 is set to be 0.1 m (grassland), and von Karman constant κ is 0.41. The friction velocity can be derived can be derived by using Equation (3.36). Then according to Equations (3.36) - (3.38), the profiles of velocity, turbulent kinetic energy, and dissipation rate can be calculated. The simulation period is 30s in this case, which is another limitation of the simulation case.

$$\bar{u} = \frac{u^*}{\kappa} \ln \frac{z}{z_0} \tag{3.36}$$

$$\epsilon = \frac{(u^*)^3}{\kappa z} \tag{3.37}$$

$$k = \frac{(u^*)^2}{\sqrt{C_\mu}} \tag{3.38}$$

The layout of the two wind turbines is shown in Figure 3.16. This is a very interesting and unique case in terms of wake-induced fatigue, which can also be found in some experiment based research. In this case, the downstream wind turbine rotor is half immersed in the upstream wind turbine wake. As a result, wind turbine wake will influence the loading history of downstream wind turbine blade. The time history of out-of-plane (or direction 0) root moment of one blade over a period of 10 seconds is illustrated in Figure 3.17. It

70

can be seen from the time series that the fluctuations of upstream and downstream wind turbines are obviously different, which is caused by the upstream wind turbine wake effect in terms of velocity deficit and an increase in turbulence intensity on the performance of downstream wind turbine.
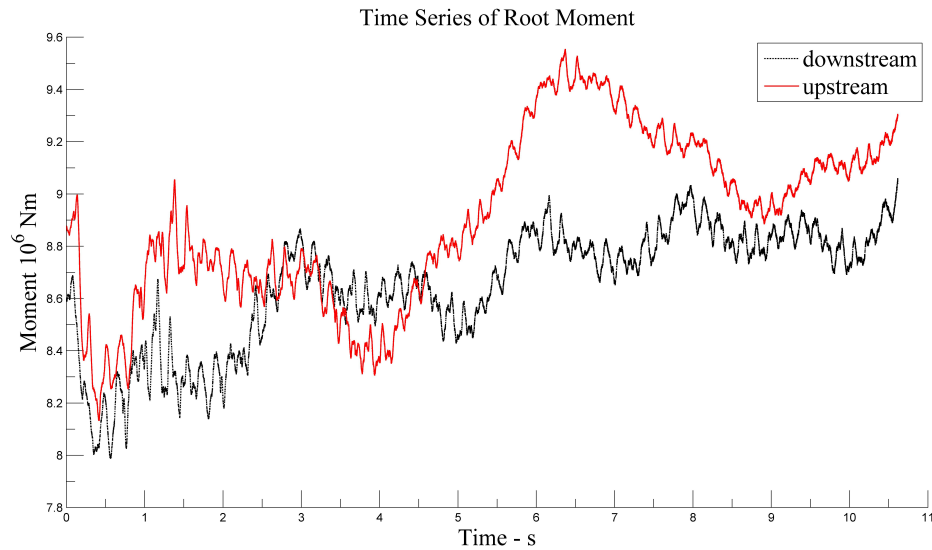
Figure 3.17 Time series of out-of-plane bending moments for upstream and downstream wind turbines.

By using the rainflow counting algorithm, the out-of-plane moment amplitude cycles for the two wind turbines can be calculated. The numbers of cycles for different moment amplitude are shown in Figure 3.18. From this figure, it can be seen that the number of cycles of high moment amplitude ($\geq 1600\ Nm$) for downstream wind turbine is larger than the upstream one, which means that the downstream wind turbine experiences larger fatigue damage.
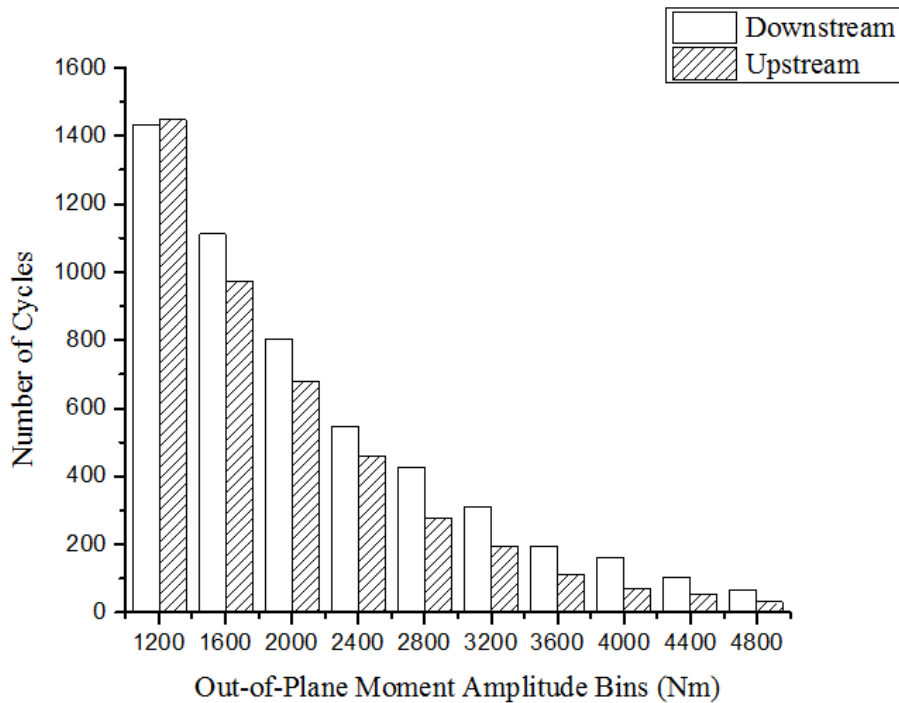
Figure 3.18 Rain-flow counting results of blade root moments (out-of-plane) for upstream and downstream wind turbines in staggered layout.

3.3 Implicit elastic actuator line and fatigue analysis methodology of wind turbine blade

In the previous section, the elastic actuator line with explicit finite difference structure model (explicit elastic actuator line) is proposed and verified by comparing its results with that of NREL FAST. On one hand, It should be mentioned here that there exist a time step difference between the structure model and actuator line model in explicit elastic actuator line. The determination of actuator line time step has been introduced in Section 2.1.2. The time step for the proposed structure model is shown in Equation (3.33). In the case study of NREL 5MW in Section 3.2, the time step of actuator line model is around 0.01 s, while the time step of structure model is calculated to be 5×10^{-4} s. Since the stiffness in Equation (3.33) is large for the composite wind turbine blade, the time step of structure model is extremely small compared with actuator line model. This will lower the efficiency of the algorithm, because the fluid equations that are computationally expensive will be solved with extremely small time step. In implicit method, larger time step can be employed, which will boost the efficiency (0.01s in the current case). However, the implicit method requires matrix inversion, which will also lower its efficiency. Overall, the implicit method in this case is 5-10 times faster than the explicit method. The simulation time of implicit method

is 400 seconds, which is also larger than that of explicit method, 30 seconds. Moreover, for fatigue analysis, hundreds of physical-time simulation is required. As a result, the problem is how to increase the time step of the structure model. To this problem above in our previous research, the implicit structure model for elastic actuator line is proposed to increase the time step limit. The implicit elastic actuator line will be verified by comparing its results with that of explicit model.

This section can be divided into two parts. In the first part, the implicit structure model for wind turbine blade is constructed and coupled with actuator line model to be the implicit elastic actuator line model. The implicit elastic actuator line model will be verified by comparing it with explicit elastic actuator line model. In the second part, based on this model, the dynamic loading on the WindPACT blade of 9-wind-turbine case in Section 2.7 will be analyzed. The load spectrum and cycle-count matrix will be presented to show the wake effect on the dynamic loading.

3.3.1 Numerical model

To remove the limitation of time step, the implicit discretized equations are derived as shown in the Equations (3.39) - (3.44), in which Crank-Nicolson for M and V is employed for temporal discretization. The governing equations in Section 3.1.2, including Equations (3.20) - (3.26), turns in to an implicit formulation.

$$\frac{V_{0,i}^{n+1} - V_{0,i}^{n}}{\Delta t} = -\frac{1}{\rho_s} \frac{(\delta^2 M_0)_i^{n+1} + (\delta^2 M_0)_j^{n}}{2\Delta r^2} + \frac{1}{\rho_s} \frac{(\delta S_0)_i^{n}}{2\Delta r} + \frac{f_{2D,0,i}^{n} + f_{g,0,i}}{\rho_{s,i}} \tag{3.39}$$

$$\frac{V_{1,i}^{n+1} - V_{1,i}^{n}}{\Delta t} = -\frac{1}{\rho_s} \frac{(\delta^2 M_1)_i^{n+1} + (\delta^2 M_1)_j^{n}}{2\Delta r^2} + \frac{1}{\rho_s} \frac{(\delta S_1)_i^{n}}{2\Delta r} + \frac{f_{2D,1,i}^{n} + f_{g,1,i}}{\rho_{s,i}} \tag{3.40}$$

$$\frac{M_{0,i}^{n+1} - M_{0,i}^{n}}{\Delta t} = (EI_{00})_i \frac{(\delta^2 V_0)_i^{n+1} + (\delta^2 V_0)_j^{n}}{2\Delta r^2} + (EI_{01})_i \frac{(\delta^2 V_1)_i^{n+1} + (\delta^2 V_1)_j^{n}}{2\Delta r^2} \tag{3.41}$$

$$\frac{M_{1,i}^{n+1} - M_{1,i}^{n}}{\Delta t} = (EI_{11})_i \frac{(\delta^2 V_1)_i^{n+1} + (\delta^2 V_1)_i^{n+1}}{2\Delta r^2} + (EI_{10})_i \frac{(\delta^2 V_0)_i^{n+1} + (\delta^2 V_0)_i^{n+1}}{2\Delta r^2} \tag{3.42}$$

$$\frac{S_{0,i}^{n+1} - S_{0,i}^{n}}{\Delta t} = N_i \frac{(\delta V_0)_i^{n+1} + (\delta V_0)_j^{n}}{4\Delta r} \tag{3.43}$$

$$\frac{S_{1,i}^{n+1} - S_{1,i}^{n}}{\Delta t} = N_i \frac{(\delta V_1)_i^{n+1} + (\delta V_1)_j^{n}}{4\Delta r} \tag{3.44}$$

Here δ and δ^2 are all central difference scheme. If we further introduce vector $\vec{p} = [V_0 \quad V_1 \quad M_0 \quad M_1]^T$, the above equations can be represented in the following matrice Equations (3.45) - (3.49).

$$- \underset{(4\times4)}{\mathbf{A}_i} \vec{p}_{i+1} + \underset{(4\times4)}{\mathbf{B}_i} \vec{p}_i - \underset{(4\times4)}{\mathbf{C}_i} \vec{p}_{i-1} = \vec{d}_i \tag{3.45}$$

Where

$$\underset{(4\times4)}{\mathbf{A}_i} = \begin{bmatrix} 0 & 0 & -\frac{\Delta t}{2\Delta r^2 \rho_{s,i}} & 0 \\ 0 & 0 & 0 & -\frac{\Delta t}{2\Delta r^2 \rho_{s,i}} \\ EI_{00,i}\frac{\Delta t}{2\Delta r^2} & EI_{01,i}\frac{\Delta t}{2\Delta r^2} & 0 & 0 \\ EI_{10,i}\frac{\Delta t}{2\Delta r^2} & EI_{11,i}\frac{\Delta t}{2\Delta r^2} & 0 & 0 \end{bmatrix} \tag{3.46}$$

$$\underset{(4\times4)}{\mathbf{B}_i} = \begin{bmatrix} 1 & 0 & -\frac{\Delta t}{\Delta r^2 \rho_{s,i}} & 0 \\ 0 & 1 & 0 & -\frac{\Delta t}{\Delta r^2 \rho_{s,i}} \\ EI_{00,i}\frac{\Delta t}{\Delta r^2} & EI_{01,i}\frac{\Delta t}{\Delta r^2} & 1 & 0 \\ EI_{10,i}\frac{\Delta t}{\Delta r^2} & EI_{11,i}\frac{\Delta t}{\Delta r^2} & 0 & 1 \end{bmatrix} \tag{3.47}$$

$$\underset{(4\times4)}{\mathbf{C}_i} = \underset{(4\times4)}{\mathbf{A}_i} \tag{3.48}$$

The right hand side is a 4×1 vector $\vec{d}_i$, which are shown in Equation (3.49).

$$\vec{d}_i = \begin{bmatrix} \frac{f_{2D,0,i}^n + f_{g,0,i}}{\rho_{s,i}} - \frac{\Delta t}{2\Delta r^2}\frac{1}{\rho_{s,i}}(M_{0,j-1}^n - 2M_{0,j}^n + M_{0,j+1}^n) - \frac{\Delta t}{2\Delta r}\frac{1}{\rho_{s,i}}(S_{0,j-1}^n - S_{0,j+1}^n) + V_{0,j}^n) \\ \frac{f_{2D,1,i}^n + f_{g,1,i}}{\rho_{s,i}} - \frac{\Delta t}{2\Delta r^2}\frac{1}{\rho_{s,i}}(M_{1,j-1}^n - 2M_{1,j}^n + M_{1,j+1}^n) - \frac{\Delta t}{2\Delta r}\frac{1}{\rho_{s,i}}(S_{1,j-1}^n - S_{1,j+1}^n) + V_{1,j}^n) \\ M_{0,j}^n + EI_{00,i}\frac{\Delta t}{2\Delta r^2}(V_{0,j-1}^n - 2V_{0,j}^n + V_{0,j+1}^n) + EI_{01}\frac{\Delta t}{2\Delta r^2}(V_{1,j-1}^n - 2V_{1,j}^n + V_{1,j+1}^n) \\ M_{1,j}^n + EI_{11,i}\frac{\Delta t}{2\Delta r^2}(V_{1,j-1}^n - 2V_{1,j}^n + V_{1,j+1}^n) + EI_{00,i}\frac{\Delta t}{2\Delta r^2}(V_{0,j-1}^n - 2V_{0,j}^n + V_{0,j+1}^n) \end{bmatrix} \tag{3.49}$$

Similar to the finite element method, the above matrice equations are for the local beam element. These equations can then be assembled as a sparse global matrix, which consists of matrix $\mathbf{A}_i$, $\mathbf{B}_i$, and $\mathbf{C}_i$. In contrast to the finite element method, shape functions are not required in these equations. In the following subsection, the proposed implicit method will be verified. The programming code is illustrated in Appendix G.2.

3.3.2 Verification case study

The proposed implicit elastic actuator line model is verified in this subsection by comparing it with the aforementioned explicit method. The numerical simulation in the Section 3.2.1 with NREL 5MW wind turbine blade will be carried out. The calculated root bending moments (direction 0 and 1, out-of-plane and in-plane) of implicit method with $5 \times 10^{-4}s$ and $5 \times 10^{-3}s$ time step will be compared with that of explicit method with $5 \times 10^{-4}s$ time step, which is shown in Figures 3.19 - 3.21. From the comparison of three blades, it can be found that the proposed implicit elastic actuator line has a good agreement with the verified explicit method presented in the previous section for both out-of-plane and in-plane bending moments. However, there still exists small discrepancies between implicit method and explicit method . With the time step increasing from $5 \times 10^{-4}s$ to $5 \times 10^{-3}s$, the accuracy does not drop obviously, especially for the M_{ip}.

 The proposed implicit elastic actuator line will be used to calculate the dynamic loading of 9 WindPACT wind turbine blades in wind farm, because larger time step can be used for this method. It should be mentioned here that the implicit method will obviously affect the low frequency vibration, which can be seen in Figures 3.19 - 3.21. This problem is solved in the Chapter 5, in which the unconditionally stable explicit model is proposed that can run with large time step and does not affect the low frequency vibrations. The green curve represents the implicit method that runs with 10 times larger time step than the red one. As a result, the difference is from the enlarged time step.
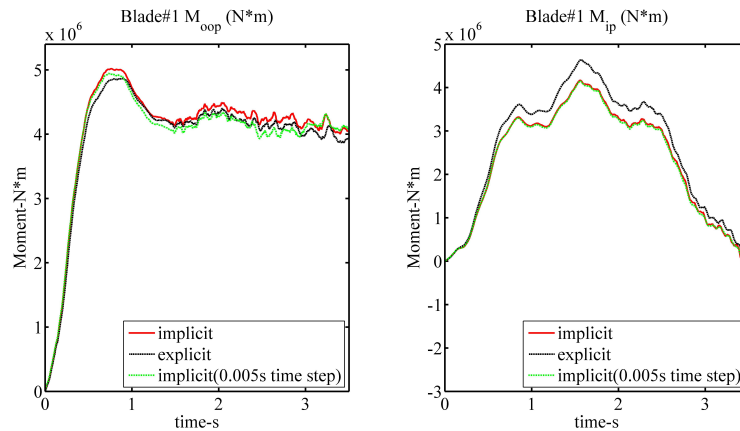
Figure 3.19 Comparison between implicit method, implicit method with large time step, and explicit method in terms of bending moments (Blade 1).
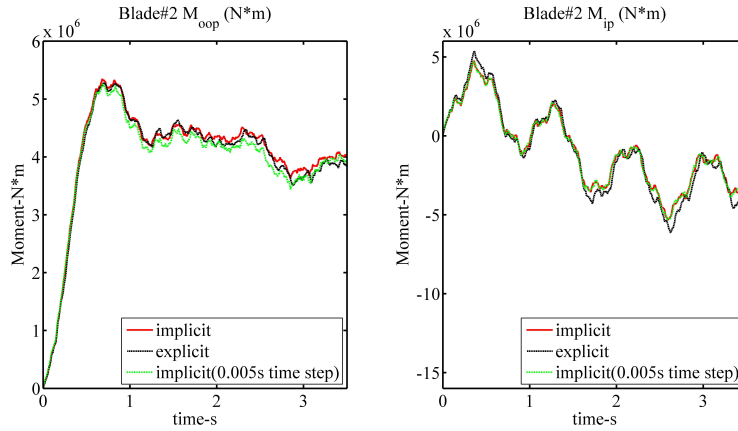
Figure 3.20 Comparison between implicit method, implicit method with large time step, and explicit method in terms of bending moments (Blade 2).
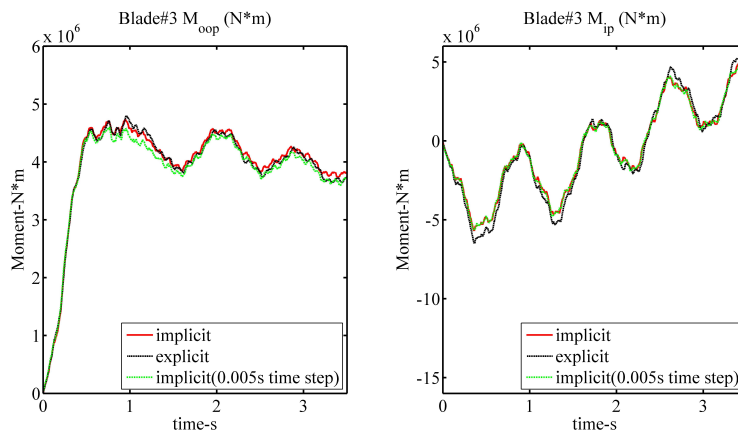
Figure 3.21 Comparison between implicit method, implicit method with large time step, and explicit method in terms of bending moments (Blade 3).

3.3.3 Case study: dynamic loading on the 9 wind turbines in wind farm

In Section 2.7, the conventional actuator line model and precursor method are coupled to simulate the wind turbine wake effect in wind farm with 9 WindPACT wind turbines. The stiffness distribution of WindPACT wind turbine blade is shown in Figure 3.22.
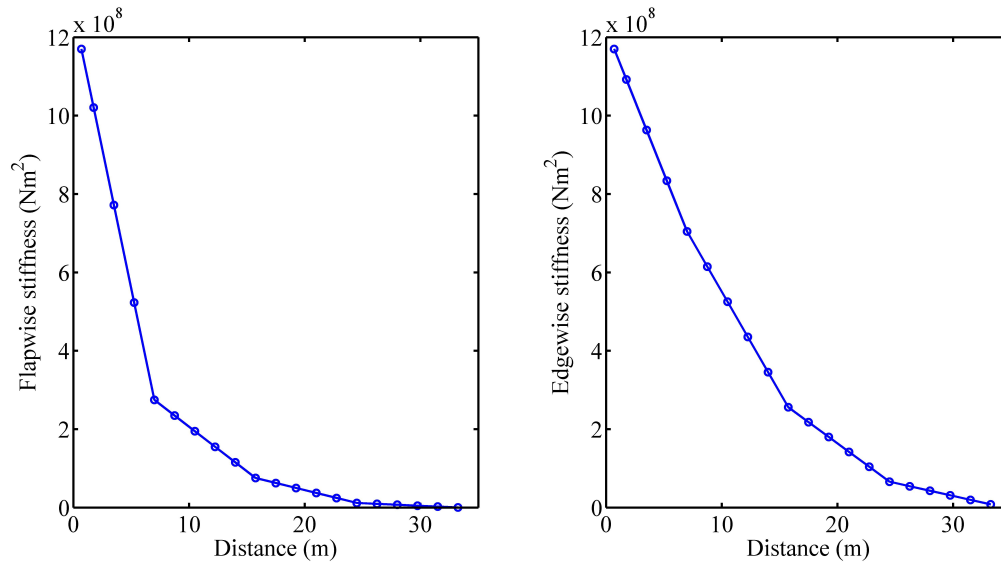
Figure 3.22 Stiffness distributions for WindPACT wind turbine blade.

In this section, the proposed implicit elastic actuator line will be employed to simulate the dynamic loading on wind turbine blade. The simulation time is 400 s (physical time, from 20001-20400 s). Firstly, the out-of-plane and in-plane moments time series are sampled on three sections (2.5 m, 5 m, and 7.5 m) from the wind turbine blade root of wind turbine 0 in Figure 3.25, which is shown in Figures 2.43 and 3.23. The load time series of different sections are shown in Figure 3.24. It can be found that the moments of sections are increasing from tip to root, not only for the amplitude and mean value of out-of-plane bending moments, but also for the in-plane bending moments. The rotational speed of rotor is assumed to be fixed, which is a limitation of the simulation case.

Since the moments fluctuation on the root section is most obvious among all the sections, we further compare the moments time series of the root sections for different wind turbine blades on the same row, which can be seen in Figure 3.25. The loading time series are shown in Figure 3.27. From this figure, we can see that the fluctuating patterns of out-of-plane moments for different wind turbines are different because of the different turbulent inflow (see Figure 3.26), but the fluctuating amplitudes are very similar. In addition, the amplitudes of in-plane bending moments are very similar to each other, which are mainly dominated
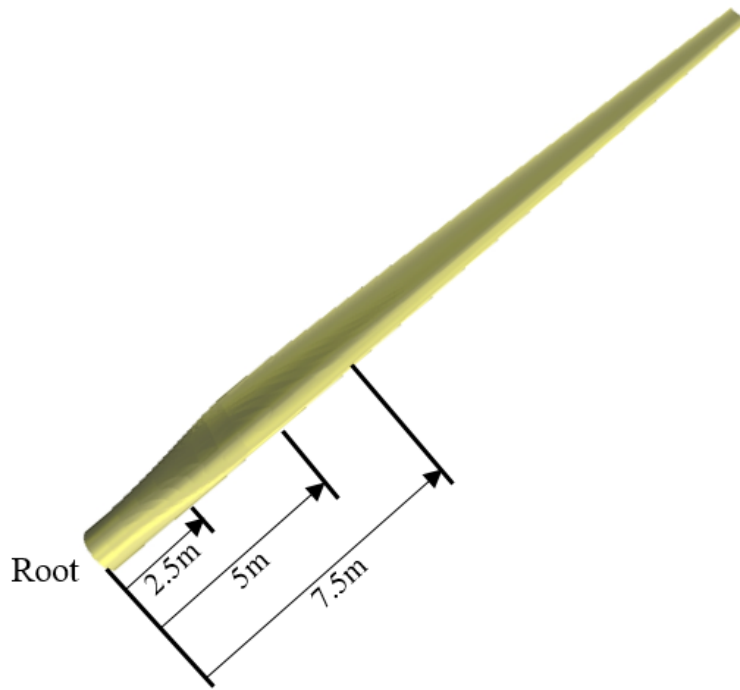
Figure 3.23 Sampling sections on wind turbine blade.
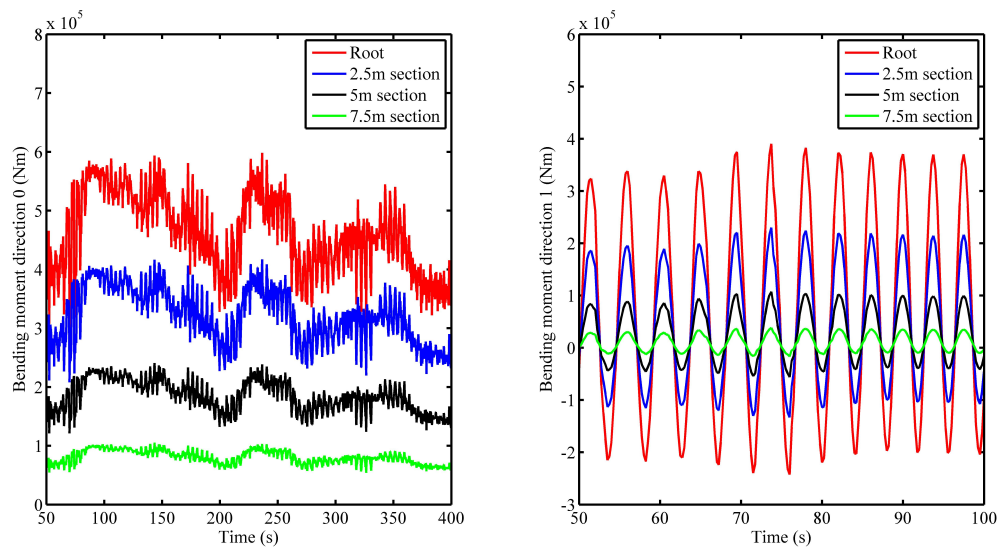
Figure 3.24 Comparison of loading time series on different sections.

by the gravitational force. We further analyse the power spectrum of the fluctuating out-of-plane bending moments, which is dominated by the dynamic aerodynamic loading. It can be found that the similar obvious two peaks occurs in all the three wind turbine blades for three wind turbines. These peaks are related to the atmospheric turbulence. In other words, although the loading of wind turbines in a row have different fluctuating patterns, they still share the same power spectrum that is shown in Figure 3.28, because there is no wake flows in front of them.
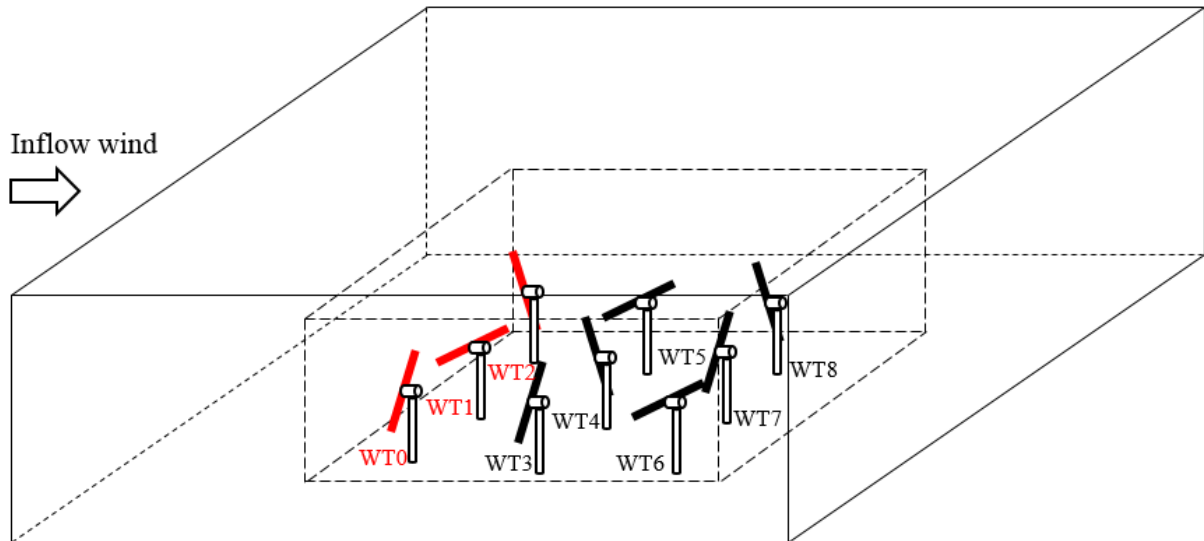
Figure 3.25 Layout of wind turbines (the sampled wind turbines are highlighted with red).
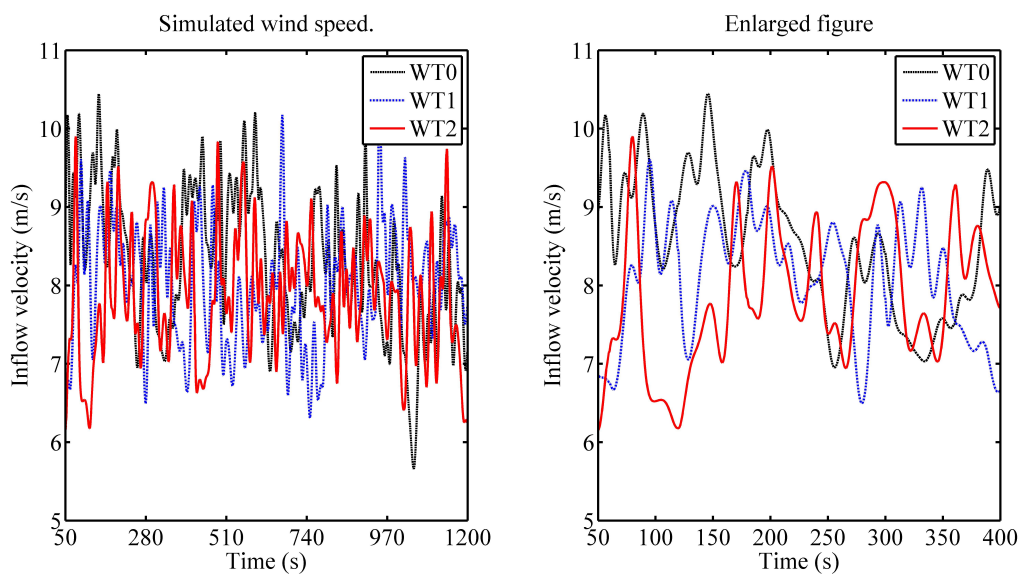
Figure 3.26 The comparison of inflow wind speed for different wind turbines (WT 0, 1, 2).
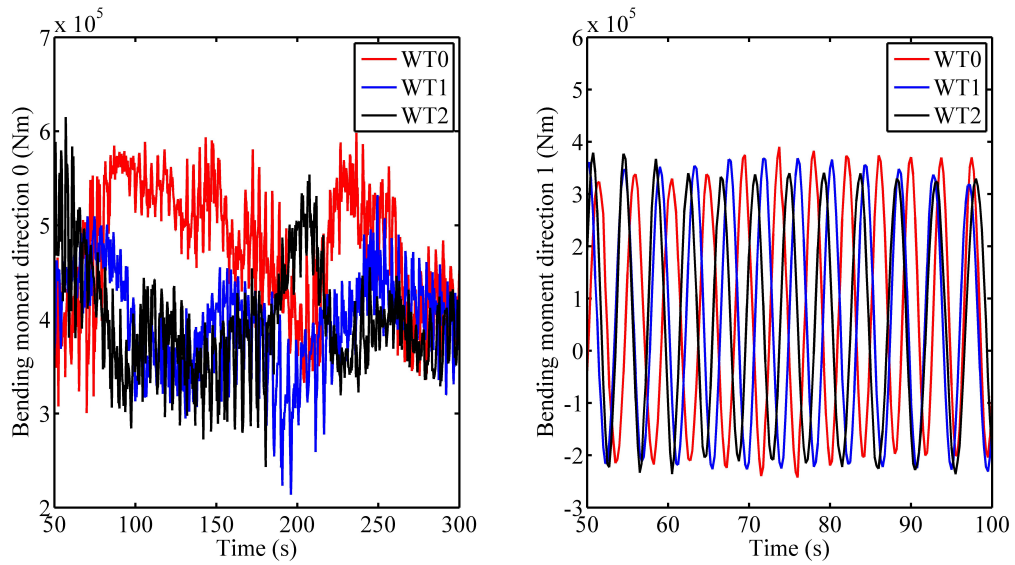
Figure 3.27 The comparison of loading time series on the wind turbine blade of wind turbines in the first row.
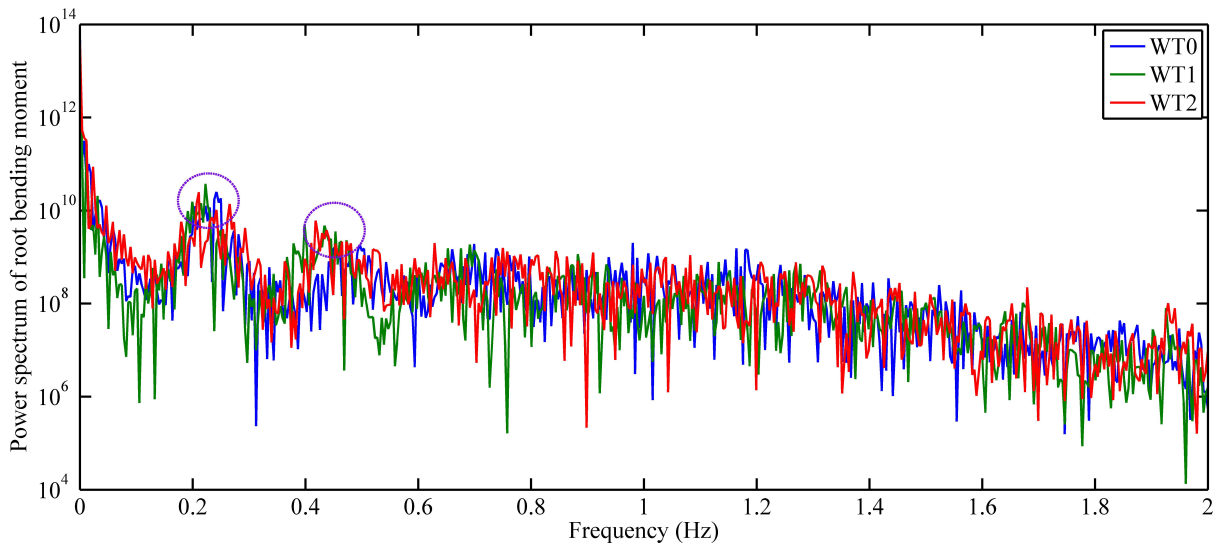
Figure 3.28 Power spectrum comparison for out-of-plane bending moments of different wind turbines in the first row.

Next, the loading of wind turbines with and without wake effects are compared with each other, which is shown in Figure 3.30. The sampled wind turbines are shown in Figure 3.29. Obviously, wind turbine 0 does not experience any wake effect, but wind turbine 3 and 6 are all operating in the wake flows. From Figure 3.30, it can be observed that amplitudes of out-of-plane bending moments of wind turbines in wake are larger than that of wind turbine 0 without wake, which is caused by the wake turbulence. The power spectrum of the out-of-plane bending moments are shown in Figure 3.31. To clearly illustrate the power spectrum, only the spectrum for wind turbine 0 and 3 are presented in Figure 3.31. Compared with Figure 3.28, an obvious difference can be found between the power spectrum of upstream wind turbine and downstream one, which is caused by the wake turbulence. In the author's view, the uniform flow field distribution caused by wake flows in the wind farm is the main reason for this shift.
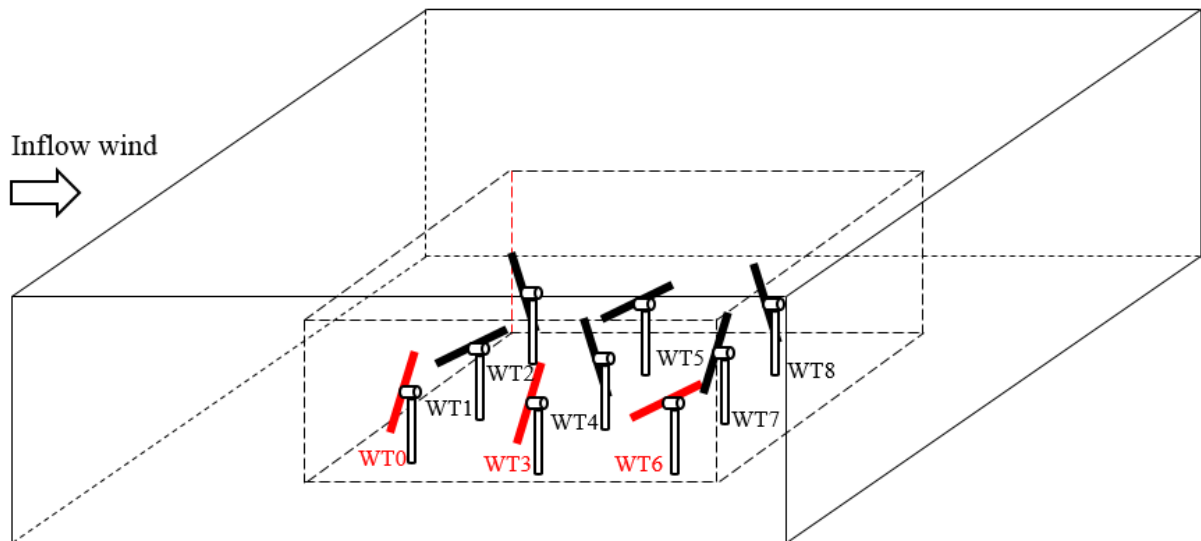
Figure 3.29 Layout of wind turbines (the sampled wind turbines are highlighted with red).

The rainflow counting for the out-of-plane moments of upstream and downstream wind turbines is carried out. The results can be seen in Figure 3.32. By comparing these two figures, it can be found that the cycles of high amplitude (above 5×10^4) increase in the downstream wind turbine blade loading with wake effect. These cycles will cause fatigue damage increase on wind turbine blade, which is the wake-induced fatigue. At the same time, the mean value of the loading will decrease in the wake region, which will alleviate the fatigue load on the wind turbine blade according to the Goodman correction. Here the author would like to compare the loading amplitude between the upstream and downstream wind turbines. The most qualitative way to compare the fatigue load between turbines is the fatigue damage analysis. As a result, the fatigue damage analysis methodology is proposed in the following section. The results are for WT0 and WT3. To quantify the fatigue damage
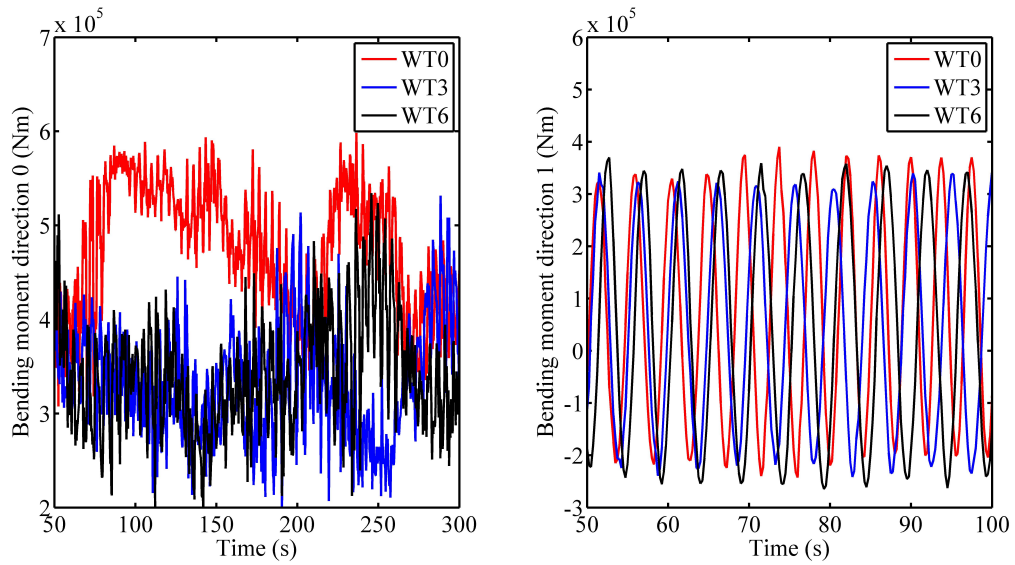
Figure 3.30 The comparison of loading time series on the wind turbine blade of wind turbines in a line.
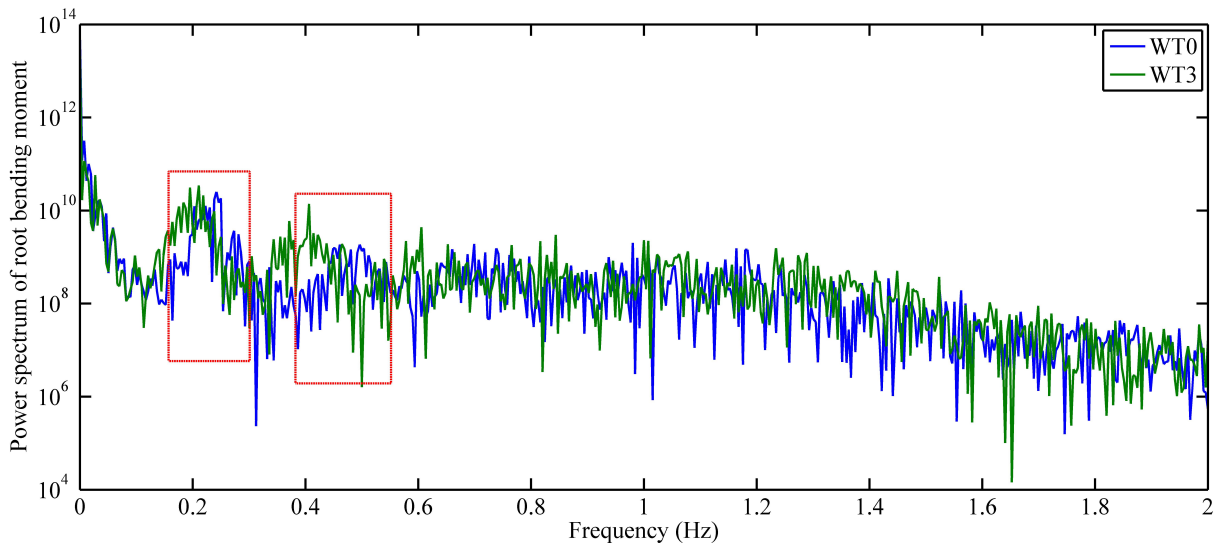
Figure 3.31 Power spectrum comparison for out-of-plane bending moments of different wind turbines in a line.

comprehensively, The comprehensive wake effect in terms of TI and mean loads will be calculated.
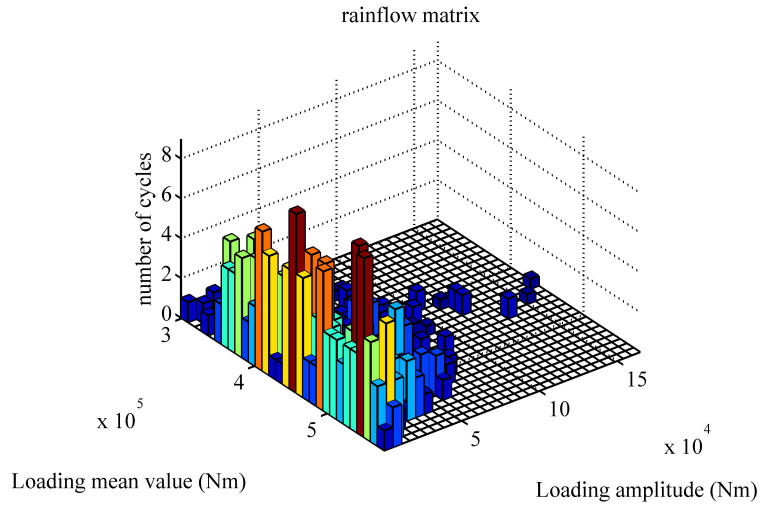
(a) Rainflow matrix for upstream wind turbine blade loading.
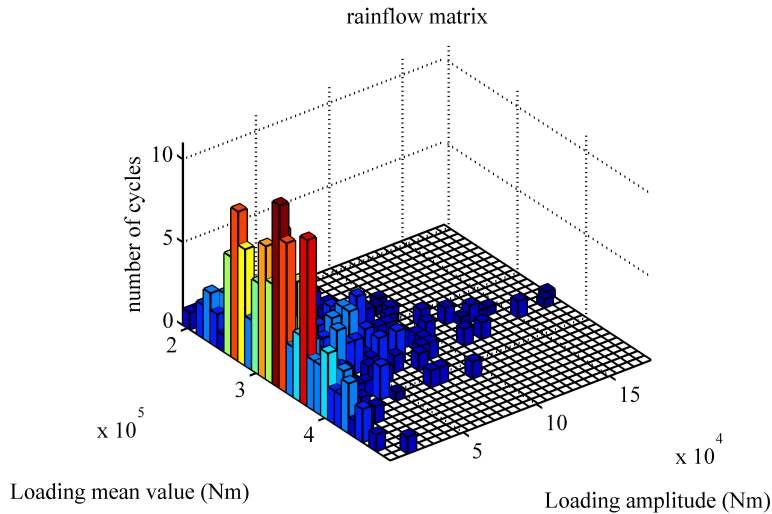
(b) Rainflow matrix for downstream wind turbine blade loading.

Figure 3.32 Rainflow matrix for upstream and downstream wind turbine blade loading.

3.4   Chapter summary

In this chapter, the elastic actuator line model, the coupled model of conventional actuator line model and FDM based structure model, which is developed. The explicit elastic actuator line model is verified by NREL FAST 7.0. From the stability analysis of the proposed model, it is found that the required time steps for the conventional actuator line

model and proposed FDM structure model are very different. The time step not only affects the numerical stability but also the efficiency of the proposed model. To enlarge the required time step of the FDM based structure model, an implicit method is applied and verified against the explicit method. By using the aforementioned models, both stochastic (Section 3.3.3) and deterministic (Section 3.2.5) wake-induced fatigue loading that is mentioned in Section 1.3.2 are simulated in the simulations. In the literature review, we have mentioned that the stochastic loading is caused by the higher turbulence intensity in wake (the wind farm case). The wind turbine blade once per revolution enters and leaves the wake region can cause deterministic loading. They are two common types of wake-induced fatigue loading.

For the proposed elastic actuator line model, there still exists several deficiencies. Firstly, the anisotropic properties of composite structure are not considered in this model, because the proposed model is based on Euler-Bernoulli beam model, which is an ad hoc beam model. Torsional deformation is not considered in this model. Secondly, the dynamic stall effect is not considered in this model, which will also affect the dynamic loading of wind turbine blade. Thirdly, although the proposed implicit method can successfully enlarge the required time step, the prediction of implicit method still has small discrepancies compared with explicit method. Lastly, the simulation cases in this chapter is about the dynamic loading of wind turbine blade. The fatigue analysis has not been carried out, because the fatigue analysis is based on the stress or strain of materials in the wind turbine blade. There is still a gap between the simulated dynamic loading (moments) and the stress (or strain) time series of materials. These problems will be solved in the following two chapters.

Chapter 4

Anisotropic wind turbine blade modelling by using FEM formulation

Wind turbine blade is commonly assumed to be a cantilever thin-walled beam. This assumption extensively simplifies the structural modelling. As mentioned in the literature review, the composite wind turbine blade is anisotropic, especially for bend-twist coupling blade, which makes it challenging to model, because the anisotropy of blade structure will break the displacement assumption in ad-hoc beam models, i.e. Euler-Bernoulli beam model. To accurately reconstruct the stress and strain of each material in the blade section for fatigue analysis, DTU BECAS (beam cross section analysis software) is employed in this chapter to reconstruct the stress and strain from the simulated sectional loading. In BECAS, the warping displacements, which are neglected in ad-hoc beam models, are seriously considered in this linear two-dimensional cross-sectional analysis. Furthermore, the one-dimensional FEM beam model is further constructed to simulate the deformations in 6 DoFs (only two deflections considered in structure model in previous section).

Specifically, the BEM model and anisotropic beam model are coupled together. On one hand, the BEM model provides the beam model with the external aerodynamic forces (axial force and tangential force) at each cross section. On the other hand, the blade is driven to vibrate by external forces. The vibration-induced velocity (along the flapwise and edgewise directions) at each section will also affect the aerodynamic force calculation of BEM in terms of the local inflow angle. In addition, the torsion of the blade induced by BTC will lead to the change of the twist angle, which will also be considered in this model. In addition, the dynamic stall for the lift coefficient is also implemented in the aeroelastic code. The simulated loading (sectional bending moments and forces) is used to reconstruct the stress and strain for different materials by using BECAS. For fatigue analysis, according to GL certification [77], the aforementioned stress-based analysis method is employed in this section. The methodology is shown in Figure 4.1. The flowchart of this two-way coupling aero-elastic model is shown in Figure 4.2. The basic theories and equations in

Figure 4.2 will be further explained in this section.
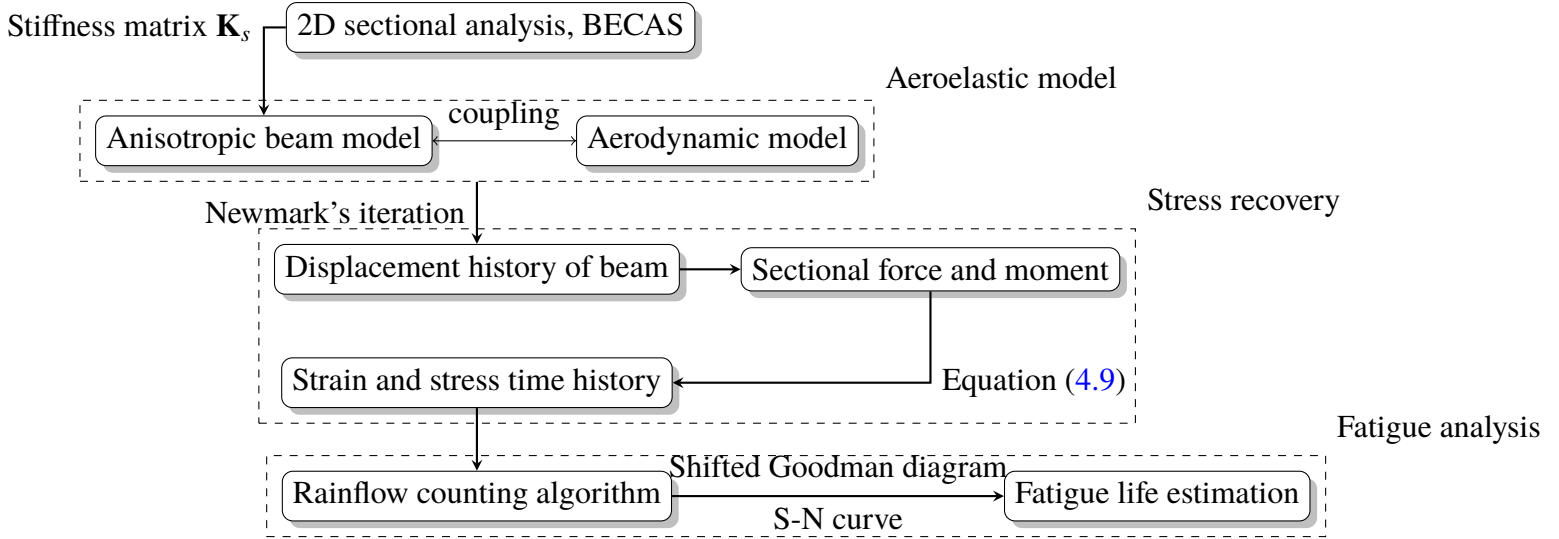
Figure 4.1 Flowchart of the structure of methodology.
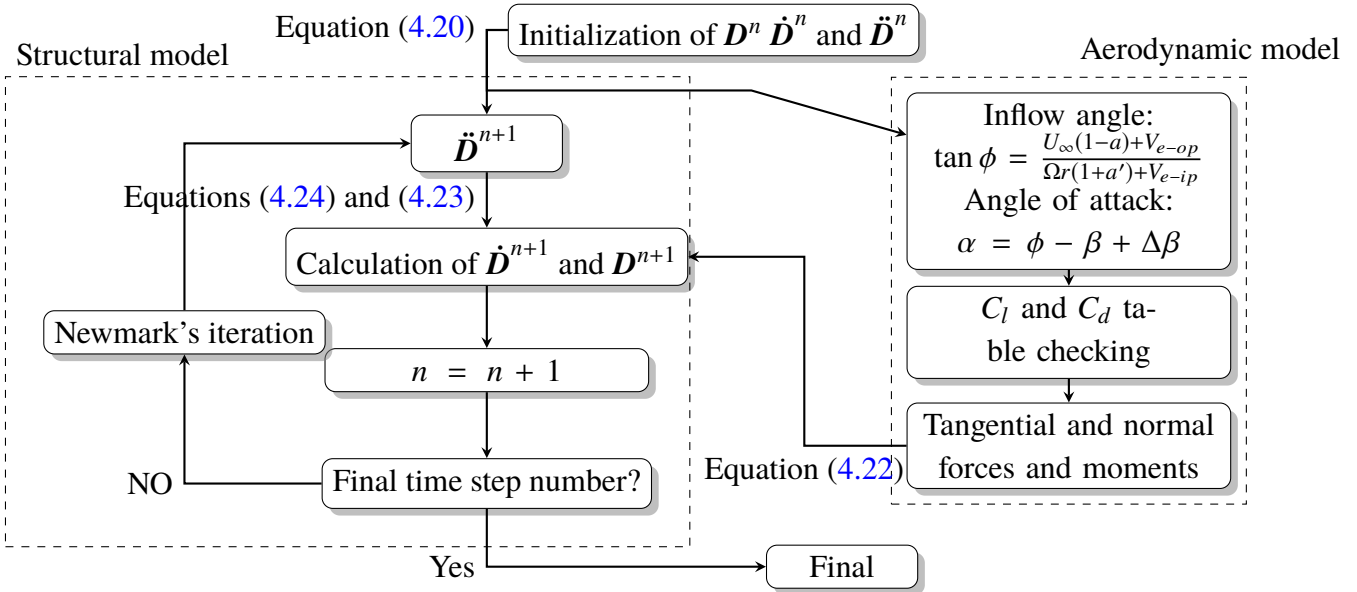
Figure 4.2 Flowchart of the aeroelastic model.

4.1 Cross-sectional analysis method

This subsection is about the two-dimensional sectional analysis. In this part, the governing equations of cross-sectional analysis, BECAS [78], will be briefly introduced. Firstly, the

displacement of a point on cross section can be decomposed into two components, including rigid-body displacements and warping displacements by the Equation (4.1) [57] (see Figure 4.3). It should be mentioned here that the warping displacements are not considered in the conventional ad-hoc beam models, i.e. the Euler-Bernoulli beam models in the previous section. The warping function, which is introduced in literature review, is important to the anisotropic wind turbine blade modelling.

$$\mathbf{s} = \mathbf{v} + \mathbf{g}_{warping} \tag{4.1}$$

Total deformation   Rigid body   In-plane and
translation and rotation   out-of-plane warping

Figure 4.3 Decomposition of deformation of the cross section [3].

In Equation (4.1), $\mathbf{s}$ is the vector of displacement; $\mathbf{v}$ is the vector associated with rotation and translation; $\mathbf{g}_{warping}$ is the warping displacement vector which is generally neglected in the ad hoc beam models, such as Euler Bernoulli. The detailed derivation of the cross sectional model can be found in [79] and is only briefly introduced in this subsection.

The governing equations of cross-sectional displacement can be assumed to be a linear and homogeneous differential equations. If the finite element formulation is employed, the relationship between the nodal warping displacement $\mathbf{U}$, generalized strain $\mathbf{\Phi}$ and the external resultant $\boldsymbol{\theta}$ (six degrees of freedom) can be represented by the following equations [78] (equations 4.2 and 4.3):

$$\underset{(n_d \times 1)}{\mathbf{U}} = \underset{(n_d \times 6)(6 \times 1)}{\mathbf{X}} \boldsymbol{\theta} \quad \underset{(n_d \times 1)}{\frac{\partial \mathbf{U}}{\partial z}} = \underset{(n_d \times 6)}{\frac{\partial \mathbf{X}}{\partial z}} \underset{(6 \times 1)}{\boldsymbol{\theta}} \quad \underset{(6 \times 1)}{\mathbf{\Phi}} = \underset{(6 \times 6)(6 \times 1)}{\mathbf{Y}} \boldsymbol{\theta} \tag{4.2}$$

$$\boldsymbol{\theta} = [F_x, F_y, F_z, M_x, M_y, M_z]^T \tag{4.3}$$

The components of generalized strain $\mathbf{\Phi}$ are shown in Equation 4.4, in which τ and κ are shear angles and curvatures of the cross section.

$$\boldsymbol{\Phi} = \left[\tau_x, \tau_y, \tau_z, \kappa_x, \kappa_y, \kappa_z\right] \tag{4.4}$$

The critical variables in Equation (4.2) can be obtained by solving the following governing Equation (4.5) and Equation (4.6). Specifically, Equation (4.6) should be solved first for $\frac{\partial \mathbf{X}}{\partial z}$ and $\frac{\partial \mathbf{Y}}{\partial z}$. Then the Equation (4.5) can be solved in terms of $\mathbf{X}$ and $\mathbf{Y}$. The z represents the spanwise direction, and the coordinate system is shown in the Fig. 4.4. $\mathbf{X}$ and $\mathbf{Y}$ are actually the solutions of warping displacements and generalized strain (rotation angles of the cross section and the curvatures of the beam) under unity stress resultant. The n_d is the total number of degrees of freedom which equals $3 \times n_n$. n_n is the number of nodes. The coefficient matrices of these equations contain the information of cross sectional materials and geometry, which are presented in Appendix. C. It should be mentioned here that $\mathbf{X}$ and $\mathbf{Y}$ do not represent the coordinate system here but the warping displacement and generalized strain solution when the resultant $\boldsymbol{\theta}$ equals $\mathbf{I}_6$ (unitary matrix).
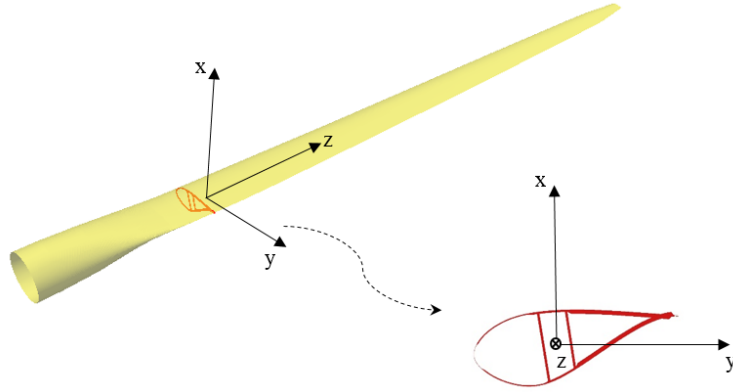
Figure 4.4 Coordinate system of a wind turbine blade.

$$
\begin{bmatrix}
\underset{(n_d \times n_d)}{\mathbf{E}} & \underset{(n_d \times 6)}{\mathbf{R}} & \underset{(n_d \times 6)}{\mathbf{D}} \\
\underset{(6 \times n_d)}{\mathbf{R}^T} & \underset{(6 \times 6)}{\mathbf{A}} & \underset{(6 \times 6)}{\mathbf{0}} \\
\underset{(6 \times n_d)}{\mathbf{D}^T} & \underset{(6 \times 6)}{\mathbf{0}} & \underset{(6 \times 6)}{\mathbf{0}}
\end{bmatrix}
\begin{bmatrix}
\underset{(n_d \times 6)}{\mathbf{X}} \\
\underset{(6 \times 6)}{\mathbf{Y}} \\
\underset{(6 \times 6)}{\mathbf{\Lambda_2}}
\end{bmatrix}
=
$$

$$
\begin{bmatrix}
\underset{(n_d \times n_d)}{(\mathbf{C} - \mathbf{C}^T)} & \underset{(n_d \times 6)}{\mathbf{L}} \\
\underset{(6 \times n_d)}{\mathbf{L}^T} & \underset{(6 \times 6)}{\mathbf{0}} \\
\underset{(6 \times n_d)}{\mathbf{0}} & \underset{(6 \times 6)}{\mathbf{0}}
\end{bmatrix}
\begin{bmatrix}
\underset{(n_d \times 6)}{\frac{\partial \mathbf{X}}{\partial z}} \\
\underset{(6 \times 6)}{\frac{\partial \mathbf{Y}}{\partial z}}
\end{bmatrix}
+
\begin{bmatrix}
\underset{(n_d \times 6)}{\mathbf{0}} \\
\underset{(6 \times 6)}{\mathbf{I}} \\
\underset{(6 \times 6)}{\mathbf{0}}
\end{bmatrix}
\tag{4.5}
$$

$$
\begin{bmatrix}
\underset{(n_d \times n_d)}{\mathbf{E}} & \underset{(n_d \times 6)}{\mathbf{R}} & \underset{(n_d \times 6)}{\mathbf{D}} \\[4pt]
\underset{(6 \times n_d)}{\mathbf{R}^T} & \underset{(6 \times 6)}{\mathbf{A}} & \underset{(6 \times 6)}{\mathbf{0}} \\[4pt]
\underset{(6 \times n_d)}{\mathbf{D}^T} & \underset{(6 \times 6)}{\mathbf{0}} & \underset{(6 \times 6)}{\mathbf{0}}
\end{bmatrix}
\begin{bmatrix}
\underset{(n_d \times 6)}{\frac{\partial \mathbf{X}}{\partial z}} \\[6pt]
\underset{(6 \times 6)}{\frac{\partial \mathbf{Y}}{\partial z}} \\[6pt]
\underset{(6 \times 6)}{\mathbf{\Lambda_1}}
\end{bmatrix}
=
\begin{bmatrix}
\underset{(n_d \times 6)}{\mathbf{0}} \\[6pt]
\underset{(6 \times 6)}{\mathbf{T}_r^T} \\[6pt]
\underset{(6 \times 6)}{\mathbf{0}}
\end{bmatrix}
\tag{4.6}
$$

The $\frac{\partial \mathbf{X}}{\partial z}$, $\frac{\partial \mathbf{Y}}{\partial z}$, $\mathbf{X}$ and $\mathbf{Y}$ can be used to calculate the compliance matrix $\mathbf{F}_s$ and $\mathbf{K}_s$ stiffness matrix for beam model. The $\mathbf{\Lambda_1}$ and $\mathbf{\Lambda_2}$ are Lagrange multipliers associated with warping displacements (constraints on warping). Without $\mathbf{\Lambda_1}$ and $\mathbf{\Lambda_2}$, the equations are unable to be solved. The other parameters in the matrices, including $\mathbf{E}$, $\mathbf{R}$, and $\mathbf{D}$, has been stated in the Appendix C. The compliance matrix and stiffness matrix in terms of $\frac{\partial \mathbf{X}}{\partial z}$, $\frac{\partial \mathbf{Y}}{\partial z}$, $\mathbf{X}$ and $\mathbf{Y}$ are shown as follows:

$$
\mathbf{F}_s =
\begin{bmatrix}
\mathbf{X} \\[4pt]
\frac{\partial \mathbf{X}}{\partial z} \\[4pt]
\mathbf{Y}
\end{bmatrix}^T
\begin{bmatrix}
\underset{(n_d \times n_d)}{\mathbf{E}} & \underset{(n_d \times n_d)}{\mathbf{C}} & \underset{(n_d \times 6)}{\mathbf{R}} \\[4pt]
\underset{(n_d \times n_d)}{\mathbf{C}^T} & \underset{(n_d \times n_d)}{\mathbf{M}} & \underset{(n_d \times 6)}{\mathbf{L}} \\[4pt]
\underset{(6 \times n_d)}{\mathbf{R}^T} & \underset{(6 \times n_d)}{\mathbf{L}^T} & \underset{(6 \times 6)}{\mathbf{A}}
\end{bmatrix}
\begin{bmatrix}
\mathbf{X} \\[4pt]
\frac{\partial \mathbf{X}}{\partial z} \\[4pt]
\mathbf{Y}
\end{bmatrix}
\tag{4.7}
$$

$$
\mathbf{K}_s = \mathbf{F}_s^{-1}
\tag{4.8}
$$

These equations are the basis of stiffness matrix construction for beam model in next chapter. The governing equations of 2D cross-sectional deformation (warping displacements and generalized strains, see Figure 4.3) are Equation (4.5) and Equation (4.6). By solving this linear equation system, $\mathbf{X}$ and $\mathbf{Y}$ in the stiffness matrix calculation of Equation (4.8) can be achieved, which means that the stiffness matrix for the anisotropic beam model can be calculated. In addition, they are also used in the following Equation (4.9) to reconstruct the strain through loading resultant $\boldsymbol{\theta}$ on the cross section. Then the nodal warping displacement $\mathbf{U}$, the generalized strain of beam $\mathbf{\Phi}$, and their first order derivatives can thus be calculated by Equation (4.2).

Since these calculated variables are related to the three-dimensional strain on each cross section element, the nodal strain can be obtained by following Equation (4.9), which is the basis of stress and strain reconstruction. $\boldsymbol{\epsilon}_n$, $\mathbf{X}_n$, $\mathbf{Y}_n$ and $(\frac{\partial \mathbf{U}}{\partial z})_n$ are nodal value of $\boldsymbol{\epsilon}$, $\mathbf{X}$, $\mathbf{Y}$ and $(\frac{\partial \mathbf{U}}{\partial z})$. $\mathbf{N}_{2d}$ is the shape function for the two-dimensional cross sectional model (four-node linear element shape function). The formulation about $\mathbf{S}$, $\mathbf{Z}$ and $\mathbf{B}$ in Equation (4.9) are all presented in the Appendix C.

$$
\underset{(6 \times 1)}{\boldsymbol{\epsilon}_n} = \underset{(6 \times 3)}{\mathbf{S}} \underset{(3 \times 6)}{\mathbf{Z}} \underset{(6 \times 6)}{\mathbf{Y}_n} \underset{(6 \times 1)}{\boldsymbol{\theta}} + \underset{(6 \times 3)}{\mathbf{B}} \underset{(3 \times 3)}{\mathbf{N}_{2d}} \underset{(3 \times 6)}{\mathbf{X}_n} \underset{(6 \times 1)}{\boldsymbol{\theta}} + \underset{(6 \times 3)}{\mathbf{S}} \underset{(3 \times 3)}{\mathbf{N}_{2d}} \underset{(3 \times 6)}{(\frac{\partial \mathbf{U}}{\partial z})_n} \underset{(6 \times 1)}{\boldsymbol{\theta}}
\tag{4.9}
$$

Until now, the two important procedures in the cross sectional analysis are introduced, including stiffness matrix calculation (Equation (4.7)) and strain reconstruction (Equation(4.9)). Next, the fatigue analysis method will be illustrated.

4.2   Structural modelling of anisotropic wind turbine blade

The finite element formulation of present one-dimensional anisotropic beam model is proposed in [57]. To expand this formulation to a dynamic beam model, the Hamilton's principle and an implicit Newmark's method, are used for solving this dynamic equation in this paper.

It should be mentioned that the one-dimensional beam model and the following aerodynamic model to be described in the next section are implemented an in-house Matlab code here, and the structural model will be verified in the next section first. The following part in this section will discuss the modelling details of one-dimensional anisotropic beam model.

$$\mathbf{L} = \mathbf{T} - \mathbf{\Pi} + \mathbf{W}_f \tag{4.10}$$

To construct the dynamic model, the Hamilton's principle (Equation(4.10)) is supposed to be used and represented by the following equation. $\mathbf{L}$ in this equation is the Lagrangian functional, which is the combination of kinetic energy, potential energy and the work of external force $\mathbf{W}_f$.

In the finite element formulation, the displacement vector $\mathbf{d}$ (6 components) of beam can be represented by the nodal displacements vector $\mathbf{d}_n$.

$$\underset{(6\times1)}{\mathbf{d}} = \underset{(6\times6N_i)}{\mathbf{N}} \underset{(6N_i\times12)}{\mathbf{N}_\alpha} \underset{(12\times1)}{\mathbf{d}_n} \tag{4.11}$$

In Equation (4.11), N_i represents the order of the shape function of beam. The details about the parameter matrices can be found in Appendix D. It should be noted here that in order to construct high-order ($N_i > 3$) polynomial shape functions for the two-node element, Kim et al. introduces a new derivation of shape functions by using the total elastic energy minimization method in his paper [57]. The high-order shape function of displacement is required, because we need to differentiate the displacement with respect to z to calculate the generalized strain of beam. This makes the formulation of N_α more complicated, which is shown in Appendix D. N_α is implemented in each term of Equation (4.10). As a result, in the following part, each term in Equation (4.10) will be represented in form of nodal displacement vector in Equation (4.11).

Firstly, the potential energy (elastic strain energy) can be represented by the following equation.

$$\Pi = \frac{1}{2}\mathbf{d}_n^T \left[(\mathbf{N}_\alpha)^T \left(\int_{L_e} \mathbf{B}_b(z)^T \mathbf{K}_s \mathbf{B}_b(z) \mathrm{d}z \right) \mathbf{N}_\alpha \right] \mathbf{d}_n$$

$$= \frac{1}{2}\mathbf{d}_n^T \mathbf{K}_e \mathbf{d}_n \tag{4.12}$$

and

$$\mathbf{K}_e = (\mathbf{N}_\alpha)^T \left(\int_{L_e} \mathbf{B}_b(z)^T \mathbf{K}_s \mathbf{B}_b(z) \mathrm{d}z \right) \mathbf{N}_\alpha \tag{4.13}$$

In this equation, $\mathbf{B}_b$ is the first derivative of shape function $\mathbf{N}$. $\mathbf{K}_s$ is the stiffness matrix, which is calculated in Equation (4.8). The $\mathbf{K}_e$ is the local stiffness matrix. L_e here represents the length of the local beam element.

Secondly, the kinetic energy equation is illustrated as follows.

$$\mathbf{T} = \frac{1}{2}\dot{\mathbf{d}}_n^T \left[(\mathbf{N}_\alpha)^T \left(\int_{L_e} \mathbf{N}(z)^T \mathbf{E}_s \mathbf{N}(z) \mathrm{d}z \right) \mathbf{N}_\alpha \right] \dot{\mathbf{d}}_n$$

$$= \frac{1}{2}\dot{\mathbf{d}}_n^T \mathbf{M}_e \dot{\mathbf{d}}_n \tag{4.14}$$

and

$$\mathbf{M}_e = (\mathbf{N}_\alpha)^T \left(\int_{L_e} \mathbf{N}(z)^T \mathbf{E}_s \mathbf{N}(z) \mathrm{d}z \right) \mathbf{N}_\alpha \tag{4.15}$$

The matrix $\mathbf{E}_s$ can be calculated by the surface integral on the cross section. The coordinate system is presented in Figure 4.4. The $\mathbf{M}_e$ is the local mass matrix defined in Equation (4.15) [78].

$$\mathbf{E}_s = \int_A \rho(x, y) \begin{bmatrix} 1 & 0 & 0 & 0 & 0 & -y \\ 0 & 1 & 0 & 0 & 0 & x \\ 0 & 0 & 1 & y & -x & 0 \\ 0 & 0 & y & y^2 & -xy & 0 \\ 0 & 0 & -x & -xy & x^2 & 0 \\ -y & x & 0 & 0 & 0 & x^2 + y^2 \end{bmatrix} dA \tag{4.16}$$

Lastly, the work of external force is given as follows:

$$\mathbf{W}_f = \mathbf{d}_n^T \int\limits_{L_e} (\mathbf{N}_\alpha)^T \, \mathbf{N}(z)^T \mathrm{d}z \cdot \mathbf{f} \tag{4.17}$$

In this equation $\mathbf{f}$ is the force on the beam element.

The above equations from Equation (4.12) to Equation (4.17) is in their local forms, which can be assembled into the global form:

$$\mathbf{K}_G \mathbf{D} + \mathbf{M}_G \ddot{\mathbf{D}} = \mathbf{F}_G \tag{4.18}$$

Here $\mathbf{K}_G$ is the global stiffness matrix. $\mathbf{M}_G$ is the global mass matrix. $\mathbf{F}_G$ is the global external force matrix, and $\mathbf{D}$ is the global displacement matrix. Equation (4.18) is solved by the Newmark's method [80]. In this equation, all the nonlinear terms are neglected, which is a limitation of the model. The boundary condition at the blade root is clamped boundary. The displacement and velocity are zero at the root.

Firstly, initial values (^{o}) are assigned to the displacement vector and its first and second order time derivatives.

$$\mathbf{D}^o = [\mathbf{0}]_{6n_{bn} \times 1} \quad \dot{\mathbf{D}}^o = [\mathbf{0}]_{6n_{bn} \times 1} \quad \ddot{\mathbf{D}}^o = [\mathbf{0}]_{6n_{bn} \times 1} \tag{4.19}$$

In Equation (4.19), the n_b is the number of beam nodes.

In the first step, the second derivative of displacement can be calculated.

$$\ddot{\mathbf{D}}^{n+1} = \mathbf{K}_{cm}^{-1} \mathbf{F}^{n+1,residual} \tag{4.20}$$

$\mathbf{K}_{cm}$ and $\mathbf{F}^{n+1,residual}$ are shown as follows.

$$\mathbf{K}_{cm} = \mathbf{K}_G \beta \Delta t^2 + \mathbf{M}_G \tag{4.21}$$

$$\mathbf{F}^{n+1,residual} = \mathbf{F}^{n+1} - \mathbf{K}_G \left[\mathbf{D}^n + \Delta t \dot{\mathbf{D}}^n + \Delta t^2 \left(\frac{1}{2} - \beta \right) \ddot{\mathbf{D}}^n \right] \tag{4.22}$$

In the second step, the displacement and its first derivative of the next time step can be calculated.

$$\mathbf{D}^{n+1} = \mathbf{D}^n + \Delta t \dot{\mathbf{D}}^n + \Delta t^2 \left[\left(\frac{1}{2} - \beta \right) \ddot{\mathbf{D}}^n + \beta \ddot{\mathbf{D}}^{n+1} \right] \tag{4.23}$$

$$\dot{\mathbf{D}}^{n+1} = \dot{\mathbf{D}}^n + \Delta t \left[(1 - \gamma) \ddot{\mathbf{D}}^n + \gamma \ddot{\mathbf{D}}^{n+1} \right] \tag{4.24}$$

And then return to the first step. If $2\beta \geq \gamma \geq \frac{1}{2}$, the algorithm is unconditionally stable. If $\gamma = \frac{1}{2}$, the algorithm can achieve second order time accuracy. If $\beta = 0$ and $\gamma = \frac{1}{2}$, the algorithm is the central difference method. If $\beta = \frac{1}{6}$ and $\gamma = \frac{1}{2}$, the algorithm is the linear acceleration method. If $\beta = \frac{1}{4}$ and $\gamma = \frac{1}{2}$, the algorithm is the implicit method. The parameters of β and γ are chosen to be $\frac{1}{4}$ and $\frac{1}{2}$ respectively to guarantee the unconditional stability of the algorithm. The programming code can be found in Appendix H.

4.3   Fatigue analysis methodology

In the introduction part, mainly three kinds of fatigue analysis methods are introduced, including the fatigue life models, phenomenological models, and progressive damage models. Among these methods, as we claim previously, the progressive damage method is the most promising method because of its capability to deal with the multi-axial fatigue analysis. The progressive method can also predict multiple fatigue damage modes, because it is based on the first principles. However, in wind energy industry, the progressive damage model has not been widely adopted in the fatigue life prediction of wind turbine blades. In the author's view, this is mainly due to its complexity and computational cost. In the GL guidelines for the certification of wind turbines, the fatigue life method is suggested for the fatigue life prediction of composite structures, which consists of the Palmgren-Miner fatigue damage accumulation rule, rainflow counting algorithm, S-N curve, and shifted Goodman diagram. The values of safety factors are also suggested in the GL guidelines. Although it is more efficient, the fatigue life method still has limitations due to its empirical nature. Its accuracy is highly dependent on the precision of the data source, including the S-N curve and Goodman diagram. The simulation time will affect the statistical convergence of the fatigue analysis. The simulation time in the following cases is 5 min and 10 min, which is a limitation of these simulation cases.

The fatigue damage of wind turbine blade material can be calculated by Miner's rule given by Equation (4.25). The basic assumption of this rule is that the damage can be accumulated linearly and independently.

$$D_p = \sum_i \frac{1}{N(\sigma_{a,i}, \sigma_{m,i})} \tag{4.25}$$

In Equation (4.25), D_p represents the total fatigue damage of the subject material in a certain period. i indicates the stress cycle number. N is the number of cycles to failure in terms of mean stress $\sigma_{m,i}$ and stress amplitude $\sigma_{a,i}$, which can be calculated by the rainflow counting algorithm. By considering S-N curve (stress vs. number of cycles) and constant life diagram (shifted Goodman relationship), the number of cycles to failure $N(\sigma_{a,i}, \sigma_{m,i})$ can be calculated by the Equation (4.27) from the GL certification guideline [77]. The life

of a wind turbine blade in years can be calculated by using the following Equation (4.26). L here is the life of the blade material, and T_p is our simulation time (5min in our case study).

$$L = \frac{1}{D_p} \frac{T_p}{365 \times 24 \times 3600} \tag{4.26}$$

$$N(\sigma_{a,i}, \sigma_{m,i}) = \left[\frac{\sigma_T + |\sigma_C| - 2|\gamma_{M_a}\sigma_{m,i} - \sigma_T + |\sigma_C||}{2\frac{\gamma_{M_b}}{C_{1b}}\sigma_{a,i}} \right]^m \tag{4.27}$$

In Equation (4.27), σ_T and σ_C are ultimate tension and compression strengths (characteristic short-term structure member resistance) for tension and compression respectively. γ_{M_a} is partial safety factors for material respectively. m is the exponential factor of the S-N curve. γ_{M_b} can be calculated by

$$\gamma_{M_b} = \gamma_{M_0} \prod_i C_{ib} \quad (i = 1, 2, 3, 4, 5) \tag{4.28}$$

or

$$\frac{\gamma_{M_b}}{C_{1b}} = \gamma_{M_0} \prod_i C_{ib} \quad (i = 2, 3, 4, 5) \tag{4.29}$$

In the above Equation (4.28) or (4.29), C_{ib} represents the safety factors in terms of temperature effect, material fabrication effect etc. The detailed value for each safety factors will be introduced in the following sections. Here γ_{M_0} equals to 1.35. These safety factors of material are from the GL guidelines for the certification of wind turbines. It should be mentioned here that the variable σ (stress) in Equations (4.25) and (4.27) can be replaced by ϵ (strain), if the $\epsilon - N$ method is employed.

4.4 Case study: modal and static analysis of NREL 5MW wind turbine blade

In the following sections, the NREL 5MW turbine blade is selected to be the research subject, which is extensively used in the research related to large wind turbines. Each of its blades is 61.5 meters long and weighs 17740 kg. This blade is designed according to the IEC standard, and the information of structural properties can be found in the NREL report [81]. The information of material properties, layup informations, and blade geometry are obtained from the Sandia report [82], which is shown in the Fig. 4.5. It should be mentioned here that this turbine blade are mainly made of four kinds of composite materials, including triaxial (TRIAX), biaxial (WEB), carbon fibre uniaxial (CUD) and glass fibre (EUD) uniaxial composite materials. The layup of different materials is shown in Fig. 4.7. The main structure, spar caps, is mainly made of carbon fibre composite, which endures large normal

stress. The glass fibre composite is mainly used to build the trailing edge reinforcement section. The triaxial fibre composite is used to build the leading edge and trailing edge of the blade. The biaxial fibre composite is the material of shear webs, which can absorb shear forces in the cross section. 40 finite elements are used in this case study.

Here BTC is simply induced by the slight orientation change on the spar caps (see Figure 4.5). Although including BTC in caps is complicated and costly from the manufacturing point of view, it is still the most simple and direct way to induce a higher BTC coefficient, because the spar caps are the main structure which endures most of the bending moment. In fact, the simulation cases presented in this and next sections, more details about BTC in caps are discovered and discussed. Here four different orientations (0°, 5°, 10° and 15°) of carbon fibre composite in spar caps are researched and compared in this paper. The BTC coefficients of these four different orientations are shown in Figure 4.6. The BTC coefficients are calculated by Equation (4.30). In this equation, EI represents the flapwise bending stiffness, GJ indicates the torsional stiffness, and g_c is the coupling stiffness. The plot of BTC coefficients at different orientations is shown in Figure 4.6. Obviously, 15° orientation design has the highest coupling coefficient.
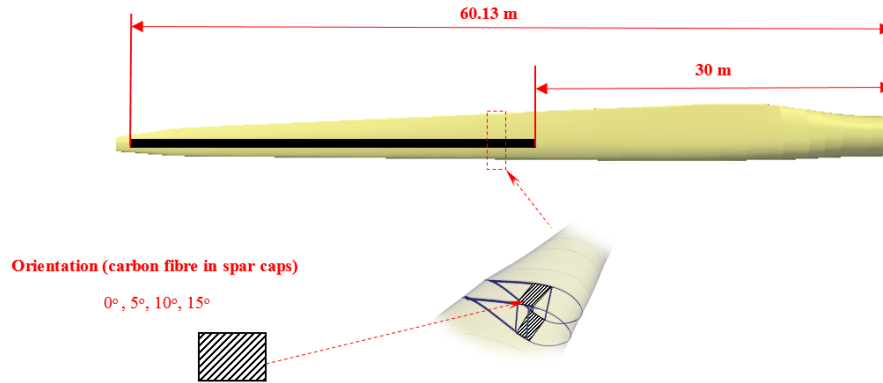
Figure 4.5 The sketch of the BTC NREL 5MW turbine blade.

$$\alpha_c = -\frac{g_c}{\sqrt{EI \times GJ}} \qquad (4.30)$$

In this section, the modal analysis and static analysis on the NREL 5MW turbine blade are carried out to preliminarily investigate the properties of BTC blade. This investigation shows a big picture about the BTC effect on the dynamic and static response of wind turbine blade. Mathematically, modal analysis is an eigenvalue problem in terms of Equation (4.18). Both elastic potential energy and inertia term are considered in the modal analysis part, which are the most important parts for the numerical implementation of the beam model. In addition, the modal analysis is used as a verification case for the present anisotropic beam model. The static analysis can reveal information about the stress and strain distributions,
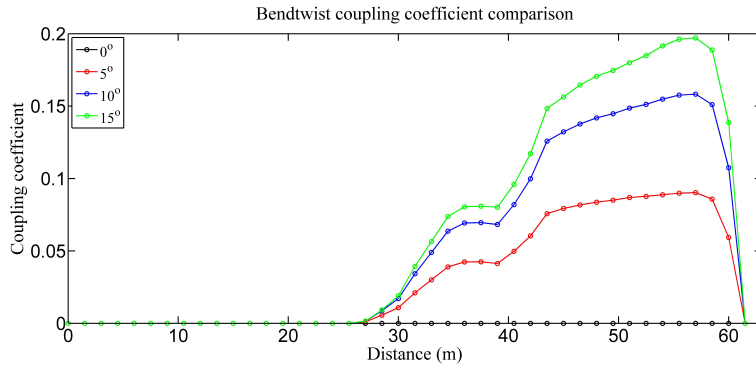
Figure 4.6 BTC coefficients for different orientations.
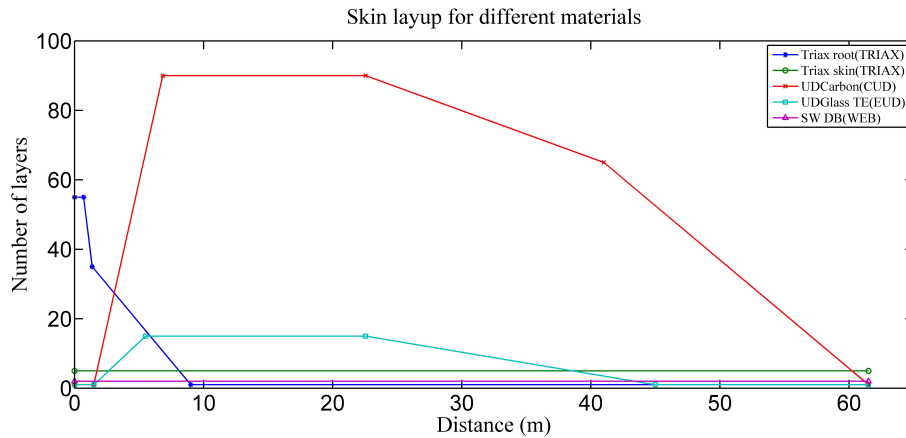
Figure 4.7 Layup of different composite materials used in the NREL 5MW turbine blade.

though inertia effects are neglected in the static analysis. It should be mentioned that the inertial effects and gravitational forces will be carefully considered in the next section of dynamic simulation.

To begin with, for modal analysis, we compute the natural frequencies and discuss the BTC effects on modes. Firstly, the present computed natural frequencies for the first six modes of an anisotropic beam and the result obtained with 3D ANSYS are compared. The results of 3D ANSYS analysis are from the Resor's paper in 2013 about design of the NREL 5MW turbine blade [82]. From Table 4.1, it can be seen that they have a good agreement. Since mode of the blade is related to the inertia and elastic potential effect, this result verifies the previous formulation and our inhouse code for the one-dimensional beam model. For illustration purpose, the first six mode shapes can be seen in Figure 5.5. In my view, the difference between the current model and ANSYS is because the ANSYS model is a high fidelity 3D model, while the structural model employed in this thesis is 1D beam model. The modal analysis is limited to the stationary rotational rotor speed.

Next, the BTC effects on natural frequencies of the blades with different spar cap

orientations are studied. Specifically, the natrual frequencies for different blades with composites at different orientations on caps are compared in Table 4.2. It shows that each natural frequency of bending modes for 5°, 10°, and 15° orientations tends to decrease, which is caused by the reduction of stiffness on longitudinal direction. In contrary, the torsional modes tend to slightly increase. It is also found that edgewise modes are less sensitive to the change of fibre orientation, which also means that the edgewise moment is less sensitive to the spar caps orientation change. Because the dominant force in the edgewise direction is gravity, the fatigue damage of materials related to the edgewise moments is also less affected by the orientation change.

Table 4.1 Comparison between results obtained with the present beam model and ANSYS in terms of predicted natural frequency.

ANSYS (Hz)	Beam model (Hz)	Description
0.87	0.89	1st Flapwise
1.06	1.04	1st Edgewise
2.68	2.72	2nd Flapwise
3.91	3.90	2nd Edgewise
5.57	5.75	3rd Flapwise
6.45	7.15	1st torsion

The static analysis is carried out under the condition of rated wind speed (at 11.4 m/s) to study the static response of the wind turbine. The root bending moment of wind turbine blade is always the maximum. For the static stress (not moment) analysis case, it is not always the case. In this case, the aerodynamic force is pre-calculated using the BEM method and the azimuth angle of the blade is 90^o(clockwise), which means that the blade is directed vertical to the ground. Here only the longitudinal stress and strain are analysed, because they are much larger than the other components and, therefore, more significant for fatigue analysis due to the blade's slender beam structure.

The wind turbine blade is made of different composite materials, which have different mechanical properties, including stiffness and strength. Among these materials, carbon fibre composite in the spar caps endures a large proportion of loading, which also means that the stress on the spar caps are much higher than in the other sections. However, it does not always mean that the spar caps are the most vulnerable part of the blade. Because different materials have different capabilities of resistance to fatigue damage. For example, the stress on the glass fibre composite (reinforcement section) is much lower than that of carbon fibre (spar caps). But the glass fibre is less resistant to the fatigue damage than carbon fibre, which can be seen from Table 4.5. As a result, the fatigue damage of different materials should be analysed separately. This is also the reason why we use BECAS to reconstruct the strain and stress in the cross sections. It should be noted that the stress is not

continuously distributed in composite structure along the blade because of the difference in material properties. Fortunately, the strain distribution is continuously distributed. To study the BTC effect, the strain distributions in a wind turbine blade for different orientation cases are firstly provided in Figure 4.9a-4.9d. These figures are produced by reconstructing the strain on different cross sections.

Table 4.2 The predicted natural frequencies of wind turbine blades with different spar cap orientations.

Description	0° (Hz)	5° (Hz)	10° (Hz)	15° (Hz)
1st Flapwise	0.89	0.88	0.85	0.82
1st Edgewise	1.04	1.04	1.04	1.03
2nd Flapwise	2.72	2.63	2.47	2.30
2nd Edgewise	3.90	3.87	3.82	3.77
3rd Flapwise	5.75	5.72	5.43	5.09
1st Torsion	7.15	7.16	7.17	7.17
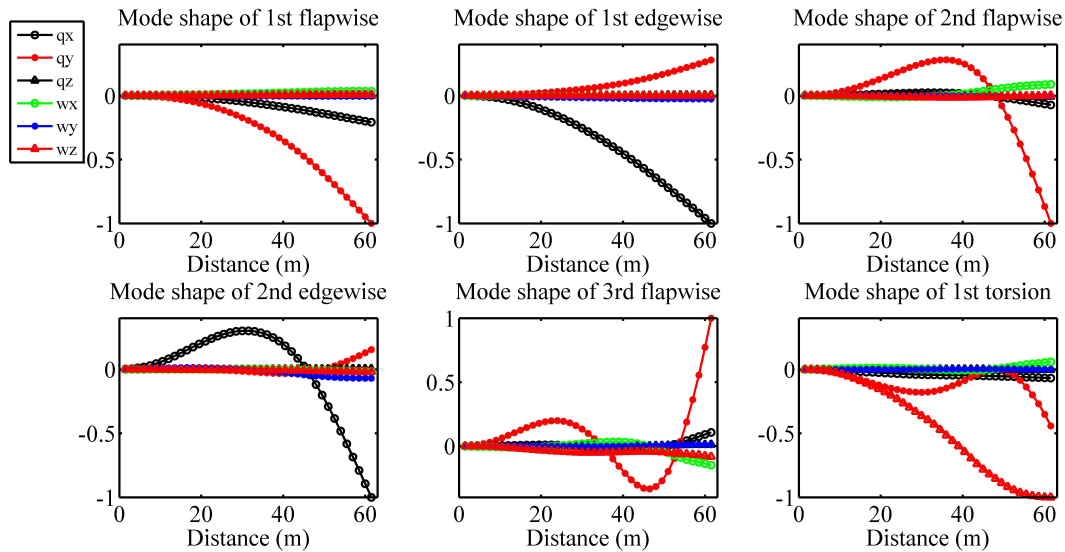
Figure 4.8 First six mode shapes.

From Figure 4.9a, it can be seen that there exist an strain-concentration zone at the transition section of the blade (from round shape to airfoil shape). The materials around the "concentration zone" will have much larger stress than the same materials in other sections. From Figures 4.9b-4.9d for the BTC blades, there occurs another "concentration zone" close to the tip around the leading (and trailing edges). It is obviously caused by the BTC effect. The plot of the maximum magnitudes of longitudinal (fibre-direction) stresses of different

materials at different cross sections (0 m from root to 45 m from root) are shown in the Figures 4.10a-4.10f. In these figures, the carbon fibre refers to the spar caps. The glass fibre refers to the reinforcement section. The triaxial composite refers to the trailing and leading edges. The biaxial composite refers to the shear webs. On one hand, although the moments are decreasing from the root to the tip, there is a stress peak for different materials in the transition section, which is within the first strain-concentration zone. On the other hand, for shear webs (biaxial composite) and triaxial composite, there is another peak at around the tip, which is within the second strain-concentration zone. To further study the stress and strain distributions of the blade, we randomly choose two cross sections from within these two "concentration zones" as two samples for further analysis. The corresponding longitudinal (fibre-direction) stress and strain distributions are shown in Figures 4.11a-4.11h and Figures 4.12a-4.12h. Figures 4.11a-4.11h are sampled at the 10.25 m section from the root of the blade. It should be mentioned here that the strain is continuously distributed because the materials are bonded with each other. If the strain is continuous, the stress is not continuous because of the difference of material properties. From these figures, there are no differences in terms of stress and strain distributions between different BTC blades at the 10.25m section. In other words, the static responses of this blade section for BTC blades with different fibre orientations are the same. In the aeroelastic simulation and fatigue analysis given in the next section, the peak and valley of stress values on this section will be minimized by the BTC effect, and the fatigue mitigation effect will be shown. Fig. 4.12a-4.12h are sampled at the 30 m section, where the orientation of carbon fibre are induced (see Figure 4.5). Two important things can be observed in these figures. On one hand, the maximum stress is slightly reduced by the orientations induced in the spar caps. Since the maximum stress exists in the spar caps, so the load of carbon fibre will be alleviated. On the other hand, the loading for other materials is increasing, because the strain value is increasing, which can be seen in these figures. In the author's view, the shear webs that are most close to the spar caps will endure a large increase in stress.
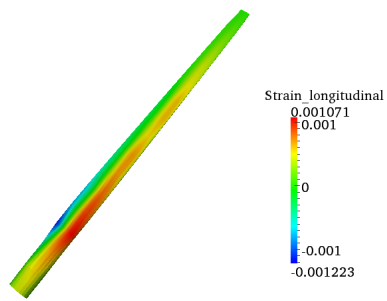
(a) Strain for 0° fibre
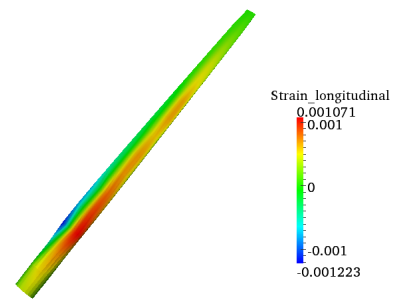
(b) Strain for 5° fibre
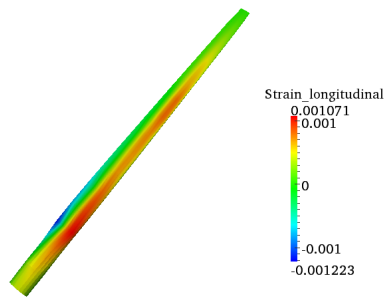
(c) Strain for 10° fibre
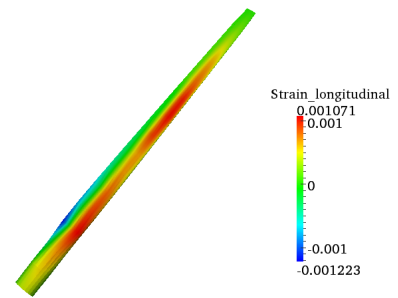
(d) Strain for 15° fibre

Figure 4.9 Strain distribution for different orientations (static analysis).

(a) Out-of-plane moment

(b) In-plane moment

(c) Carbon fibre (UD)

(d) Biaxial composite

(e) Glass fibre (UD)

(f) Triaxial composite
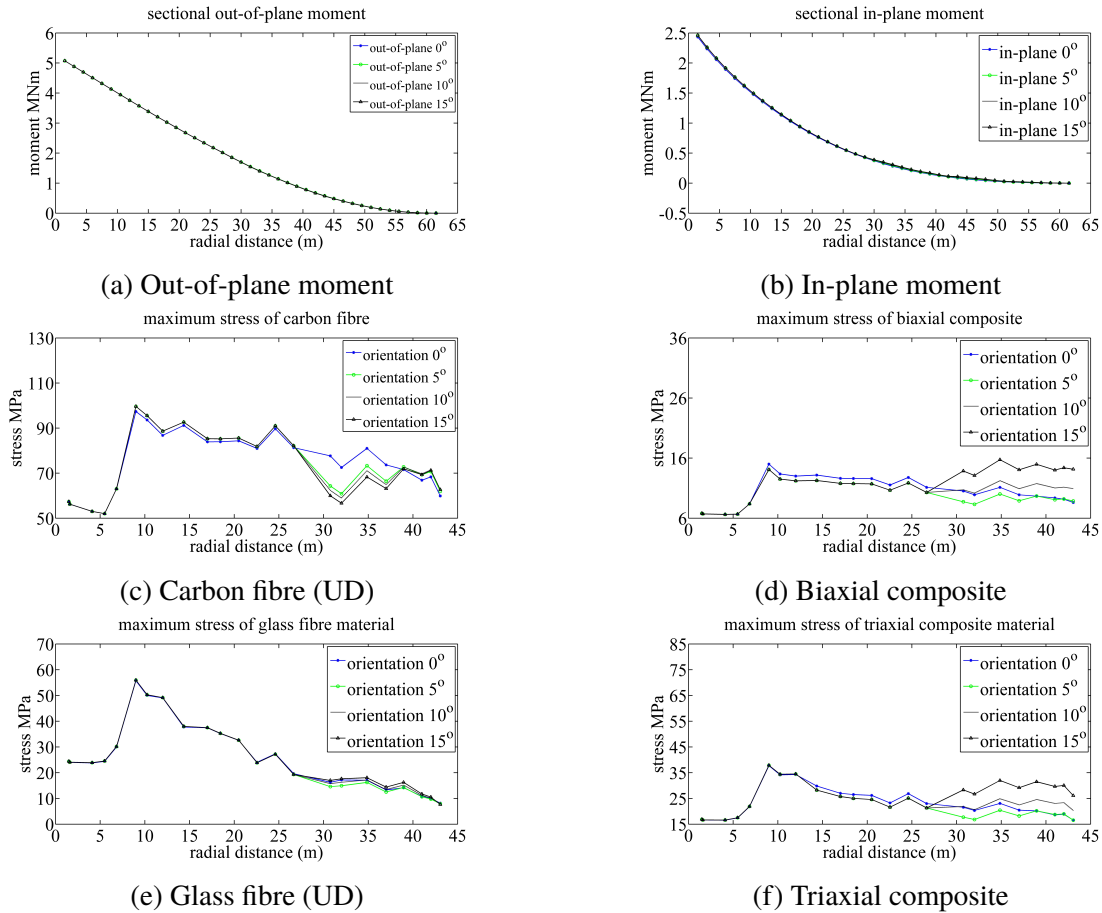
Figure 4.10 Distribution of moment and maximum stress for different materials for different fibre orientations (spar cap).
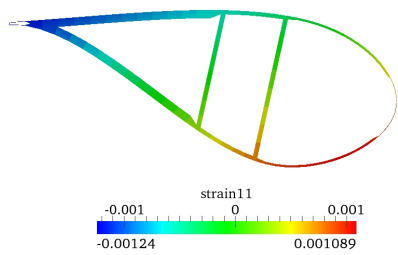
(a) Strain for 0° fibre
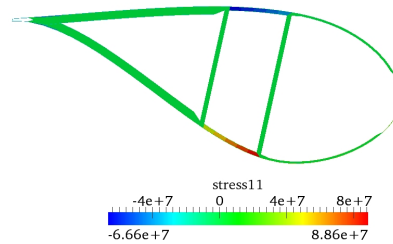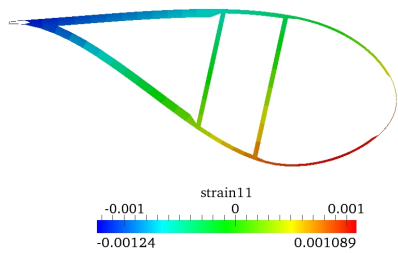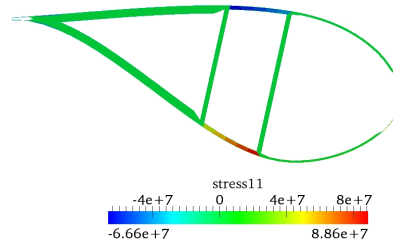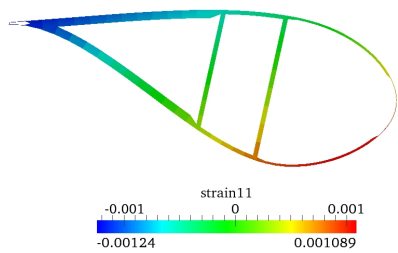
(b) Stress for 0° fibre (Pa)

(c) Strain for 5° fibre

(d) Stress for 5° fibre (Pa)

(e) Strain for 10° fibre
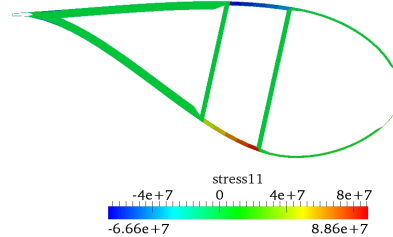
(f) Stress for 10° fibre (Pa)
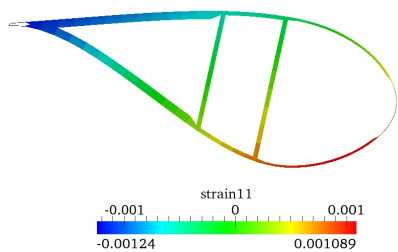
(g) Strain for 15° fibre
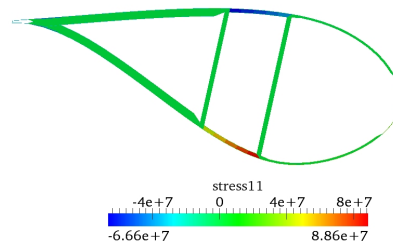
(h) Stress for 15° fibre (Pa)

Figure 4.11 Longitudinal (fibre-direction) stress and strain isopleths for different fibre orientations on the section 10.25m.

(a) Strain for 0° fibre

(b) Stress for 0° fibre (Pa)

(c) Strain for 5° fibre

(d) Stress for 5° fibre (Pa)

(e) Strain for 10° fibre

(f) Stress for 10° fibre (Pa)

(g) Strain for 15° fibre

(h) Stress for 15° fibre (Pa)
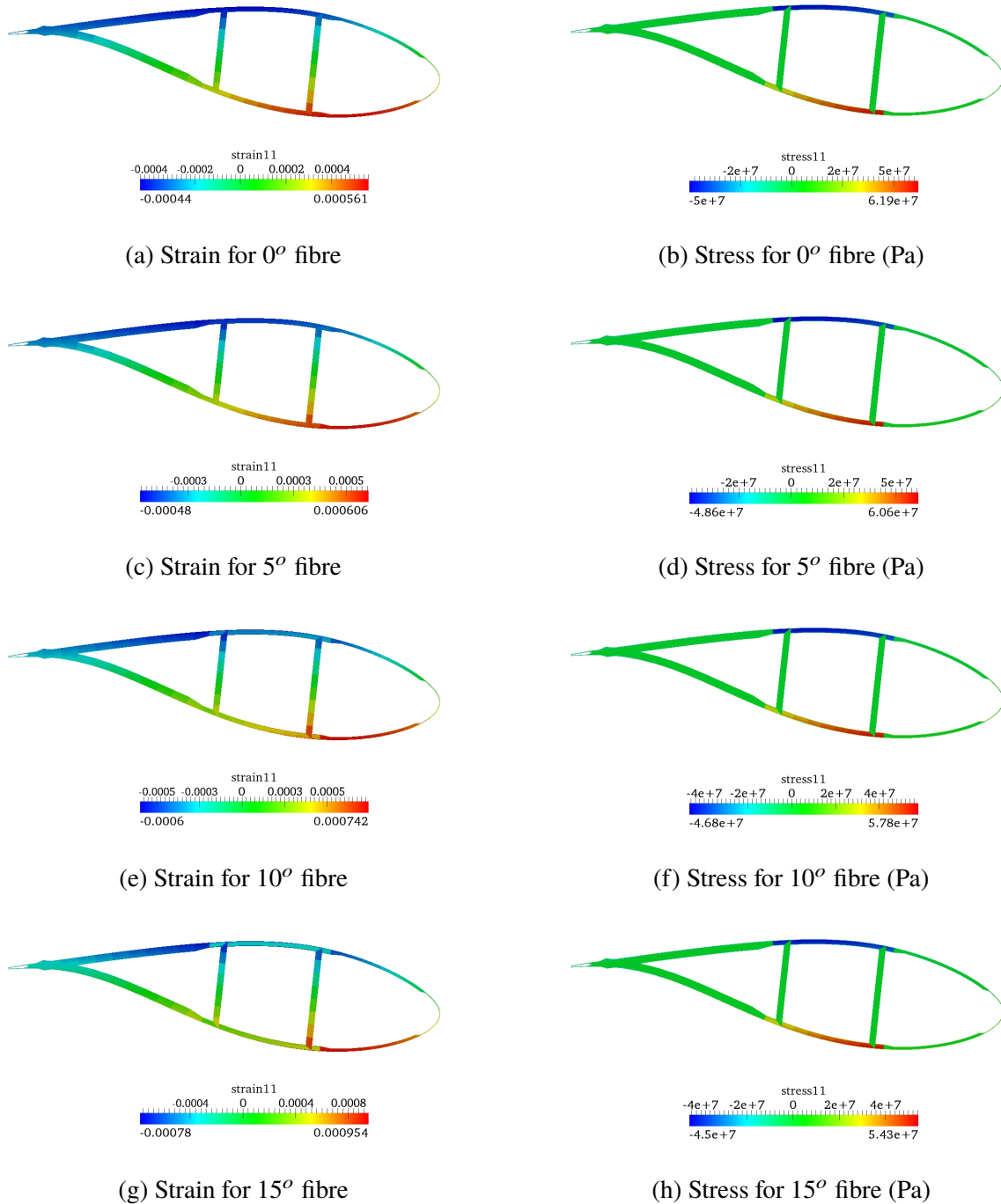
Figure 4.12 Longitudinal(fibre-direction) stress and strain isopleths for different fibre orientations on the section 30m.

4.5 Aeroelastic modelling of anisotropic wind turbine blade

In this section, the aeroelastic model will be established by combining the aforementioned beam model (structural model) with an aerodynamic model. The aerodynamic force can be determined by the local lift and drag coefficients, namely C_l and C_d, which can be obtained through the look-up table of lift and drag coefficients with respect to the local angle of attack α based on the inflow angle ϕ, pitch angle β and blade twist angle due to the blade torsion $\Delta\beta$:

$$\alpha = \phi - \beta + \Delta\beta \tag{4.31}$$

From the blade element analysis, the local inflow angle ϕ can be calculated by using the following equation:

$$\tan\phi = \frac{(U_\infty + U_n')(1 - a) + V_{e-op}}{(\Omega r + U_t')(1 + a') + V_{e-ip}} \tag{4.32}$$

The V_{e-op} and V_{e-ip} are out-of-plane and in-plane velocities induced by the vibration of the blade, which are predicted from the structure model. U_∞ and Ωr are free stream velocity and rotational velocity respectively. It is assumed that the near wake is stable, the axial and tangential induction factors a and a' are constant, which can be calculated by the blade element momentum (BEM) method. The procedure of BEM can be seen from the Figure 4.13 [83]. The U_n' and U_t' are two components of the fluctuating velocity, which can be obtained from a turbulent wind model to be introduced later. In Figure 4.13, $F = F_{tip}$ ($F_{root} = 1$), which is the tip loss factor and calculated by equations (4.33) - (4.34). In these equations, B is the number of blades, r is the radial distance from root, and R is the tip radius of the blade. In Figure 4.13, σ' is the local solidity, which is calculated by Equation (4.35), in which $c(r)$ is the local chord length. In this model, it is assumed that the frequencies of the structural vibration is higher than the frequencies of turbulence, which is also a limitation of the current model. It is also assumed that the induction factors are fixed throughout the whole simulation. The near wake is assumed to be steady during the simulation. The induction factors are derived from the steady wind conditions. The induced velocities are precalculated. The elastic twist has been included in the aerodynamic load calculation. The turbulence is assumed uniformly distributed across the rotor. The spatial coherence is neglected.

$$F = \frac{2}{\pi}\arccos(e^{-f'}) \tag{4.33}$$

$$f' = \frac{B}{2}\frac{R - r}{r\sin(\phi)} \tag{4.34}$$

$$\sigma' = \frac{Bc(r)}{2\pi r} \tag{4.35}$$
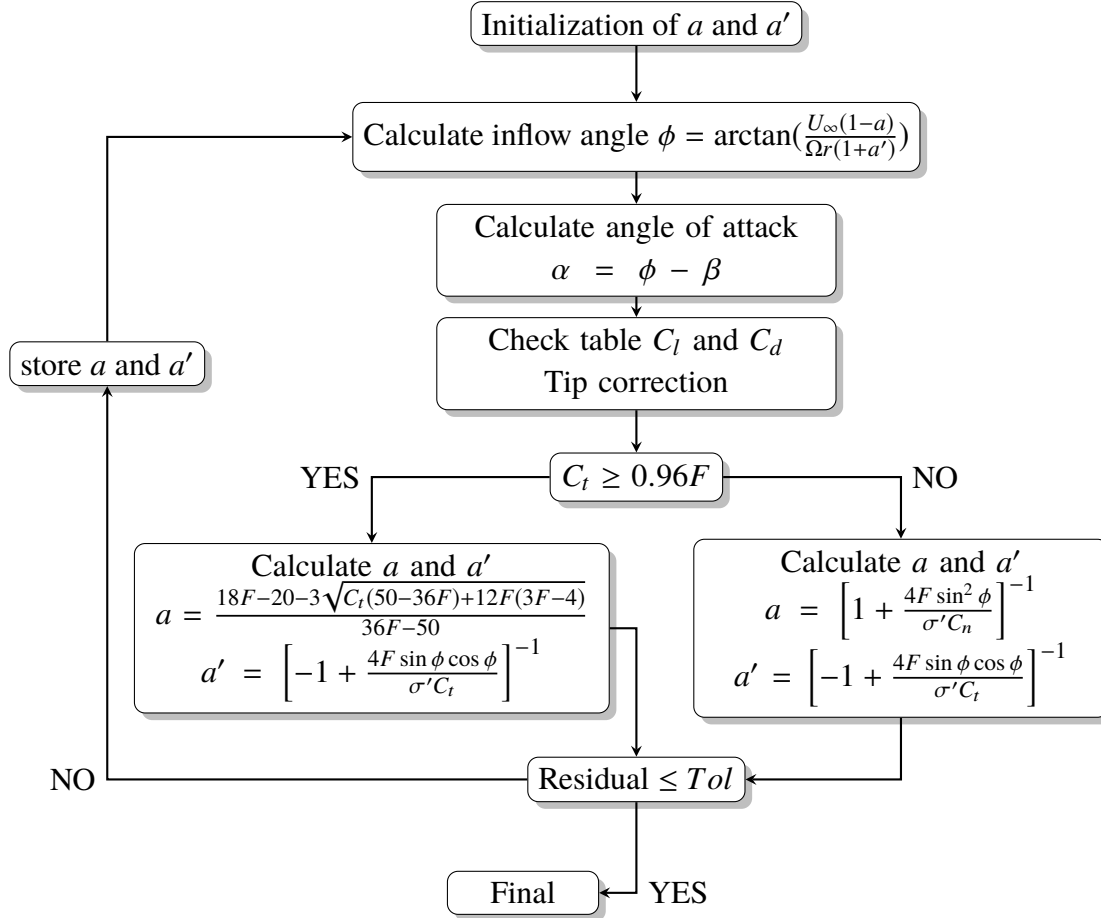
Figure 4.13 Flowchart of blade element momentum method.

The aerodynamic forces can be calculated by Equation (4.36).

$$f_a(\alpha) = L(\alpha)\frac{1}{2}\rho V_{rel}^2 c\,dr \tag{4.36}$$

where $L(\alpha)$ is the coefficient matrix from the

$$L(\alpha) = \begin{bmatrix} -\cos\phi & \sin\phi & 0 \\ \sin\phi & \cos\phi & 0 \\ 0 & 0 & 1 \end{bmatrix} \begin{bmatrix} C_d \\ C_l \\ C_m c \end{bmatrix} \tag{4.37}$$

The C_m and c are aerodynamic moment coefficient and chord respectively. This aerodynamic model can be coupled with the aforementioned structural model (1D anisotropic beam model). The structure of the aeroelastic model is shown in Figure 4.2.

The *Risø* model [84] is employed as the dynamic stall model for lift coefficient, in which the non-dimensional parameter f defined in Equation (4.42), a measure of the degree of separation, is introduced to correct the aforementioned lift coefficient. The dynamic angle of attack α_d (a function of time t) is also introduced which is shown in Equation (4.38).

$$\alpha_d(t) = \alpha(1 - A_1 - A_2) + c_1(t) + c_2(t) \tag{4.38}$$

in which $c_1(t)$ and $c_2(t)$ are two variables to describe the delayed lift coefficient. A_1 and A_2 are two parameters, which are shown in Table 4.3. The dynamic linear lift is calculated as:

$$C_{l0,d} = C_{l0}(\alpha) + \frac{\pi c \dot{\alpha}}{2u_{rel}} \tag{4.39}$$

Where

$$C_{l0}(\alpha) = \frac{dC_l}{d\alpha}\Big|_{\alpha_0}(\alpha - \alpha_0) \tag{4.40}$$

in which α_0 is the angle of attack under which the lift coefficient is zero. If the separation parameter f is equal to 0 (fully separated condition), the $C_{l0} = 4C_l^{st}$, in which C_l^{st} is from the table checking of static lift coefficients (the superscript "st" means static). The variables can be determined by the following Equation (4.41). In this equation, C_{l0}' is the retarded lift coefficient.

$$\begin{bmatrix} \dot{c}_1 \\ \dot{c}_2 \\ \dot{C}_{l0}' \\ \dot{f}_d \end{bmatrix} = \begin{bmatrix} -(\omega_1 + \frac{\dot{u}_{rel}}{u_{rel}}) & 0 & 0 & 0 \\ 0 & -(\omega_2 + \frac{\dot{u}_{rel}}{u_{rel}}) & 0 & 0 \\ 0 & 0 & -\omega_4 & 0 \\ 0 & 0 & 0 & -\omega_3 \end{bmatrix} \begin{bmatrix} c_1 \\ c_2 \\ C_{l0}' \\ f_d \end{bmatrix} + \begin{bmatrix} \omega_1 A_1 \alpha \\ \omega_2 A_2 \alpha \\ \omega_4 C_{l0,d} \\ \omega_3 f(\alpha_f) \end{bmatrix} \tag{4.41}$$

The separation parameter f can be calculated by Equation (4.42).

$$f(\alpha) = (2\sqrt{\frac{C_{l0}(\alpha)}{C_l^{st}(\alpha)}} - 1)^2 \tag{4.42}$$

The dynamic lift coefficient for aerodynamic model can be calculated by Equation (4.43).

$$C_{l,d}(t) = f_d(t)C_{l0}(\alpha_d) + (1 - f_d)C_{l1}(\alpha_d) \tag{4.43}$$

In Equation (4.43), the C_{l1} can be calculated by the following Equation

$$C_{l1}(\alpha_d) = \begin{cases} \dfrac{C_{l0}(\alpha_d)}{2} & f = 1 \\ \dfrac{[C_{l,d}^{st}(\alpha_d) - C_{L,0}(\alpha_d)f]}{1 - f} & else \end{cases} \qquad (4.44)$$

Table 4.3 Parameters of dynamic stall model.

Parameters	Values
ω_1	0.0455
ω_2	0.3
ω_3	0.0875
ω_4	0.4125
A_1	0.165
A_2	0.335

Two test cases (one for) of DU-40 airfoil for the dynamic stall model are carried out. The prescribed change of α is shown in equations below.

$$\alpha(t) = 5 + 5sin(12t) \quad (^o) \qquad (4.45)$$

$$\alpha(t) = 20 + 50sin(12t) \quad (^o) \qquad (4.46)$$

The comparison between the static and dynamic (corrected) lift coefficients are compared in Figure 4.14 and 4.15. The lift coefficient for dynamic stall model is slightly different from the static lift coefficient. The dynamic lift coefficients varies along the blue circle, which is the delayed effect.
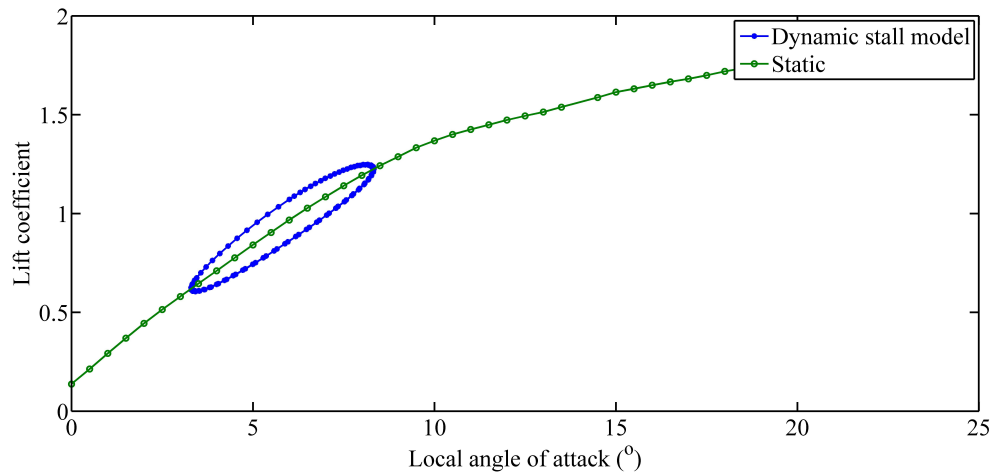
Figure 4.14 Test case 1 for dynamic stall model.
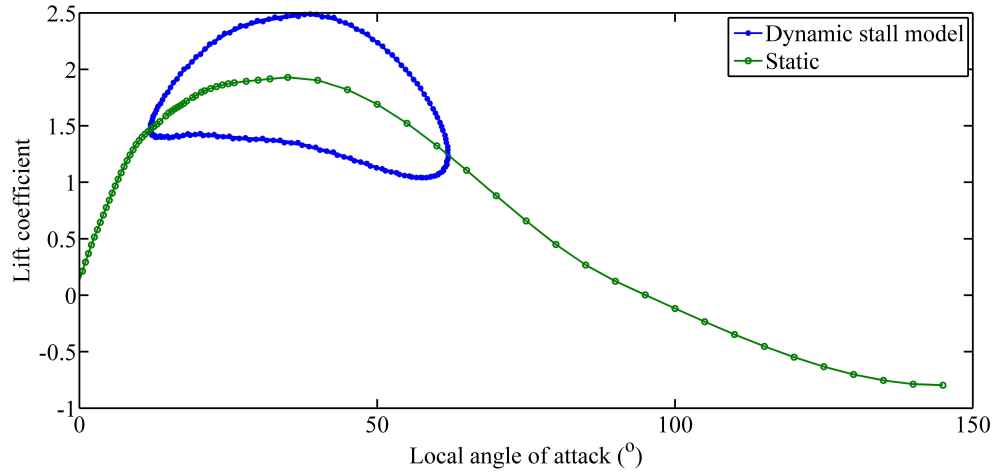
Figure 4.15 Test case 2 for dynamic stall model.

4.6 Case study 1: fatigue load alleviation of single wind turbine under rated wind speed condition

In this section, the dynamic loading under rated wind speed (11.4 m/s) condition will be simulated without dynamic stall model. The loading time series of wind turbine blade with different fibre orientations on spar caps are compared with each other to illustrate the bend-twist coupling effect. Fatigue analysis for different materials with different fibre orientations on different sections will also be carried out . The fatigue analysis under wide range of wind speed conditions with dynamic stall model will be presented in case study 3.

108

4.6.1 Turbulent inflow simulation and problem statement

The aero-elastic simulation (dynamic simulation) is carried out for the NREL 5MW wind turbine. The rotational speed is 12.1 rpm, the wind speed is 11.4 m/s and the turbulence intensity is 10%. It is assumed that the wind speed is evenly distributed for all the wind directions. The fluctuating wind speed is simulated by the Sandia method [85]. In this method, the fluctuating wind speed is assumed to be coloured noise, whose spectrum (Kaimal spectrum) is shown in Equation (4.47).

$$\frac{f S_k(f)}{\sigma_k^2} = \frac{4 f L_k / V_{hub}}{(1 + 6 f L_k / V_{hub})^{\frac{5}{3}}} \tag{4.47}$$

where f is the frequency in Hz, k is the index referring to the velocity component direction (1 = longitudinal, 2 = lateral, 3 = upward), $S_k(f)$ is the single-sided velocity component spectrum, σ_k is the velocity standard deviation, L_k is the velocity component integral scale parameter, and V_{hub} is the wind velocity at the hub height. Instead of using a white noise, the transformation matrix can be obtained from the above spectrum, by which the matrix is used to generate the simulated wind speed in frequency domain. Lastly the wind speed can be recovered by employing the inverse Fourier transform. The simulated wind speed is shown in Figure 4.16. The comparison between the power spectrum of simulated wind speed and Kaimal wind spectrum is shown in FIgure 4.17.
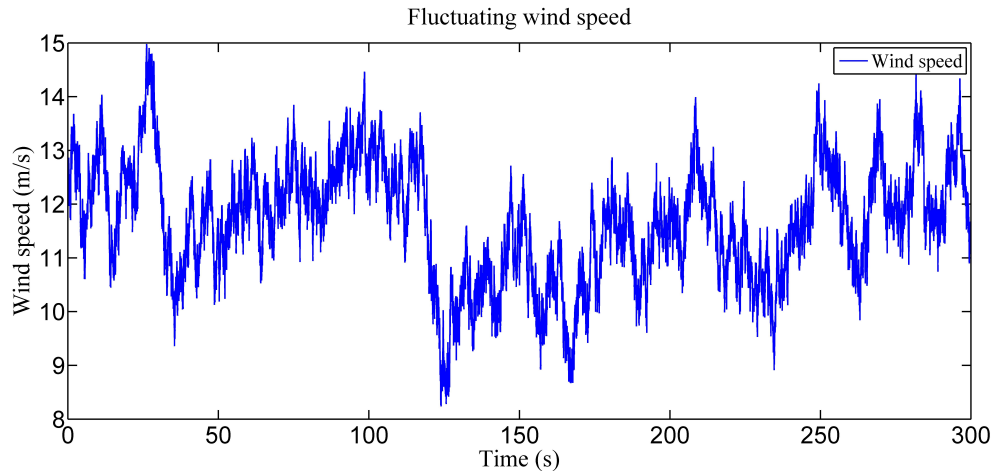
Figure 4.16 Fluctuating longitudinal wind speed under normal wind condition.

The methodology of aeroelastic simulation and fatigue analysis has already been presented in previous sections. For fatigue analysis, the safety factors, thickness and strength of different materials of NREL 5MW turbine blade can be seen in Tables 4.4 and 4.5. In Table 4.4, the γ_{M_a} is the partial safety factor for the material. C_{ib} represents the safety factor in terms of temperature effect, material fabrication effect, etc. Obviously, the fatigue
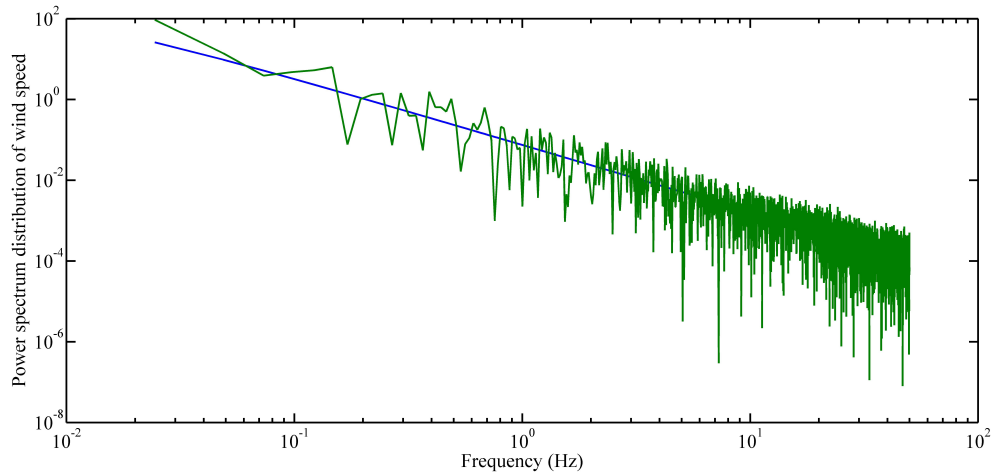
Figure 4.17 The comparison between the power spectrum of simulated turbulent wind and Karmal spectrum.

properties of 0° UD composite will be different from that of other UD composites with offset angles. To apply the properties of 0° UD, material coordinate system is employed for the UD composites with offset angles, which is explained in the BECAS manual (2015, pages 60-61). The longitudinal stress can be transformed to the material coordinate system (along the fibre) by multiplying rotation matrix.
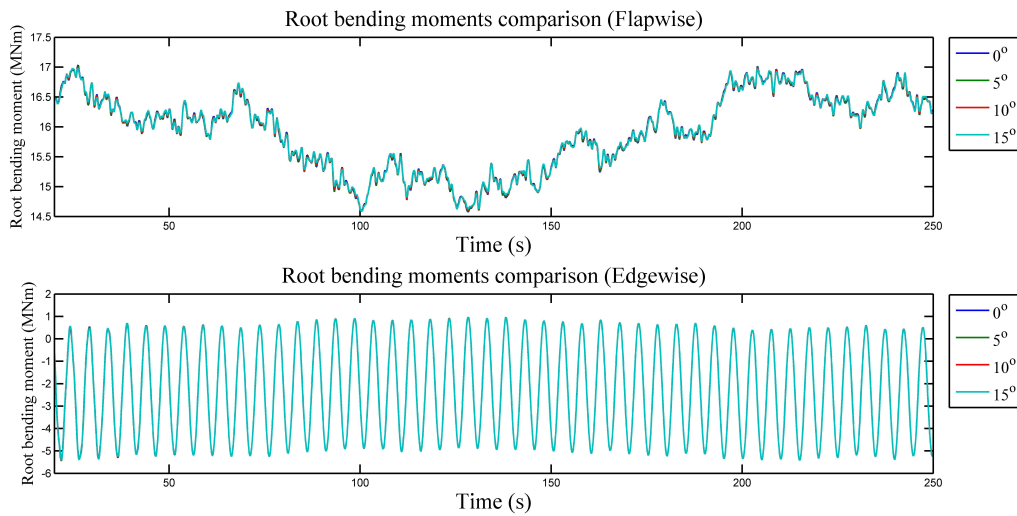
Figure 4.18 Fluctuating root bending moments under normal wind condition.
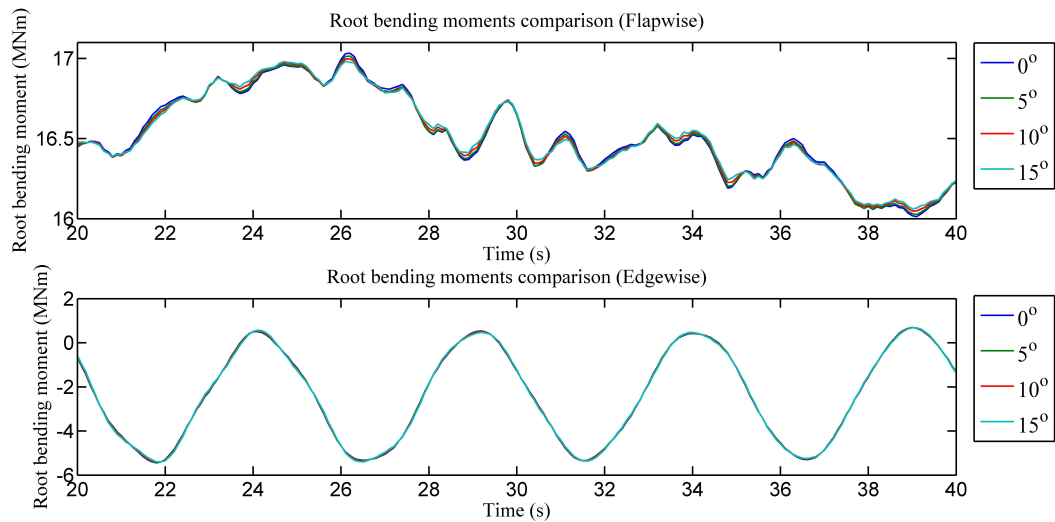
Figure 4.19 Fluctuating root bending moments under the normal wind condition (enlarged view).
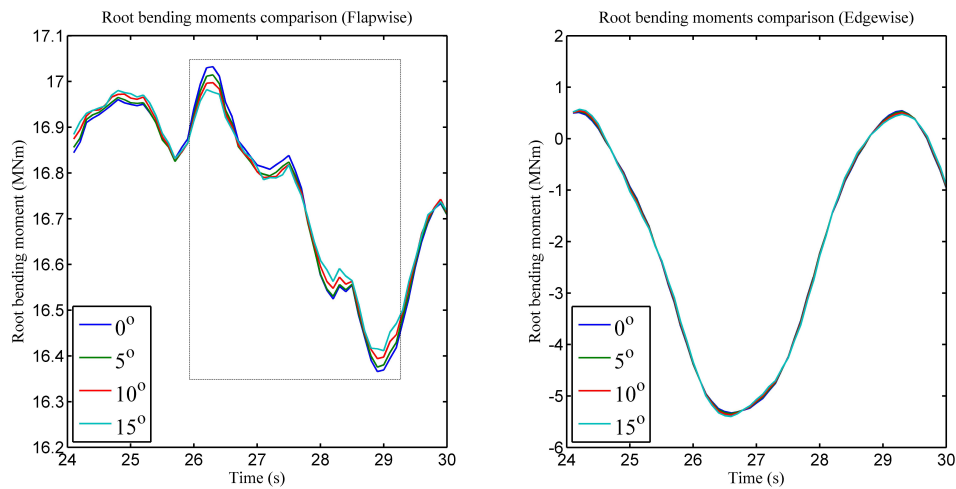
Figure 4.20 Fluctuating root bending moments under the normal wind condition (further enlarged view).

4.6.2 Dynamic loading and fatigue analysis

In this section, the loading, tip displacements, and the fatigue damage of a single wind turbine with different orientations of carbon fibre will be compared under the rated wind speed condition (turbulence intensity of 0.1). The fluctuating wind speed is shown in Figure 4.16. The fluctuating root bending moments of each blade are illustrated in the Figure 4.18. Figures 4.19 and 4.20 are the partial enlarged figure of Figure 4.18. It can be seen that the minimization of the peaks and valleys of fluctuating flapwise bending moments is achieved by the BTC effect. With an increase in orientation angle, the mitigation effect is more
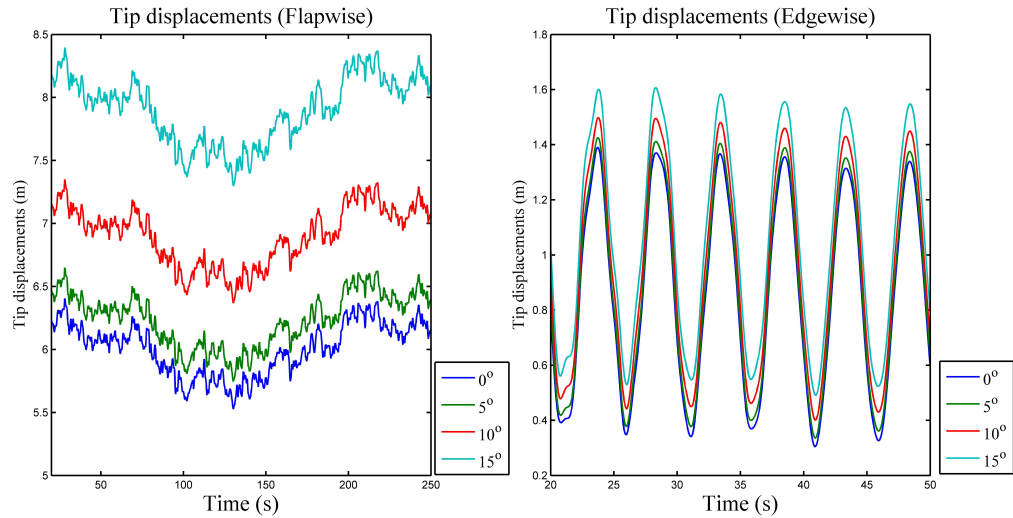
Figure 4.21 Fluctuating tip displacements under the normal wind condition.

obvious. For the edgewise bending moment, the mitigation effect is not observed, because the edgewise bending moment is dominated by the gravity force instead of the aerodynamic force. For the tip displacements, both the flapwise and edgewise tip displacements of BTC blades are shifted upward, which can be seen in the Figure 4.21. In the figure of edgewise displacement, the amplitudes of vibrations are 1.5476m, 1.5975m, 1.6795m, and 1.7648m for the 0, 5, 10, and 15 offset angles respectively. In other words, there exist an increase of the amplitudes with an increase in offset angles. Compared with blades without the BTC effect, the shifted values of the flapwise and edgewise displacements for the 15° BTC blade are 2m and 0.2m respectively. This extra tip displacement will affect the designed gap between the blade and tower. Figure 4.22 shows the minimum fatigue life of different materials on different cross sections. There is a lowest point of fatigue life for different materials. If we recall the "strain-concentration" zone in the previous section, the lowest point is located in this zone (10.25 m from the root). This fatigue damage is caused by the large strain (or stress) value for different materials. As a result, the 10.25 m section, a section with standard airfoil shape most close to the lower point, is determined to be the section for further fatigue analysis. From our calculations, it should be noted that the longevity of carbon fibre composite in spar caps, which is the main structure, has increased with an increase in orientation angle due to the BTC effect. For the section around the tip, the fatigue mitigation effect is obvious for spar caps. In fact, the lowest value of fatigue life in spar caps increases from 337 years to 404 years for the 15° case. It should be noticed that this fatigue mitigation effect is due to the aforementioned peak-valley minimization in terms of bending moments. The fatigue life of other materials, including EUD, TRIAX, does not change too much.

112

Table 4.4 Safety factors for different materials.

Material	γ_{M_a}	C_{2b}	C_{3b}	C_{4b}	C_{5b}	m
EUD (Glass fibre)	2.65	1.1	1.0	1.1	1.2	10
TRIAX (Triaxial fibre)	2.65	1.1	1.2	1.1	1.2	10
WEB (Biaxial fibre)	2.65	1.1	1.2	1.1	1.2	10
CUD (Carbon fibre)	2.65	1.1	1.0	1.1	1.2	14

Table 4.5 Thickness(each layer) and strength of different materials.

Material	Thickness (mm)	σ_T (MPa)	σ_C (MPa)
EUD (Glass fibre)	0.47	793.05	-542.49
TRIAX (Triaxial fibre)	0.94	700	-700
WEB (Biaxial fibre)	1	144	-213
CUD (Carbon fibre)	0.47	1546	-1047
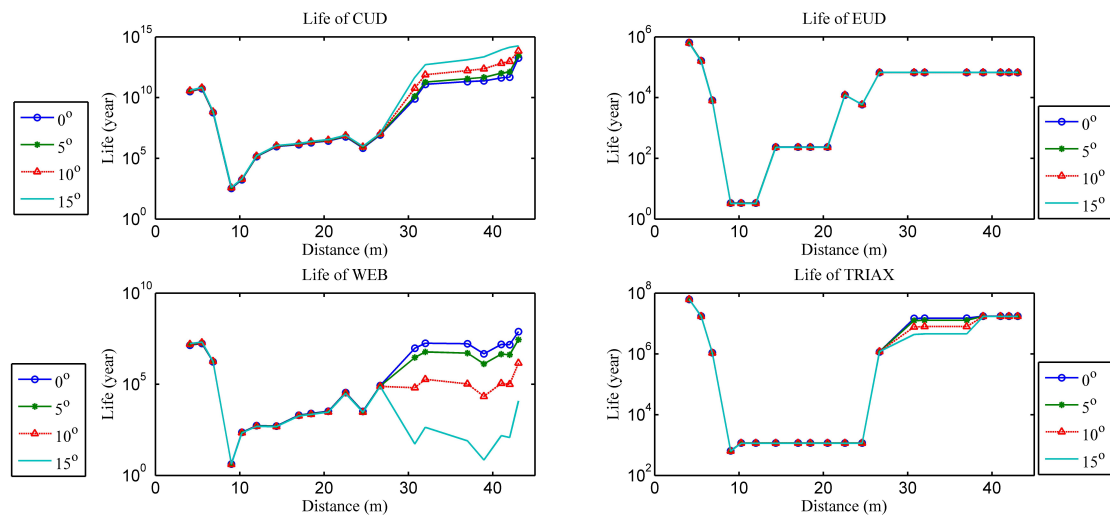
Figure 4.22 Longevity of different materials on different sections under the normal wind condition.

4.7 Case study 2: fatigue analysis of multiple wind turbines in the wind farm (wake condition)

In this section, wake effect on the wind turbine blade is considered, which is also an important factor for fatigue load increase. The dynamic stall effect is neglected in this case study, which will be considered in case study 3. This wake condition is also referred to as the IEC61400-1 standard for wind turbines. The effective turbulence intensity in the wake region can be calculated by using the following equations. The probability distribution for

wind direction is assumed to be uniform.

$$I_{eff} = \frac{\hat{\sigma}_{eff}}{V_{hub}} = \frac{1}{V_{hub}}[(1 - Np_w)\hat{\sigma}^m + p_w \sum_{i=1}^{N} \hat{\sigma}_T^m(d_i)]^{\frac{1}{m}} \tag{4.48}$$

$$\hat{\sigma}_T = \sqrt{\frac{0.9V_{hub}^2}{1.5 + 0.3d_i\sqrt{V_{hub}}} + \hat{\sigma}^2} \tag{4.49}$$

In Equation (4.48), I_{eff} is the effective turbulence intensity under the wake condition. $\hat{\sigma}_{eff}$ is the standard turbulence deviation under wake condition. V_{hub} is the wind speed at the hub height (11.4 m/s in this case). N is the number of neighbouring turbines. p_w is a constant (0.06 for uniformly distributed wind direction). $\hat{\sigma}_T$ is the added turbulence standard deviation. m is the coefficients for the S-N curve. $\hat{\sigma}$ is the ambient turbulence standard deviation. d_i is the distance between wind turbines, which is normalized by diameter. The uniformly distributed wind direction is used here to employ the effective turbulence equations of wake, which is a limitation of the current simulation.

Two different layouts are analysed, including three wind turbines in a line, and nine wind turbines in array. The longitudinal distance is 5D (D is the diameter of the wind turbine rotor). The lateral distance is 3D. From Figure 4.23, it can be seen that the turbulence intensity for an array of nine wind turbines is much higher than that of the three turbines in a line. In this figure, the percentage number beside the circle represents the turbulence intensity. In Figure 4.24, each bar represents the aforementioned "lowest point" for different materials at different cross sections, which are also the lowest fatigue lives of different materials at different sections. As a result, Figure 4.24 shows the fatigue life of different materials under different wake conditions. It should be noted that the wake mitigation effect for spar caps is obvious for different cases. There exist a large decrease of life for both CUD (spar caps) and BIAX (shear webs) under the wake condition. The high turbulence intensity in the wake region will induce large stress fluctuations, which will directly affect the fatigue life of CUD that endures large loading. From Figure 4.24, it can be seen that the spar caps (CUD) of WT 8 among all the wind turbines because of the higher turbulence intensity in wake. The analysis in this section is just qualitative analysis, because the dynamic stall and the probability density distribution of wind speed are all neglected. In the next section, the WT 8 will be chosen to be the subject for wake-induced fatigue analysis.

Layout 1
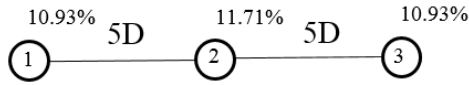
Layout 2
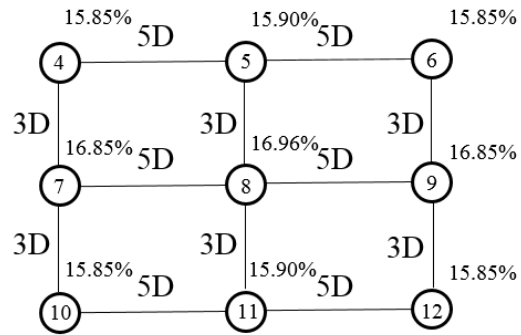
Figure 4.23 Wind turbine layouts.
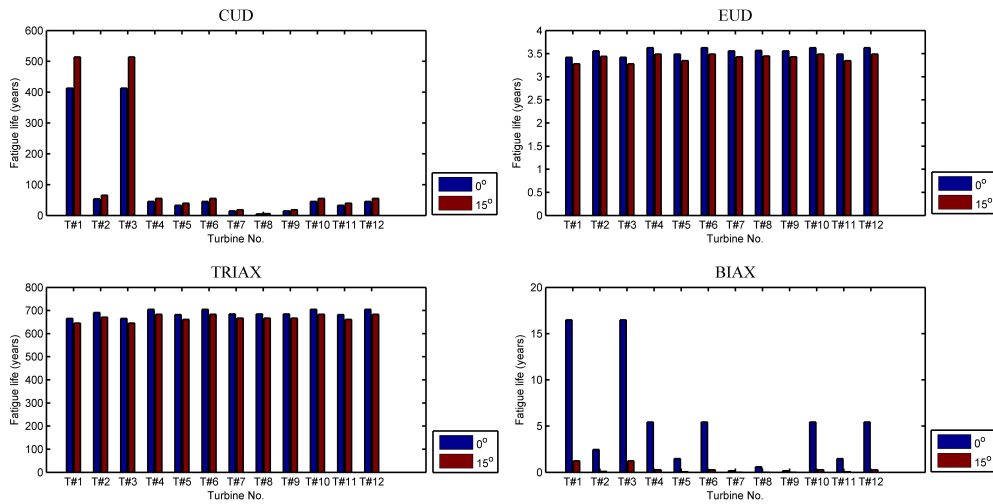
Figure 4.24 Fatigue life comparison between two different orientations of different wind turbine blades with different materials .

4.8 Case study 3 with dynamic stall model and under wide range of wind speed

In this section, the fatigue life of materials of wind turbine blade will be calculated under wide range of wind speed conditions (design load cases, DLC, power production condition in IEC 61400-1). The turbulence intensity for different wind conditions is calculated based on the normal turbulence model (NTM). Dynamic stall effect is also considered in this case.

4.8.1 Dynamic stall effect

In this section, the dynamic stall effect is considered. Firstly, the simulated dynamic loading of the numerical model with and the without dynamic stall model are compared in Figure 4.25. From this figure, it can be seen that the fluctuating patterns in the initial period are obviously different during the period from 0 s to 10 s. In this period, the wind turbine blade is loaded with aerodynamic force. The fluctuation part (with the mean value subtracted) of out-of-plane moments are further compared with each other, which is shown in Figure 4.26. The power spectrum for the fluctuation parts of the simulated loading with and without dynamic stall model is further compared in Figure 4.27, from which it can be seen that the two fluctuations share the same spectrum for the low frequency (below 1 Hz).
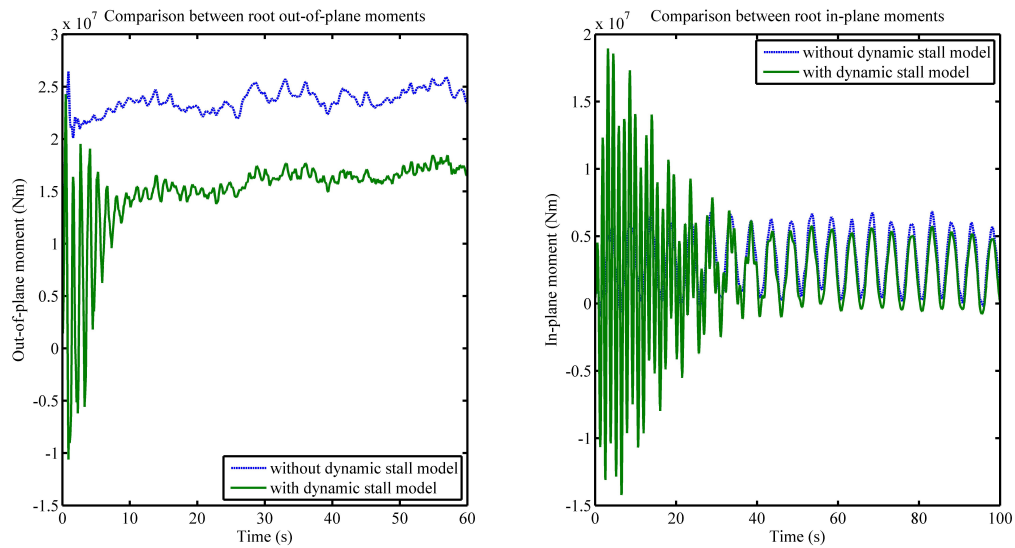
Figure 4.25 The comparison between the simulated moments of the numerical model with and without dynamic stall model.
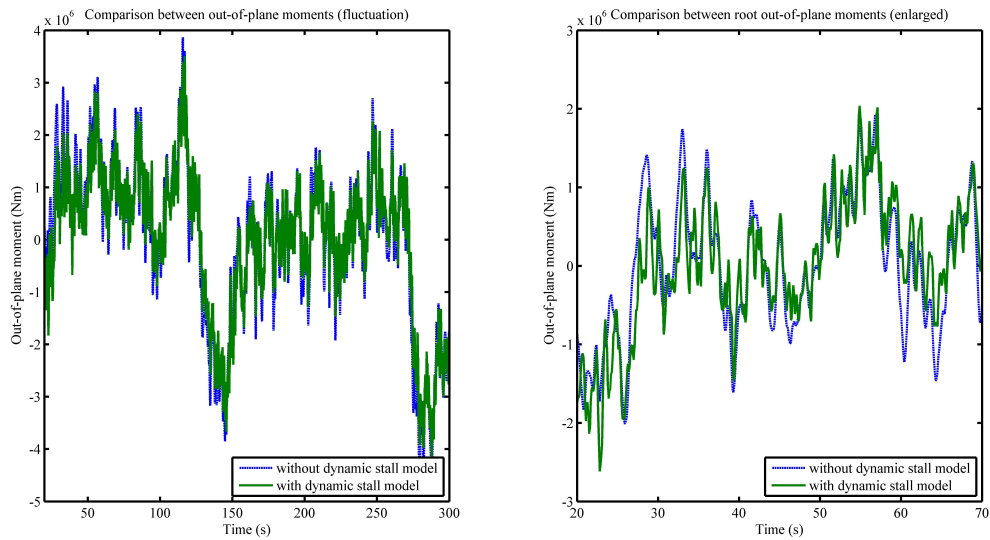
Figure 4.26 Comparison between the out-of-plane bending moments (with mean value subtracted) with and without dynamic stall model.
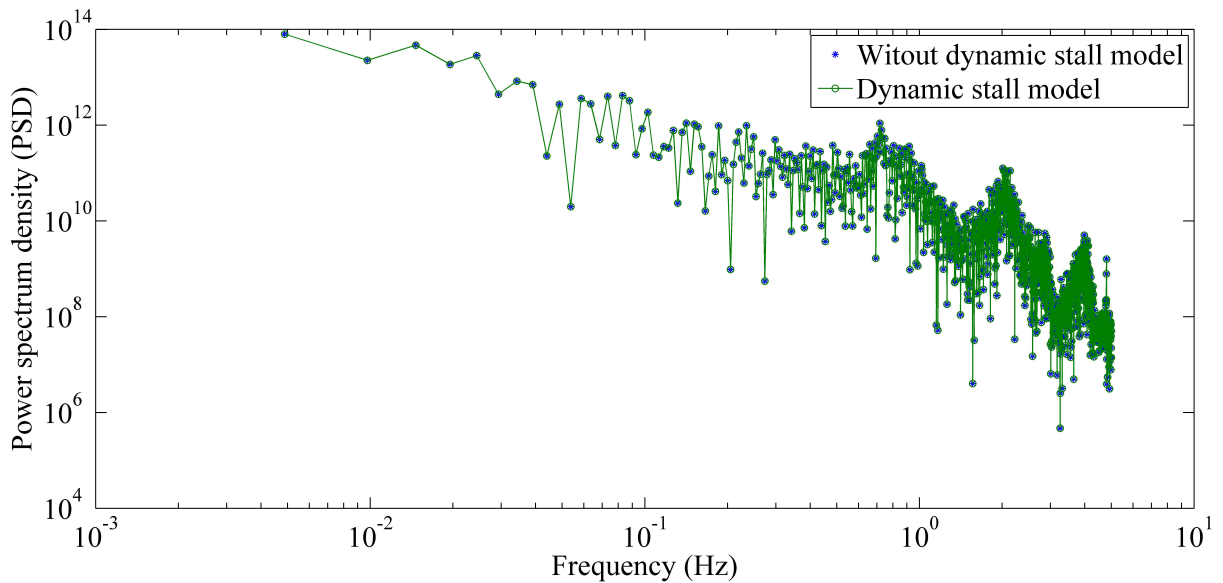
Figure 4.27 Comparison between the power spectrum of out-of-plane bending moments (with mean value subtracted) with and without dynamic stall model.

4.8.2 Fatigue life analysis for single wind turbine

In the previous sections, the fatigue analysis of the blade is performed based only on simulations at one wind speed (11.4 m/s). Moreover, the analysis is performed at a turbulence intensity of 10 %. This is of course not representative of the conditions encountered by a wind turbine which operates in a wide range of wind velocities (3-25 m/s). In order to obtain realistic values of the fatigue damage, simulations are performed over the whole range of operational conditions. The weights of the different wind conditions are introduced through a representative Weibull distribution. In addition, the turbulence intensity are also calculated according to IEC 61400-1. In other words a realistic fatigue spectrum will be composed in order to deal with the realistic lifetime results in this section. The wind turbine is analysed under the condition of wind class IB and power production (design load case 1.2 with normal turbulence model) in IEC 61400-1. For wind class IB, the reference turbulence intensity is 0.14 according to IEC 61400-1. The standard deviation of velocity for different wind speed (at hub height) can be calculated by the Equation (4.50). The rotational speed of wind turbine rotor is assumed to be fixed which is a limitation of the simulation cases.

$$\sigma_1 = I_{ref}(0.75V_{hub} + 5.6) \tag{4.50}$$

The Equation (4.51) is the function of Weibull distribution, which is the probability density function of wind speed in wind farm. The plot of Weibull distribution is shown in Figure 4.28.

$$f(V) = (\frac{k}{c})(\frac{V}{c})^{k-1}e^{-(\frac{V}{c})^k} \tag{4.51}$$

The simulated wind speed and loading (out-of-plane moments) for different wind speed range is shown in Figure 4.29 and 4.30.

The control strategy of wind turbine can be divided into two stages. In the first stage, from 0 - 11.4 m/s (rated wind speed), the rotational speed of rotor is the control variable to optimizing the power production (optimum tip speed ratio (TSR)), and the pitch angle is 0°. In the stage 2, from 11.4 - 25.0 m/s, the rotational speed is fixed (12.1 rpm), and the pitch angle becomes the control variable. The data for these parameters is shown in Table 4.6 along with the turbulence intensity.

The fatigue lives for different materials under different wind conditions are calculated based on the fatigue damage of the 10.25 m section, which are shown in Table 4.7. From this table, it can be seen that the lives for different wind speed conditions are very different. The life at around rated wind speed (9 - 13 m/s) is the lowest one for all the materials. The total calculated life for different materials is shown in Table 4.8. It should be mentioned here that the calculated life of main structure, carbon fibre composite on spar caps, is very close to the design life, 20 years. The biaxial composite in the shear webs has the shortest
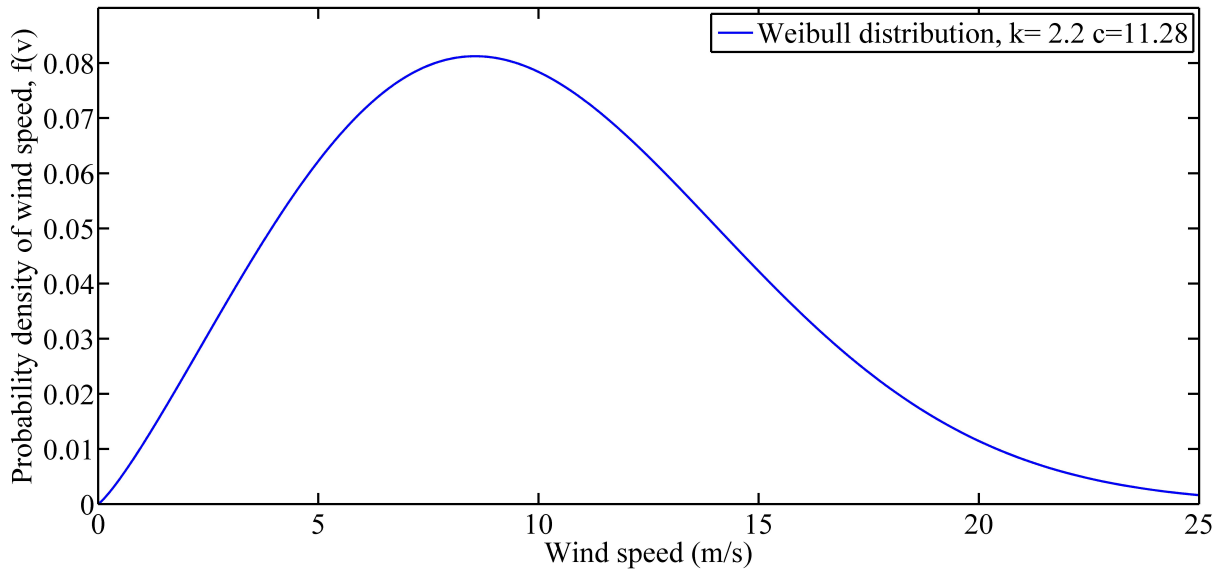
Figure 4.28 Weibull distribution of wind speed for the simulation case.
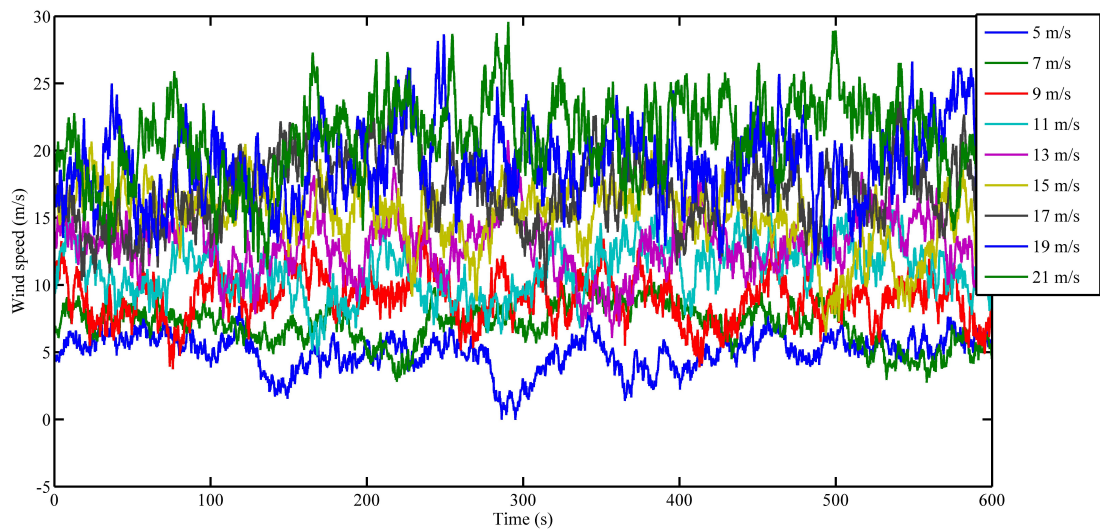
Figure 4.29 Simulated wind speed for different wind conditions.

life, 2.62 years. In next section, the fatigue life of different materials under wake conditions will be presented to show fatigue-induced fatigue damage.
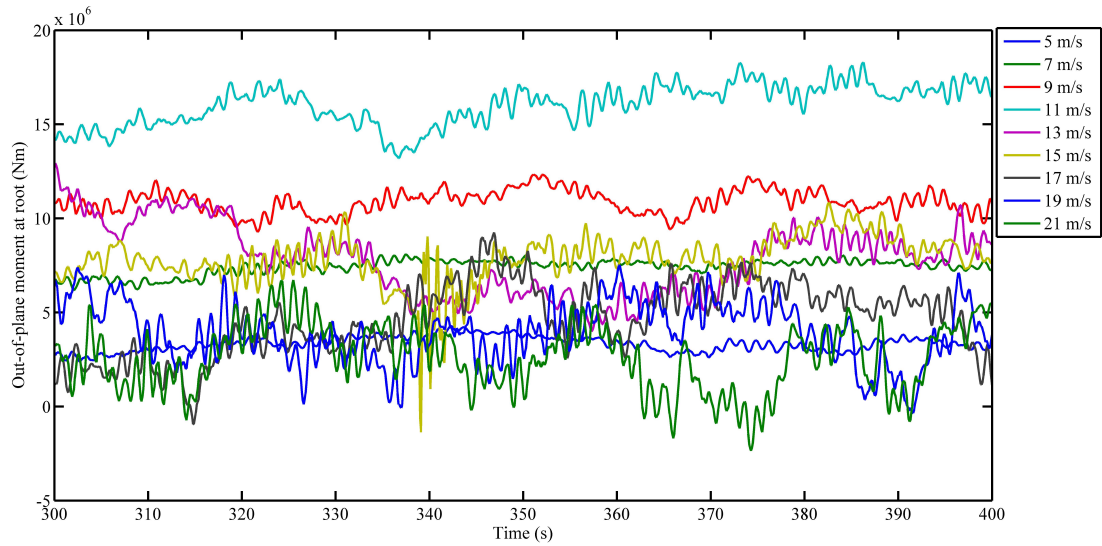
Figure 4.30 Simulated out-of-plane moments for different wind conditions.

Table 4.6 Parameters for the different wind speed range (from 3 m/s - 25 m/s).

Wind speed range (m/s)	Characteristic wind speed (m/s)	Rotational speed (rpm)	Pitch angle (^{o})	Turbulence intensity
3-5	5	5.31	0	0.262
5-7	7	7.43	0	0.217
7-9	9	9.55	0	0.192
9-11	11	12.1	0	0.176
11-13	13	12.1	6.60	0.165
13-15	15	12.1	10.45	0.157
15-17	17	12.1	13.54	0.151
17-19	19	12.1	16.23	0.146
19-21	21	12.1	18.70	0.142
21-23	23	12.1	21.18	0.139
23-25	25	12.1	23.47	0.136

Table 4.7 Calculated fatigue life for different materials under different wind speed conditions.

Wind speed range (m/s)	CUD (years)	EUD (years)	TRIAX (years)	BIAX (years)	Weights (Weibull)
3-5	1.5986e+9	53.9377	3.7694e+3	1.7199e+5	0.1377
5-7	2.2980e+7	31.1932	2.4859e+3	1.7459e+5	0.1717
7-9	4.3345e+4	17.1537	1.6062e+3	727.5506	0.1792
9-11	5.6153	9.8457	1.1439e+3	1.1046	0.1627
11-13	15.9887	24.0427	1.1897e+3	5.1545	0.1306
13-15	302.7857	30.9046	963.6181	0.4809	0.0935
15-17	125.8710	21.9941	433.0670	21.6409	0.0600
17-19	100.9939	18.0107	289.6136	7.8679	0.0346
19-21	115.6948	18.0496	208.3771	4.7127	0.0180
21-23	2.1208e+3	13.0352	213.2192	7.6625	0.0084
23-25	3.0045e+3	5.2837	124.6927	1.4742	0.0035

Table 4.8 Calculated fatigue life for different materials.

Wind speed range (m/s)	Fatigue life (years)
CUD	26.0187
EUD	19.8213
TRIAX	1.0219e+3
WEB	2.6190

4.8.3 Fatigue life analysis for wind turbine under wake condition and compact layout

In this subsection the wake effect will be considered. The fatigue life of turbine 8 (see Figure 4.23, 9 wind turbines in array) will be calculated. The turbulence intensity under wake conditions is calculated by Equation (4.48). The parameters are shown in Table 4.9. The simulated wind speed and root out-of-plane bending moments are shown in Figure 4.31 and 4.32 respectively. The calculated fatigue life for different materials under different wind conditions are shown in Table 4.10. By comparing Table 4.10 with Table 4.7 (no wake), the fatigue lives of different materials all decrease under wake condition. The calculated fatigue life for the main structure (CUD) is much lower (1.7388 years) in Table 4.11 than that of condition without wake effect (26.0187 years). The wake-induced fatigue is obvious. This also is because, in author's view, the layout is too compact. The lateral distance is 3D, and longitudinal distance is 5D. Normally, the lateral and longitudinal distances are at least 5D and 7D respectively. Next, the fatigue damage under normal layout will be analysed.
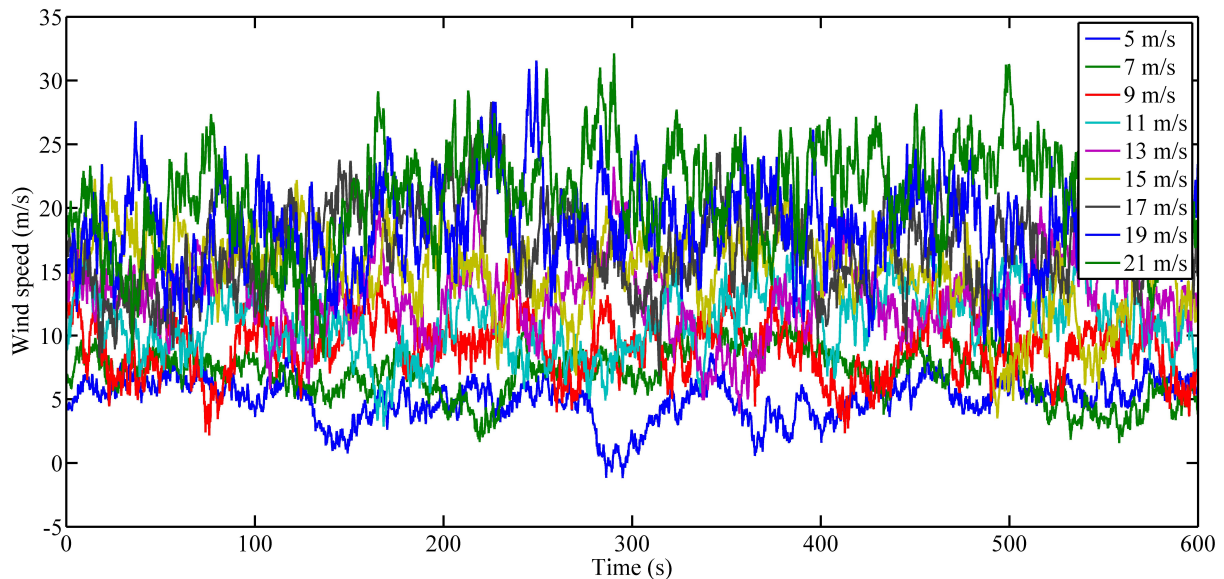
Figure 4.31 Simulated wind speed for wake conditions.
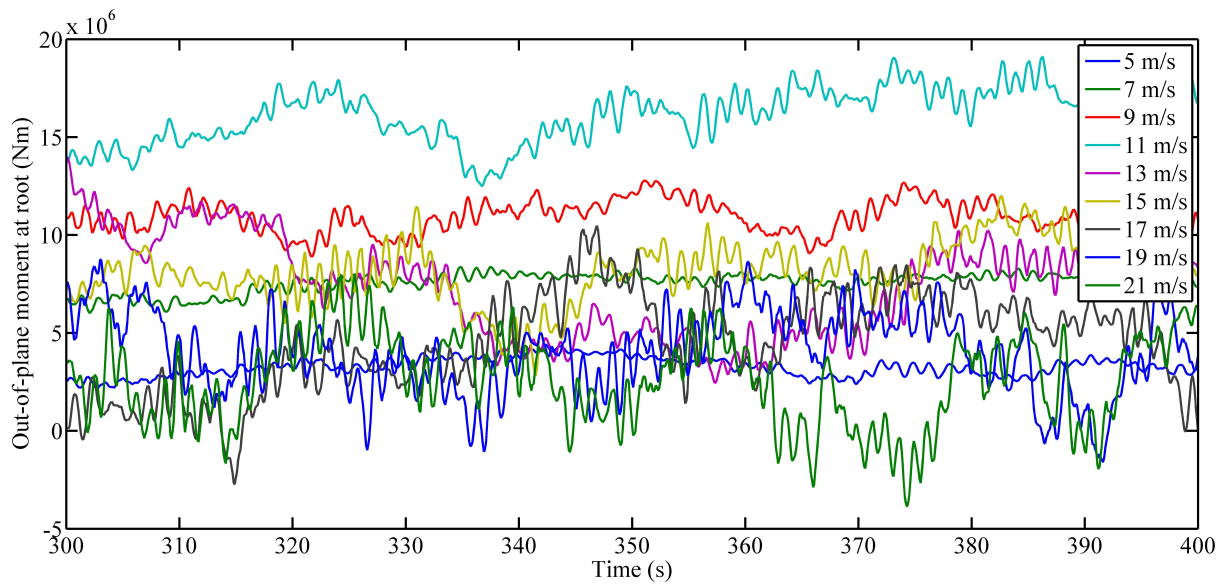
Figure 4.32 Simulated out-of-plane moments for wake conditions.

Table 4.9 Parameters for the different wind speed range (from 3 m/s - 25 m/s) under wake condition.

Wind speed range (m/s)	Characteristic wind speed (m/s)	Rotational speed (rpm)	Pitch angle (^{o})	Turbulence intensity
3-5	5	5.31	0	0.321
5-7	7	7.43	0	0.276
7-9	9	9.55	0	0.249
9-11	11	12.1	0	0.230
11-13	13	12.1	6.60	0.217
13-15	15	12.1	10.45	0.206
15-17	17	12.1	13.54	0.198
17-19	19	12.1	16.23	0.190
19-21	21	12.1	18.70	0.184
21-23	23	12.1	21.18	0.179
23-25	25	12.1	23.47	0.174

Table 4.10 Calculated fatigue life for different materials under wake conditions.

Wind speed range (m/s)	CUD (years)	EUD (years)	TRIAX (years)	BIAX (years)	Weights (Weibull)
3-5	6.7595e+8	53.4924	2.7273e+3	1.1202e+5	0.1377
5-7	6.1500e+6	31.1441	2.4572e+3	5.4080e+5	0.1717
7-9	6.5015e+3	16.6784	1.5444e+3	119.7997	0.1792
9-11	0.4827	9.4055	1.0728e+3	0.1476	0.1627
11-13	0.6079	20.0514	343.9903e+3	0.5905	0.1306
13-15	63.8614	25.5055	725.0841	1.0879	0.0935
15-17	5.1503	12.5421	132.5835	1.9407	0.0600
17-19	4.5651	10.0683	91.6298	1.0541	0.0346
19-21	4.4335	10.6346	34.5358	0.7288	0.0180
21-23	87.8126	6.1392	64.8479	1.2029	0.0084
23-25	168.3429	2.0313	37.2014	0.2011	0.0035

Table 4.11 Calculated fatigue life for different materials.

Wind speed range (m/s)	Fatigue life (years)
CUD	1.7388
EUD	16.8524
TRIAX	406.6164
WEB	0.6563

4.8.4 Fatigue life analysis for wind turbine under wake conditions and normal layout

In this section, the fatigue lives for wind turbines under wake conditions and normal wind farm layout (9 wind turbines in array, 5D for lateral distance and 7D for longitudinal distance) are calculated. The parameters for different wind speed conditions are shown in Table 4.12. The simulated wind speeds and out-of-plane root bending moments are illustrated in figures 4.33 and 4.34. The fatigue analysis results are shown in Tables 4.13 and 4.14. When compared these two tables with the Table 4.7 (no wake), it can be seen that the wake effect is still very significant to the fatigue life of wind turbine blade. The fatigue life of spar caps (main structure) drops from 26.0187 years to 6.9084 years. Although some less dominant factors are not considered in this case, i.e. non-uniform wind directions, it still can be concluded that the wake-induced fatigue has an large impact on the fatigue life of wind turbine blade. Compared the results in Table 4.14 with that in Table 4.11 (compact layout), the fatigue life increases from 1.7388 years to 6.9084 years. It can be concluded that the layout of wind turbine also has a impact on the fatigue damage of wind turbine blades. Next the performance of BTC blade with 15° fibre orientation on the carbon fibre composite in the spar caps in the previous section is studied (for WT8). The fatigue lives of different materials in BTC wind turbine blade are shown in Table 4.15 and 4.16. The fatigue damage is alleviated by introducing the bend-twist coupling effect. Comparing the fatigue life of carbon fibre composite in BTC blade with that of normal wind turbine blade under wake condition, it can be found that the total fatigue life of carbon fibre composite increases from 6.9084 years to 6.9532 years. It should be mentioned here that the BTC design in this thesis (introduce constant 15° offset on spar cap) is not optimal design for this wind turbine blade, which can be seen in Figure 4.6 that the coupling coefficients are not very high. But the fatigue load alleviation effect is still obvious in some wind speed range, e.g. 11-15 m/s.
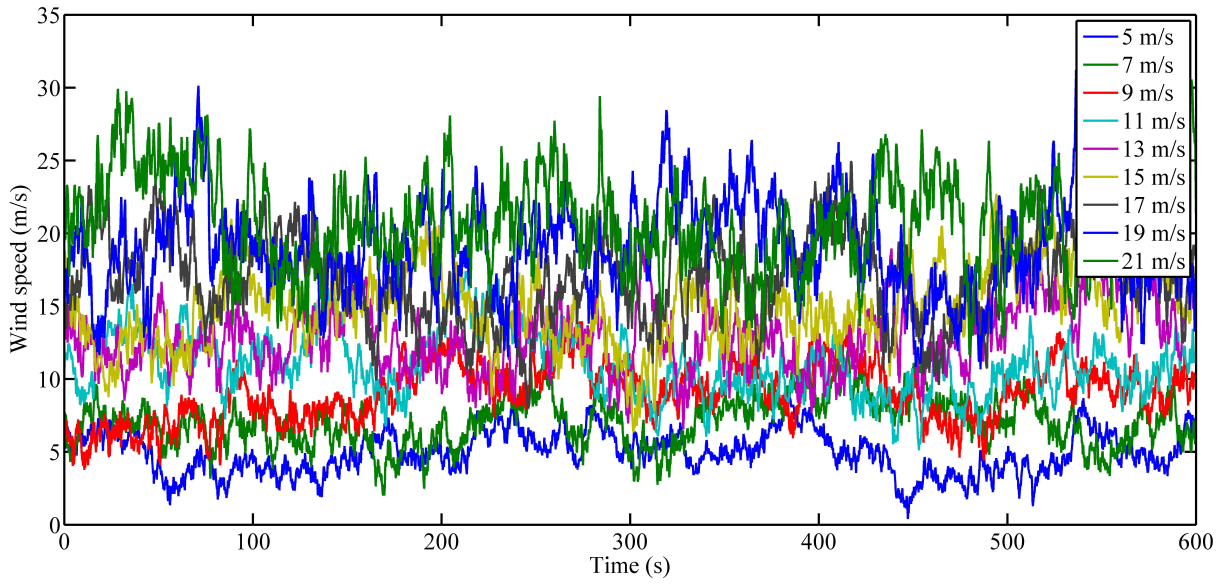
Figure 4.33 Simulated wind speed for wake conditions and normal layout.
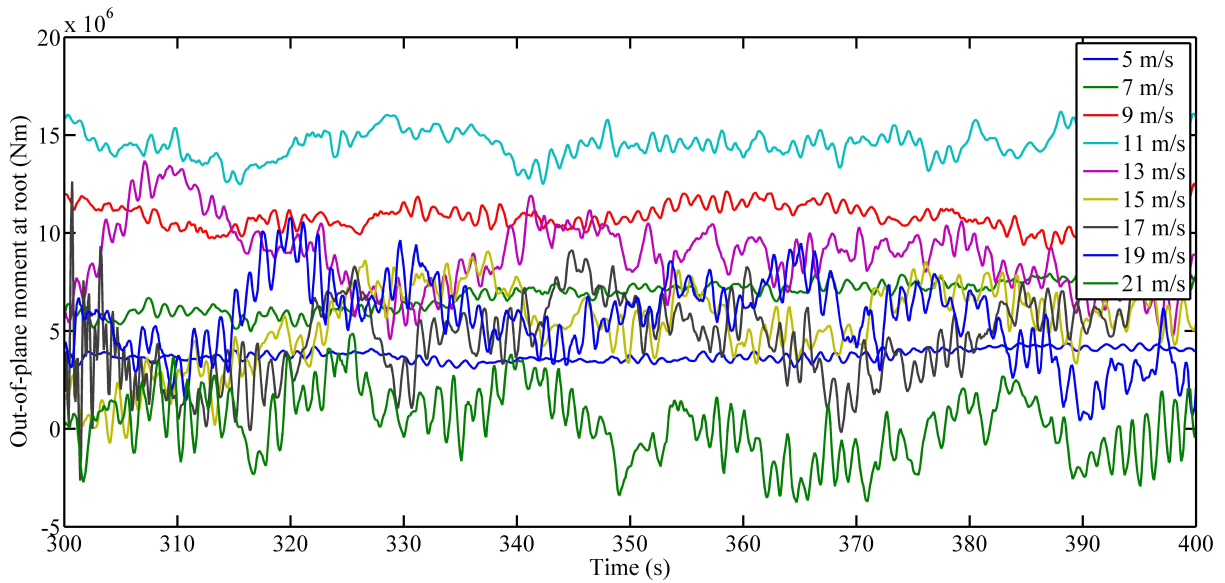
Figure 4.34 Simulated out-of-plane moments for wake conditions and normal layout.

126

Table 4.12 Parameters for the different wind speed range (from 3 m/s - 25 m/s) under wake conditions and normal layout.

Wind speed range (m/s)	Characteristic wind speed (m/s)	Rotational speed (rpm)	Pitch angle (^{o})	Turbulence intensity
3-5	5	5.31	0	0.2911
5-7	7	7.43	0	0.2450
7-9	9	9.55	0	0.2183
9-11	11	12.1	0	0.2006
11-13	13	12.1	6.60	0.1879
13-15	15	12.1	10.45	0.1784
15-17	17	12.1	13.54	0.1710
17-19	19	12.1	16.23	0.1648
19-21	21	12.1	18.70	0.1596
21-23	23	12.1	21.18	0.1556
23-25	25	12.1	23.47	0.1517

Table 4.13 Calculated fatigue life for different materials under wake conditions and normal layout.

Wind speed range (m/s)	CUD (years)	EUD (years)	TRIAX (years)	BIAX (years)	Weights (Weibull)
3-5	2.0312e+9	51.0607	3.5647e+3	1.9869e+5	0.1377
5-7	9.9102e+6	30.8361	2.4187e+3	9.1604e+4	0.1717
7-9	2.8041e+4	17.1227	1.5980e+3	739.0295	0.1792
9-11	1.2108	9.6709	1.1171e+3	0.3079	0.1627
11-13	21.0242	22.4947	1.0453e+3	2.7883	0.1306
13-15	39.9979	25.9339	697.1048	4.9734	0.0935
15-17	143.2279	25.5949	530.6142	3.2463	0.0600
17-19	44.4458	15.2231	219.5617	2.3996	0.0346
19-21	229.5693	11.9032	247.8988	7.3153	0.0180
21-23	88.3748	8.7207	118.7112	2.2269	0.0084
23-25	7.6653	4.1704	34.3980	1.1356	0.0035

Table 4.14 Calculated fatigue life for different materials for normal layout.

Wind speed range (m/s)	Fatigue life (years)
CUD	6.9084
EUD	18.7893
TRIAX	874.4315
WEB	1.5712

Table 4.15 Calculated fatigue life for different materials under wake conditions for BTC blade.

Wind speed range (m/s)	CUD (years)	EUD (years)	TRIAX (years)	BIAX (years)	Weights (Weibull)
3-5	2.7593e+9	54.9027	3.8601e+3	2.3339e+5	0.1377
5-7	1.4935e+7	29.0696	2.3079e+3	9.3524e+4	0.1717
7-9	2.7796e+4	16.5784	1.5452e+3	834.5782	0.1792
9-11	1.1838	9.5579	1.1099e+3	0.3079	0.3466
11-13	42.1325	22.2240	1.0443e+3	2.7883	3.8398
13-15	45.3534	21.2948	575.2739	4.9734	6.1749
15-17	507.0271	17.5519	385.7082	3.2463	3.4022
17-19	104.3946	13.8084	192.5606	2.3996	12.2359
19-21	359.1663	8.7844	178.3102	7.3153	9.8222
21-23	69.3830	4.8082	62.2503	2.2269	1.4874
23-25	5.8628	2.4603	20.5534	1.1356	0.6109

Table 4.16 Calculated fatigue life for different materials for BTC blade.

Wind speed range (m/s)	Fatigue life (years)
CUD	6.9532
EUD	17.3377
TRIAX	712.3523
WEB	1.8097

4.9 Chapter summary

In this chapter, the fatigue analysis methodology for different materials of wind turbine blade is proposed. To fill the gap between the loading time series and the stress (or strain) of materials, the cross sectional analysis method BECAS is employed. The loading time series is simulated by the aero-elastic model, which is the coupled model of aerodynamic model and anisotropic wind turbine blade structure model. The anisotropic structure, i.e. bendtwist coupling wind turbine blade, is studied in this chapter in terms of modal analysis, static analysis, and fatigue analysis. From the case studies, it can be found that the wake effect has a significant impact on the fatigue life of wind turbine blade, which can be affected by the layout of wind turbines. The wake effect can be alleviated by introducing bendtwist coupling in wind turbine blade.

In this chapter, the structure model is based on the FEM formulation. To improve the structure model in elastic actuator line, the FDTD anisotropic beam model (FDM based method) for wind turbine blade will be constructed and validated.

Chapter 5

Anisotropic wind turbine blade modelling by using FDTD method

In the previous chapter, the FEM model is employed for the structure modelling. In this chapter, a novel structure model for an anisotropic wind turbine blade structure is proposed based on the Newtonian method and finite-difference time-domain method (FDTD). The proposed structure model will be verified and validated by three cases. It should be mentioned here that the proposed explicit FDTD model is the general formulation of the structure model of the verified explicit elastic actuator line in Chapter 3. The stability analysis for the proposed FDTD model is also carried out to uncover the root cause of the instability of the explicit FDTD method. Based on this analysis, the unconditionally stable explicit FDTD model is proposed to overcome its limitations on time step with little effect on its solution accuracy.

5.1   Governing equations of anisotropic wind turbine blade

The theoretical equations of an anisotropic beam includes two parts. The first part is the equilibrium equations of the deformed beam element. The second part is the constitutive equations, which depict the constitutive relation between the sectional moments (and forces) and the sectional strains (curvatures and angles of rotation). The equilibrium equations can be either derived by the Newtonian method or the energy method (such as variational method). In this research, the former one is employed. The Newtonian method is based on the force and moment balance of each beam element. The coordinate system (inertia frame) of the beam element is shown in Figure 5.1. In this coordinate system, the $\mathbf{r}$ direction is the longitudinal direction or span-wise direction. Equation (5.1) shows the aforementioned equilibrium equations. In this equation, $\mathbf{M}$ and $\mathbf{F}$ are sectional moments and forces respectively. $\mathbf{F}_e$ and $\mathbf{M}_e$ are the external force and moment vectors. $\mathbf{F}_{B'}$ is the

sectional force vector of the section B' for the deformed beam element. $d\mathbf{r}_l$ is the differential vector of the deformed beam element. In previous ad hoc beam models, $d\mathbf{r}_l$ is assumed to be equal to $d\mathbf{r}$. This small deflection assumption will eliminate the non-linearity of the equations for simplicity. It should be noted here that this assumption is dropped in this research, which means that the present model can consider large deflection effect. Naturally, the present anisotropic beam model is non-linear. The derivation of the proposed model is shown in Appendix E.
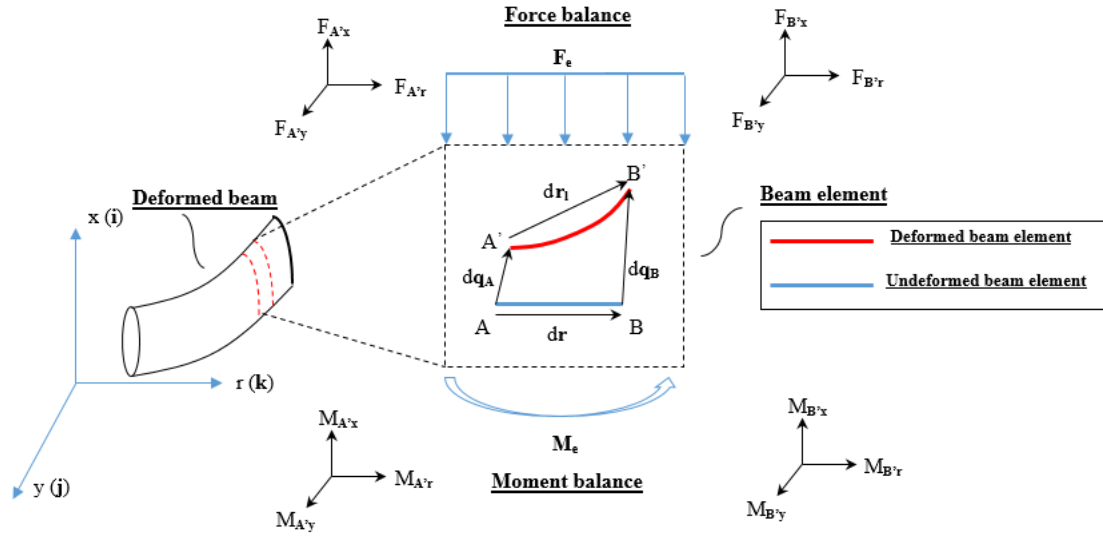
Figure 5.1 Coordinate system of the beam element.

$$\begin{cases} d\mathbf{M} + d\mathbf{r}_l \times \mathbf{F}_{B'} + \mathbf{M}_e = 0 & \text{moment balance} \\ d\mathbf{F} + \mathbf{F}_e = 0 & \text{force balance} \end{cases} \tag{5.1}$$

To illustrate the non-linearity of the present equations, we expand the previous equilibrium equations by introducing the following definition of several vectors and inertia forces under the inertia frame:

$$\mathbf{F} = \begin{bmatrix} F_x & F_y & F_r \end{bmatrix}^T \tag{5.2}$$

$$\mathbf{M} = \begin{bmatrix} M_x & M_y & M_r \end{bmatrix}^T \tag{5.3}$$

$$\mathbf{q} = \begin{bmatrix} q_x & q_y & q_r \end{bmatrix}^T \tag{5.4}$$

$$\mathbf{M}_e = \mathbf{M}_{ei} + \mathbf{M}_{el} \tag{5.5}$$

$$\mathbf{F}_e = \mathbf{F}_{ei} + \mathbf{F}_{el} \tag{5.6}$$

It should be mentioned here that there are still terms of nonlinearity are not considered in the proposed model, e.g. geometric nonlinearity.

$\mathbf{F}_{ei}$ and $\mathbf{M}_{ei}$ are the inertia force and moment vectors of the inertia frame. $\mathbf{F}_{el}$ and $\mathbf{M}_{el}$ are other external forces except for inertia force and moment, e.g. aerodynamic force. By using these definitions, the expanded governing equations can be derived as shown in the following equations.

$$\rho_s \frac{\partial^2 q_x}{\partial t^2} - \rho_s y_m \frac{\partial^2 \varphi_r}{\partial t^2} = \frac{\partial F_x}{\partial r} + F_{el,x} \tag{5.7}$$

$$\rho_s \frac{\partial^2 q_y}{\partial t^2} + \rho_s x_m \frac{\partial^2 \varphi_r}{\partial t^2} = \frac{\partial F_y}{\partial r} + F_{el,y} \tag{5.8}$$

$$\rho_s \frac{\partial^2 q_r}{\partial t^2} + \rho_s y_m \frac{\partial^2 \varphi_x}{\partial t^2} - \rho_s x_m \frac{\partial^2 \varphi_y}{\partial t^2} = \frac{\partial F_r}{\partial r} + F_{el,r} \tag{5.9}$$

$$\rho_s y_m \frac{\partial^2 q_r}{\partial t^2} + I_{xx} \frac{\partial^2 \varphi_x}{\partial t^2} - I_{xy} \frac{\partial^2 \varphi_y}{\partial t^2} = \frac{\partial M_x}{\partial r} + F_r \frac{\partial q_y}{\partial r} - F_y \frac{\partial q_r}{\partial r} - F_y + M_{el,x} \tag{5.10}$$

$$-\rho_s x_m \frac{\partial^2 q_r}{\partial t^2} - I_{xy} \frac{\partial^2 \varphi_x}{\partial t^2} + I_{yy} \frac{\partial^2 \varphi_y}{\partial t^2} = \frac{\partial M_y}{\partial r} - F_r \frac{\partial q_x}{\partial r} + F_x \frac{\partial q_r}{\partial r} + F_x + M_{el,y} \tag{5.11}$$

$$-\rho_s y_m \frac{\partial^2 q_x}{\partial t^2} + \rho_s x_m \frac{\partial^2 q_y}{\partial t^2} + (I_{xx} + I_{yy}) \frac{\partial^2 \varphi_r}{\partial t^2} = \frac{\partial M_r}{\partial r} + F_y \frac{\partial q_x}{\partial r} - F_x \frac{\partial q_y}{\partial r} + M_{el,r} \tag{5.12}$$

In Equations (5.10) - (5.12), it can be seen that the nonlinear terms occurs on the right hand side (such as $F_r \frac{\partial q_y}{\partial r}$ in Equation (5.10)). In the above equations, φ represents the angle of rotation. (x_m, y_m) is the position of the gravity center of the cross section (or beam element). The parameters of the cross section, namely ρ_s and I, are the mass per unit length and moments of inertia of beam element, which can be calculated by the following Equation (5.13):

$$\begin{bmatrix} \rho_s & 0 & 0 \\ 0 & I_{xx} & I_{xy} \\ 0 & 0 & I_{yy} \end{bmatrix} = \int_A \begin{bmatrix} 1 & 0 & 0 \\ 0 & y^2 & xy \\ 0 & 0 & x^2 \end{bmatrix} \rho(x, y) dA \tag{5.13}$$

In the above 6 equilibrium equations (Equations (5.7) - (5.12)), we have 12 unknowns. As a result, additional 6 equations are required, which are exactly the aforementioned constitutive equations. In the ad hoc beam models, such as Euler-Bernoulli beam model or Timoshenko beam model, the constitutive equations are derived by the analytical kinematics analysis of the beam section. By substituting the prescribed displacement fields into the strain-displacement relation and employing Hooke's law, the constitutive relation between the sectional forces and sectional strain parameters (such as curvatures) can be constructed. In fact, these ad hoc beam models are still popular in today's wind turbine blade structural models for their simplicity. Nevertheless, the prescribed displacement fields restrict their applications in the anisotropic beam cases, especially for BTC blade, because the displacement fields of anisotropic beam are much more complicated as mentioned in the introduction. To overcome this limitation, researchers recently proposed the linear sectional analysis method (FEM analysis) to construct the generalized constitutive relation. The linear sectional analysis can be carried out by employing the software, such as VABS or DTU BECAS. The generalized constitutive equations in this research are shown below. The matrix K in Equation (5.14) can be calculated by using VABS or BECAS [86]. It should be noticed here that the matrix of K will be diagonal if the beam is isotropic. Therefore, the anisotropic beam modelling is obviously more complicated than that of isotropic beam.

$$
\begin{bmatrix} F_x \\ F_y \\ F_r \\ M_x \\ M_y \\ M_r \end{bmatrix} = \begin{bmatrix} K_{11} & K_{12} & K_{13} & K_{14} & K_{15} & K_{16} \\ K_{21} & K_{22} & K_{23} & K_{24} & K_{25} & K_{26} \\ K_{31} & K_{32} & K_{33} & K_{34} & K_{35} & K_{36} \\ K_{41} & K_{42} & K_{43} & K_{44} & K_{45} & K_{46} \\ K_{51} & K_{52} & K_{53} & K_{54} & K_{55} & K_{56} \\ K_{61} & K_{62} & K_{63} & K_{64} & K_{65} & K_{66} \end{bmatrix} \begin{bmatrix} \frac{\partial q_x}{\partial r} - \varphi_y \\ \frac{\partial q_y}{\partial r} + \varphi_x \\ \frac{\partial q_r}{\partial r} \\ \frac{\partial \varphi_x}{\partial r} \\ \frac{\partial \varphi_y}{\partial r} \\ \frac{\partial \varphi_r}{\partial r} \end{bmatrix} \tag{5.14}
$$

Until now, the governing equations of non-linear anisotropic beam for wind turbine blade are derived, including Equations (5.7) - (5.12) and Equation (5.14). In previous research, the next step is to substitute the constitutive equations (Equation (5.14)) into equilibrium equations (Equations (5.7) - (5.12)) to construct a system in which displacements (and angles of rotation) are dependent variables. Then equations of local elements will be assembled together into global system and solved simultaneously by numerical methods. Obviously, this process will lead to high order of derivatives with respect to both time and space, which complicates the discretization and the construction of boundary conditions for finite difference (or finite volume) methods. In the author's opinion, this is the main reason why finite-difference method is not popular in the structural modelling of a wind turbine blade. In fact, the structural model of the wind turbine blade is 1D beam model, which means that the mesh of the blade is one dimensional. For this 1D beam problem, finite difference method has several obvious advantages, such as the intuitive and simple discretization. In addition, the stability analysis of the numerical model is much more straight forward,

which is important for the further application of the model. In this research, to apply the finite difference method to the anisotropic beam model, the equations are manipulated into two new sets of equations instead of merging them together. Rather than solving system simultaneously, these two sets of equations are solved element by element alternately and explicitly, which boosts the efficiency of the simulation. The manipulation is shown in the following part of this section.

Firstly, for the equilibrium equations (Equations (5.7) - (5.12)), 9 variables are introduced, which are shown in Equation (5.15) - (5.17).

$$V_x = \frac{\partial q_x}{\partial t} \qquad V_y = \frac{\partial q_y}{\partial t} \qquad V_r = \frac{\partial q_r}{\partial t} \tag{5.15}$$

$$\omega_x = \frac{\partial \varphi_x}{\partial t} \qquad \omega_y = \frac{\partial \varphi_y}{\partial t} \qquad \omega_r = \frac{\partial \varphi_r}{\partial t} \tag{5.16}$$

$$S_x = \frac{\partial q_x}{\partial r} \qquad S_y = \frac{\partial q_y}{\partial r} \qquad S_r = \frac{\partial q_r}{\partial r} \tag{5.17}$$

Obviously, V and ω are velocity and angular velocity of the beam element respectively. S is the first order spatial derivative of displacement with respect to r. After substituting these newly defined variables into equilibrium equations, the original equilibrium equations are transformed into a new formulation with lower-order time and spatial derivatives:

$$\rho_s \frac{\partial V_x}{\partial t} - \rho_s y_m \frac{\partial \omega_r}{\partial t} = \frac{\partial F_x}{\partial r} + F_{el,x} \tag{5.18}$$

$$\rho_s \frac{\partial V_y}{\partial t} + \rho_s x_m \frac{\partial \omega_r}{\partial t} = \frac{\partial F_y}{\partial r} + F_{el,y} \tag{5.19}$$

$$\rho_s \frac{\partial V_r}{\partial t} + \rho_s y_m \frac{\partial \omega_x}{\partial t} - \rho_s x_m \frac{\partial \omega_y}{\partial t} = \frac{\partial F_r}{\partial r} + F_{el,r} \tag{5.20}$$

$$\rho_s y_m \frac{\partial V_r}{\partial t} + I_{xx} \frac{\partial \omega_x}{\partial t} - I_{xy} \frac{\partial \omega_y}{\partial t} = \frac{\partial M_x}{\partial r} + F_r S_y - F_y S_r - F_y + M_{el,x} \tag{5.21}$$

$$- \rho_s x_m \frac{\partial V_r}{\partial t} - I_{xy} \frac{\partial \omega_x}{\partial t} + I_{yy} \frac{\partial \omega_y}{\partial t} = \frac{\partial M_y}{\partial r} - F_r S_x + F_x S_r + F_x + M_{el,y} \tag{5.22}$$

$$- \rho_s y_m \frac{\partial V_x}{\partial t} + \rho_s x_m \frac{\partial V_y}{\partial t} + (I_{xx} + I_{yy}) \frac{\partial \omega_r}{\partial t} = \frac{\partial M_r}{\partial r} + F_y S_x - F_x S_y + M_{el,r} \tag{5.23}$$

135

Secondly, for the constitutive equations (Equation (5.14)) and Equation (5.17), we take the first order derivative with respect to time.

$$\frac{\partial S_x}{\partial t} = \frac{\partial V_x}{\partial r} \qquad \frac{\partial S_y}{\partial t} = \frac{\partial V_y}{\partial r} \qquad \frac{\partial S_r}{\partial t} = \frac{\partial V_r}{\partial r} \tag{5.24}$$

$$\begin{bmatrix} \frac{\partial F_x}{\partial t} \\ \frac{\partial F_y}{\partial t} \\ \frac{\partial F_r}{\partial t} \\ \frac{\partial M_x}{\partial t} \\ \frac{\partial M_y}{\partial t} \\ \frac{\partial M_r}{\partial t} \end{bmatrix} = \begin{bmatrix} K_{11} & K_{12} & K_{13} & K_{14} & K_{15} & K_{16} \\ K_{21} & K_{22} & K_{23} & K_{24} & K_{25} & K_{26} \\ K_{31} & K_{32} & K_{33} & K_{34} & K_{35} & K_{36} \\ K_{41} & K_{42} & K_{43} & K_{44} & K_{45} & K_{46} \\ K_{51} & K_{52} & K_{53} & K_{54} & K_{55} & K_{56} \\ K_{61} & K_{62} & K_{63} & K_{64} & K_{65} & K_{66} \end{bmatrix} \begin{bmatrix} \frac{\partial V_x}{\partial r} - \omega_y \\ \frac{\partial V_y}{dr} + \omega_x \\ \frac{\partial V_r}{\partial r} \\ \frac{\partial \omega_x}{\partial r} \\ \frac{\partial \omega_y}{\partial r} \\ \frac{\partial \omega_r}{\partial r} \end{bmatrix} \tag{5.25}$$

Equations (5.18) - (5.25) are our newly derived governing equations to solve. As is mentioned, there are two sets of equations. The first set of equations includes Equations (5.18) - (5.23). In these equations, the left hand side is about the first order time derivatives of V and ω. The right hand side is about the first order spatial derivatives of S, F, and M. Interestingly, this situation is exactly opposite in the other set of equations (Equations (5.24) - (5.25)). In other words, the spatial derivatives of V and ω lead to the change of S, F, and M in the time domain, and vice versa. This is very similar to the Maxwell equations, in which the spatial derivatives of electric field induces the change of magnetic field in the time domain and vice versa. It can be imagined that there exist two sets of waves in the blade structure, which are waves of forces and velocities. These two waves excite each other to maintain the vibration of the blade structure. This similarity inspired the authors to apply the computational electromagnetics method to solve the aforementioned anisotropic beam model, which is the novelty of this research.

5.2 Explicit FDTD anisotropic wind turbine blade model

In this section, the finite-difference time-domain (FDTD) method is applied to discretize and numerically solve the above governing equations. Three important features of the FDTD method are inherited by the numerical model in this research. The first feature is the central difference scheme in time, which guarantees the second order time accuracy. The second feature is the staggered grid for two sets of variables, which represents the waves of forces and velocities as mentioned above. This staggered grid arrangement is also known as the Yee lattice, which is shown in the Figure 5.2. This guarantees the second order spatial accuracy of the numerical model. Noticeably, to achieve the same level spatial and time accuracy in the FEM model, in which displacements are dependent variables, at least a fourth order scheme in space (to calculate moments) and a third order scheme in time (to

calculate velocities) should be used. Taking advantages of the newly introduced two sets of variables and the leapfrog manner, the FDTD method makes the discretization of the current model simpler. The numerical model is shown below. Equations (5.18) - (5.25) are discretized to be Equations (5.26) - (5.33). In addition, since the wind turbine blade is a cantilever beam, the boundary condition at the free end is Neumann boundary condition (no moments and forces at the end) for conventional FEM models, in which displacements are dependent variables. In the proposed model, the Neumann boundary condition turns out to be Dirichlet boundary condition, which is simpler and can be seen in the Figure 5.2. The third feature is that the two sets of equations are solved element by element alternately and explicitly instead of solving the equations simultaneously. This feature makes the simulation of this model more efficient. The solving process of FDTD is shown in Figure 5.3. Firstly, variables $\mathbf{V}$ and ω are calculated at time $n + \frac{1}{2}$ by variables $\mathbf{F}$, $\mathbf{M}$, and $\mathbf{S}$ at time n according to the Equations (5.26) - (5.31). Secondly, the variables $\mathbf{F}$, $\mathbf{M}$, and $\mathbf{S}$ at time $n + 1$ are predicted by the calculated variables $\mathbf{V}$ and φ at time $n + \frac{1}{2}$ according to Equations (5.32) - (5.33). This process is repeated by marching in time (see Figure 5.3).
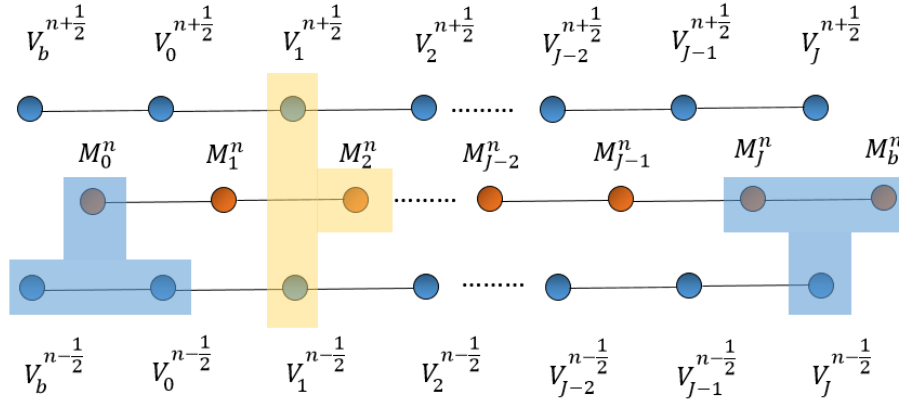
Figure 5.2 Computational grid in time and space (Yee lattice).

$$\rho_{s,j} \frac{V_{x,j}^{n+\frac{1}{2}} - V_{x,j}^{n-\frac{1}{2}}}{\Delta t} - \rho_{s,j} y_{m,j} \frac{\omega_{r,j}^{n+\frac{1}{2}} - \omega_{r,j}^{n-\frac{1}{2}}}{\Delta t} = \frac{F_{x,j+1}^{n} - F_{x,j}^{n}}{\Delta r} + F_{e,lx,j}^{n} \qquad (5.26)$$

$$\rho_{s,j} \frac{V_{y,j}^{n+\frac{1}{2}} - V_{y,j}^{n-\frac{1}{2}}}{\Delta t} + \rho_{s,j} x_{m,j} \frac{\omega_{r,j}^{n+\frac{1}{2}} - \omega_{r,j}^{n-\frac{1}{2}}}{\Delta t} = \frac{F_{y,j+1}^{n} - F_{y,j}^{n}}{\Delta r} + F_{e,ly,j}^{n} \qquad (5.27)$$

$$\rho_{s,j} \frac{V_{r,j}^{n+\frac{1}{2}} - V_{r,j}^{n-\frac{1}{2}}}{\Delta t} + \rho_{s,j} y_{m,j} \frac{\omega_{x,j}^{n+\frac{1}{2}} - \omega_{x,j}^{n-\frac{1}{2}}}{\Delta t} - \rho_{s,j} x_{m,j} \frac{\omega_{y,j}^{n+\frac{1}{2}} - \omega_{y,j}^{n-\frac{1}{2}}}{\Delta t} = \frac{F_{r,j+1}^{n} - F_{r,j}^{n}}{\Delta r} + F_{e,lr,j}^{n}$$
$$(5.28)$$

$$\rho_{s,j} y_{m,j} \frac{V_{r,j}^{n+\frac{1}{2}} - V_{r,j}^{n-\frac{1}{2}}}{\Delta t} + I_{xx,j} \frac{\omega_{x,j}^{n+\frac{1}{2}} - \omega_{x,j}^{n-\frac{1}{2}}}{\Delta t} - I_{xy,j} \frac{\omega_{y,j}^{n+\frac{1}{2}} - \omega_{y,j}^{n-\frac{1}{2}}}{\Delta t} = \frac{M_{x,j+1}^n - M_{x,j}^n}{\Delta r}$$
$$+ \frac{F_{r,j+1}^n + F_{r,j}^n}{2} \frac{S_{y,j+1}^n + S_{y,j}^n}{2} - \frac{F_{y,j+1}^n + F_{y,j}^n}{2} \frac{S_{r,j+1}^n + S_{r,j}^n}{2} - \frac{F_{y,j+1}^n + F_{y,j}^n}{2} + M_{e,lx,j}^n \tag{5.29}$$

$$-\rho_{s,j} x_{m,j} \frac{V_{r,j}^{n+\frac{1}{2}} - V_{r,j}^{n-\frac{1}{2}}}{\Delta t} - I_{xy,j} \frac{\omega_{x,j}^{n+\frac{1}{2}} - \omega_{x,j}^{n-\frac{1}{2}}}{\Delta t} + I_{yy,j} \frac{\omega_{y,j}^{n+\frac{1}{2}} - \omega_{y,j}^{n-\frac{1}{2}}}{\Delta t} = \frac{M_{y,j+1}^n - M_{y,j}^n}{\Delta r}$$
$$- \frac{F_{r,j+1}^n + F_{r,j}^n}{2} \frac{S_{x,j+1}^n + S_{x,j}^n}{2} + \frac{F_{x,j+1}^n + F_{x,j}^n}{2} \frac{S_{r,j+1}^n + S_{r,j}^n}{2} + \frac{F_{x,j+1}^n + F_{x,j}^n}{2} + M_{e,ly,j}^n \tag{5.30}$$

$$-\rho_{s,j} y_{m,j} \frac{V_{x,j}^{n+\frac{1}{2}} - V_{x,j}^{n-\frac{1}{2}}}{\Delta t} + \rho_{s,j} x_{m,j} \frac{V_{y,j}^{n+\frac{1}{2}} - V_{y,j}^{n-\frac{1}{2}}}{\Delta t} + (I_{xx,j} + I_{yy,j}) \frac{\omega_{r,j}^{n+\frac{1}{2}} - \omega_{r,j}^{n-\frac{1}{2}}}{\Delta t} =$$
$$\frac{M_{r,j+1}^n - M_{r,j}^n}{\Delta r} + \frac{F_{y,j+1}^n + F_{y,j}^n}{2} \frac{S_{x,j+1}^n + S_{x,j}^n}{2} - \frac{F_{x,j+1}^n + F_{x,j}^n}{2} \frac{S_{y,j+1}^n + S_{y,j}^n}{2} + M_{e,lr,j}^n \tag{5.31}$$

$$\begin{bmatrix} \frac{F_{x,j}^{n+1} - F_{x,j}^n}{\Delta t} \\ \frac{F_{y,j}^{n+1} - F_{y,j}^n}{\Delta t} \\ \frac{F_{r,j}^{n+1} - F_{r,j}^n}{\Delta t} \\ \frac{M_{x,j}^{n+1} - M_{x,j}^n}{\Delta t} \\ \frac{M_{y,j}^{n+1} - M_{y,j}^n}{\Delta t} \\ \frac{M_{r,j}^{n+1} - M_{r,j}^n}{\Delta t} \end{bmatrix} = \begin{bmatrix} K_{11} & K_{12} & K_{13} & K_{14} & K_{15} & K_{16} \\ K_{21} & K_{22} & K_{23} & K_{24} & K_{25} & K_{26} \\ K_{31} & K_{32} & K_{33} & K_{34} & K_{35} & K_{36} \\ K_{41} & K_{42} & K_{43} & K_{44} & K_{45} & K_{46} \\ K_{51} & K_{52} & K_{53} & K_{54} & K_{55} & K_{56} \\ K_{61} & K_{62} & K_{63} & K_{64} & K_{65} & K_{66} \end{bmatrix} \begin{bmatrix} \frac{V_{x,j}^{n+\frac{1}{2}} - V_{x,j-1}^{n+\frac{1}{2}}}{\Delta r} - \frac{\omega_{y,j}^{n+\frac{1}{2}} + \omega_{y,j-1}^{n+\frac{1}{2}}}{2} \\ \frac{V_{y,j}^{n+\frac{1}{2}} - V_{y,j-1}^{n+\frac{1}{2}}}{\Delta r} - \frac{\omega_{x,j}^{n+\frac{1}{2}} + \omega_{x,j-1}^{n+\frac{1}{2}}}{2} \\ \frac{V_{r,j}^{n+\frac{1}{2}} - V_{r,j-1}^{n+\frac{1}{2}}}{\Delta r} \\ \frac{\omega_{x,j}^{n+\frac{1}{2}} - \omega_{x,j-1}^{n+\frac{1}{2}}}{\Delta r} \\ \frac{\omega_{y,j}^{n+\frac{1}{2}} - \omega_{y,j-1}^{n+\frac{1}{2}}}{\Delta r} \\ \frac{\omega_{r,j}^{n+\frac{1}{2}} - \omega_{r,j-1}^{n+\frac{1}{2}}}{\Delta r} \end{bmatrix} \tag{5.32}$$

$$\frac{S_{x,j}^{n+1} - S_{x,j}^n}{\Delta t} = \frac{V_{x,j+1}^{n+\frac{1}{2}} - V_{x,j}^{n+\frac{1}{2}}}{\Delta r} \qquad \frac{S_{y,j}^{n+1} - S_{y,j}^n}{\Delta t} = \frac{V_{y,j+1}^{n+\frac{1}{2}} - V_{y,j}^{n+\frac{1}{2}}}{\Delta r} \qquad \frac{S_{r,j}^{n+1} - S_{r,j}^n}{\Delta t} = \frac{V_{r,j+1}^{n+\frac{1}{2}} - V_{r,j}^{n+\frac{1}{2}}}{\Delta r}$$
$$\tag{5.33}$$

In this section, the theoretical and numerical models of anisotropic wind turbine blade have been constructed based on the Newtonian method and the FDTD method. The application of the proposed model is also an important part of our research. Since the proposed method is very different from the conventional FEM model, it is necessary to derive and show how to apply the proposed model in different application cases; for example the

Initialization of
$V_{x,j}^{-\frac{1}{2}}$, $V_{y,j}^{-\frac{1}{2}}$, $V_{r,j}^{-\frac{1}{2}}$, $\varphi_{x,j}^{-\frac{1}{2}}$, $\varphi_{y,j}^{-\frac{1}{2}}$, $\varphi_{r,j}^{-\frac{1}{2}}$

Initialization of
$F_{x,j}^{0}$, $F_{y,j}^{0}$, $F_{r,j}^{0}$, $M_{x,j}^{0}$, $M_{y,j}^{0}$, $M_{r,j}^{0}$

Calculate
$V_{x,j}^{\frac{1}{2}}$, $V_{y,j}^{\frac{1}{2}}$, $V_{r,j}^{\frac{1}{2}}$, $\varphi_{x,j}^{\frac{1}{2}}$, $\varphi_{y,j}^{\frac{1}{2}}$, $\varphi_{r,j}^{\frac{1}{2}}$

Calculate
$F_{x,j}^{1}$, $F_{y,j}^{1}$, $F_{r,j}^{1}$, $M_{x,j}^{1}$, $M_{y,j}^{1}$, $M_{r,j}^{1}$

Eq (5.26) - (5.31)

Eq (5.32) - (5.33)

Calculate
$V_{x,j}^{n-\frac{1}{2}}$, $V_{y,j}^{n-\frac{1}{2}}$, $V_{r,j}^{n-\frac{1}{2}}$, $\varphi_{x,j}^{n-\frac{1}{2}}$, $\varphi_{y,j}^{n-\frac{1}{2}}$, $\varphi_{r,j}^{n-\frac{1}{2}}$

Calculate
$F_{x,j}^{n}$, $F_{y,j}^{n}$, $F_{r,j}^{n}$, $M_{x,j}^{n}$, $M_{y,j}^{n}$, $M_{r,j}^{n}$

Calculate
$V_{x,j}^{n+\frac{1}{2}}$, $V_{y,j}^{n+\frac{1}{2}}$, $V_{r,j}^{n+\frac{1}{2}}$, $\varphi_{x,j}^{n+\frac{1}{2}}$, $\varphi_{y,j}^{n+\frac{1}{2}}$, $\varphi_{r,j}^{n+\frac{1}{2}}$

Calculate
$F_{x,j}^{n+1}$, $F_{y,j}^{n+1}$, $F_{r,j}^{n+1}$, $M_{x,j}^{n+1}$, $M_{y,j}^{n+1}$, $M_{r,j}^{n+1}$

Eq (5.26) - (5.31)

Eq (5.32) - (5.33)

Time marching

Figure 5.3 Flowchart of FDTD method.

modal analysis of anisotropic beam structure, dynamic simulation under rotating (floating) frame, etc. As a result, in the following sections, three application cases are carried out to further illustrate and validate the proposed model. The programming code can be found in Appendix I.

5.3 Validation case 1: anisotropic box beam

The conventional modal analysis of a wind turbine blade is mostly based on FEM formulation rather than the proposed FDTD model. As a result, in this section, the method of modal analysis under the proposed FDTD method is firstly derived. Then the validation case of an anisotropic rectangular box beam is carried out to validate the proposed model. The comparison between predicted natural frequencies of HAWC2 (Kim), VABS (Hodges) [86], and MSC/Nastran is shown in this section. The coupling modes will also be shown and discussed in the last part of this section.

5.3.1 Problem statement

The anisotropic rectangular box beam is made of T300/5208 Graphite/Epoxy. The dimension and layups are shown in the Figure 5.4. The stiffness matrix K_s is shown in Equation (5.34). Some off-diagonal terms are nonzero, which means that there exist structural couplings, such as edgewise deflection - flapwise bending (K_{14}) coupling, flapwise deflection - edgewise bending (K_{25}), and axial deflection - torsion (K_{36}). It should be mentioned here that the rectangular box beam is uniform and symmetric. As a result, the I_{xy}, x_m, y_m in the above equations are all zero. The structural properties of the rectangular box beam are shown in Table 5.1.
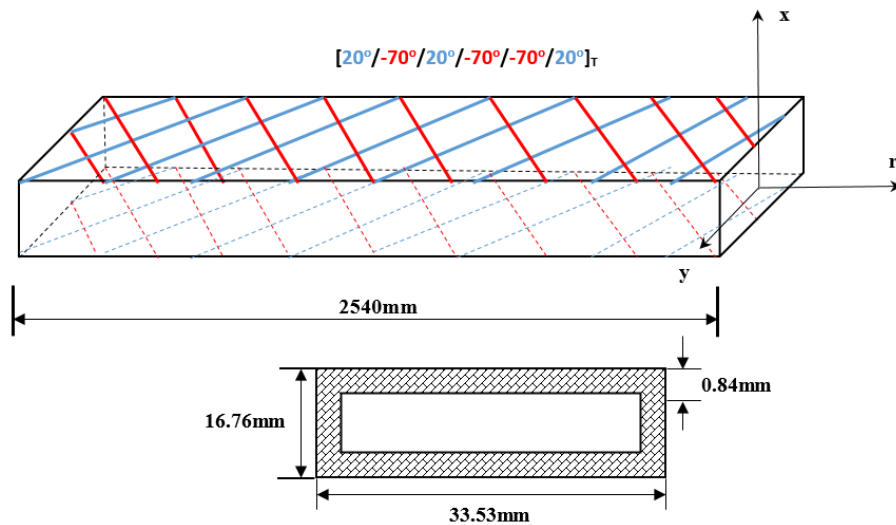
Figure 5.4 Anisotropic rectangular box beam.

$$\mathbf{K}_s = \begin{bmatrix} K_{11} & 0 & 0 & K_{14} & 0 & 0 \\ 0 & K_{22} & 0 & 0 & K_{25} & 0 \\ 0 & 0 & K_{33} & 0 & 0 & K_{36} \\ K_{41} & 0 & 0 & K_{44} & 0 & 0 \\ 0 & K_{52} & 0 & 0 & K_{55} & 0 \\ 0 & 0 & K_{63} & 0 & 0 & K_{66} \end{bmatrix} \qquad (5.34)$$

Table 5.1 Structural properties for the rectangular box beam[61].

Material	T300/5208 Graphite/Epoxy
Properties	Rectangular box beam
E_{11}	11.03 GPa
E_{33}	146.79 GPa
G_{12}	4.82 GPa
G_{13}, G_{23}	6.20 GPa
ν_{12}	0.28
ρ_s	1599 kg/m^3
K_{11}	7.7440×10^5 N
K_{14}	8.3266×10^3 Nm
K_{22}	2.9557×10^5 N
K_{25}	9.0666×10^3 Nm
K_{33}	5.0574×10^6 Nm
K_{36}	-1.7195×10^4 Nm
K_{44}	2.4576×10^2 Nm^2
K_{55}	7.4439×10^2 Nm^2
K_{66}	1.5040×10^2 Nm^2

5.3.2 Method of modal analysis based on the proposed FDTD formulation

Since modal analysis is based on a linear system, the non-linear terms in Equations (5.29) - (5.31) are firstly dropped. The Equations (5.29) - (5.31) become:

$$\rho_{s,j} y_{m,j} \frac{V_{r,j}^{n+\frac{1}{2}} - V_{r,j}^{n-\frac{1}{2}}}{\Delta t} + I_{xx,j} \frac{\omega_{x,j}^{n+\frac{1}{2}} - \omega_{x,j}^{n-\frac{1}{2}}}{\Delta t} - I_{xy,j} \frac{\omega_{y,j}^{n+\frac{1}{2}} - \omega_{y,j}^{n-\frac{1}{2}}}{\Delta t} = \frac{M_{x,j+1}^{n} - M_{x,j}^{n-\frac{1}{2}}}{\Delta r} - \frac{F_{y,j+1}^{n} + F_{y,j}^{n}}{2} + M_{e,lx,j}^{n}$$

$$(5.35)$$

$$-\rho_{s,j} x_{m,j} \frac{V_{r,j}^{n+\frac{1}{2}} - V_{r,j}^{n-\frac{1}{2}}}{\Delta t} - I_{xy,j} \frac{\omega_{x,j}^{n+\frac{1}{2}} - \omega_{x,j}^{n-\frac{1}{2}}}{\Delta t} + I_{yy,j} \frac{\omega_{y,j}^{n+\frac{1}{2}} - \omega_{y,j}^{n-\frac{1}{2}}}{\Delta t} = \frac{M_{y,j+1}^{n} - M_{y,j}^{n}}{\Delta r} + \frac{F_{x,j+1}^{n} + F_{x,j}^{n}}{2} + M_{e,ly,j}^{n}$$

$$(5.36)$$

$$-\rho_{s,j} y_{m,j} \frac{V_{x,j}^{n+\frac{1}{2}} - V_{x,j}^{n-\frac{1}{2}}}{\Delta t} + \rho_{s,j} x_{m,j} \frac{V_{y,j}^{n+\frac{1}{2}} - V_{y,j}^{n-\frac{1}{2}}}{\Delta t} + (I_{xx,j} + I_{yy,j}) \frac{\omega_{r,j}^{n+\frac{1}{2}} - \omega_{r,j}^{n-\frac{1}{2}}}{\Delta t} = \frac{M_{r,j+1}^{n} - M_{r,j}^{n}}{\Delta r} + M_{e,lr,j}^{n}$$

$$(5.37)$$

The above Equations (5.26) - (5.28), Equations (5.35) - (5.37), and Equations (5.32) - (5.33) can be rewritten in the following simple formulations (Equations (5.38) - (5.39)). $\mathbf{D}_P$ and $\mathbf{D}_Q$ are linear operators.

$$\mathbf{Q}^{n+\frac{1}{2}} = \mathbf{Q}^{n-\frac{1}{2}} - \mathbf{D}_P \mathbf{P}^n \Delta t \qquad (5.38)$$

$$\mathbf{P}^{n+1} = \mathbf{P}^n + \mathbf{D}_Q \mathbf{Q}^{n+\frac{1}{2}} \Delta t \qquad (5.39)$$

where

$$\mathbf{P} = \begin{bmatrix} \mathbf{F}^T & \mathbf{M}^T \end{bmatrix}^T \qquad (5.40)$$

$$\mathbf{Q} = \begin{bmatrix} \mathbf{V}^T & \omega^T \end{bmatrix}^T \qquad (5.41)$$

The above formulation can be further rewritten in the following way (Equations (5.42) - (5.43)):

$$\frac{\partial \mathbf{Q}}{\partial t} = -\mathbf{D}_P \mathbf{P} \qquad (5.42)$$

$$\frac{\partial \mathbf{P}}{\partial t} = \mathbf{D}_Q \mathbf{Q} \qquad (5.43)$$

Eliminating vector $\mathbf{P}$, we merged the two first order equations into one second order equation of vector $\mathbf{Q}$:

$$\frac{\partial^2 \mathbf{Q}}{\partial t^2} = -(\mathbf{D}_P \mathbf{D}_Q)\mathbf{Q} = -\mathbf{M}\mathbf{Q} \qquad (5.44)$$

where

$$\mathbf{M} = \mathbf{D}_P \mathbf{D}_Q \tag{5.45}$$

And the eigenvalue (ξ_i) and eigenvector ($\mathbf{V}_{Q,i}$) of matrix $\mathbf{M}$ are defined by the following Equation (5.46):

$$(\mathbf{M} - \xi_i \mathbf{I})\mathbf{V}_{Q,i} = \mathbf{0} \tag{5.46}$$

Now this formulation (Equation (5.46)) is similar to the equations of modal analysis in the previous research. The eigenvectors of $\mathbf{M}$ forms a complete set of basis to represent the $\mathbf{Q}$, which is the velocities and angular velocities vector. As a result, we have the following Equation (5.47).

$$\mathbf{Q} = \sum_i \mathbf{V}_Q y_i(t) \tag{5.47}$$

We further substitute Equation (5.47) into Equation (5.44), ODE of y_i (Equation (5.48)), which is the transient part of $\mathbf{Q}$.

$$\frac{\partial^2 y_i}{\partial t^2} + \xi_i y_i = 0 \tag{5.48}$$

By solving this second order homogeneous ODE, the solution of y_i for vector $\mathbf{Q}$ (velocities and angular velocities) can be calculated and shown in Equation (5.50). χ_i is the phase angle.

$$y_i = a_i \cos(\sqrt{\xi_i} t) + b_i \sin(\sqrt{\xi_i} t) \tag{5.49}$$

$$y_i = \sqrt{a_i^2 + b_i^2} \sin(\sqrt{\xi_i} t + \chi_i) \tag{5.50}$$

Previous research of modal analysis mainly focuses on the displacement, which is the time integral of velocity. The transient of displacement (z_i) is shown in Equation (5.51), where χ_i' is the phase angle.

$$z_i = \sqrt{\frac{a_i^2 + b_i^2}{\xi_i}} \sin(\sqrt{\xi_i} t + \chi_i') \tag{5.51}$$

Comparing Equations (5.50) and (5.51), it can be found that the modes of displacement and velocity share the same natural frequencies $\sqrt{\xi_i}$, in which ξ_i is the eigenvalue of mode i. Here the natural frequencies are angular frequencies. The modes of displacement and velocity also share the same mode shapes. In other words, the modal analysis can be carried out by the eigenanalysis of matrix $\mathbf{M}$. In the modal analysis, the rotational speed effect is neglected, which is a limitation of the proposed model.

5.3.3 Results and discussion

By using the modal analysis method described in the previous subsection, the natural frequency and mode shape can be calculated based on the eigenanalysis of matrix **M**. The predicted natural frequencies are compared with those obtained with HAWC2 (FEM model), VABS (Hodges's method), and commercial software MSC/Nastran. The MSC/-Nastran (high-fidelity model) case is carried out in [61], in which the 4-node shell element is used. The structure is meshed with 38 elements circumferentially and 1015 elements longitudinally. The comparison between the proposed FDTD method and the aforementioned three models in terms of the predicted natural frequencies is shown in Table 5.2. In this table, it can be seen that the proposed FDTD model is in a very good agreement with MSC/Nastran, VABS, and HAWC2 in this case, which also validates the proposed model. Among these models, HAWC2 model is also a kind of beam model. Although the derivation and formulation of the proposed FDTD model is totally different from the HAWC2 model as mentioned above, their predicted natural frequencies are very similar to each other for different modes.

Table 5.2 Comparison between the calculated natural frequencies of FDTD, HAWC2, VABS, and Nastran [61].

Mode	FDTD [Hz]	HAWC2 [Hz]	Hodges [Hz]	MSC/Nastran [Hz]
1st (Flap-Edge)	2.99	3.00	3.00	2.98
2nd (Edge-Flap)	5.18	5.19	5.19	5.12
3rd (Flap-Edge)	18.78	18.79	19.04	18.65
4th (Edge-Flap)	32.40	32.41	32.88	32.02
5th (Flap-Edge)	52.55	52.57	54.69	52.17
6th (Edge-Flap)	89.56	89.54	-	93.39

Furthermore, the calculated first 6 mode shapes are also shown in Figure 5.5. From these figures, it can be seen that the FDTD model can capture the coupled mode shapes clearly, which is the most important feature for an anisotropic beam. Since the first two modes have small coupling effects, it is not easy to reproduce the coupled behaviour. It should be mentioned here that these calculated mode shapes are also very similar to the results of HAWC2, which can be found in [61].
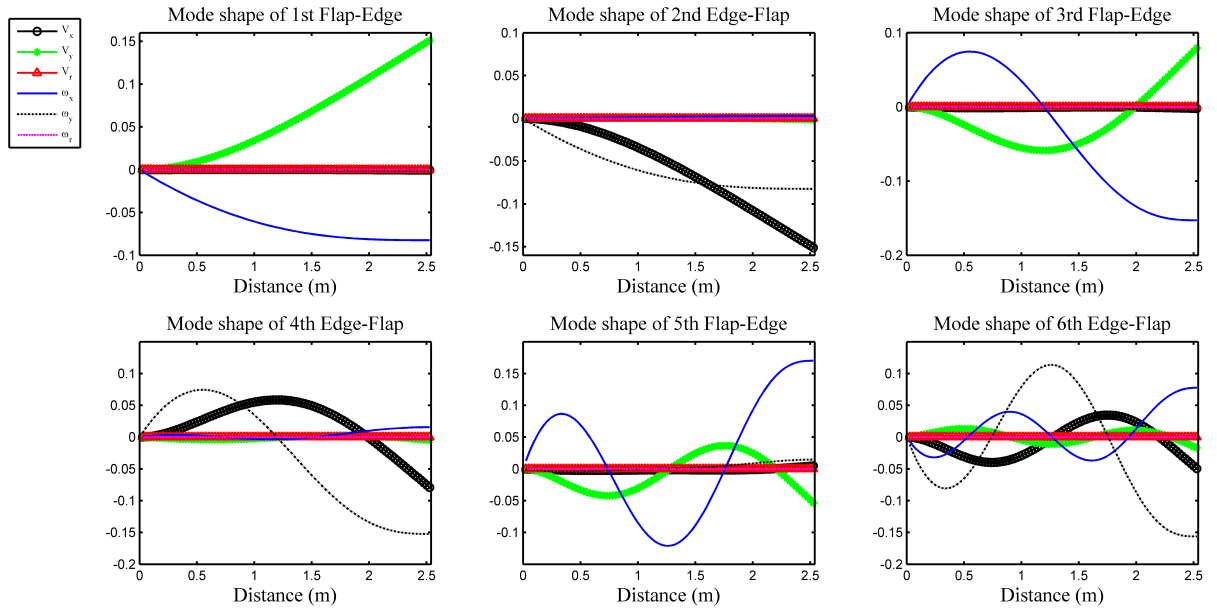
Figure 5.5 First 6 mode shapes of the anisotropic rectangular box beam.

5.4   Validation case 2: spin-up manuever

This spin-up maneuver case under floating frame was proposed by Kane [87] to validate a non-linear dynamic model. Furthermore, there exist complicated inertia forces of the floating frame, which are also important for the structural modelling of wind turbine blade. This case also exits in [61] to validate the FEM anisotropic beam model. In this research, this validation case is also carried out for our proposed FDTD method.

5.4.1   Problem statement

The beam is rotating along the direction $\mathbf{j}_1$ ($\mathbf{j}_0$ in Figure 5.7), which is shown in Figure 5.6. The prescribed rotating angle at the end is presented in Equation (5.52). Obviously, the frame is rotating with changing angular acceleration, which induces Euler force, Coriolis force, and the centrifugal force in the floating frame (the floating frame is attached to the shadow beam in Figure 5.7). It should be noted here that the aforementioned governing equations can be reduced, because three degrees of freedom out of total six are dropped in this case (rotations along direction $\mathbf{i}$ and $\mathbf{k}$, and deflection along direction $\mathbf{j}$). The simplified governing equations and inertia forces will be derived and illustrated in the following part, which is based on the floating frame ($\mathbf{i}_1$, $\mathbf{j}_0$, and $\mathbf{k}_1$). To derive the sectional strain without small rotation assumption, the frame attached to the deformed beam section is further introduced ($\mathbf{i}_2$, $\mathbf{j}_0$, and $\mathbf{k}_2$ in Figure 5.7). The structural properties of the rotating beam are

145

shown in the Table 5.3. The beam section is assumed to be symmetric for axis $\mathbf{i}_1$ and $\mathbf{k}_1$. The effect of gravity is insignificant, which is neglected in the model. This case is a 2D case, which is the limitation of the validation case.
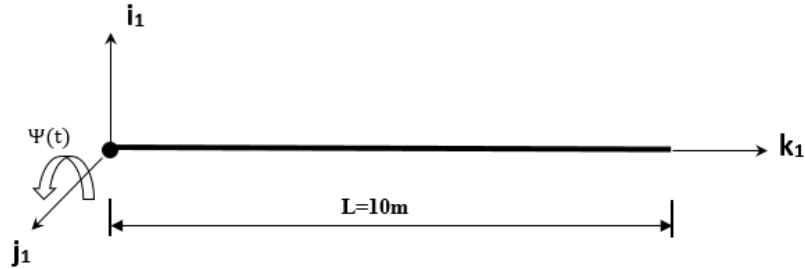
Figure 5.6 Sketch of spin-up maneuver.

$$\Psi(t) = \begin{cases} \frac{6}{15}[\frac{t^2}{2} + (\frac{15}{2\pi})^2(\cos\frac{2\pi t}{15} - 1)] & rad \quad 0 \le t \le 15s \\ (6t - 45) \quad rad & t > 15 \end{cases} \tag{5.52}$$
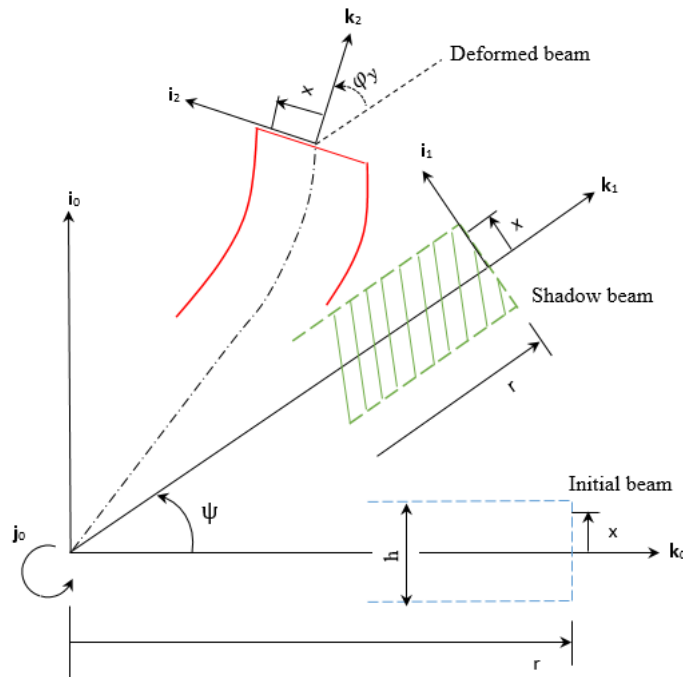
Figure 5.7 Coordinate system of the spin-up maneuver.

Table 5.3 Structural properties for the rotating beam.

ρ_s	$1.2\ kg/m$
I	$6.0 \times 10^{-4}\ kgm$
L	$10\ m$
K_{11}	$1.00 \times 10^7\ N$
K_{22}	$1.00 \times 10^7\ N$
K_{33}	$2.80 \times 10^7\ N$
K_{44}	$1.40 \times 10^4\ Nm^2$
K_{55}	$1.40 \times 10^4\ Nm^2$
K_{66}	$9.98 \times 10^3\ Nm^2$

5.4.2 Construction of FDTD model of spin-up maneuver case based on the floating frame

The simplified governing equations for the rotating beam are shown in the following Equations (5.53) - (5.58). The detailed derivations are shown in the Appendix F. It should be mentioned here that Equations (5.56) - (5.57) show the small rotation assumption ($\varphi_y \approx 0$). Ω is the rotational speed of the shadow beam, which is a virtual rotational rigid beam with the same rotational speed as the prescribed rotational speed $\Psi(t)$ of the beam end. It can be also seen that the non-linear terms and inertia forces are rigorously considered in the following equations.

$$\rho_s \frac{\partial V_x}{\partial t} = \frac{\partial F_x}{\partial r} - \rho_s[2V_r\Omega + (r + q_r)\dot{\Omega} + q_x\Omega^2] \tag{5.53}$$

$$\rho_s \frac{\partial V_r}{\partial t} = \frac{\partial F_r}{\partial r} + \rho_s[2V_x\Omega + q_x\dot{\Omega} + (r + q_r)\Omega^2] \tag{5.54}$$

$$I_{yy} \frac{\partial \omega_y}{\partial t} = \frac{\partial M_y}{\partial r} - F_r \frac{\partial q_x}{\partial r} + F_x \frac{\partial q_r}{\partial r} + F_x - I_{yy}\dot{\Omega} \tag{5.55}$$

$$\frac{\partial F_r}{\partial t} = EA(\frac{\partial V_r}{\partial r} + \omega_y \sin(\varphi_y)) \approx EA\frac{\partial V_r}{\partial r} \tag{5.56}$$

$$\frac{\partial F_x}{\partial t} = GA(\frac{\partial V_x}{\partial r} - \omega_y \cos(\varphi_y)) \approx GA(\frac{\partial V_x}{\partial r} - \omega_y) \tag{5.57}$$

$$\frac{\partial M_y}{\partial t} = EI\frac{\partial \omega_y}{\partial r} \tag{5.58}$$

Based on the proposed FDTD method, the numerical dynamic model is shown in the Equations (5.59) - (5.66). The two sets of Equations (Equations (5.59) - (5.61) and Equations (5.62) - (5.66)) are solved element by element alternately in the FDTD manner.

$$\rho_{s,j}\frac{V_{x,j}^{n+\frac{1}{2}} - V_{x,j}^{n-\frac{1}{2}}}{\Delta t} = \frac{F_{x,j+1}^n - F_{x,j}^n}{\Delta r} - \rho_{s,j}[2\frac{V_{r,j}^{n+\frac{1}{2}} + V_{r,j}^{n-\frac{1}{2}}}{2}\Omega + (r_j + \frac{q_{r,j+1}^n + q_{r,j}^n}{2})\dot{\Omega} + \frac{q_{x,j+1}^n + q_{x,j}^n}{2}\Omega^2] \tag{5.59}$$

$$\rho_{s,j}\frac{V_{r,j}^{n+\frac{1}{2}} - V_{r,j}^{n-\frac{1}{2}}}{\Delta t} = \frac{F_{r,j+1}^n - F_{r,j}^n}{\Delta r} + \rho_{s,j}[2\frac{V_{x,j}^{n+\frac{1}{2}} + V_{x,j}^{n-\frac{1}{2}}}{2}\Omega + (r_j + \frac{q_{r,j+1}^n + q_{r,j}^n}{2})\Omega^2 + \frac{q_{x,j+1}^n + q_{x,j}^n}{2}\dot{\Omega}] \tag{5.60}$$

$$I_{yy,j} \frac{\omega_{y,j}^{n+\frac{1}{2}} - \omega_{y,j}^{n-\frac{1}{2}}}{\Delta t} = \frac{M_{y,j+1}^n - M_{y,j}^n}{\Delta r} - \frac{F_{r,j+1}^n + F_{r,j}^n}{2} \frac{q_{x,j+1}^n - q_{x,j}^n}{\Delta r}$$
$$+ \frac{F_{x,j+1}^n + F_{x,j}^n}{2} \frac{q_{r,j+1}^n - q_{r,j}^n}{\Delta r} + \frac{F_{x,j+1}^n + F_{x,j}^n}{2} - I_{yy,j}\dot{\Omega} \tag{5.61}$$

$$\frac{F_{r,j}^{n+1} - F_{r,j}^n}{\Delta t} = (EA)_j \frac{V_{r,j}^{n+\frac{1}{2}} - V_{r,j-1}^{n+\frac{1}{2}}}{\Delta r} \tag{5.62}$$

$$\frac{F_{x,j}^{n+1} - F_{x,j}^n}{\Delta t} = (GA)_j \left(\frac{V_{x,j}^{n+\frac{1}{2}} - V_{x,j-1}^{n+\frac{1}{2}}}{\Delta r} - \frac{\omega_{y,j}^{n+\frac{1}{2}} + \omega_{y,j-1}^{n+\frac{1}{2}}}{2} \right) \tag{5.63}$$

$$\frac{M_{y,j}^{n+1} - M_{y,j}^n}{\Delta t} = (EI)_j \frac{\omega_{y,j}^{n+\frac{1}{2}} - \omega_{y,j-1}^{n+\frac{1}{2}}}{\Delta r} \tag{5.64}$$

$$\frac{q_{x,j}^{n+1} - q_{x,j}^n}{\Delta t} = \frac{V_{x,j}^{n+\frac{1}{2}} + V_{x,j-1}^{n+\frac{1}{2}}}{2} \tag{5.65}$$

$$\frac{q_{r,j}^{n+1} - q_{r,j}^n}{\Delta t} = \frac{V_{r,j}^{n+\frac{1}{2}} + V_{r,j-1}^{n+\frac{1}{2}}}{2} \tag{5.66}$$

5.4.3 Results and discussion

In this part, the predicted tip displacements and rotation angle are compared with the results in [87]. The first simulation is carried out with small rotation assumption. From Figure 5.8, the predicted results of tip displacement in **x** direction ($\mathbf{i}_1$) and twist angle in **y** direction ($\mathbf{j}_0$) have a good agreement with Simo's results. There exist small discrepancies in these two figures in the final oscillation part. The most obvious discrepancy occurs in the tip displacement in **r** direction ($\mathbf{k}_1$). Although the predicted offset is correct, the model failed to predict the valley of the curve. However, if we compare the tip displacement in **x** direction ($\mathbf{i}_1$) and the tip displacement in **r** direction ($\mathbf{k}_1$), it can be easily found that the former one is much larger than the latter. As a result, the current model captures the main physical behaviour of the rotating beam. In the author's opinion, the discrepancy is caused by the small rotation assumption. To capture more detailed information of the rotating beam, the numerical model without small rotation assumption is constructed.

The results of FDTD model without small rotation assumption are shown in the Figure 5.10. From this figure, it can be seen that the predicted values of FDTD model and Simo's
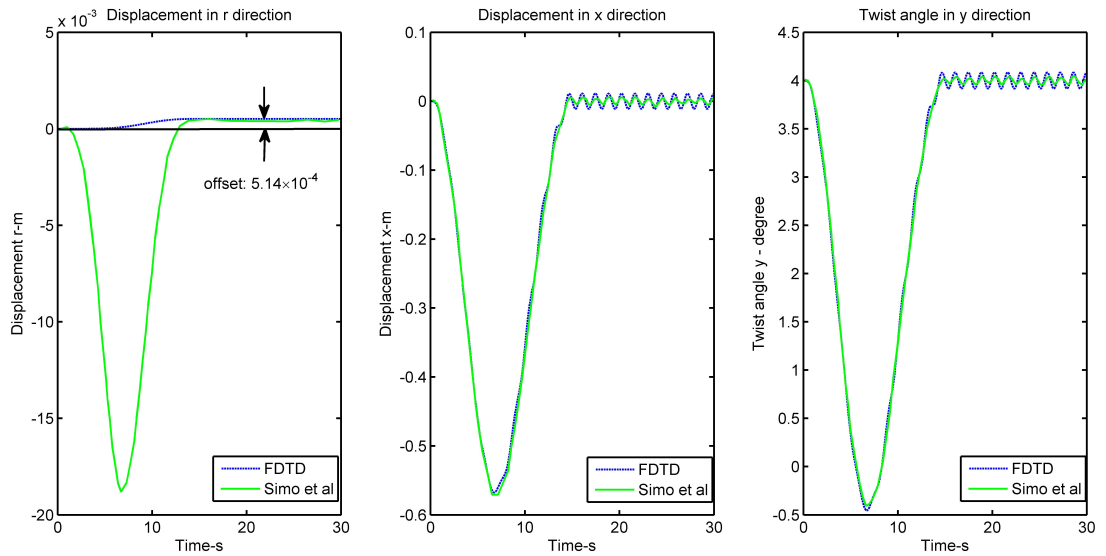
Figure 5.8 Comparison between the results of proposed FDTD model (with small rotation assumption) and Simo's benchmark data.
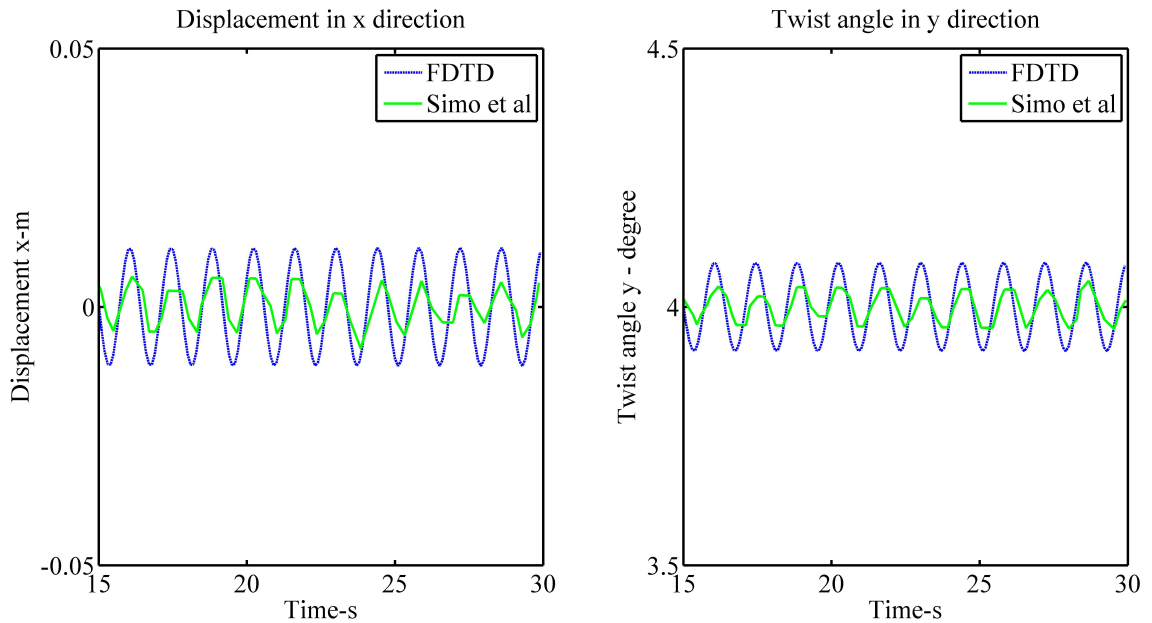
Figure 5.9 Comparison between the results of proposed FDTD model (with small rotation assumption) and Simo's benchmark data (oscillation part enlarged).

results have a very good agreement, which validates the proposed model. Considering large rotation is necessary for the numerical model in this case. As a result, the proposed model can be extended to model large rotations.

150
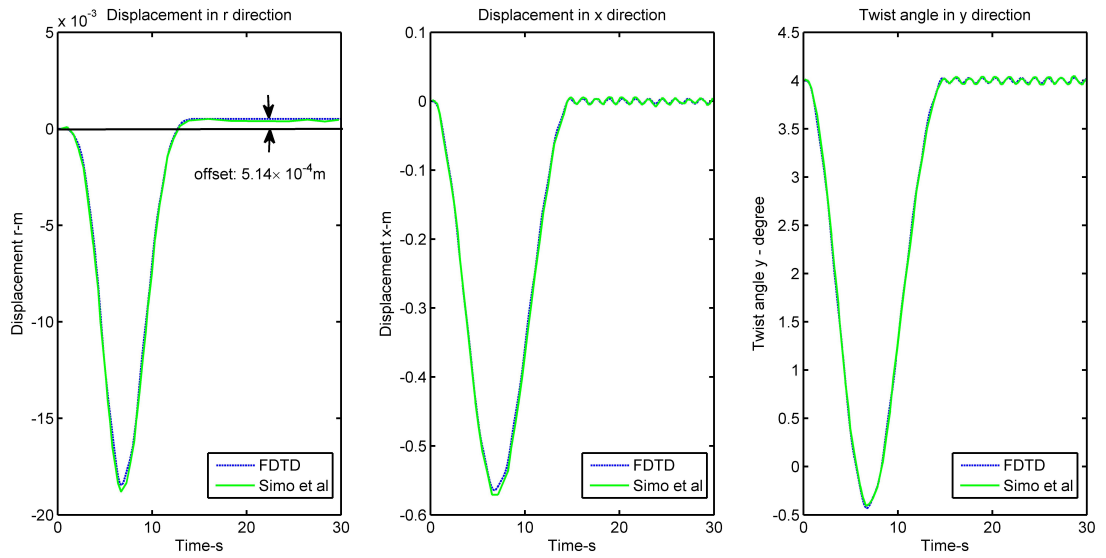
Figure 5.10 Comparison between the results of proposed FDTD model (without small rotation assumption) and Simo's benchmark data.
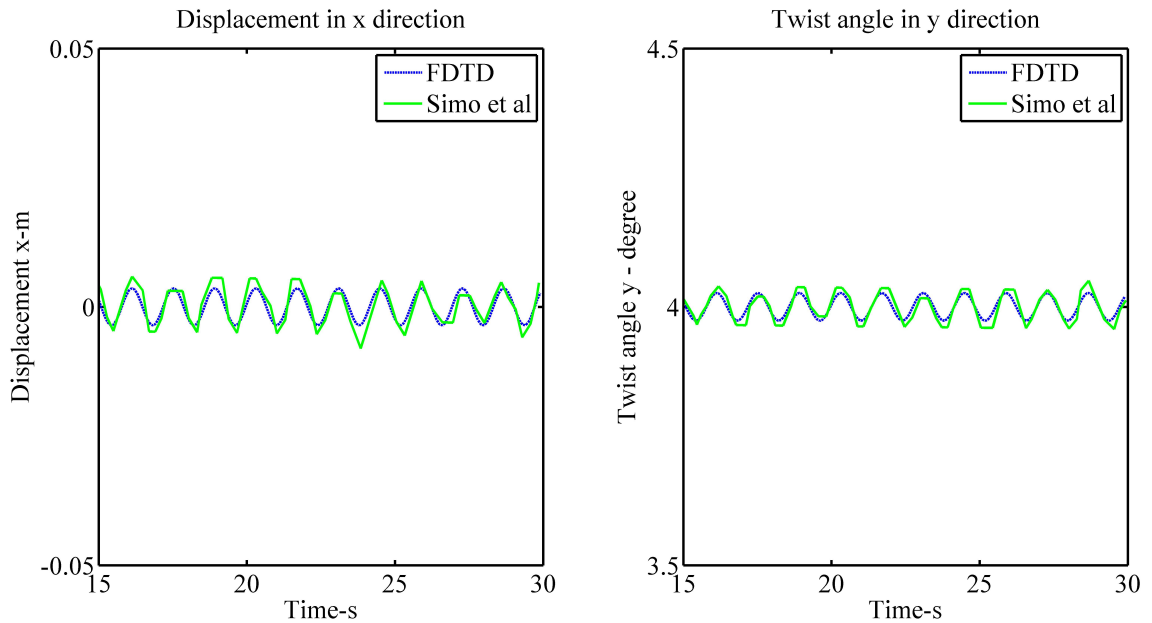
Figure 5.11 Comparison between the results of proposed FDTD model (without small rotation assumption) and Simo's benchmark data (oscillation part enlarged).

151

5.5 Validation case 3: NREL 5MW and WindPACT wind turbine blade

In the previous two case studies, the beam is uniform, and the beam sections are symmetric. In this case study, the case study of real wind turbine blades with nonuniform and asymmetric sections, namely NREL 5MW and WindPACT wind turbine blades, is carried out to further validate the proposed FDTD model. The method of modal analysis presented in the case study 1 is employed in this section to calculate the natural frequencies and mode shapes of the wind turbine blade. Because the beam section is non-uniform and asymmetric, there exist some modifications (M') for Equation (5.42), which is as follows:

$$\mathbf{M'Q}_j^{n+\frac{1}{2}} = \mathbf{M'Q}_j^{n-\frac{1}{2}} - \mathbf{D}_{P,j}\mathbf{P}_j^n dt \tag{5.67}$$

where

$$\mathbf{M'} = \begin{bmatrix} 1 & 0 & 0 & 0 & 0 & -y_{m,j} \\ 0 & 1 & 0 & 0 & 0 & x_{m,j} \\ 0 & 0 & 1 & y_{m,j} & -x_{m,j} & 0 \\ 0 & 0 & y_{m,j} & \frac{I_{xx,j}}{\rho_{s,j}} & -\frac{I_{xy,j}}{\rho_{s,j}} & 0 \\ 0 & 0 & -x_{m,j} & -\frac{I_{xy,j}}{\rho_{s,j}} & \frac{I_{yy,j}}{\rho_{s,j}} & 0 \\ -y_{m,j} & x_{m,j} & 0 & 0 & 0 & \frac{I_{xx,j}+I_{yy,j}}{\rho_{s,j}} \end{bmatrix} \tag{5.68}$$

From Equation (5.69), we can see that $(\mathbf{M'})^{-1}\mathbf{D}_{P,j}$ will be our new $\mathbf{D}_{P,j}$.

$$\mathbf{Q}_j^{n+\frac{1}{2}} = \mathbf{Q}_j^{n-\frac{1}{2}} - (\mathbf{M'})^{-1}\mathbf{D}_{P,j}\mathbf{P}_j^n dt \tag{5.69}$$

The predicted first 6 natural frequencies are compared with that of ANSYS model, which are shown in Tables 5.4 and 5.5. From this comparison, it can be seen that the proposed FDTD results match very well with the ANSYS results. This further validate the proposed model. The first 6 calculated mode shapes are shown in Figures 5.12 and 5.13. This modal analysis does not include the rotational speed, which is the limitation of this simulation.

Table 5.4 Comparison between the calculated natural frequencies of FDTD and ANSYS for NREL 5MW wind turbine blade.

Mode No.	FDTD [Hz]	ANSYS [Hz]	Description
1st	0.88	0.87	1st flapwise bending
2nd	1.03	1.06	1st edgewise bending
3rd	2.69	2.68	2nd flapwise bending
4th	3.86	3.91	2nd edgewise bending
5th	5.91	5.57	3rd flapwise bending
6th	6.64	6.45	1st torsion
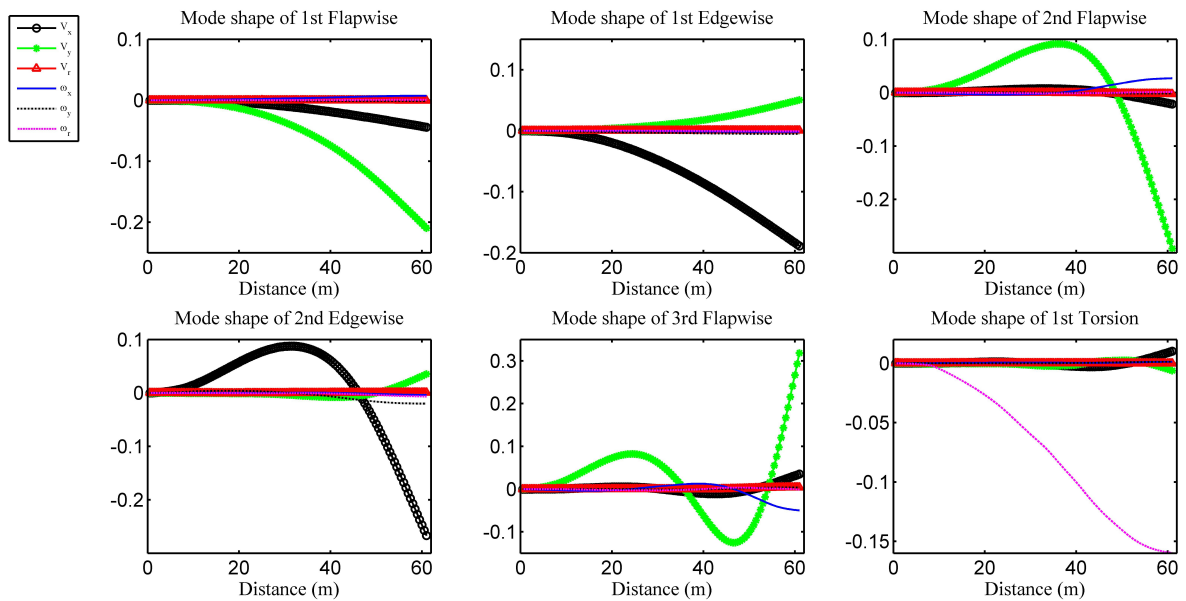
Figure 5.12 Predicted mode shapes of NREL 5MW wind turbine blade by using FDTD model.

Table 5.5 Comparison between the calculated natural frequencies of FDTD and ANSYS for WindPACT wind turbine blade.

Mode No.	FDTD [Hz]	ANSYS [Hz]	Description
1st	1.0923	1.0783	1st flapwise bending
2nd	1.7202	1.7001	1st edgewise bending
3rd	2.8424	2.9804	2nd flapwise bending
4th	4.8144	5.0382	2nd edgewise bending
5th	6.1099	6.3093	3rd flapwise bending
6th	10.2781	10.305	1st torsion
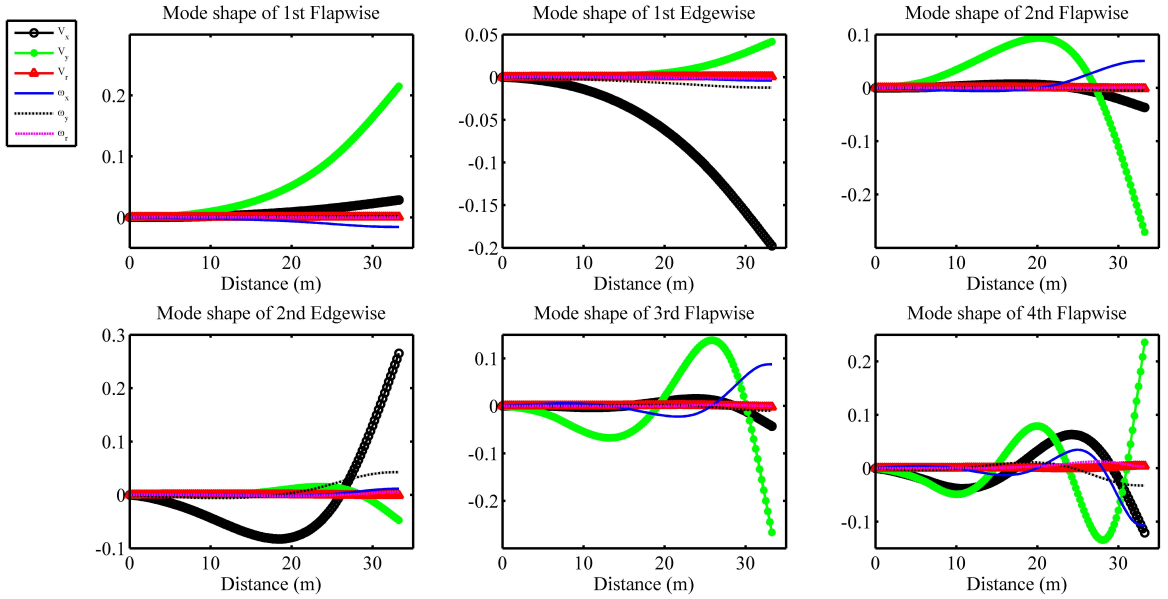
Figure 5.13 Predicted mode shapes of NREL WindPACT wind turbine blade by using FDTD model.

5.6 Unconditionally stable explicit FDTD anisotropic wind turbine blade model

In this section, the stability analysis for the aforementioned explicit FDTD method is firstly carried out to discover the root cause of the instability. Based on this analysis, the unconditionally stable explicit FDTD method is proposed.

5.6.1 Stability analysis of explicit FDTD model

The stability analysis in this subsection is based on the D. Jiao's paper on electromagnetic simulation [4]. For the stability analysis, it is assumed that the instability is mainly caused by the linear part of the governing equations. The Equations (5.26) - (5.33) can be simplified as the Equation (5.70) (drop the source terms).

$$
\begin{bmatrix} \mathbf{Q}^{n+\frac{1}{2}} \\ \mathbf{P}^{n+1} \end{bmatrix} = \begin{bmatrix} \mathbf{I} & -\Delta t \mathbf{D}_P \\ \Delta t \mathbf{D}_Q & \mathbf{I} - \Delta t^2 \mathbf{M} \end{bmatrix} \begin{bmatrix} \mathbf{Q}^{n-\frac{1}{2}} \\ \mathbf{P}^{n} \end{bmatrix} \tag{5.70}
$$

The amplitude matrix $\mathbf{G}$ is shown in the Equation (5.71).

$$
\mathbf{G} = \begin{bmatrix} \mathbf{I} & -\Delta t \mathbf{D}_P \\ \Delta t \mathbf{D}_Q & \mathbf{I} - \Delta t^2 \mathbf{M} \end{bmatrix} \tag{5.71}
$$

Define vector U pertinent to Equation (5.70) as follows.

$$\mathbf{U}^n = \begin{bmatrix} \mathbf{Q}^{n-\frac{1}{2}} \\ \mathbf{P}^n \end{bmatrix} \tag{5.72}$$

Then the Equation (5.70) can be rewritten as Equation (5.73).

$$\mathbf{U}^{n+1} = \mathbf{G}\mathbf{U}^n \tag{5.73}$$

To guarantee the stability, the spectral radius of amplitude matrix $\mathbf{G}$ should be less than one. In other words, the modulus of the eigenvalues of $\mathbf{G}$ should be less than one. The diagonal matrix $\tilde{\mathbf{\Lambda}}_G$ of eigen-values of matrix $\mathbf{G}$ is shown in Equation (5.74).

$$\mathbf{G}\mathbf{V} = \mathbf{V}\tilde{\mathbf{\Lambda}}_G \tag{5.74}$$

And Equation (5.74) can be also rewritten as Equation (5.75).

$$(\mathbf{G} - \mathbf{I})\mathbf{V} = \mathbf{V}(\tilde{\mathbf{\Lambda}}_G - \mathbf{I}) \tag{5.75}$$

We further substitute $\mathbf{G}$ in Equation (5.71) into Equation 5.75,

$$\begin{bmatrix} \mathbf{0} & -\Delta t\mathbf{D}_P \\ \Delta t\mathbf{D}_Q & -\Delta t^2\mathbf{M} \end{bmatrix} \begin{bmatrix} \mathbf{V}_Q \\ \mathbf{V}_P \end{bmatrix} = \begin{bmatrix} \mathbf{V}_Q \\ \mathbf{V}_P \end{bmatrix} \tilde{\Lambda}_G \tag{5.76}$$

Where

$$\tilde{\mathbf{\Lambda}}_G = \mathbf{\Lambda}_G - \mathbf{I} \tag{5.77}$$

The Equation 5.76 can be rewritten as:

$$-\Delta t\mathbf{D}_P\mathbf{V}_P = \mathbf{V}_Q\tilde{\mathbf{\Lambda}}_G \tag{5.78}$$

$$\Delta t\mathbf{D}_Q\mathbf{V}_Q - \Delta t^2\mathbf{M}\mathbf{V}_P = \mathbf{V}_P\tilde{\mathbf{\Lambda}}_G \tag{5.79}$$

Multiply Equation (5.79) from right by $\tilde{\mathbf{\Lambda}}_G$ ans substitute Equation (5.76) into it.

$$-\Delta t^2\mathbf{M}\mathbf{V}_P(\mathbf{I} + \tilde{\mathbf{\Lambda}}_G) = \mathbf{V}_P\tilde{\mathbf{\Lambda}}_G^2 \tag{5.80}$$

which yields

$$-\Delta t^2\mathbf{M}\mathbf{V}_{P,i} = \frac{(\gamma_i - 1)^2}{\gamma_i}\mathbf{V}_{P,i} \tag{5.81}$$

In Equation (5.81), the γ_i is the ith eigenvalue of matrix $\mathbf{G}$. If the ith eigenvalues of $\mathbf{M}$ is ξ_i, we have:

$$- \Delta t^2 \xi_i = \frac{(\gamma_i - 1)^2}{\gamma_i} \tag{5.82}$$

As mentioned above, to guarantee the numerical stability, the γ_i should met the requirements of Equation (5.83).

$$|\gamma_i| \leq 1 \tag{5.83}$$

Combining Equation (5.82) and (5.83), we have the condition for time step:

$$\Delta t \leq \frac{2}{\sqrt{\xi_i}} \tag{5.84}$$

In Equation (5.84), it can be found that the time step is dependent on the ξ_i, which is the ith eigenvalue of $\mathbf{M}$. In Section 5.3.2, ξ_i is proven to be related to the predicted natural frequency ($\sqrt{\xi_i}$) of the structure. In other words, the root cause of the explicit FDTD method is the high frequency waves. With the resolved frequency increasing, the time step becomes extremely small. However, in fact, we do not need to capture the highest frequency wave. For example, low frequency fluctuations loading plays the dominant role in the fatigue damage of wind turbine blade. In other words, the highest frequency wave we want to resolve is often much lower than the highest natural frequency of the FDTD model, which obviously makes the time step much smaller in the application cases. Based on this fact, the stability of modal approach, explicit FDTD method can be analysed. For the modal approach, only four or five modes are considered, which means that large range of frequencies are truncated, which guarantee the large time step. However, the accuracy of the model will also decrease because of the truncated frequencies. For explicit FDTD model, all of the frequencies are kept for high accuracy, which also means that the time step will be extremely small. This analysis is presented in Figure 5.14.

The idea of unconditionally stable FDTD method is that we can choose the time step Δt according to the highest frequency which is required to resolve (f_{max}). For example, the f_{max} can be the highest frequency related to the fatigue damage or can be calculated according to the required time step of actuator line ($f_{max} = \frac{1}{2\Delta t}$). The frequencies between f_{max} and $\sqrt{\xi_{max}}$ will be truncated, which can enlarge the time step without loosing the accuracy. In other words, it strikes a balance between accuracy and efficiency. The unconditionally stable explicit FDTD model for wind turbine blade structure will be constructed in the following subsection.
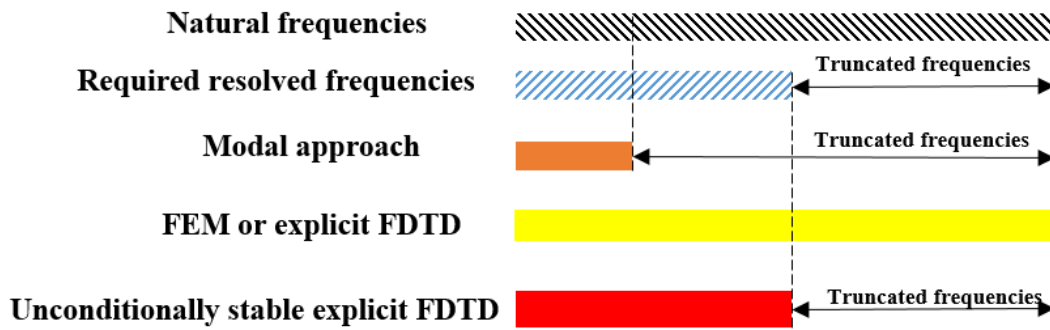
Figure 5.14 Illustration of unconditionally stable FDTD.

5.6.2   Unconditionally stable explicit FDTD model

The $\mathbf{V}_{P,st}$ and $\mathbf{V}_{Q,st}$ are the truncated eigen vectors of $\mathbf{P}$ and $\mathbf{Q}$, which is shown in the Equations (5.85) and (5.86).

$$\mathbf{P}_s = \mathbf{V}_{P,st}\, y_P \tag{5.85}$$

$$\mathbf{Q}_s = \mathbf{V}_{Q,st}\, y_Q \tag{5.86}$$

By using these two eigen vectors, the Equation (5.70) turns into Equation (5.87) - (5.88).

$$\mathbf{V}_{Q,st}\, y_Q^{n+\frac{1}{2}} = \mathbf{V}_{Q,st}\, y_Q^{n-\frac{1}{2}} - \Delta t \mathbf{D}_P \mathbf{V}_{P,st}\, y_P^n - \Delta t \mathbf{S}_P^n \tag{5.87}$$

$$\mathbf{V}_{p,st}\, y_P^{n+1} = \mathbf{V}_{p,st}\, y_P^n - \Delta t \mathbf{D}_Q \mathbf{V}_{Q,st}\, y_Q^{n+\frac{1}{2}} - \Delta t \mathbf{S}_Q^{n+\frac{1}{2}} \tag{5.88}$$

which yields

$$y_Q^{n+\frac{1}{2}} = y_Q^n - \Delta t \mathbf{V}_{Q,st}^{-1}\mathbf{D}_P\mathbf{V}_{P,st}\, y_P^n - \Delta t \mathbf{V}_{Q,st}^{-1}\mathbf{S}_P^n \tag{5.89}$$

$$y_P^{n+1} = y_P^n - \Delta t \mathbf{V}_{p,st}^{-1}\mathbf{D}_Q\mathbf{V}_{Q,st}\, y_Q^{n+\frac{1}{2}} - \Delta t \mathbf{V}_{p,st}^{-1}\mathbf{S}_Q^{n+\frac{1}{2}} \tag{5.90}$$

The $\mathbf{V}_{Q,st}^{-1}$ and $\mathbf{V}_{p,st}^{-1}$ can be precalculated. A simulation case for the NREL 5MW wind turbine blade is carried out to verify the proposed unconditionally stable FDTD method. A constant force (20 N/m) along x direction (see Figure 5.1) is applied on the stationary wind turbine blade (from root to the tip). The calculated 20-second root bending moments along different directions of unconditionally stable FDTD method and implicit method with time step 1×10^{-3} (e.g. time step of actuator line model) are compared with that of explicit FDTD method, which is shown in Figures 5.15 to 5.17. The implicit method is formulated by replacing the F^n and M^n in the right hand side by F^{n+1} and M^{n+1} in Equation (5.26) - (5.31). The required largest time step for explicit FDTD method is 1×10^{-5}, which means that the time step of unconditionally stable explicit method and implicit method is 100 times larger than that of explicit FDTD method in this case.

Unlike the implicit method, the unconditionally stable explicit method captures the fluctuations accurately, which can be seen from the Figures 5.15 (root bending moment along x direction) and 5.16 (root bending moment along y direction). The unconditionally stable method lose accuracy for the bending moment along r direction (see Figure 5.17), which is obviously smaller than the other two components in this case and will have less effect on the fatigue damage. In summary, the unconditionally stable explicit FDTD model can overcome its limitations on time step with little effect on its solution accuracy.
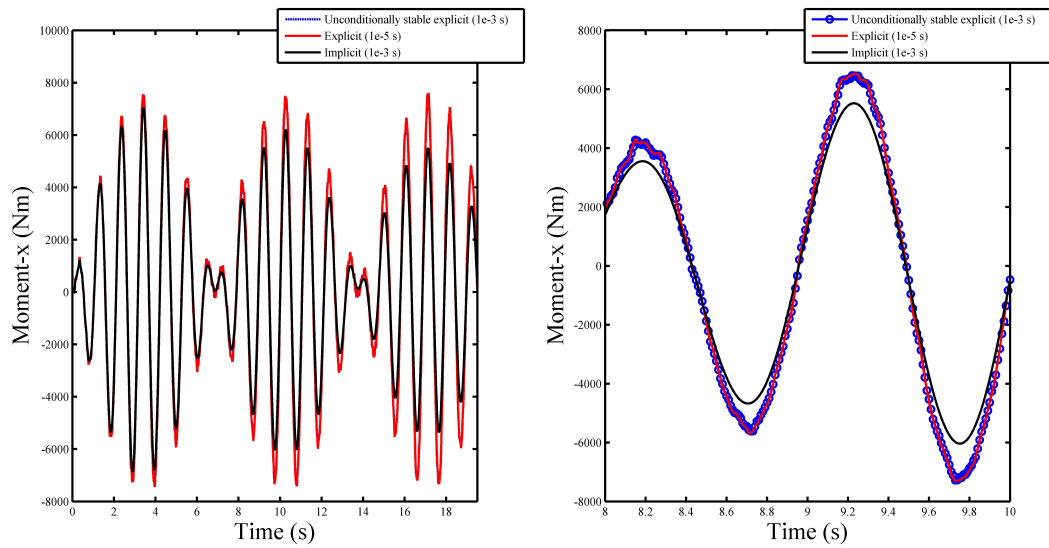
Figure 5.15 Comparison between unconditionally stable explicit, implicit, and explicit FDTD method in terms of root moment along x direction.
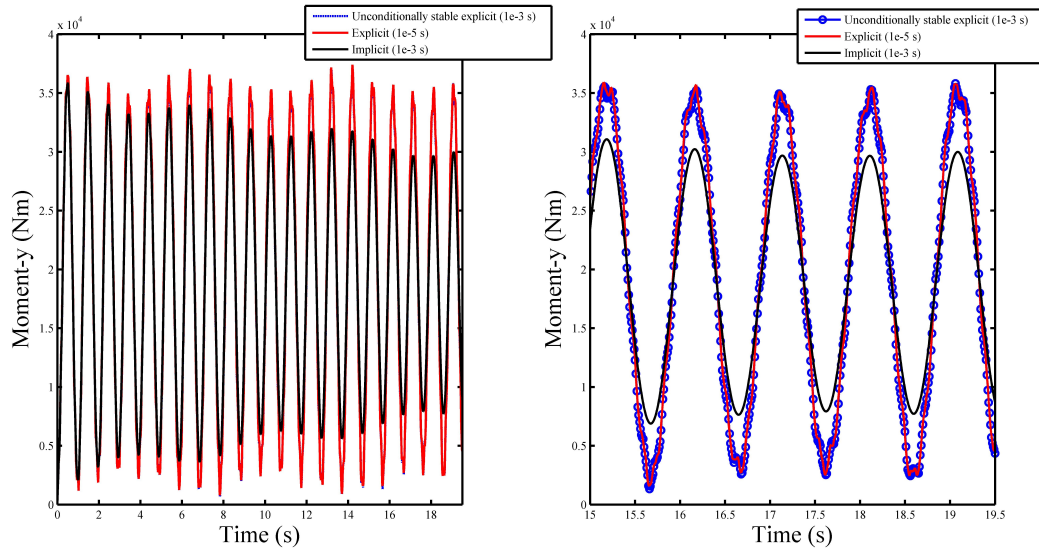
Figure 5.16 Comparison between unconditionally stable explicit, implicit, and explicit FDTD method in terms of root moment along y direction.
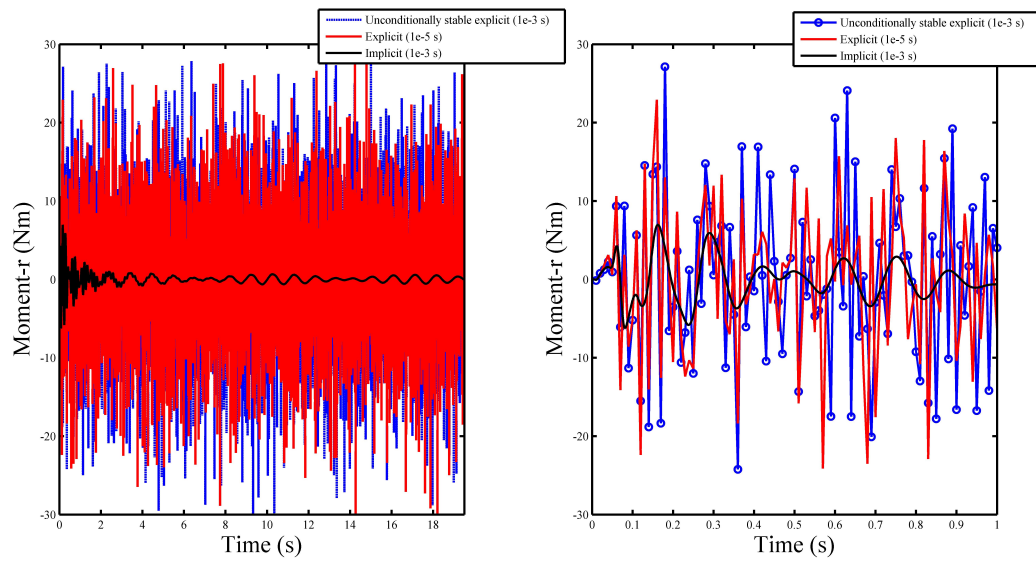
Figure 5.17 Comparison between unconditionally stable explicit and explicit FDTD method in terms of root moment along r direction.

5.7   Chapter summary

In this chapter, the structure model based on FDTD method is proposed and validated by three cases in terms of deformation coupling, non-inertia coordinate system, and non-uniform blade sections (for NREL 5MW and WindPACT wind turbine blades). This FDTD model is a generalized formulation of the structure model presented in Chapter 3, which further considers the anisotropic nature of composite wind turbine blade. In addition, the modal analysis method based on this formulation is also proposed and validated. From the stability analysis, it can be concluded that the root cause for instability for the proposed numerical method is the highest frequency mode in the model. Based on this analysis, the unconditionally stable explicit FDTD structure model is proposed, constructed, and verified, which strikes a balance between accuracy and efficiency. Compared with implicit method, the unconditionally stable explicit FDTD model can overcome its limitations on time step with little effect on its solution accuracy.

Chapter 6

Conclusions and future work

In this thesis, firstly, the actuator line model is validated in terms of thrust coefficient and flow field prediction. Secondly, Based on NREL SOWFA, the elastic actuator line model is constructed as an aero-elastic model for wake conditions to simulate the dynamic loading of wind turbine blade. Thirdly, the performance of normal and bend-twist coupling wind turbine blade with anisotropic composite structure in wake conditions are studied by using the aero-elastic model based on anisotropic structure model, cross sectional analysis, and fatigue analysis method. Lastly, the structure model based on FDTD method is constructed for anisotropic wind turbine blade and validated, which strikes balance between accuracy and efficiency. The main conclusions are as follows:

(1) The nacelle effect has impact on the velocity profile around wake center region. The proposed single-point nacelle model, single momentum source point smeared by Gaussian function, can be used to reproduce the nacelle effect not only for RANS turbulence model but also for LES turbulence model.

(2) The proposed elastic actuator line model can be used to simulate the fatigue loading in wake. Instead of employing displacements as dependent variables in conventional structure models, velocity and moment are dependent variables which is suitable for the coupled model of conventional actuator line model and structure model (velocity is required), and the fatigue analysis (moment is required). The FDM based structure model is the first contribution of the current thesis. The stochastic and deterministic wake-induced fatigue can all be reproduced by the proposed elastic actuator line model. Compared with the explicit elastic actuator line model, the implicit elastic actuator line can run with larger time step. However, the accuracy of implicit method will decrease.

(3) The fatigue analysis methodology is proposed based on the anisotropic wind turbine blade structure model and cross sectional analysis method. Based on this fatigue analysis methodology, the fatigue life of NREL 5MW wind turbine blade is analysed. The predicted fatigue life (26.0187 years) of the main structure is very close to the design life (20 years).

161

From the fatigue analysis for wind turbine blade in wake conditions, it is found that the wake-induced fatigue has a significant impact on the fatigue life of wind turbine blades (fatigue life drops from 26.0187 years to 1.7388 years under compact layout). Wind farm layout can affect the wake-induced fatigue damage (increase from 1.7388 years (compact layout) to 6.9084 years (normal layout)). Furthermore, it is also found that the bend-twist coupling wind turbine blade can alleviate the fatigue load under wake condition.

(4) Based on the FDTD method, a novel anisotropic beam model for wind turbine blade is constructed and validated in terms of beams with deformation coupling, non-inertia coordinate system, and non-uniform sections (real wind turbine blade). The stability analysis for the proposed FDTD model is carried out, which shows that the root cause of the numerical instability for the proposed method is the highest-frequency mode in numerical model. Based on this analysis, the unconditionally stable explicit FDTD structure model is proposed and constructed, which strikes a balance between accuracy and efficiency. Compared with implicit method, the unconditionally stable explicit FDTD overcomes its limitations on time step with little effect on its solution accuracy. This is the second contribution of the thesis.

In the future, the proposed fatigue analysis methodology and anisotropic wind turbine blade structure model will be employed in the elastic actuator line model, which will be further verified by NREL FAST 8.0, fluid-structure-interaction model, and measured data.

References

[1] F. Pierella, P. A. Krogstad, Blind Test 2 calculations for two in-line model wind turbines where the downstream turbine operates at various rotational speeds., Renewable energy. 70(2014). (2014.) 62–77.

[2] F. Pierella, P. A. Krogstad, Blind Test 3 calculations for performance and wake development behind two in-line and offset model wind turbines., Renewable energy. 52(2015) (2015) 65–80.

[3] J. P. Blasques., User's Manual for BECAS., Riso report. (2015.) 29.

[4] M. Gaffar, D. Jiao., An explicit and unconditionally stable FDTD method for electromagnetic analysis., IEEE TRANSACTIONS ON MICROWAVE THEORY AND TECHNIQUES. 62(11) (2014.) 2538–2542.

[5] D. Smith, G. J. Taylor., Further analysis of turbine wake development and interaction data., National power technology 1(1) (1999) 56–58.

[6] N. O. Jensen., A note on wind generator interaction, Riso report (1983) 20–25.

[7] G. C. Larsen., A simple wake calculation procedure, Riso report (1988) 23–28.

[8] D. J. Renkema, Further analysis of turbine wake development and interaction data., National power technology. (1999) 56–58.

[9] J. N. Sorensen, W. Z. Shen, X. Mundunate., Analysis of wake states by a full-field actuator disc model., Wind energy 1(1998) (1998) 73–88.

[10] T. Han., The assessment of dynamic wake effects on loading., Master thesis, TU Delft .

[11] B. Sanderse, et al., Review of computational fluid dynamics for wind turbine wake aerodynamics., Wind energy 14(7) (2011) 799–819.

[12] J. N. Sorensen, W. Z. Shen, X. Mundunate., Analysis of wake states by a full-field actuator disc model., Wind energy 1(1998) (1998) 73–88.

[13] C. Leclerc, C. Masson., Toward blade tip vortex simulation with an actuator lifting surface model., 42nd AIAA aerospace sciences meeting (2004) 667.

[14] C. Leclerc, C. Masson., Wind turbine performance predictions using a differential actuator-lifting disc model., Journal of solar energy engineering. 127(2005) (2005) 200–208.

[15] P. E. Rethore, P. Laan, N. Troldborg., Verification and validation of an actuator disc model., Wind energy 17(6) (2014) 919–937.

[16] R. Mikkeken., Actuator disc methods applied to wind turbines., Ph. D. thesis, DTU .

[17] S. Ivanell, Numerical computation of wind turbine wakes., Ph. D. thesis, KTH .

[18] J. N. Sorensen, W. Z. Shen., Numerical modelling of wind turbine wakes., Journal of fluids engineering. 124(2002) (2002) 393–399.

[19] N. Troldborg, Actuator line modelling of wind turbine wakes., Ph. D. thesis, DTU .

[20] H. Lu, F. P. Agel., Large eddy simulation of a very large wind farm in a stable atmospheric boundary layer., Physics of fluids. 23(2011) (2011) 23.

[21] Resource(online), http://www.windlogics.com/wp-content/uploads/2012/04/WindLogics2010-Development-and-Testing-of-a-Wind-Simulator-at-an-Operating-Wind-Farm.pdf .

[22] I. Dobrev, F. Massouh, M. Rapin., Actuator surface model hybrid model., The science of making torque from wind. 75(2007) (2007) 1–7.

[23] W. Z. Shen, J. H. Zhang, J. N. Sorensen., The actuator surface model: a new Navier-Stokes based model for rotor computations., Journal of solar energy engineering. 131(2009) (2009) 1–8.

[24] N. N. Sorensen, M. Hansen., Rotor performance predictions using a Navier-Stokes method., AIAA. (1998) 98–125.

[25] E. Duque, C. P. Dam, S. C. Hughes., Navier-Stokes simulations of the NREL combined experiment phase II rotor., AIAA. (2003) 99.

[26] E. Duque, M. D. Burklun, W. Johnson., Navier-Stokes and comprehensive analysis performance predictions of the NREL Phase VI experiment., AIAA. (2003) 355.

[27] G. Xu, L. N. Sankar., Effects of transition, turbulence, and yaw on the performance of horizontal axis wind turbines., AIAA. (2000) 48.

[28] H. A. Madsen, N. N. Sorensen, S. Schreck., Yaw aerodynamics analyzed with three codes in comparison with experiment., AIAA. (2003) 519.

[29] A. W. Lavely, G. Vijayakumar, M. P. Kinzel., Space-time loadings on wind turbine blades driven by atmospheric boundary layer turbulence., AIAA. (2011) 635.

[30] C. Sim, L. Manuel, S. Basu., A comparison of wind turbine load statistics for inflow turbulence fields based on conventional spectral methods and large eddy simulation., AIAA. (2010) 829.

[31] S. Lee, M. Churchfield, P. Moriarty, et al., Atmospheriic and wake turbulence impacts on wind turbine fatigue loading., NREL report. (2012) 1–15.

[32] M. O. L. Hansen, J. N. Sorensen, et al., State of the art in wind turbine aerodynamics and aero-elasticity., Progress in Aerospace Sciences 42(2006) (2006) 285–330.

[33] G. C. Larsen, etc., Dynamic wake meandering modelling., Riso report. Riso-R-1607 (2007.) 2538–2542.

[34] G. D. Sorensen, etc., Fatigue reliability and effective turbulence model in wind farms., Applications of Statistics and Probability in Civil Engineering. (2007) (2007.) 443–444.

[35] J. A. Dahlberg, M. Poppen, S. E. Thor., Load/fatigue effects on a wind turbine generator in a wind farm., Journal of wind engineering and industrial aerodynamics 39(1992) (1992) 199–209.

[36] P. Volund, Loads on a horizontal axis wind turbine operating in wake., Journal of wind engineering and industrial aerodynamics 37(1992) (1992) 317–328.

[37] S. Frandsen, L. Chacon, A. Crespo, et al., Measurements on and modelling of offshore wind farms., Riso report (1996) 903.

[38] K. Thomsen, P. Sorensen., Fatigue loads for wind turbines operating in wakes, Journal of wind engineering and industrial aerodynamics. 80(1999) (1999) 121–136.

[39] S. H. Kim, H. K. Shin, Y. C. Joo, et al., A study of the wake effects on the wind characteristics and fatigue loads for the turbines in a wind farm., Renewable energy 74(2015) (2015) 536–543.

[40] L. J. Vermeer, Wind turbine wake aerodynamics., Progress in aerospace sciences 39(6-7) (2003) 467–510.

[41] P. S. Veers, T. D. Ashwill., Trends in the design, manufacture and evaluation of wind turbine blades., Wind Energy. 6. (3.) (2003.) 245–259., ISSN 10954244.

[42] K. Thomsen, S. Poul., Fatigue loads for wind turbines operating in wakes., Journal of Wind Engineering. 80 (1999) 121–136.

[43] S. Lee, M. Churchfield., Atmospheric and Wake Turbulence Impacts on Wind Turbine Fatigue Loading., NREL Report. (December 2011.).

[44] A. Rezaeiha, R. Pereira., Fluctuations of angle of attack and lift coef fi cient and the resultant fatigue loads for a large Horizontal Axis Wind turbine., Renewable Energy. 114 (2017) 904–916, ISSN 0960-1481.

[45] K. Hayatand, et al., Load mitigation of wind turbine blade by aeroelastic tailoring via unbalanced laminates composites., Composite Structures. 128. (2015.) 122–133.

[46] A. P. Vassilopoulos., Introduction to the fatigue life prediction of composite materials and structures: past, present and future prospects., Woodhead Publishing. (2010.) 1–10.

[47] L. Nijssen., Fatigue Life Prediction and Strength Degradation of Wind Turbine Rotor Blade., Ph. D. Thesis. (2006.) 8–11.

[48] F. L. Ponta, A. D. Otero, et al., Energy for Sustainable Development The adaptive-blade concept in wind-power applications., Energy for Sustainable Development. 22. (2014.) 3–12, ISSN 0973-0826.

[49] D. W. Lobitz, P. S.Veers, Load mitigation with bending/twist-coupled blades on rotors using modern control strategies, Wind Energy 6 (2) (2003) 105–117, ISSN 10954244.

[50] A. R. Stäbleinand, H. Morten, et al., Fundamental aeroelastic properties of a bend–twist coupled blade section., Journal of Fluids and Structures. 68. (October 2016.) (2017.) 72–89.

[51] D. M. Andrea, D. B. Stefano, C. Raciti., Proposal for a coupled aerodynamic structural wind turbine blade optimization, Composite Structures 159 (2017) 144–156, ISSN 02638223.

[52] Z. J. Chen, K. A. Stol, B. R. Mace., Wind turbine blade optimisation with individual pitch and trailing edge flap control, Renewable Energy 103 (2017) 750–765, ISSN 09601481.

[53] M. O. L. Sørensen, et al., State of the art in wind turbine aerodynamics and aeroelasticity., Progress in Aerospace Sciences. 42. (2006.) 285–330.

[54] J. A. Epaarachchiand, D. Philip, The development of a fatigue loading spectrum for small wind turbine blades., Journal of Wind Engineering and Industrial Aerodynamics. 94 (2006) 207–223.

[55] D. H. Hodgesand, Assessment of Beam Modeling Methods for Rotor Blade Applications., Material and Computer Modelling 33. (2001.) 1099–1112.

[56] V. Giavotto, M. Borri, P. Mantegazza, et al., Anisotropic beam theory and applications, Computers & Structures 16 (1-4) (1983) 403–413, ISSN 00457949.

[57] T. Kim, A. M. Hansen, K. Branner., Development of an anisotropic beam finite element for composite wind turbine blades in multibody system., Renewable Energy. 59 (2013) 172–183, ISSN 09601481.

[58] D. H. Hodges., Nonlinear composite beam theory., American Institute of Aeronautics and Astronautics 213.

[59] D. H. Hodges, W. Yu., A rigorous, engineer-friendly approach for modelling realistic, composite rotor blades., Wind Energy 10(2007) (2007) 179–193.

[60] H. Chen, W. B. Yu, et al., A critical assessment of computer tools for calculating composite wind turbine blade properties., Wind Energy 13(2010) (2010) 497–516.

[61] T. Kim, A. M. Hansen, et al., Development of an anisotropic beam finite element for composite wind turbine blades in multibody system., Renewable Energy 59(2013) (2013) 172–183.

[62] S. Oye., FLEX4 simulation of wind turbine dynamics., In Proceedings of 28th IEA meeting. .

[63] F. Cianetti, A. Cetrini, et al., Dynamic modelling of wind turbines. Experimental tuning of a multibody model., Procedia Structural Integrity. 8(2018) (2018) 56–66.

[64] G. Fernandez, H. Usabiaga, et al., An efficient procedure for the calculation of the stress distribution in a wind turbine blade under aerodynamic loads., Journal of Wind Engineering and Industrial Aerodynamics. 172(2018) (2018) 42–54.

[65] A. Bajric, J. Hogsberg, et al., Evaluation of damping estimates by automated operational modal analysis for offshore wind turbine tower vibrations., Renewable Energy. 116(2018) (2018) 153–163.

[66] L. Wang, X. Liu, et al., State of the art in the aero-elasticity of wind turbine blades: aero-elastic modelling., Renewable and Sustainable Energy Reviews 64(2016) (2016) 195–210.

[67] H. Pollayi, W. Yu, et al., Modelling matrix cracking in composite rotor blades within VABS framework., Composite Structures 110(2014) (2014) 62–76.

[68] S. Shi, W. Shao, et al., Newmark-beta-FDTD method for super-resolution analysis of time reversal waves., Journal of Computational Physics 345(2017) (2017) 475–483.

[69] K. Yee., Numerical solution of initial boundary value problems involving Maxwell's equations in isotropic media., IEEE Transactions on Antennas and Propagation 14(3) (1966) 302–307.

[70] J. Smagorinsky, General Circulation Experiments with the Primitive Equations., Monthly Weather Review 91(3) (1963) 99–164.

[71] S. Huang, Q. S. Li, A new dynamic one-equation subgrid-scale model for large eddy simulations., International journal for numerical methods in engineering 81 (2010) 835–865.

[72] N. Troldborg, Actuator Line Modeling of Wind Turbine Wakes., DTU Ph. D. thesis. 136 (2009) 25–26.

[73] P. K. Jha, M. J. Churchfield, P. J. Moriaty, Guidelines for Volume Force Distributions Within Actuator Line Modeling of Wind Turbines on Large-Eddy Simulation-Type Grids., Journal of solar energy engieering. 136 (2014) 1–11.

[74] P. A. Krogstad, P. E. Eriksen, Blind test calculations of the performance and wake development for a model wind turbine., Renewable energy. 50(2013) (2013) 325–333.

[75] U. Schumann., Subgrid scale model for finite difference simulations of turbulent flows in plane channels and annuli., Journal of computational physics. 18(4). (1975.) 376–404.

[76] M. Churchfield, S. Lee, et al., A Numerical Study of the Effects of Atmospheric and Wake Turbulence on Wind Turbine Dynamics., Journal of turbulence. 13(14). (2012.) 1–32.

[77] GL, Guideline for the Certification of Wind Turbines, Lloyd Rules and Guidelines, IV–Industrial Services (2010) 155 – 164(pdf).

[78] P. Blasques, R. Bitsche, V. Fedorov, M. Eder., Applications of the BEam Cross Section Analysis Software (BECAS) (2013) 1–4.

[79] J. P. Blasques, M. Stolpe., Multi-material topology optimization of laminated composite beam cross sections., Composite Structures 94 (11) (2012) 3278–3289, ISSN 02638223.

[80] N. M. Newmark, A method of computation for structural dynamics, Journal of Engineering Mechanics 85 ((EM3)) (1959) 67–94.

[81] J. Jonkman, S. Butterfield, W. Musial, G. Scott, Definition of a 5-MW reference wind turbine for offshore system development, Contract (February) (2009) 1–75, ISSN 01487299.

[82] B. R. Resor, Definition of a 5MW/61.5m Wind Turbine Blade Reference Model (Sandia Report) (2013) 50.

[83] M. R. Luhur, J. Peinke, M. Kuhn., Stochastic model for aerodynamic force dynamics on wind turbine blades in unsteady wind inflow., Journal of computational nonlinear dynamics. 10(4) (2015.) 1–12.

[84] J. W. Larsen, S. R. K. Nielsen, S. Krenk., Dynamic stall model for wind turbine airfoils., Journal of fluids and structures. 23(2007) (2007.) 959–982.

[85] P. S. Veers., Three Dimensional Wind Simulation (Sandia Report) (1988) 40.

[86] A. D. Otero, F. L.Ponta., Structural Analysis of Wind-Turbine Blades by a Generalized Timoshenko Beam Model, Journal of Solar Energy Engineering 132 (1) (2010) 011015, ISSN 01996231.

[87] J. C. Simo, L. Vu-Quoc, et al., On the dynamics of flexible beams under large overall motions., Journal of Applied Mechanics 53(4) (1986) 849–854.

[88] J. Crank, P. Nicolson, A Practical Method for Numerical Evaluation of Solutions of Partial Differential Equations of Heat Conduction Type., Proc. Camb. Phil. Soc. 43 (1947.) 50–67.

Appendix A

Derivation of structure model for explicit elastic actuator line

A.1 Equilibrium equations (the dynamics of beam element)

In this section, the one-dimensional equilibrium equations are constructed on each beam element by using Newtonian method. The balance of moments and forces of direction 0 is based on the coordinate system in Figure A.1. The F and M are sectional shear force and bending moments. f_e and M_e are external force and moments on the beam section.

The equilibrium of force resultant along direction 0 is shown in Equation (A.1).

$$\frac{dF_0}{dr} + f_{e,0} = 0 \tag{A.1}$$

The equilibrium of moment resultant along direction 0 is shown in Equation (A.2).

$$\frac{dM_0}{dr} - m_{e,0} - F_0 = 0 \tag{A.2}$$

Combing the Equations (A.1) and (A.2), we have the Equation (A.4).

$$\frac{d^2M_0}{dr^2} - \frac{dm_{e,0}}{dr} + f_{e,0} = 0 \tag{A.3}$$

Based on Figure A.2, the equation for direction 1 is shown in Equation (A.4).

$$\frac{d^2M_1}{dr^2} - \frac{dM_{e,1}}{dr} + f_{e,1} = 0 \tag{A.4}$$
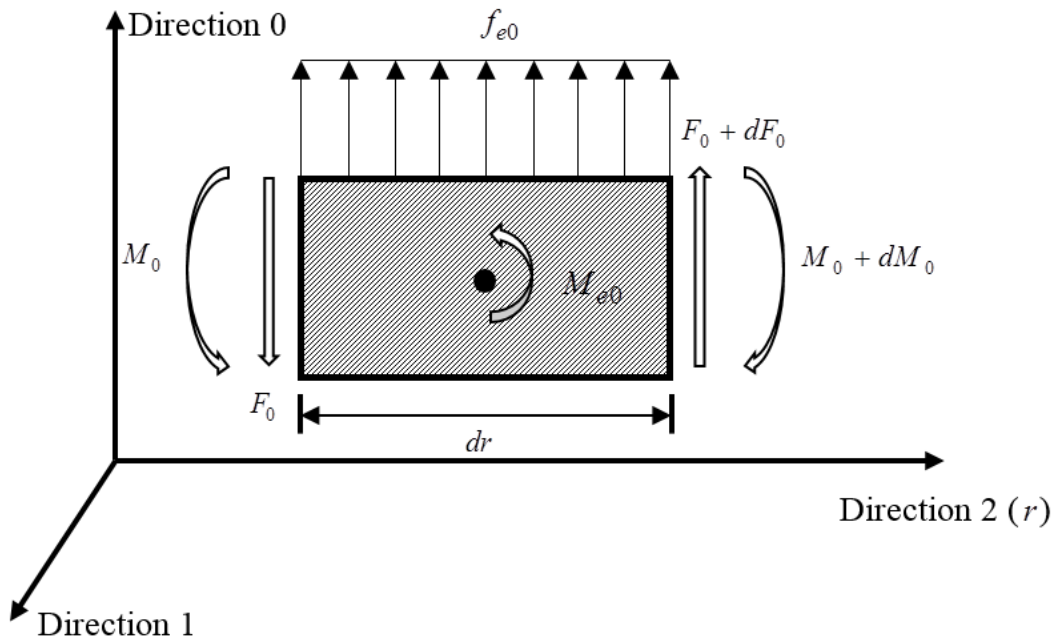
Figure A.1 The sketch for the moments and forces along direction 0.
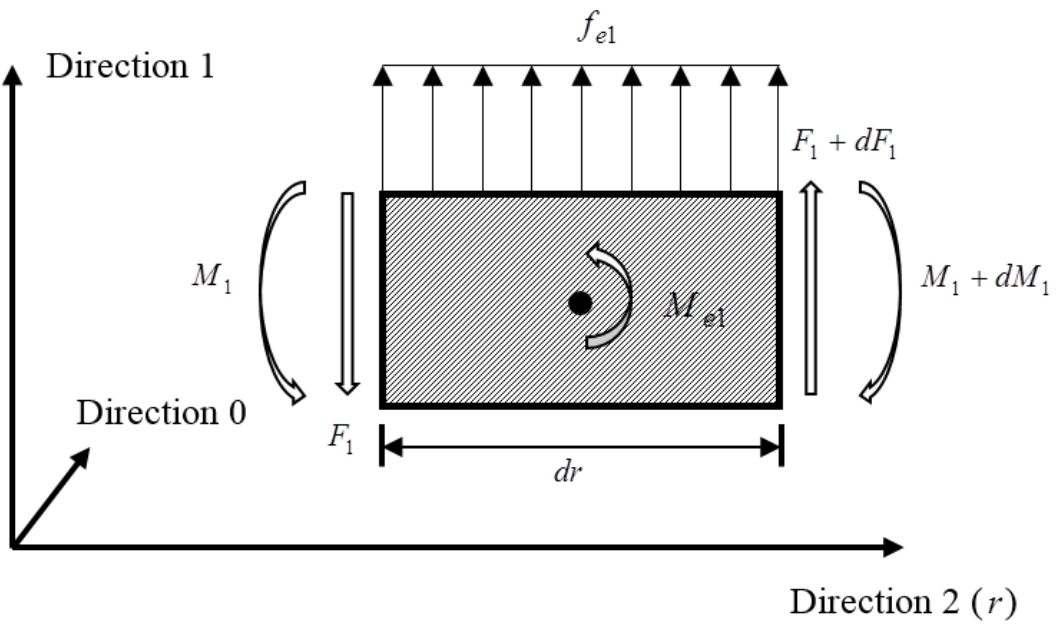
Figure A.2 The sketch for the moments and forces along direction 1.

To further analyse and establish the governing structure equations of wind turbine blade, the external force and moments should be seriously considered, which consists of three parts: inertia force (centrifugal force), aerodynamic force, and gravitational force.

$$\vec{f_e} = \rho_s \vec{a} + \vec{f_a} + \rho_s \vec{g} = -\rho_s \frac{d^2 \vec{q}}{dt^2} + \vec{f_a} + \vec{f_g} \tag{A.5}$$

The external moments is caused by the centrifugal force:

$$\vec{M_e} = -N(r) \frac{d\vec{q}}{dr} \tag{A.6}$$

Among this equation, $N(r)$ is the centrifugal force:

$$N(r) = \int_r^R \rho_s(r) \Omega^2 r \, dr \tag{A.7}$$

The derived equilibrium equations are:

$$\rho_s \frac{\partial^2 q_0}{\partial t^2} - \frac{\partial^2 M_0}{\partial r^2} - \frac{\partial}{\partial r}(N(r) \frac{\partial q_0}{\partial r}) - f_{a,0} - f_{g,0} \tag{A.8}$$

$$\rho_s \frac{\partial^2 q_1}{\partial t^2} - \frac{\partial^2 M_1}{\partial r^2} - \frac{\partial}{\partial r}(N(r) \frac{\partial q_1}{\partial r}) - f_{a,1} - f_{g,1} \tag{A.9}$$

A.2 Kinematics of the beam element based on Euler-Bernoulli assumption

The derived Equations (A.8) and (A.9) have two variables redundant, which are M_0 and M_1. To remove the redundant variables, the relation between moments and displacements should be built by applying the kinematics analysis of the beam. For ad-hoc beam models, the displacement field (kinematics) for each point in the beam is assumed to be a function of displacements of the beam section. The Euler-Bernoulli assumptions for beam models are as follows:

(1) the cross section is infinitely rigid in its own plane, and any material point in the plane of the cross section solely consists of two rigid body translations.

(2) the cross section of a beam remains the same plane after deformation.

(3) the cross section remains normal to the deformed axis of the beam (see Figure A.3 and A.4).

The derivation also neglects the impact of transverse deflection and the associated radial shortening on the centrifugal force.
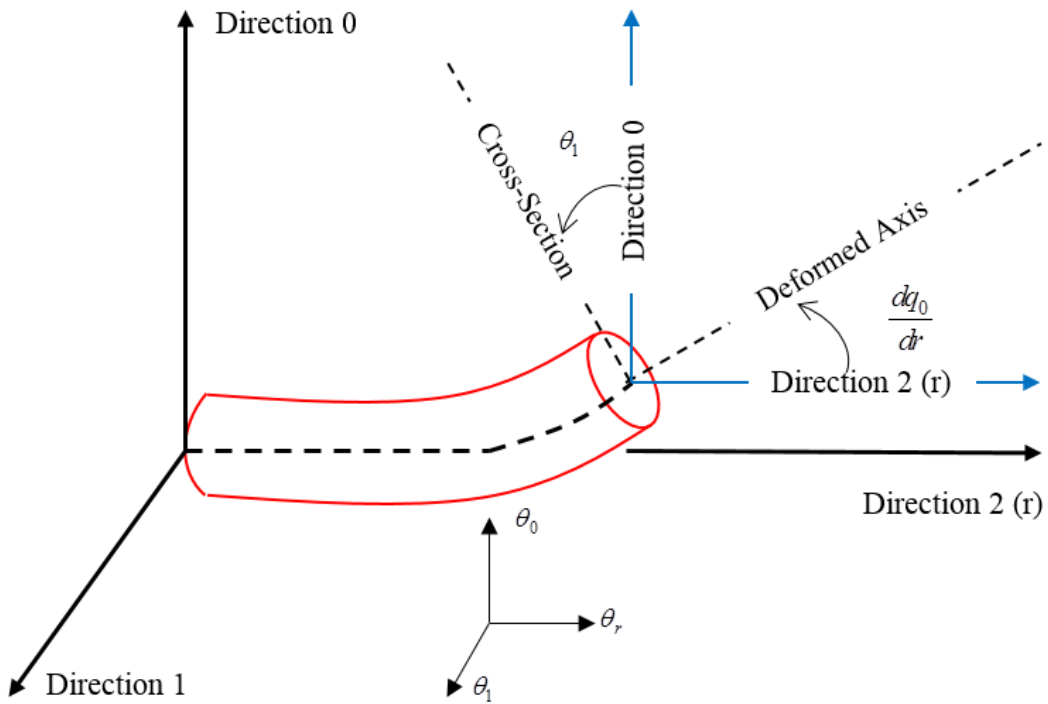
Figure A.3 Illustration of Euler-Bernoulli assumption.
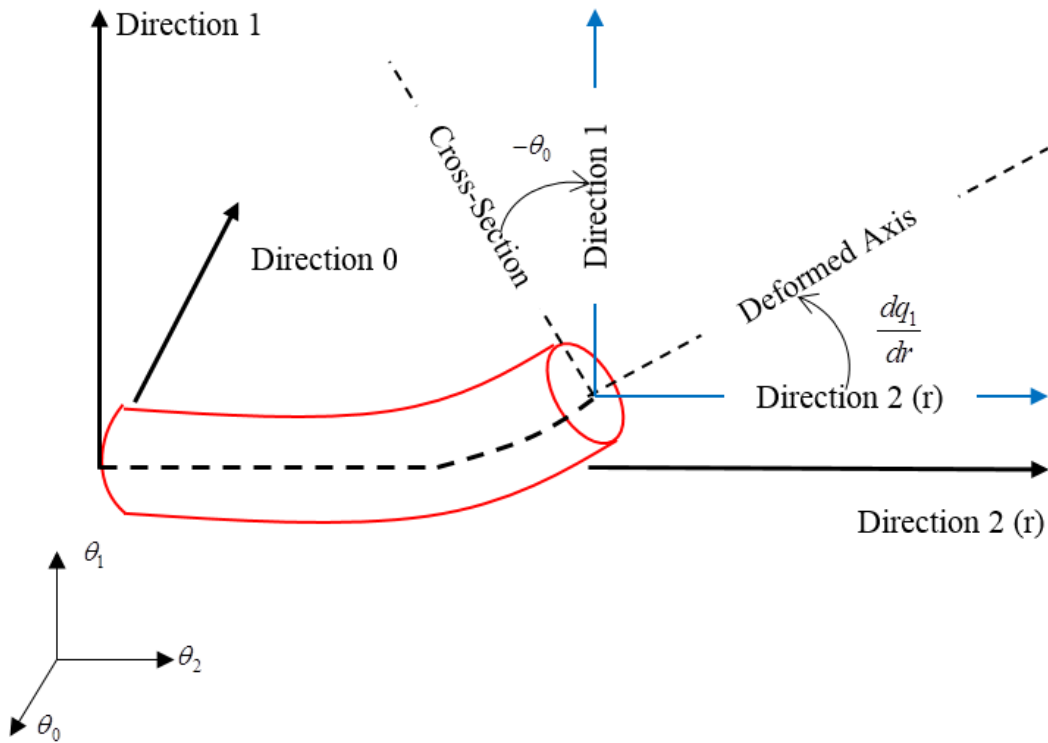
Figure A.4 Illustration of Euler-Bernoulli assumption.

Based on the first assumption, the displacements for each point (q') along directions 0 and 1 are:

$$q'_0(x_0, x_1, r) = q_0(r) \tag{A.10}$$

$$q'_1(x_0, x_1, r) = q_1(r) \tag{A.11}$$

According to the second assumption, the q'_r can be derived:

$$q'_r(x_0, x_1, r) = q_r(r) - x_0\omega_1(r) + x_1\omega_0(r) \tag{A.12}$$

According to the third assumption, we have:

$$\omega_1 = \frac{dq_0(r)}{dr} \tag{A.13}$$

$$\omega_0 = \frac{dq_1(r)}{dr} \tag{A.14}$$

$$q'_r(x_0, x_1, r) = q_r(r) - x_0\frac{dq_0(r)}{dr} + x_1\frac{dq_1(r)}{dr} \tag{A.15}$$

Based on the infinitesimal strain field assumption, we have

$$\epsilon_{ij} = \frac{1}{2}(q'_{i,j} + q'_{j,i}) \tag{A.16}$$

In which

$$\epsilon_{rr} = \frac{dq_r(r)}{dr} - x_0\frac{d^2q_0(r)}{dr^2} - x_1\frac{d^2q_1(r)}{dr^2} \tag{A.17}$$

By applying Hooke's law, the stress can be calculated as

$$\sigma_{rr} = E\epsilon_{rr} = E(\frac{dq_r(r)}{dr} - x_0\frac{d^2q_0(r)}{dr^2} - x_1\frac{d^2q_1(r)}{dr^2}) \tag{A.18}$$

The moments M_0 and M_1 are

$$M_0 = \int_A x_0\sigma_{rr}dA = \int_A x_0 E(\frac{dq_r(r)}{dr} - x_0\frac{d^2q_0(r)}{dr^2} - x_1\frac{d^2q_1(r)}{dr^2})dA \tag{A.19}$$

$$M_1 = \int_A x_1\sigma_{rr}dA = \int_A x_1 E(\frac{dq_r(r)}{dr} - x_0\frac{d^2q_0(r)}{dr^2} - x_1\frac{d^2q_1(r)}{dr^2})dA \tag{A.20}$$

As a result, we derived the equations of M and displacements:

$$\begin{bmatrix} M_0 \\ M_1 \end{bmatrix} = \begin{bmatrix} -\int_A E x_0^2 dA & -\int_A E x_0 x_1 dA \\ -\int_A E x_0 x_1 dA & -\int_A E x_1^2 dA \end{bmatrix} \begin{bmatrix} \frac{d^2 q_0}{dr^2} \\ \frac{d^2 q_1}{dr^2} \end{bmatrix} \tag{A.21}$$

The governing equations (Equation (3.2) - (3.3)) can be derived by combining the equilibrium and kinematics equations.

Appendix B

Stability analysis of the structure model in elastic actuator line.

According to von Neumann stability analysis [88]

$$V_i = \sum_{k=0}^{J-1} A_k \omega_i^k \tag{B.1}$$

$$M_i = \sum_{k=0}^{J-1} B_k \omega_i^k \tag{B.2}$$

$$\omega_i^k = e^{il_k x} \tag{B.3}$$

Here A_k is the error amplitude. l_k is the wave number.

Substitute the above equations into the governing equations (drop the aerodynamic force and gravitational force terms), we have:

$$\frac{A_k^{n+1} - A_k^n}{\Delta t} = -\frac{1}{\rho_s} \frac{B_k^n (2\cos\frac{2\pi k}{J} - 2)}{\Delta r^2} \tag{B.4}$$

$$\frac{B_k^{n+1} - B_k^n}{\Delta t} = EI \frac{A_k^n (2\cos\frac{2\pi k}{J} - 2)}{\Delta r^2} \tag{B.5}$$

Then

$$A_k^{n+1} = A_k^n + \eta_1 B_k^n \tag{B.6}$$

$$A_k^{n+1} + \eta_2 B_k^{n+1} = B_k^n \tag{B.7}$$

Where

$$\eta_1 = \frac{4\Delta t}{\rho_s \Delta r^2} \sin^2 \frac{\pi k}{J} \tag{B.8}$$

$$\eta_2 = \frac{4\Delta t}{\Delta r^2} EI \sin^2 \frac{\pi k}{J} \tag{B.9}$$

Then we can derive:

$$\begin{bmatrix} A_k^{n+1} \\ B_k^{n+1} \end{bmatrix} = \mathbf{G} \begin{bmatrix} A_k^n \\ B_k^n \end{bmatrix} \tag{B.10}$$

Where

$$\mathbf{G} = \begin{bmatrix} 1 & \eta_1 \\ -\eta_2 & 1 - \eta_1\eta_2 \end{bmatrix} \tag{B.11}$$

To guarantee the stability of the numerical equations, $|G^n|$ should be bounded.

$$\mathbf{G}^n = \mathbf{T} \begin{bmatrix} \lambda^{(1)} & \cdots & \cdots & 0 \\ \vdots & \lambda^{(2)} & \cdots & 0 \\ \vdots & \vdots & \ddots & \vdots \\ 0 & 0 & \cdots & \lambda^{(P)} \end{bmatrix} \mathbf{T}^{-1} \tag{B.12}$$

T is the normalized eigenvector of G (p is the number of columns of G), and

$$|(\mathbf{T}^{-1})_{ij}| \le \frac{1}{|\Delta|} \tag{B.13}$$

Δ is the determinant of T, so that

$$|(G^n)_{ij}| \le \frac{p^2}{|\Delta|} R^n \tag{B.14}$$

Where

$$R = \max |\lambda^i| \tag{B.15}$$

Then

$$|\mathbf{G}^n| \le \frac{p^3}{|\Delta|} R^n \tag{B.16}$$

As a result, $|\Delta|$ should not be equal to zero to guarantee stability. According to this, the appropriate time step can be derived:

$$4(\frac{\Delta t}{\Delta r^2})^2 \frac{EI}{\rho_s} \sin^4 \frac{\pi k}{J} - 1 < 0 \qquad \text{(B.17)}$$

$$\Delta t < \frac{1}{2}\sqrt{\frac{\rho_s}{EI}} \Delta r^2 \qquad \text{(B.18)}$$

Appendix C

Two-dimensional cross-sectional model (BECAS)

The elements in parameter matrices for 2D sectional model (from Equation (4.5) to Equation (4.6)) are listed in this appendix. All of these information is summarized from the BECAS tutorial [79]. Most of the parameters are about surface integral of blade section.

$$\underset{(6\times6)}{\mathbf{A}} = \sum_{e=1}^{n_e} \int_A \mathbf{Z}_e^T \mathbf{S}_e^T \mathbf{Q}_e \mathbf{S}_e \mathbf{Z}_e dA \tag{C.1}$$

$$\underset{(n_d\times6)}{\mathbf{R}} = \sum_{e=1}^{n_e} \int_A \mathbf{B}_e^T \mathbf{Q}_e \mathbf{S}_e \mathbf{Z}_e dA \tag{C.2}$$

$$\underset{(n_d\times n_d)}{\mathbf{E}} = \sum_{e=1}^{n_e} \int_A \mathbf{B}_e^T \mathbf{Q}_e \mathbf{B}_e dA \tag{C.3}$$

$$\underset{(n_d\times n_d)}{\mathbf{C}} = \sum_{e=1}^{n_e} \int_A \mathbf{B}_e^T \mathbf{Q}_e \mathbf{S}_e \mathbf{N}_{2d,e} dA \tag{C.4}$$

$$\underset{(6\times n_d)}{\mathbf{L}} = \sum_{e=1}^{n_e} \int_A \mathbf{Z}_e^T \mathbf{S}_e^T \mathbf{Q}_e \mathbf{S}_e \mathbf{N}_{2d,e} dA \tag{C.5}$$

$$\underset{(n_d\times n_d)}{\mathbf{M}} = \sum_{e=1}^{n_e} \int_A \mathbf{N}_{2d,e}^T \mathbf{S}_e^T \mathbf{Q}_e \mathbf{S}_e \mathbf{N}_{2d,e} dA \tag{C.6}$$

$$\underset{(n_d\times6)}{\mathbf{D}} = \begin{bmatrix} \mathbf{I}_3 & \cdots & \mathbf{I}_3 \\ \mathbf{n}_1 & \cdots & \mathbf{n}_{n_n} \end{bmatrix}^T \tag{C.7}$$

In Equation (C.7), $\mathbf{n}$ has the same form of the $\mathbf{n}_e$ in Equation (C.10). And $\mathbf{I}_3$ is a unitary matrix. In those equations, $\mathbf{N}_{2d,e}$ is the two-dimensional shape function for a finite

179

element on the cross section of the blade, which is four-node element in this study. $\mathbf{Q}_e$ is the elementary material constitutive matrix in Hooke's law, in which $\boldsymbol{\sigma}_e = \mathbf{Q}_e \boldsymbol{\epsilon}_e$ ($\boldsymbol{\sigma}_e$ is the elementary stress and $\boldsymbol{\epsilon}_e$ is the elementary strain).

$$\mathbf{B}_e = \begin{bmatrix} \frac{\partial}{\partial x} & 0 & 0 \\ 0 & \frac{\partial}{\partial y} & 0 \\ \frac{\partial}{\partial y} & \frac{\partial}{\partial x} & 0 \\ 0 & 0 & \frac{\partial}{\partial x} \\ 0 & 0 & \frac{\partial}{\partial y} \\ 0 & 0 & 0 \end{bmatrix} \tag{C.8}$$

$$\mathbf{Z}_e_{(3\times6)} = \begin{bmatrix} \mathbf{I}_3 & \mathbf{n}_e \end{bmatrix} \tag{C.9}$$

$$\mathbf{n}_e = \begin{bmatrix} 0 & 0 & y \\ 0 & 0 & -x \\ -y & x & 0 \end{bmatrix} \tag{C.10}$$

$$\mathbf{S}_e = \begin{bmatrix} 0 & 0 & 0 \\ 0 & 0 & 0 \\ 0 & 0 & 0 \\ 1 & 0 & 0 \\ 0 & 1 & 0 \\ 0 & 0 & 1 \end{bmatrix} \tag{C.11}$$

$$\mathbf{T}_r = \begin{bmatrix} 0 & 0 & 0 & 0 & -1 & 0 \\ 0 & 0 & 0 & 0 & 1 & 0 \\ 0 & 0 & 0 & 0 & 0 & 0 \\ 0 & 0 & 0 & 0 & 0 & 0 \\ 0 & 0 & 0 & 0 & 0 & 0 \\ 0 & 0 & 0 & 0 & 0 & 0 \end{bmatrix} \tag{C.12}$$

Appendix D

One-dimensional beam model

This appendix is about the parameters of one dimensional anisotropic beam model. The derivation of the model can be found in [57]. To begin with, the shape function is given as follows:

$$\underset{(6\times24)}{\mathbf{N}} = \begin{bmatrix} \underset{(6\times6)}{\mathbf{I}} & \underset{(6\times6)}{z\mathbf{I}} & \underset{(6\times6)}{(z)^2\mathbf{I}} & \underset{(6\times6)}{(z)^3\mathbf{I}} \end{bmatrix} \tag{D.1}$$

Where z in Equation (D.1) is defined in Figure 1. The following equations are used to deal with $\mathbf{N}_\alpha$ from Equation (4.11). z_1 and z_2 are the z positions of two nodes of one beam element.

$$\underset{(24\times24)}{\mathbf{N}_d} = \begin{bmatrix} \underset{(12\times24)}{\mathbf{N}(z_1)} \\ \underset{(12\times24)}{\mathbf{N}(z_2)} \end{bmatrix} = \begin{bmatrix} \underset{(24\times12)}{\mathbf{N}_1} & \underset{(24\times12)}{\mathbf{N}_2} \end{bmatrix} \tag{D.2}$$

$$\underset{(6\times24)}{\mathbf{A}_{\alpha1}} = \begin{bmatrix} \underset{(12\times12)}{\mathbf{I}} \\ \underset{(12\times12)}{\mathbf{0}} \end{bmatrix} \tag{D.3}$$

$$\underset{(6\times24)}{\mathbf{A}_{\alpha2}} = \begin{bmatrix} \underset{(12\times12)}{\mathbf{0}} \\ \underset{(12\times12)}{\mathbf{I}} \end{bmatrix} \tag{D.4}$$

$$\mathbf{Y}_1 = \mathbf{A}_{\alpha1}\mathbf{N}_1^{-1} \tag{D.5}$$

$$\mathbf{Y}_2 = \mathbf{A}_{\alpha2} - \mathbf{A}_{\alpha1}\mathbf{N}_1^{-1}\mathbf{N}_2 \tag{D.6}$$

$$\mathbf{B}_s = \mathbf{T}_r\mathbf{N}(z') + \mathbf{I}_6\mathbf{N}'(z) \tag{D.7}$$

$$\mathbf{D}_s = \int_{z_1}^{z_2} \mathbf{B}_s^T\mathbf{K}_s\mathbf{B}_s dz \tag{D.8}$$

$$\mathbf{P} = \mathbf{Y}_2^T\mathbf{D}_s\mathbf{Y}_1 \tag{D.9}$$

$$\mathbf{Q} = -\mathbf{Y}_2^T\mathbf{D}_s\mathbf{Y}_2 \tag{D.10}$$

Lastly, the formula of $\mathbf{N}_\alpha$ is as follows:

$$\mathbf{N}_\alpha = \mathbf{Y}_1 + \mathbf{Y}_2\mathbf{Q}^{-1}\mathbf{P} \qquad\qquad (\text{D.11})$$

Appendix E

Derivation for the equilibrium and constitutive equations

According to Figure 5.1, the deformed beam element vector $\mathbf{AB}$ is as follows:

$$\mathbf{A'B'} = d\mathbf{r}_l = d\mathbf{r} + \mathbf{q}_B - \mathbf{q}_A = dr\mathbf{k} + d\mathbf{q} \tag{E.1}$$

where

$$d\mathbf{r} = dr\mathbf{k} \tag{E.2}$$

and

$$d\mathbf{q} = \mathbf{q}_B - \mathbf{q}_A \tag{E.3}$$

For the moments and forces balance, we have:

$$\begin{cases} \mathbf{M}_{B'} - \mathbf{M}_{A'} + d\mathbf{r}_l \times \mathbf{F}_{B'} + \mathbf{M}_e = 0 & \text{moment balance} \\ \mathbf{F}_{B'} - \mathbf{F}_{A'} + \mathbf{F}_e = 0 & \text{force balance} \end{cases} \tag{E.4}$$

where

$$\mathbf{M}_{B'} - \mathbf{M}_{A'} = d\mathbf{M} \tag{E.5}$$

and

$$\mathbf{F}_{B'} - \mathbf{F}_{A'} = d\mathbf{F} \tag{E.6}$$

It is also known that

$$dr_l \times F = \begin{vmatrix} \mathbf{i} & \mathbf{j} & \mathbf{k} \\ dq_x & dq_y & dq_r + dr \\ F_x & F_y & F_r \end{vmatrix} = [F_r dq_y - F_y(dq_r + dr)]\mathbf{i} + [F_x(dq_r + dr) - F_r dq_x]\mathbf{j} + (F_y dq_x - F_x dq_y)\mathbf{k}$$

$$(E.7)$$

Substitute Equations (E.5) - (E.7) into Equation (E.4), we have the following equations:

$$\frac{dF_x}{dr} + F_{e,x} = 0 \tag{E.8}$$

$$\frac{dF_y}{dr} + F_{e,y} = 0 \tag{E.9}$$

$$\frac{dF_r}{dr} + F_{e,r} = 0 \tag{E.10}$$

$$\frac{dM_x}{dr} + F_r \frac{dq_y}{dr} - F_y \frac{dq_r}{dr} - F_y + M_{e,x} = 0 \tag{E.11}$$

$$\frac{dM_y}{dr} - F_r \frac{dq_x}{dr} + F_x \frac{dq_r}{dr} + F_x + M_{e,y} = 0 \tag{E.12}$$

$$\frac{dM_r}{dr} + F_y \frac{dq_x}{dr} - F_x \frac{dq_y}{dr} + M_{e,r} = 0 \tag{E.13}$$

And we further substitute the inertia forces (non-inertia frame), which are shown as the following equations, into above equations.

$$\begin{bmatrix} F_{ei,x} \\ F_{ei,y} \\ F_{ei,r} \\ M_{ei,x} \\ M_{ei,y} \\ M_{ei,r} \end{bmatrix} = - \begin{bmatrix} \rho_s & 0 & 0 & 0 & 0 & -\rho_s y_m \\ 0 & \rho_s & 0 & 0 & 0 & \rho_s x_m \\ 0 & 0 & \rho_s & \rho_s y_m & -\rho_s x_m & 0 \\ 0 & 0 & \rho_s y_m & I_{xx} & -I_{xy} & 0 \\ 0 & 0 & -\rho_s x_m & -I_{xy} & I_{yy} & 0 \\ -\rho_s y_m & \rho_s x_m & 0 & 0 & 0 & I_{xx} I_{yy} \end{bmatrix} \begin{bmatrix} \ddot{q}_x \\ \ddot{q}_y \\ \ddot{q}_r \\ \ddot{\varphi}_x \\ \ddot{\varphi}_y \\ \ddot{\varphi}_r \end{bmatrix} \tag{E.14}$$

We will finally have the equilibrium equations of anisotropic wind turbine blade (Equations (5.7) - (5.12)).

The generalized strain (with small rotation assumption) for the cross section is:

$$\epsilon = \begin{bmatrix} \frac{dq_x}{dr} - \varphi_y & \frac{dq_y}{dr} + \varphi_x & \frac{dq_r}{dr} & \frac{d\varphi_x}{dr} & \frac{d\varphi_y}{dr} & \frac{d\varphi_r}{dr} \end{bmatrix}^T \tag{E.15}$$

The constitutive equation is:

$$\mathbf{P} = \mathbf{K}_s \boldsymbol{\epsilon} \qquad (E.16)$$

which is the Equation (5.14).

Appendix F

Derivation of inertia forces (floating frame)

From Figure 5.7, we have the displacement for a point on the cross section:

$$\vec{\phi}(r, x, t) = \vec{\phi}_0(r, t) + x\vec{t_2}(r, t) \tag{F.1}$$

where

$$\vec{\phi}_0(r, t) = [r + q_r(r, t)]\vec{k}_1 + q_x(r, t)\vec{i}_1 \tag{F.2}$$

and

$$\vec{t_1}(r, t) = \cos(\varphi_y(r, t))\vec{k}_1 + \sin(\varphi_y(r, t))\vec{i}_1 \tag{F.3}$$

$$\vec{t_2}(r, t) = -\sin(\varphi_y(r, t))\vec{k}_1 + \cos(\varphi_y(r, t))\vec{i}_1 \tag{F.4}$$

The time derivatives for the vectors are as follows:

$$\dot{\vec{k}}_1 = \Omega\vec{i}_1 \tag{F.5}$$

$$\dot{\vec{i}}_1 = -\Omega\vec{k}_1 \tag{F.6}$$

$$\dot{\vec{t}}_1 = (\omega_y + \Omega)\vec{t}_2 \tag{F.7}$$

$$\dot{\vec{t}}_2 = -(\omega_y + \Omega)\vec{t}_1 \tag{F.8}$$

The first order time derivative of the displacement vector (velocities) is as follows:

$$\dot{\vec{\phi}} = \dot{\vec{\phi}}_0 - x(\omega_y + \Omega)\vec{t}_1 \tag{F.9}$$

Further expanding the above equation, we have:

$$\dot{\vec{\phi}}(r, x, t) = (V_r - \Omega q_x)\vec{k}_1 + [V_x + \Omega(r + q_r)]\vec{i}_1 - x(\omega_y + \Omega)\vec{t}_1 \tag{F.10}$$

And the second order time derivative (acceleration):

$$\ddot{\vec{\phi}}(r, x, t) = [\frac{\partial V_r}{\partial t} - 2V_x\Omega - q_x\dot{\Omega} - (r+q_r)\Omega^2]\vec{k}_1 + [\frac{\partial V_x}{\partial t} + 2V_r\Omega + (r+q_r)\dot{\Omega} - q_x\Omega^2]\vec{i}_1 - x(\omega_y - \Omega)^2\vec{t}_2 - x(\frac{\partial \omega_y}{\partial t} + \dot{\Omega})\vec{t}_1 \tag{F.11}$$

The above equation illustrate the inertia forces in the floating frame. And the shear strain and the curvature for the beam section are:

$$\vec{\gamma} = \frac{\partial \vec{\phi}_0}{\partial r} - \vec{t}_1 = (1 + \frac{\partial q_r}{\partial r} - \cos(\varphi_y))\vec{k}_1 + (\frac{\partial q_x}{\partial r} - \sin(\varphi_y))\vec{i}_1 = \gamma_r\vec{k}_1 + \gamma_x\vec{i}_1 \tag{F.12}$$

$$\vec{\kappa} = \frac{\partial \varphi_y}{\partial r}\vec{t}_3 = \frac{\partial \varphi_y}{\partial r}\vec{j}_1 = \kappa_y\vec{j}_1 \tag{F.13}$$

The constitutive equations for the beam section in the spin-up maneuver case is as follows:

$$F_r = EA(1 + \frac{\partial q_r}{\partial r} - \cos(\varphi_y)) \approx EA\frac{\partial q_r}{\partial r} \tag{F.14}$$

$$F_x = GA(\frac{\partial q_x}{\partial r} - \sin(\varphi_y)) \approx GA(\frac{\partial q_x}{\partial r} - \varphi_y) \tag{F.15}$$

$$M_y = EI\frac{\partial \varphi_y}{\partial r} \tag{F.16}$$

Appendix G

Elastic actuator line code example

G.1 Explicit elastic actuator line

```cpp
void horizontalAxisWindTurbinesALM::deformation()
{

    Info<<"deformation start hi this is perturb"<<endl;
    // Proceed turbine by turbine.

    IOdictionary def_inivalue
    (
     IOobject
     (
      "def_inivalue",
      runTime_.constant(),"turbineProperties",
      mesh_,
      IOobject::MUST_READ,
      IOobject::AUTO_WRITE
     )
    );

    IOdictionary turbineArrayProperties
    (
        IOobject
        (
            "turbineArrayProperties",
            runTime_.constant(),
            mesh_,
            IOobject::MUST_READ,
            IOobject::AUTO_WRITE
        )
    );
```

```cpp
30
31
32        // clear the initial values
33        def_inivalue.lookup("M00").clear();
34        def_inivalue.lookup("M10").clear();
35        def_inivalue.lookup("Def0").clear();
36        def_inivalue.lookup("Def1").clear();
37        def_inivalue.lookup("Sc00").clear();
38        def_inivalue.lookup("Sc10").clear();
39        def_inivalue.lookup("v00").clear();
40        def_inivalue.lookup("v10").clear();
41        def_inivalue.lookup("dvel0").clear();
42        def_inivalue.lookup("dvel1").clear();
43
44    // build new initial value
45
46        def_inivalue.lookup("M00").append(word("("));
47        def_inivalue.lookup("M10").append(word("("));
48        def_inivalue.lookup("Def0").append(word("("));
49        def_inivalue.lookup("Def1").append(word("("));
50        def_inivalue.lookup("Sc00").append(word("("));
51        def_inivalue.lookup("Sc10").append(word("("));
52        def_inivalue.lookup("v00").append(word("("));
53        def_inivalue.lookup("v10").append(word("("));
54        def_inivalue.lookup("dvel0").append(word("("));
55        def_inivalue.lookup("dvel1").append(word("("));
56
57     forAll(windVectors, i)
58     {
59         turbineArrayProperties.subDict(turbineName[i]).lookup("Azimuth")
    .clear();
60         turbineArrayProperties.subDict(turbineName[i]).lookup("Azimuth")
    .append(azimuth[i]/degRad);
61         turbineArrayProperties.subDict(turbineName[i]).lookup("RotSpeed"
    ).clear();
62         turbineArrayProperties.subDict(turbineName[i]).lookup("RotSpeed"
    ).append(rotSpeed[i]/rpmRadSec);
63         turbineArrayProperties.subDict(turbineName[i]).lookup("TorqueGen
    ").clear();
64         turbineArrayProperties.subDict(turbineName[i]).lookup("TorqueGen
    ").append(torqueGen[i]);
65         turbineArrayProperties.subDict(turbineName[i]).lookup("Pitch").
    clear();
66         turbineArrayProperties.subDict(turbineName[i]).lookup("Pitch").
    append(pitch[i]);
67         turbineArrayProperties.subDict(turbineName[i]).lookup("NacYaw").
    clear();
```

```
68          turbineArrayProperties.subDict(turbineName[i]).lookup("NacYaw").
     append(nacYaw[i]/degRad);
69
70          Info<<"dt="<<dt<<endl;
71          Info<<"deltt="<<deltt[i]<<endl;
72          Info<<"deltNo="<<dt/deltt[i]<<endl;
73          Info<<"deltNoint="<<int(dt/deltt[i]+1)<<endl;
74
75          for(int l=0;l<int(dt/deltt[i]+1);l++)
76          {
77
78          if (actuatorlinetype[i] == "elastic")
79   {
80
81   if (l == 0)
82   {
83
84          def_inivalue.lookup("M00").append(word("("));
85          def_inivalue.lookup("M10").append(word("("));
86          def_inivalue.lookup("Def0").append(word("("));
87          def_inivalue.lookup("Def1").append(word("("));
88          def_inivalue.lookup("Sc00").append(word("("));
89          def_inivalue.lookup("Sc10").append(word("("));
90          def_inivalue.lookup("v00").append(word("("));
91          def_inivalue.lookup("v10").append(word("("));
92          def_inivalue.lookup("dvel0").append(word("("));
93          def_inivalue.lookup("dvel1").append(word("("));
94   }
95 //Info<<"deformation initialiation done"<<endl;
96          // Proceed blade by blade.
97          forAll(windVectors[i], j)
98          {
99
100            //- interpolation force    fluid->structure
101            for(int m=0;m < numdefPoints[i]-3;m++)
102            {
103                fq0[i][j][m] = interpolate(cantileverRadius[i][j][m]-0.5*
     deltr[i], bladeRadius[i][j], Force0[i][j]);
104                fq1[i][j][m] = interpolate(cantileverRadius[i][j][m]-0.5*
     deltr[i], bladeRadius[i][j], Force1[i][j]);
105                fq0[i][j][m]=fq0[i][j][m]/db[i][0]*deltr[i]+(bladegravity
     [i][j][m] & bladeAlignedVectors[i][j][0])*deltr[i];
106            fq1[i][j][m]=fq1[i][j][m]/db[i][0]*deltr[i]+(bladegravity[i][j
     ][m] & bladeAlignedVectors[i][j][1])*deltr[i];
107
108                //- save sectional force gravity and centrifugal force
```

191

```
109                         gravitylong[i][j][m]=Gc[turbineTypeID[i]][0][m]/dens[
        turbineTypeID[i]][0][m]*(bladegravity[i][j][m] & bladeAlignedVectors
        [i][j][2]);//gravity force normal section
110                         centriforce[i][j][m]=rotSpeed[i]*rotSpeed[i]*Nc[
        turbineTypeID[i]][0][m];//centrifugal force normal section
111                     }
112  //Info<<"interpolation force done"<<endl;
113                 //- boundary condition for M, second order in space
114                 M00[i][j][numdefPoints[i]-1]=0.0;
115                 M10[i][j][numdefPoints[i]-1]=0.0;
116                 //- boundary condition for S, second order in space
117                 Sc00[i][j][numdefPoints[i]-1]=0.0;
118                 Sc10[i][j][numdefPoints[i]-1]=0.0;
119                 //- first computation loop for v (v from 2~(N-2), parameters
        from 0~(N-4))
120                 for(int m=2;m < numdefPoints[i]-1;m++)
121                 {
122                         v01[i][j][m]=v00[i][j][m]-deltt[i]/dens[turbineTypeID[i
        ]][0][m-2]*(M00[i][j][m-1]-2*M00[i][j][m]+M00[i][j][m+1])/deltr[i]/
        deltr[i]+fq0[i][j][m-2]/dens[turbineTypeID[i]][0][m-2]*deltt[i]*
        fluidDensity[i];
123                         v11[i][j][m]=v10[i][j][m]-deltt[i]/dens[turbineTypeID[i
        ]][0][m-2]*(M10[i][j][m-1]-2*M10[i][j][m]+M10[i][j][m+1])/deltr[i]/
        deltr[i]+fq1[i][j][m-2]/dens[turbineTypeID[i]][0][m-2]*deltt[i]*
        fluidDensity[i];
124                         //- centrifugal correction
125      if (stifftype[i] == "centrifugal")
126      {
127         v01[i][j][m]=v01[i][j][m]+deltt[i]/dens[turbineTypeID[i]][0][m
        -2]*(Sc00[i][j][m]-Sc00[i][j][m-1])/1.0/deltr[i];
128         v11[i][j][m]=v11[i][j][m]+deltt[i]/dens[turbineTypeID[i]][0][m
        -2]*(Sc10[i][j][m]-Sc10[i][j][m-1])/1.0/deltr[i];
129      }
130
131                 }
132  //Info<<"velocity done"<<endl;
133                 //- boundary condition for v, second order in space
134                 v01[i][j][0]=0.0;
135                 v11[i][j][0]=0.0;
136                 //- second computation loop for M (M from 1~(N-3), parameters
         from 0~(N-4))
137                 for(int m=1;m < numdefPoints[i]-2;m++)
138                 {
139                         M01[i][j][m]=M00[i][j][m]+EI0[turbineTypeID[i]][0][m
        -1]*deltt[i]/deltr[i]/deltr[i]*(v01[i][j][m-1]-2*v01[i][j][m]+v01[i
        ][j][m+1])+EIc[turbineTypeID[i]][0][m-1]*deltt[i]/deltr[i]/deltr[i
        ]*(v11[i][j][m-1]-2*v11[i][j][m]+v11[i][j][m+1]);
```

```
140                       M11[i][j][m]=M10[i][j][m]+EI1[turbineTypeID[i]][0][m
       -1]*deltt[i]/deltr[i]/deltr[i]*(v11[i][j][m-1]-2*v11[i][j][m]+v11[i
       ][j][m+1])+EIc[turbineTypeID[i]][0][m-1]*deltt[i]/deltr[i]/deltr[i
       ]*(v01[i][j][m-1]-2*v01[i][j][m]+v01[i][j][m+1]);
141                   }
142               //- centrifugal force for S (S from 1~(N-3), parameters from
       0~(N-4))
143               if (stifftype[i] == "centrifugal")
144         {
145           for(int m=1;m < numdefPoints[i]-2;m++)
146           {
147             Sc01[i][j][m]=Sc00[i][j][m]+rotSpeed[i]*rotSpeed[i]*Nc[
       turbineTypeID[i]][0][m-1]*deltt[i]/1.0/deltr[i]*(v01[i][j][m]-v01[i
       ][j][m-1]);
148             Sc11[i][j][m]=Sc10[i][j][m]+rotSpeed[i]*rotSpeed[i]*Nc[
       turbineTypeID[i]][0][m-1]*deltt[i]/1.0/deltr[i]*(v11[i][j][m]-v11[i
       ][j][m-1]);
149               //- shearforce save
150                   shearforce0[i][j][m-1]=-1.0*(M01[i][j][m+1]-M01[i][j][m])
       /deltr[i]+Sc01[i][j][m];
151                   shearforce1[i][j][m-1]=-1.0*(M11[i][j][m+1]-M11[i][j][m])
       /deltr[i]+Sc11[i][j][m];
152           }
153               }
154  //Info <<"Moment done"<<endl;
155             if (stifftype[i] != "centrifugal")
156       {
157         for(int m=1;m < numdefPoints[i]-2;m++)
158         {
159           //- shearforce save
160                   shearforce0[i][j][m-1]=-1.0*(M01[i][j][m+1]-M01[i][j][m])
       /deltr[i];
161                   shearforce1[i][j][m-1]=-1.0*(M11[i][j][m+1]-M11[i][j][m])
       /deltr[i];
162         }
163               }
164  //Info <<"shearforce done"<<endl;
165           //- resave the M for interpolation
166             for(int m=1;m<numdefPoints[i]-2;m++)
167             {
168               M01_inter[i][j][m-1]=M01[i][j][m];
169               M11_inter[i][j][m-1]=M11[i][j][m];
170             }
171  //Info <<"save moment done"<<endl;
172         //- interpolation on critical section for stress recovery and
       fatigue analysis
173  //Info <<"interpolation start"<<endl;
```

```cpp
174    // Info<<"crisec"<<crisec[i]<<endl;
175    // Info<<"cantileverRadius"<<cantileverRadius[i][j]<<endl;
176    // Info<<"shearforce0"<<interpolate(crisec[i], cantileverRadius[i][j],
       shearforce0[i][j])<<endl;
177                shearforce0_cri[i][j]=interpolate(crisec[i],
       cantileverRadius[i][j], shearforce0[i][j]);
178    // Info<<"shearforce0 done"<<endl;
179                shearforce1_cri[i][j]=interpolate(crisec[i],
       cantileverRadius[i][j], shearforce1[i][j]);
180    // Info<<"shearforce1 done"<<endl;
181                gravitylong_cri[i][j]=interpolate(crisec[i],
       cantileverRadius[i][j], gravitylong[i][j]);
182    // Info<<"gravitylong done"<<endl;
183                centriforce_cri[i][j]=interpolate(crisec[i],
       cantileverRadius[i][j], centriforce[i][j]);
184    // Info<<"centriforce done"<<endl;
185                M0_cri[i][j]=interpolate(crisec[i], cantileverRadius[i][j],
       M01_inter[i][j]);
186    // Info<<"M0 done"<<endl;
187                M1_cri[i][j]=interpolate(crisec[i], cantileverRadius[i][j],
       M11_inter[i][j]);
188    // Info<<"M1 done"<<endl;
189    // Info<<"critical done"<<endl;
190            }
191
192            forAll(windVectors[i], j)
193            {
194
195    if (l == 0)
196    {
197    def_inivalue.lookup("M00").append(word("("));
198            def_inivalue.lookup("M10").append(word("("));
199            def_inivalue.lookup("Sc00").append(word("("));
200            def_inivalue.lookup("Sc10").append(word("("));
201            def_inivalue.lookup("v00").append(word("("));
202            def_inivalue.lookup("v10").append(word("("));
203            def_inivalue.lookup("dvel0").append(word("("));
204            def_inivalue.lookup("dvel1").append(word("("));
205    }
206
207            for(int n=0; n < numdefPoints[i];n++)
208            {
209                    if (l == 0)
210                {
211                    def_inivalue.lookup("M00").append(M00[i][j][n]);
212                    def_inivalue.lookup("M10").append(M10[i][j][n]);
213                    def_inivalue.lookup("Sc00").append(Sc00[i][j][n]);
```

```
214                    def_inivalue.lookup("Sc10").append(Sc10[i][j][n]);
215                    def_inivalue.lookup("v00").append(v00[i][j][n]);
216                    def_inivalue.lookup("v10").append(v10[i][j][n]);
217               }
218                    v00[i][j][n]=v01[i][j][n];
219                    M00[i][j][n]=M01[i][j][n];
220        Sc00[i][j][n]=Sc01[i][j][n];
221                    v10[i][j][n]=v11[i][j][n];
222                    M10[i][j][n]=M11[i][j][n];
223        Sc10[i][j][n]=Sc11[i][j][n];
224               }
225
226            for(int m = 0; m < numBladePoints[i]; m++)
227            {
228                //- interpolation the save force to the critical section
229
230
231                if (l == 0)
232                {
233                    def_inivalue.lookup("dvel0").append(dvel0[i][j][m]);
234                    def_inivalue.lookup("dvel1").append(dvel1[i][j][m]);
235                }
236          if((bladeRadius[i][j][m]>=cantileverstart[i])&&(bladeRadius[i][j
      ][m]<=(cantileverend[i])))
237          {
238             dvel0[i][j][m]=interpolate(bladeRadius[i][j][m],
      cantileverRadius[i][j],v00[i][j]);
239             dvel1[i][j][m]=interpolate(bladeRadius[i][j][m],
      cantileverRadius[i][j],v10[i][j]);
240                 //bladePoints[i][j][m]=bladePoints[i][j][m]+dvel0[i][j][
      m]*bladeAlignedVectors[i][j][0]*deltt[i]+dvel1[i][j][m]*
      bladeAlignedVectors[i][j][1]*deltt[i];
241
242          }
243             }
244
245          if (l == 0)
246    {
247          def_inivalue.lookup("Def0").append(Def0[i][j]);
248          def_inivalue.lookup("Def1").append(Def1[i][j]);
249    def_inivalue.lookup("M00").append(word(")"));
250          def_inivalue.lookup("M10").append(word(")"));
251          def_inivalue.lookup("Sc00").append(word(")"));
252          def_inivalue.lookup("Sc10").append(word(")"));
253          def_inivalue.lookup("v00").append(word(")"));
254          def_inivalue.lookup("v10").append(word(")"));
255          def_inivalue.lookup("dvel0").append(word(")"));
```

```
256          def_inivalue.lookup("dvel1").append(word(")"));
257      }
258              Def0[i][j]=Def0[i][j]+v00[i][j][numdefPoints[i]-2]*deltt[i];
259              Def1[i][j]=Def1[i][j]+v10[i][j][numdefPoints[i]-2]*deltt[i];
260          }
261
262          if (l == 0)
263      {
264          def_inivalue.lookup("M00").append(word(")"));
265          def_inivalue.lookup("M10").append(word(")"));
266          def_inivalue.lookup("Def0").append(word(")"));
267          def_inivalue.lookup("Def1").append(word(")"));
268          def_inivalue.lookup("Sc00").append(word(")"));
269          def_inivalue.lookup("Sc10").append(word(")"));
270          def_inivalue.lookup("v00").append(word(")"));
271          def_inivalue.lookup("v10").append(word(")"));
272          def_inivalue.lookup("dvel0").append(word(")"));
273          def_inivalue.lookup("dvel1").append(word(")"));
274      }
275          }
276      }
277
278        }
279          def_inivalue.lookup("M00").append(word(")"));
280          def_inivalue.lookup("M10").append(word(")"));
281          def_inivalue.lookup("Def0").append(word(")"));
282          def_inivalue.lookup("Def1").append(word(")"));
283          def_inivalue.lookup("Sc00").append(word(")"));
284          def_inivalue.lookup("Sc10").append(word(")"));
285          def_inivalue.lookup("v00").append(word(")"));
286          def_inivalue.lookup("v10").append(word(")"));
287          def_inivalue.lookup("dvel0").append(word(")"));
288          def_inivalue.lookup("dvel1").append(word(")"));
289    runTime_.write();
290
291 }
```

G.2 Implicit elastic actuator line code

```
1  void horizontalAxisWindTurbinesALM::deformation()
2  {
3
4
5
6      Info<<"deformation start hi this is perturb"<<endl;
```

```
7      // Proceed turbine by turbine.
8
9      IOdictionary def_inivalue
10     (
11      IOobject
12      (
13       "def_inivalue",
14       runTime_.constant(),"turbineProperties",
15       mesh_,
16       IOobject::MUST_READ,
17       IOobject::AUTO_WRITE
18      )
19     );
20
21     IOdictionary turbineArrayProperties
22     (
23         IOobject
24         (
25             "turbineArrayProperties",
26             runTime_.constant(),
27             mesh_,
28             IOobject::MUST_READ,
29             IOobject::AUTO_WRITE
30         )
31     );
32
33
34         Info<<"start1"<<endl;
35       //clear the initial values
36         def_inivalue.lookup("M00").clear();
37         def_inivalue.lookup("M10").clear();
38         def_inivalue.lookup("Def0").clear();
39         def_inivalue.lookup("Def1").clear();
40         def_inivalue.lookup("Sc00").clear();
41         def_inivalue.lookup("Sc10").clear();
42         def_inivalue.lookup("v00").clear();
43         def_inivalue.lookup("v10").clear();
44         def_inivalue.lookup("dvel0").clear();
45         def_inivalue.lookup("dvel1").clear();
46
47   //build new initial value
48
49         def_inivalue.lookup("M00").append(word("("));
50         def_inivalue.lookup("M10").append(word("("));
51         def_inivalue.lookup("Def0").append(word("("));
52         def_inivalue.lookup("Def1").append(word("("));
53         def_inivalue.lookup("Sc00").append(word("("));
```

```cpp
54          def_inivalue.lookup("Sc10").append(word("("));
55          def_inivalue.lookup("v00").append(word("("));
56          def_inivalue.lookup("v10").append(word("("));
57          def_inivalue.lookup("dvel0").append(word("("));
58          def_inivalue.lookup("dvel1").append(word("("));
59
60     forAll(windVectors, i)
61     {
62
63          turbineArrayProperties.subDict(turbineName[i]).lookup("Azimuth")
    .clear();
64          turbineArrayProperties.subDict(turbineName[i]).lookup("Azimuth")
    .append(azimuth[i]/degRad);
65          turbineArrayProperties.subDict(turbineName[i]).lookup("RotSpeed"
    ).clear();
66          turbineArrayProperties.subDict(turbineName[i]).lookup("RotSpeed"
    ).append(rotSpeed[i]/rpmRadSec);
67          turbineArrayProperties.subDict(turbineName[i]).lookup("TorqueGen
    ").clear();
68          turbineArrayProperties.subDict(turbineName[i]).lookup("TorqueGen
    ").append(torqueGen[i]);
69          turbineArrayProperties.subDict(turbineName[i]).lookup("Pitch").
    clear();
70          turbineArrayProperties.subDict(turbineName[i]).lookup("Pitch").
    append(pitch[i]);
71          turbineArrayProperties.subDict(turbineName[i]).lookup("NacYaw").
    clear();
72          turbineArrayProperties.subDict(turbineName[i]).lookup("NacYaw").
    append(nacYaw[i]/degRad);
73
74
75
76          deltt[i]=dt/1.0;
77          for(int l=0;l<1;l++)
78          {
79
80          if (actuatorlinetype[i] == "elastic")
81     {
82
83     if (l == 0)
84     {
85
86          def_inivalue.lookup("M00").append(word("("));
87          def_inivalue.lookup("M10").append(word("("));
88          def_inivalue.lookup("Def0").append(word("("));
89          def_inivalue.lookup("Def1").append(word("("));
90          def_inivalue.lookup("Sc00").append(word("("));
```

```
91            def_inivalue.lookup("Sc10").append(word("("));
92            def_inivalue.lookup("v00").append(word("("));
93            def_inivalue.lookup("v10").append(word("("));
94            def_inivalue.lookup("dvel0").append(word("("));
95            def_inivalue.lookup("dvel1").append(word("("));
96    }
97
98            // Proceed blade by blade.
99            forAll(windVectors[i], j)
100           {
101
102              //- assembly the global matrix search every single control
       point each point is a matrix
103               for(int m=1;m < numdefPoints[i]-1;m++)
104               {
105
106      // Info<<"initialization matrix"<<endl;
107       //- A matrix
108      Am[0][0]=0.0;
109      Am[0][1]=0.0;
110      Am[0][2]=-1.0*deltt[i]/2.0/deltr[i]/deltr[i]/dens[turbineTypeID[
       i]][0][m-1];
111      Am[0][3]=0.0;
112      Am[1][0]=0.0;
113      Am[1][1]=0.0;
114      Am[1][2]=0.0;
115      Am[1][3]=-1.0*deltt[i]/2.0/deltr[i]/deltr[i]/dens[turbineTypeID[
       i]][0][m-1];
116      Am[2][0]=EI0[turbineTypeID[i]][0][m-1]*deltt[i]/2.0/deltr[i]/
       deltr[i];
117      Am[2][1]=EIc[turbineTypeID[i]][0][m-1]*deltt[i]/2.0/deltr[i]/
       deltr[i];
118      Am[2][2]=0.0;
119      Am[2][3]=0.0;
120      Am[3][0]=EIc[turbineTypeID[i]][0][m-1]*deltt[i]/2.0/deltr[i]/
       deltr[i];
121      Am[3][1]=EI1[turbineTypeID[i]][0][m-1]*deltt[i]/2.0/deltr[i]/
       deltr[i];
122      Am[3][2]=0.0;
123      Am[3][3]=0.0;
124       //Info<<"initialization matrix B"<<endl;
125       //- B matrix
126      // damp[i]=10.0;//comtemprary
127      Bm[0][0]=1.0+damp[i]*4.0*3.1415926/100.0*deltt[i];
128      Bm[0][1]=0.0;
129      Bm[0][2]=-1.0*deltt[i]/deltr[i]/deltr[i]/dens[turbineTypeID[i
       ]][0][m-1];
```

```cpp
130        Bm[0][3]=0.0;
131        Bm[1][0]=0.0;
132        Bm[1][1]=1.0+damp[i]*4.0*3.1415926/100.0*deltt[i]; //+damp[i
       ]*4.0*3.1415926/100.0*deltt[i];
133        Bm[1][2]=0.0;
134        Bm[1][3]=-1.0*deltt[i]/deltr[i]/deltr[i]/dens[turbineTypeID[i
       ]][0][m-1];
135        Bm[2][0]=EI0[turbineTypeID[i]][0][m-1]*deltt[i]/deltr[i]/deltr[i
       ];
136        Bm[2][1]=EIc[turbineTypeID[i]][0][m-1]*deltt[i]/deltr[i]/deltr[i
       ];
137        Bm[2][2]=1.0;
138        Bm[2][3]=0.0;
139        Bm[3][0]=EIc[turbineTypeID[i]][0][m-1]*deltt[i]/deltr[i]/deltr[i
       ];
140        Bm[3][1]=EI1[turbineTypeID[i]][0][m-1]*deltt[i]/deltr[i]/deltr[i
       ];
141        Bm[3][2]=0.0;
142        Bm[3][3]=1.0;
143        //Info<<"initialization matrix C"<<endl;
144        //- C matrix
145        Cm[0][0]=0.0;
146        Cm[0][1]=0.0;
147        Cm[0][2]=-1.0*deltt[i]/2.0/deltr[i]/deltr[i]/dens[turbineTypeID[
       i]][0][m-1];
148        Cm[0][3]=0.0;
149        Cm[1][0]=0.0;
150        Cm[1][1]=0.0;
151        Cm[1][2]=0.0;
152        Cm[1][3]=-1.0*deltt[i]/2.0/deltr[i]/deltr[i]/dens[turbineTypeID[
       i]][0][m-1];
153        Cm[2][0]=EI0[turbineTypeID[i]][0][m-1]*deltt[i]/2.0/deltr[i]/
       deltr[i];
154        Cm[2][1]=EIc[turbineTypeID[i]][0][m-1]*deltt[i]/2.0/deltr[i]/
       deltr[i];
155        Cm[2][2]=0.0;
156        Cm[2][3]=0.0;
157        Cm[3][0]=EIc[turbineTypeID[i]][0][m-1]*deltt[i]/2.0/deltr[i]/
       deltr[i];
158        Cm[3][1]=EI1[turbineTypeID[i]][0][m-1]*deltt[i]/2.0/deltr[i]/
       deltr[i];
159        Cm[3][2]=0.0;
160        Cm[3][3]=0.0;
161
162            //- external force matrix
163          // Info<<"external force matrix fq0"<<endl;
```

```
164              fq0[i][j][m] = interpolate(cantileverRadius[i][j][m],
      bladeRadius[i][j], Force0[i][j]);
165              fq1[i][j][m] = interpolate(cantileverRadius[i][j][m],
      bladeRadius[i][j], Force1[i][j]);
166              fq0[i][j][m] = fq0[i][j][m]/db[i][0]*deltr[i]+(
      bladegravity[i][j][m-1] & bladeAlignedVectors[i][j][0])*deltr[i];
167       fq1[i][j][m] = fq1[i][j][m]/db[i][0]*deltr[i]+(bladegravity[i][j][m
      -1] & bladeAlignedVectors[i][j][1])*deltr[i];
168
169          //- save sectional force gravity and centrifugal force
170              gravitylong[i][j][m]=Gc[turbineTypeID[i]][0][m-1]/dens[
      turbineTypeID[i]][0][m-1]*(bladegravity[i][j][m-1] &
      bladeAlignedVectors[i][j][2]);//gravity force normal section
171              centriforce[i][j][m]=rotSpeed[i]*rotSpeed[i]*Nc[
      turbineTypeID[i]][0][m-1]+(bladegravity[i][j][m-1] &
      bladeAlignedVectors[i][j][2])*Gc[turbineTypeID[i]][0][m-1]/dens[
      turbineTypeID[i]][0][m-1];//centrifugal force normal section
172
173          // Info<<"external force matrix dm"<<endl;
174              dm[0]   = fq0[i][j][m]*deltt[i]/dens[turbineTypeID[i
      ]][0][m-1]-deltt[i]/2.0/deltr[i]/deltr[i]/dens[turbineTypeID[i]][0][
      m-1]*(M00[i][j][m-1]-2*M00[i][j][m]+M00[i][j][m+1])-deltt[i]/2.0/
      deltr[i]/dens[turbineTypeID[i]][0][m-1]*(Sc00[i][j][m-1]-Sc00[i][j][
      m+1])+v00[i][j][m];
175              dm[1]   = fq1[i][j][m]*deltt[i]/dens[turbineTypeID[i
      ]][0][m-1]-deltt[i]/2.0/deltr[i]/deltr[i]/dens[turbineTypeID[i]][0][
      m-1]*(M10[i][j][m-1]-2*M10[i][j][m]+M10[i][j][m+1])-deltt[i]/2.0/
      deltr[i]/dens[turbineTypeID[i]][0][m-1]*(Sc10[i][j][m-1]-Sc10[i][j][
      m+1])+v10[i][j][m];
176              dm[2]   = M00[i][j][m]+EI0[turbineTypeID[i]][0][m-1]*
      deltt[i]/2.0/deltr[i]/deltr[i]*(v00[i][j][m-1]-2*v00[i][j][m]+v00[i
      ][j][m+1])+EIc[turbineTypeID[i]][0][m-1]*deltt[i]/2.0/deltr[i]/deltr
      [i]*(v10[i][j][m-1]-2*v10[i][j][m]+v10[i][j][m+1]);
177              dm[3]   = M10[i][j][m]+EI1[turbineTypeID[i]][0][m-1]*
      deltt[i]/2.0/deltr[i]/deltr[i]*(v10[i][j][m-1]-2*v10[i][j][m]+v10[i
      ][j][m+1])+EIc[turbineTypeID[i]][0][m-1]*deltt[i]/2.0/deltr[i]/deltr
      [i]*(v00[i][j][m-1]-2*v00[i][j][m]+v00[i][j][m+1]);
178
179          //- two conditions for centrifugal force S
180          // Info<<"external force matrix ds"<<endl;
181          if (m==1)
182          {
183          dm[0]=fq0[i][j][m]*deltt[i]/dens[turbineTypeID[i]][0][m
      -1]-deltt[i]/2.0/deltr[i]/deltr[i]/dens[turbineTypeID[i]][0][m-1]*(
      M00[i][j][m-1]-2*M00[i][j][m]+M00[i][j][m+1])-deltt[i]/1.0/deltr[i]/
      dens[turbineTypeID[i]][0][m-1]*(Sc00[i][j][m]-Sc00[i][j][m+1])+v00[i
      ][j][m];
```

```cpp
184              dm[1]=fq1[i][j][m]*deltt[i]/dens[turbineTypeID[i]][0][m
-1]-deltt[i]/2.0/deltr[i]/deltr[i]/dens[turbineTypeID[i]][0][m-1]*(
M10[i][j][m-1]-2*M10[i][j][m]+M10[i][j][m+1])-deltt[i]/1.0/deltr[i]/
dens[turbineTypeID[i]][0][m-1]*(Sc10[i][j][m]-Sc10[i][j][m+1])+v10[i
][j][m];
185              }
186
187              if(m==numdefPoints[i]-2)
188              {
189              dm[0]=fq0[i][j][m]*deltt[i]/dens[turbineTypeID[i]][0][m
-1]-deltt[i]/2.0/deltr[i]/deltr[i]/dens[turbineTypeID[i]][0][m-1]*(
M00[i][j][m-1]-2*M00[i][j][m]+M00[i][j][m+1])-deltt[i]/1.0/deltr[i]/
dens[turbineTypeID[i]][0][m-1]*(Sc00[i][j][m-1]-Sc00[i][j][m])+v00[i
][j][m];
190              dm[1]=fq1[i][j][m]*deltt[i]/dens[turbineTypeID[i]][0][m
-1]-deltt[i]/2.0/deltr[i]/deltr[i]/dens[turbineTypeID[i]][0][m-1]*(
M10[i][j][m-1]-2*M10[i][j][m]+M10[i][j][m+1])-deltt[i]/1.0/deltr[i]/
dens[turbineTypeID[i]][0][m-1]*(Sc10[i][j][m-1]-Sc10[i][j][m])+v10[i
][j][m];
191              }
192
193
194        // Info<<"assembly global matrix"<<endl;
195        //- Assembly the global matrix G0
196        for(int n=0;n < 4;n++)
197        {
198        for(int mm=0;mm < 4;mm++)
199        {
200              G0[n+(m-1)*4][mm+(m-1)*4]=-1.0*Cm[n][mm];
201              G0[n+(m-1)*4][mm+(m)*4]=Bm[n][mm];
202              G0[n+(m-1)*4][mm+(m+1)*4]=-1.0*Am[n][mm];
203        }
204        }
205
206
207
208        // Info<<"assembly global matrix G1"<<endl;
209        //- Assembly the global matrix G1
210        for(int n=0;n < 4;n++)
211        {
212
213              G1[n+(m-1)*4][0]=G0[n+(m-1)*4][2];
214              G1[n+(m-1)*4][1]=G0[n+(m-1)*4][3];
215
216              for(int nn=2;nn < 4*numdefPoints[i]-10;nn++)
217              {
218                  G1[n+(m-1)*4][nn]=G0[n+(m-1)*4][nn+4];
```

```
219                    }
220
221                    G1[n+(m−1)∗4][4∗numdefPoints[i]−10]=G0[n+(m−1)∗4][4∗
         numdefPoints[i]−4];
222                    G1[n+(m−1)∗4][4∗numdefPoints[i]−9]=G0[n+(m−1)∗4][4∗
         numdefPoints[i]−3];
223                }
224        // Info<<"assembly global matrix ds"<<endl;
225        //− Assembly the matrix ds
226        for(int nn=0;nn < 4;nn++)
227        {
228            ds[(m−1)∗4+nn]=dm[nn];
229        }
230        // Info<<"end"<<endl;
231
232        }
233
234
235
236        //− assembly done
237        // Info<<"solving matrix"<<endl;
238        //− Matrix inversion
239        us=invimplicit(G1,numdefPoints[i],ds);//inverse matrix
240
241        //−next time step value velocity
242        for(int m=2;m<numdefPoints[i]−1;m++)
243        {
244          v01[i][j][m]=us[4+(m−2)∗4];
245          v11[i][j][m]=us[5+(m−2)∗4];
246        }
247          v01[i][j][numdefPoints[i]−1]=us[4∗numdefPoints[i]−10];
248          v11[i][j][numdefPoints[i]−1]=us[4∗numdefPoints[i]−9];
249
250        //−next time step value moment
251        for(int m=1;m<numdefPoints[i]−2;m++)
252        {
253          M01[i][j][m]=us[2+(m−1)∗4];
254          M11[i][j][m]=us[3+(m−1)∗4];
255        }
256          M01[i][j][0]=us[0];
257          M11[i][j][0]=us[1];
258
259        //−next time step centrifugal stress
260        for(int m=1;m<numdefPoints[i]−1;m++)
261        {
262            Sc01[i][j][m]=Sc00[i][j][m]+rotSpeed[i]∗rotSpeed[i]∗Nc[
         turbineTypeID[i]][0][m−1]∗deltt[i]/4.0/deltr[i]∗((v00[i][j][m+1]−v00
```

```cpp
           [i][j][m-1])+(v01[i][j][m+1]-v01[i][j][m-1]));
               Sc11[i][j][m]=Sc10[i][j][m]+rotSpeed[i]*rotSpeed[i]*Nc[
     turbineTypeID[i]][0][m-1]*deltt[i]/4.0/deltr[i]*((v10[i][j][m+1]-v10
     [i][j][m-1])+(v11[i][j][m+1]-v11[i][j][m-1]));
               shearforce0[i][j][m]=-1.0*(M01[i][j][m]-M01[i][j][m-1])/
     deltr[i]+Sc01[i][j][m];
               shearforce1[i][j][m]=-1.0*(M11[i][j][m]-M11[i][j][m-1])/
     deltr[i]+Sc11[i][j][m];


           }


// Info<<"shearforce0"<<interpolate(crisec[i], cantileverRadius[i][j],
     shearforce0[i][j])<<endl;
               shearforce0_cri[i][j]=interpolate(crisec[i],
     cantileverRadius[i][j], shearforce0[i][j]);
// Info<<"shearforce0 done"<<endl;
               shearforce1_cri[i][j]=interpolate(crisec[i],
     cantileverRadius[i][j], shearforce1[i][j]);
// Info<<"shearforce1 done"<<endl;
               gravitylong_cri[i][j]=interpolate(crisec[i],
     cantileverRadius[i][j], gravitylong[i][j]);
// Info<<"gravitylong done"<<endl;
               centriforce_cri[i][j]=interpolate(crisec[i],
     cantileverRadius[i][j], centriforce[i][j]);
// Info<<"centriforce done"<<endl;
               M0_cri[i][j]=interpolate(crisec[i], cantileverRadius[i][j],
     M01[i][j]);
// Info<<"M0 done"<<endl;
               M1_cri[i][j]=interpolate(crisec[i], cantileverRadius[i][j],
     M11[i][j]);



       }



       //- save the data
       forAll(windVectors[i], j)
       {

  if (1 == 0)
  {
  def_inivalue.lookup("M00").append(word("("));
       def_inivalue.lookup("M10").append(word("("));
       def_inivalue.lookup("Sc00").append(word("("));
       def_inivalue.lookup("Sc10").append(word("("));
       def_inivalue.lookup("v00").append(word("("));
       def_inivalue.lookup("v10").append(word("("));
```

```
298          def_inivalue.lookup("dvel0").append(word("("));
299          def_inivalue.lookup("dvel1").append(word("("));
300      }

301
302              for(int n=0; n < numdefPoints[i];n++)
303              {
304                      if (1 == 0)
305                  {
306                      def_inivalue.lookup("M00").append(M00[i][j][n]);
307                      def_inivalue.lookup("M10").append(M10[i][j][n]);
308                      def_inivalue.lookup("Sc00").append(Sc00[i][j][n]);
309                      def_inivalue.lookup("Sc10").append(Sc10[i][j][n]);
310                      def_inivalue.lookup("v00").append(v00[i][j][n]);
311                      def_inivalue.lookup("v10").append(v10[i][j][n]);
312                  }
313                      v00[i][j][n]=v01[i][j][n];
314                      M00[i][j][n]=M01[i][j][n];
315          Sc00[i][j][n]=Sc01[i][j][n];
316                      v10[i][j][n]=v11[i][j][n];
317                      M10[i][j][n]=M11[i][j][n];
318          Sc10[i][j][n]=Sc11[i][j][n];
319              }

320
321              for(int m = 0; m < numBladePoints[i]; m++)
322              {
323                  if (1 == 0)
324                  {
325                      def_inivalue.lookup("dvel0").append(dvel0[i][j][m]);
326                      def_inivalue.lookup("dvel1").append(dvel1[i][j][m]);
327                  }
328          if((bladeRadius[i][j][m]>=cantileverstart[i])&&(bladeRadius[i][j
      ][m]<=cantileverend[i]))
329          {
330              dvel0[i][j][m]=interpolate(bladeRadius[i][j][m],
      cantileverRadius[i][j],v00[i][j]);
331              dvel1[i][j][m]=interpolate(bladeRadius[i][j][m],
      cantileverRadius[i][j],v10[i][j]);
332                  // bladePoints[i][j][m]=bladePoints[i][j][m]+dvel0[i][j][m
      ]*bladeAlignedVectors[i][j][0]*deltt[i]+dvel1[i][j][m]*
      bladeAlignedVectors[i][j][1]*deltt[i];

333
334          }
335              }

336
337          if (1 == 0)
338      {
339          def_inivalue.lookup("Def0").append(Def0[i][j]);
```

```cpp
            def_inivalue.lookup("Def1").append(Def1[i][j]);
    def_inivalue.lookup("M00").append(word(")"));
            def_inivalue.lookup("M10").append(word(")"));
            def_inivalue.lookup("Sc00").append(word(")"));
            def_inivalue.lookup("Sc10").append(word(")"));
            def_inivalue.lookup("v00").append(word(")"));
            def_inivalue.lookup("v10").append(word(")"));
            def_inivalue.lookup("dvel0").append(word(")"));
            def_inivalue.lookup("dvel1").append(word(")"));
    }
                for(int m = 0; m < numBladePoints[i]; m++)
                {
                def0[i][j][m]=def0[i][j][m]+v00[i][j][m]*deltt[i];
                def1[i][j][m]=def1[i][j][m]+v10[i][j][m]*deltt[i];
                }
            }

            if (l == 0)
    {
            def_inivalue.lookup("M00").append(word(")"));
            def_inivalue.lookup("M10").append(word(")"));
            def_inivalue.lookup("Def0").append(word(")"));
            def_inivalue.lookup("Def1").append(word(")"));
            def_inivalue.lookup("Sc00").append(word(")"));
            def_inivalue.lookup("Sc10").append(word(")"));
            def_inivalue.lookup("v00").append(word(")"));
            def_inivalue.lookup("v10").append(word(")"));
            def_inivalue.lookup("dvel0").append(word(")"));
            def_inivalue.lookup("dvel1").append(word(")"));
    }
            }
    }

        }
            def_inivalue.lookup("M00").append(word(")"));
            def_inivalue.lookup("M10").append(word(")"));
            def_inivalue.lookup("Def0").append(word(")"));
            def_inivalue.lookup("Def1").append(word(")"));
            def_inivalue.lookup("Sc00").append(word(")"));
            def_inivalue.lookup("Sc10").append(word(")"));
            def_inivalue.lookup("v00").append(word(")"));
            def_inivalue.lookup("v10").append(word(")"));
            def_inivalue.lookup("dvel0").append(word(")"));
            def_inivalue.lookup("dvel1").append(word(")"));
    runTime_.write();

}
```

Appendix H

FEM anisotropic beam model code

```matlab
close all
clear all
clc

%% Setup the case

%Set base path
[ BECAS_basepath ] = BECAS_initialize ( ) ;

%Set folder path
addpath ( genpath ( fullfile ( BECAS_basepath , 'BECAS' , 'src' , 'matlab' ) ) )
addpath ( genpath ( fullfile ( BECAS_basepath , 'FRANS' , 'src' , 'matlab' ) ) )
addpath ( genpath ( fullfile ( BECAS_basepath , 'SHEFE' , 'src' , 'matlab' ) ) )

%known section
distance =[0  0.3  0.4  0.5  0.6  0.7  0.8  1.37  1.5  1.6  4.1  5.5  6.83  9  10.25  12
       14.35  17  18.45  20.5  22.55  24.6  26.65  30.75  32  34.85  37  38.95  41  42
       43.05  45  47.15  51.25  54.67  57.4  60.13];
distance1 =[0.3  0.4  0.5  0.6  0.7  0.8  1.37  1.5  1.6  4.1  5.5  6.83  9  10.25  12
       14.35  17  18.45  20.5  22.55  24.6  26.65  30.75  32  34.85  37  38.95  41  42
       43.05  45  47.15  51.25  54.67  57.4  60.13  61.5];
dis =[0  0.3  0.4  0.5  0.6  0.7  0.8  1.37  1.5  1.6  4.1  5.5  6.83  9  10.25  12
       14.35  17  18.45  20.5  22.55  24.6  26.65  30.75  32  34.85  37  38.95  41  42
       43.05  45  47.15  51.25  54.67  57.4  60.13  61.5];

%twist angle
rot =[13.31*ones (1 ,15) ,12.53 ,11.48 ,10.68 ,10.16 ,9.63 ,
9.01 ,8.4 ,7.79 ,6.54 ,6.18 ,5.36 ,4.75 ,4.19 ,3.66 ,
3.4 ,3.13 ,2.74 ,2.32 ,1.53 ,0.86 ,0.37 ,0.11 ,0];
rot=rot /180* pi ;

%finite element mesh
```

```matlab
27  d = 1.5 ;
28  dis1 =[0:d:61.5];
29  length = distance1 − distance ;
30
31  %aerodynamic force
32  force = xlsread ('C:\ Study  field \ thesis \ data \forceNREL5MW. xlsx ' , 'force ');
33  forcecolum = zeros (6∗ size ( dis1 ,2) ,1);
34
35  %azimuth angle
36  theta =2∗pi /2;
37
38  for  i =1:1: size ( dis1 ,2)
39       forcecolum (( i −1)∗6+1)= force ( i ,3);
40       forcecolum (( i −1)∗6+2)= force ( i ,2);
41  end
42
43  % initialization  of  global  matrix
44  KG= zeros (6∗ size ( dis1 ,2) ,6∗ size ( dis1 ,2));%stiffness  matrix
45  MG= zeros (6∗ size ( dis1 ,2) ,6∗ size ( dis1 ,2));%mass  matrix
46  FG= zeros (6∗ size ( dis1 ,2) ,1);%external  force
47
48
49  %%% Element  analysis
50
51  %stiffness  matrix  and  mass  matrix  from  sections
52  for  i =1:1:38
53  %%% Options
54  % Folder name contining input data (MUST BE DEFINED)
55  options . foldername = fullfile (BECAS_basepath , 'BECAS' , 'examples ' , '
          NREL5MW3_nrel_rotation ' , num2str ( i ));
56
57  %%% Build  arrays  for  BECAS
58  [ utils  ] = BECAS_Utils ( options  );
59
60  %%% Optional  mesh  checking  routine
61  [ meshcheck  ] = BECAS_CheckMesh ( utils  );
62
63  %%% Call BECAS module for  the  evaluation  of  the  cross  section  stiffness
          matrix
64  [ constitutive .Ks , solutions ] = BECAS_Constitutive_Ks ( utils );
65  Ksave (: ,: , i )= constitutive .Ks ;
66
67  %%% Call BECAS module for  the  evaluation  of  the  cross  section  mass  matrix
68  [ constitutive .Ms] = BECAS_Constitutive_Ms ( utils );
69  Msave (: ,: , i )= constitutive .Ms ;
70
71  end
```

```matlab
72
73
74  %interp the mass matrix and stiffness matrix
75  for i=1:6
76      for j=1:6
77          for k=1:size(dis1,2)
78              Kint(i,j,k)=interp1(dis,reshape(Ksave(i,j,:),1,size(dis,2)),
                    dis1(k));
79              Mint(i,j,k)=interp1(dis,reshape(Msave(i,j,:),1,size(dis,2)),
                    dis1(k));
80          end
81      end
82  end
83
84  %interp the twist angle
85  for i=1:size(dis1,2)
86      rot1(i)=interp1(dis,rot,dis1(i));
87  end
88
89  %% assembly matrix
90  for i=2:1:size(dis1,2)
91  % define variables
92  syms z;
93  % strain displacement matrix
94  B0=zeros(6,6);
95  B0(1,5)=-1;
96  B0(2,4)=1;
97  B1=diag([1,1,1,1,1,1]',0);
98  % polynomial matrix
99  N=[eye(6),z*eye(6),z^2*eye(6),z^3*eye(6)];
100 N1st=[eye(6),z*eye(6)];
101 Nd1st=[subs(N1st,z,dis1(i-1));subs(N1st,z,dis1(i))];
102
103 %Nd=[eye(6),zeros(6,6);eye(6),L*eye(6)];
104 NN=[subs(N,z,dis1(i-1));subs(N,z,dis1(i))];
105 N1=NN(1:12,1:12);
106 N2=NN(1:12,13:end);
107 Alpha1=[eye(12);zeros(12,12)];
108 Alpha2=[zeros(12,12);eye(12)];
109 Y1=Alpha1*inv(N1);
110 Y2=Alpha2-Alpha1*inv(N1)*N2;
111
112 % stiffness matrix
113 B=B0*N+B1*diff(N,'z');
114 D=int(B'*Kint(:,:,i)*B,'z',dis1(i-1),dis1(i));
115 P=Y2'*D*Y1;
116 Q=-1*(Y2'*D*Y2);
```

```matlab
117  Na=Y1+Y2*inv(Q)*P;
118  K=(Na)'*D*Na;
119
120  Nasave(:,:,i-1)=Na;
121
122  %record the stiffness
123  Kflap(i-1)=Kint(4,4,i);
124  Ktorsion(i-1)=Kint(6,6,i);
125  Massden(i-1)=Mint(1,1,i);
126
127  % Mass matrix
128  D=int(N'*Mint(:,:,i)*N,'z',dis1(i-1),dis1(i));
129  M=(Na)'*D*Na;
130
131  %force matrix
132  fe=forcecolum(6*(i-2)+1:6*i);
133  gravity=[Mint(1,1,i-1)*9.8*[cos(theta);0;sin(theta);0;0;0];Mint(1,1,i)
         *9.8*[cos(theta);0;sin(theta);0;0;0]];
134  Ffe=int((Na)'*N'*(N1st*inv(Nd1st)*(fe+gravity)),'z',dis1(i-1),dis1(i));
135
136  Nsave(:,:,i)=int((Na)'*N','z',dis1(i-1),dis1(i));
137
138  % assmbly global matrix
139  KG(1+6*(i-2):6*i,1+6*(i-2):6*i)=KG(1+6*(i-2):6*i,1+6*(i-2):6*i)+K;
140  MG(1+6*(i-2):6*i,1+6*(i-2):6*i)=MG(1+6*(i-2):6*i,1+6*(i-2):6*i)+M;
141  FG(1+6*(i-2):6*i,1)=FG(1+6*(i-2):6*i,1)+Ffe;
142  end
143
144  KGs=KG(7:end,7:end);
145  MGs=MG(7:end,7:end);
146  nodedis=dis1+1.5;
147
148  %%% modal analysis
149  [Mode,FreqM]=eig(KG(7:end,7:end),MG(7:end,7:end));%Mode
150  Structure_frequency=sqrt(diag(FreqM))/2/pi;%frequency
151  save('C:\paper\composite_structures\revised20171215\data\output\Mode.mat
         ','Mode','Structure_frequency');
152
153  %KGs1=diag(diag(Mode'*KGs*Mode));
154  %MGs1=diag(diag(Mode'*MGs*Mode));
155  Mode1=Mode(:,229:end);
156  KGs1=diag(diag(Mode1'*KGs*Mode1));
157  MGs1=diag(diag(Mode1'*MGs*Mode1));
158  save('C:\Study field\thesis\data\NREL_5MW\NREL5MWdata\
         stiffness_mass_data_10.mat','KGs','MGs','nodedis','Mint','Kint','
         dis1','Nsave','Nasave','KGs1','MGs1','Mode','Mode1');
159
```

```matlab
160  xlswrite('C:\Study field\thesis\data\Mode.xlsx',Mode,'mode25');
161
162  %% static analysis
163  DG=inv(KG(7:end,7:end))*FG(7:end);%displacement
164  Displacement=[zeros(6,1);DG];
165  xlswrite('C:\Study field\thesis\data\Displacement.xlsx',DG,'
         Displacement25');
166
167  %% recover generalized strain
168  for i=1:1:size(dis1,2)-1
169  strain1(:,i)=(Displacement(7+6*(i-1):12+6*(i-1))-Displacement(1+6*(i-1)
         :6*i))/d;
170  end
171  strain_save=strain1;
```

Appendix I

FDTD anisotropic beam model code

```matlab
close all
clear all
clc

%% Setup the case

%Set base path
[ BECAS_basepath ] = BECAS_initialize( );

%Set folder path
addpath(genpath(fullfile(BECAS_basepath,'BECAS','src','matlab')))
addpath(genpath(fullfile(BECAS_basepath,'FRANS','src','matlab')))
addpath(genpath(fullfile(BECAS_basepath,'SHEFE','src','matlab')))

%known section
dis=[0  0.7  1.6  2.5  3.4  4.3  5.2  6.1  7  8.75  10.5  12.25  14  15.75  17.5  19.25
     21  22.75  24.5  26.25  28  29.75  31.5  33.25];
dr=0.25;
dis1=0:dr:33.25;

for  i=1:1:24
%% Options
% Folder name contining input data (MUST BE DEFINED)
options.foldername=fullfile(BECAS_basepath,'BECAS','examples','windpact'
    ,num2str(i-1));

%% Build arrays for BECAS
[ utils ] = BECAS_Utils( options );

%% Optional mesh checking routine
[ meshcheck ] = BECAS_CheckMesh( utils );
```

```matlab
31 %% Call BECAS module for the evaluation of the cross section stiffness
        matrix
32 [constitutive.Ks,solutions] = BECAS_Constitutive_Ks(utils);
33 Ksave(:,:,i)=constitutive.Ks;
34
35 %% Call BECAS module for the evaluation of the cross section mass matrix
36 [constitutive.Ms] = BECAS_Constitutive_Ms(utils);
37 Msave(:,:,i)=constitutive.Ms;
38
39 end
40
41 for i=1:6
42     for j=1:6
43         for k=1:size(dis1,2)
44             Kint(i,j,k)=interp1(dis,reshape(Ksave(i,j,:),1,size(dis,2)),
    dis1(k));
45             Mint(i,j,k)=interp1(dis,reshape(Msave(i,j,:),1,size(dis,2)),
    dis1(k));
46         end
47     end
48 end
49
50 L=33.25;%length of the beam
51 N=size(Kint,3);%cell number
52 dr=0.25;%cell length
53
54 Mav=zeros(N*6,N*6+6);
55 Mam=zeros(N*6,N*6+6);
56
57 for j=1:N
58
59 rho=Mint(1,1,j);
60 xm=Mint(6,2)/rho;
61 ym=Mint(3,4)/rho;
62 Jx=Mint(4,4,j);
63 Jy=Mint(5,5,j);
64 Jxy=-Mint(4,5,j);
65 Jr=(Jx+Jy);
66
67
68 Ks=Kint(:,:,j);
69
70 Mp=[1,0,0,0,0,-ym;...
71       0,1,0,0,0,xm;...
72       0,0,1,ym,-xm,0;...
73       0,0,rho*ym/Jx,1,-Jxy/Jx,0;...
74       0,0,-rho*xm/Jy,-Jxy/Jy,1,0;...
```

214

```
75        -rho*ym/Jr , rho*xm/Jr ,0 ,0 ,0 ,1];

76

77   % Mp=eye(6,6);

78

79   A=[-1/rho/dr ,0 ,0 ,0 ,0 ,0;...
80         0 ,-1/rho/dr ,0 ,0 ,0 ,0;...
81         0 ,0 ,-1/rho/dr ,0 ,0 ,0;...
82         0 ,-1/2/Jx ,0 ,-1/Jx/dr ,0 ,0;...
83         1/2/Jy ,0 ,0 ,0 ,-1/Jy/dr ,0;
84         0 ,0 ,0 ,0 ,0 ,-1/Jr/dr];

85

86   B=[1/rho/dr ,0 ,0 ,0 ,0 ,0;...
87         0 ,1/rho/dr ,0 ,0 ,0 ,0;...
88         0 ,0 ,1/rho/dr ,0 ,0 ,0;...
89         0 ,-1/2/Jx ,0 ,1/Jx/dr ,0 ,0;...
90         1/2/Jy ,0 ,0 ,0 ,1/Jy/dr ,0;
91         0 ,0 ,0 ,0 ,0 ,1/Jr/dr];

92

93   C=[-1/dr ,0 ,0 ,0 ,-1/2 ,0;...
94         0 ,-1/dr ,0 ,1/2 ,0 ,0;...
95         0 ,0 ,-1/dr ,0 ,0 ,0;...
96         0 ,0 ,0 ,-1/dr ,0 ,0;...
97         0 ,0 ,0 ,0 ,-1/dr ,0;...
98         0 ,0 ,0 ,0 ,0 ,-1/dr];

99

100  D=[1/dr ,0 ,0 ,0 ,-1/2 ,0;...
101        0 ,1/dr ,0 ,1/2 ,0 ,0;...
102        0 ,0 ,1/dr ,0 ,0 ,0;...
103        0 ,0 ,0 ,1/dr ,0 ,0;...
104        0 ,0 ,0 ,0 ,1/dr ,0;...
105        0 ,0 ,0 ,0 ,0 ,1/dr];

106

107        Mav(1+(j-1)*6:6+(j-1)*6,1+(j-1)*6:6+(j-1)*6)=-inv(Mp)*A;
108        Mav(1+(j-1)*6:6+(j-1)*6,7+(j-1)*6:12+(j-1)*6)=-inv(Mp)*B;
109        Mam(1+(j-1)*6:6+(j-1)*6,1+(j-1)*6:6+(j-1)*6)=Ks*C;
110        Mam(1+(j-1)*6:6+(j-1)*6,7+(j-1)*6:12+(j-1)*6)=Ks*D;
111  end

112

113  Mav(:,end-5:end)=[];
114  Mam(:,1:6)=[];

115

116  M=Mav*Mam;

117

118  [V,D]=eig(M);
119  delt=2/max(max(D));

120

121  frequency=diag(sqrt(D))/2/pi;
```

```
122
123 save ( 'C:\paper\appliedenergy2\mode_casewindpact.mat' , 'dis1' , 'V' ) ;
```

Appendix J

Published and submitted papers

1. H. Meng, F. S. Lien, L. Li. (2018). "Elastic actuator line modelling for wake-induced fatigue analysis of horizontal axis wind turbine blade." Renewable Energy 116(Part A): 423-437. (https://doi.org/10.1016/j.renene.2017.08.074).

2. H. Meng, F. S. Lien, G. Glinka. "Study on the fatigue life of bend-twist coupling wind turbine blade based on anisotropic beam model and stress-based fatigue analysis method." Composite Structures (Under Revision).

3. H. Meng, F. S. Lien, G. Glinka, L. Li, J. Zhang. "Study on wake-induced fatigue on wind turbine blade based on elastic actuator line model and two-dimensional finite element model." Wind Engineering (Under Review).

4. H. Meng, F. S. Lien, J. F. Shen."Modelling of anisotropic beam for rotating composite wind turbine blade by using finite-difference time-domain (FDTD) method" (Ready to submit)